Recovery of critical metals from waste electronics using environmentally sustainable processes

Luke Martin Mark Kinsman

Doctor of Philosophy

The University of Edinburgh

2022

Preface and declaration

The author has been engaged in a programme of full-time research under the supervision of Professor Jason B. Love, Professor Carole A. Morrison and Professor Bryne T. Ngwenya at The University of Edinburgh since September 2018.

The work presented in this document is the original work of the author, except where references are made to other sources. No part of the work referred to in this thesis has been submitted previously in whole or in part for another degree or qualification from this or any other university or institute of learning. In accordance with university regulations this thesis does not exceed 100,000 words in length

Luke Martin Mark Kinsman

March 2022

Lay Summary

Metals are essential to modern technology in the 21st century. The average smartphone contains up to 30 different chemical elements and our reliance on these elements is continually increasing with the continuous rise in consumer populations along with constant advances in technology. This rise in demand has led to the supply of many critical metals becoming under threat either because they are found in low concentrations in the earth or because they are extracted in conflict zones and are sold to perpetuate fighting.

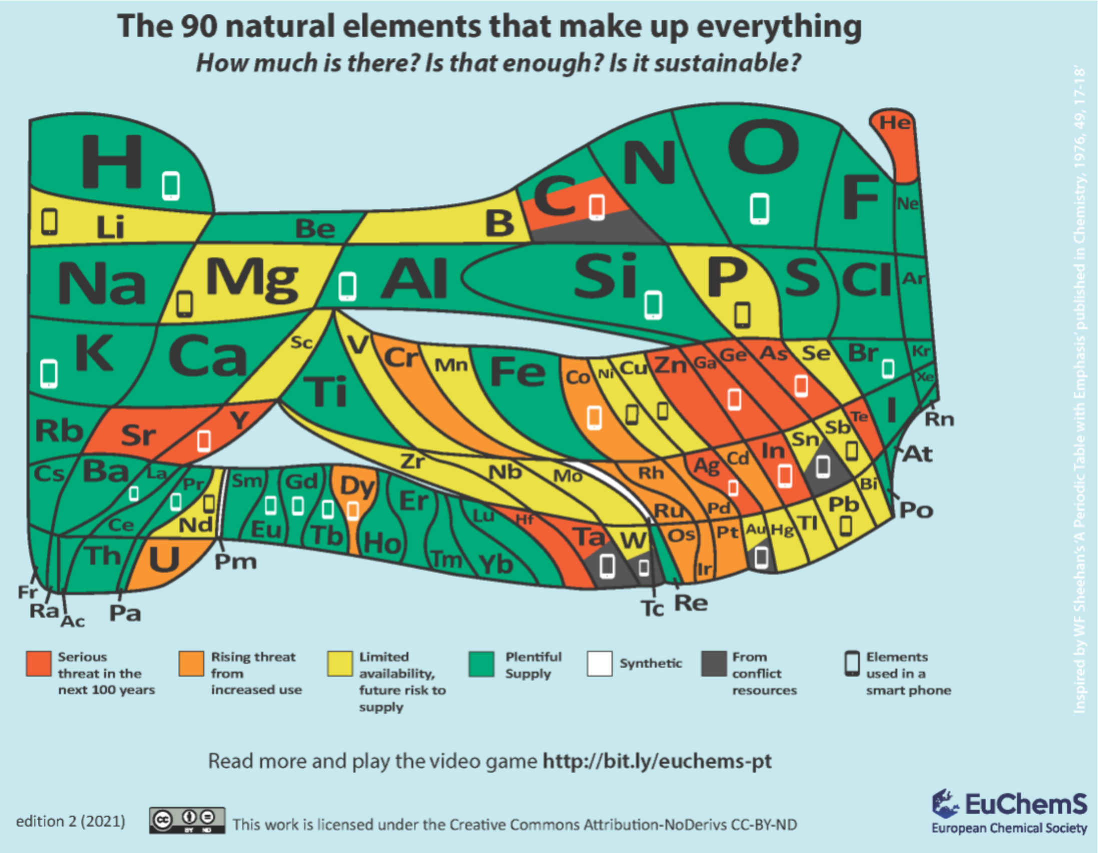

Figure 1 – EuChemS Periodic table of element abundance. The areas of each element relate to the number of atoms of each element on a logarithmic scale (some elements are excluded or have been exaggerated in size). Elements in red or orange face are of increasing concern if nothing is done to improve the supply or restrict its use. Elements in grey are sourced from mines in conflict zones.

Conventionally, metals are recovered from their natural sources (ores) by a process called extractive metallurgy. This requires vast amounts of energy and resources to separate metals from one another using either high temperatures (pyrometallurgy), solution chemistry (hydrometallurgy) or a combination of the two. Unfortunately, the highly complex nature of electronic waste means that current well-established extractive metallurgy processes are ineffective at properly recycling metals from e-waste and so recycling rates of critical metals are very poor. Waste electronics are becoming one of the fastest growing global waste streams and so it has never been more important to design metal separation processes for the recycling of metals from electronic waste in order to conserve natural resources and provide resource security. Furthermore, some of the metals used in electronic waste can be present in higher concentrations than in their natural ores and so this waste stream can be viewed as a valuable “secondary resource”. This work aims to use and advance some of the well-established methods of extractive hydrometallurgy so that resource critical metals may be separated from electronic waste and circular economy visions may be realised.

Specifically, this work focusses on the design and use of simple reagents that can selectively associate with a desired metal in preference to others in solution. The target metal can then be separated by a technique called solvent extraction, where the reagent transfers the target metal from a water-based liquid to an oil-based liquid, or by precipitation, where the target metal and reagent form an insoluble solid (the precipitate) that can be filtered off and separated from the other metals that remain in solution. This work also seeks to better understand some of the underlying chemistry that underpins these metal separation processes so that more efficient and selective reagents may be developed.

Abstract

Electronic waste (e-waste) is one of the fastest growing global waste streams with almost 54 million tonnes being generated in 2018. Only 20-30% of e-waste is currently recycled and can be attributed to its complex composition, comprising a myriad of different metals of varying future use and value. With many metals in e-waste present in greater quantities than their primary ores, e-waste can be viewed as a valuable secondary source of precious and base metals. This work aims to develop and understand new reagents that can selectively recover valuable and resource-critical metals typically found in e-waste.

Chapter 2 evaluates simple primary (1°), secondary (2°), and tertiary (3°) amides as reagents that selectively separate gold from other metals typically found in e-waste by a solvent extraction process. Previous work has shown that while gold extraction efficiency from single metal solutions is ordered 3° > 2° > 1°, the 3° and 2° amides are ineffective at gold transport from mixed-metal solutions of concentrations representative of e-waste due to the formation of insoluble third phases. This chapter examines the identities of the species that reside in the organic and third phases by a combination of mass spectrometry, NMR spectroscopy, and ICP-OES methods with a view to better understand what triggers 3rd phase formation. Some strategies to overcome this issue are then demonstrated.

Chapter 3 builds on the findings from Chapter 2 that differences in an extractant's structure can result in variable solvent extraction performance with, in some cases, precipitation being favoured. In changing from a branched aliphatic tertiary diamide to a simpler phenyl substituted diamide, selective precipitation of gold and other chloridometalates from complex acidic mixtures without the need for an organic diluent is found. The precipitation of a variety of metals from a range of HCl concentrations is examined, with the diamide being primarily selective for gold among up to 28 other elements. The X-ray crystal structure of $[HL^6][AuCl_4]$ displays an infinite chain of HL^+ cations, formed through an intermolecular proton chelate, interleaved with $AuCl_4^-$ anions. Tailoring of the selectivity of metal precipitation is demonstrated by altering either the HCl concentration or the stoichiometry of the precipitant with complete uptake of gold, iron, tin, and platinum by the diamide seen at 6 M HCl when excess precipitant is used, while only gold uptake is seen when one equivalent of diamide is used. A selective metal stripping process is developed; treatment of iron, tin and platinum precipitates with 2 M HCl releases the metals back in to solution, whereas gold is released quantitatively from the isolated precipitate as $HAuCl_4$ by contact with water, so recycling the diamide for further use. Factors governing the strength, selectivity and efficiency of precipitation were then explored by synthesising and testing derivatives of the tertiary diamide with differing structural and electronic properties.

Chapter 4 concerns the solvent extraction process for tantalum, which is typically extracted from acidic fluoride media. However, this work has shown that its extraction by the same 1° amide as used in Chapter 2 was more effective under chloride conditions compared to the typical fluoride conditions. The mode of action of the system is studied using similar techniques to Chapter 2, revealing that an anion-swing mechanism operates where tantalum is transported to the organic phase as its halometalate, $TaCl_6^-$, through an outer-sphere mechanism. In contrast to $TaCl_6^-$, transport of TaF_5Cl^- or TaF_6^- was poor; this is thought to be due to their greater charge densities, which carry higher hydration enthalpies. The process described provides a potentially safer, fluoride-free route to recycling Ta from waste electronics, using milder reagents than the current commercial methods.

Chapter 5 describes the use of a dual-purpose ionic liquid, methyltrioctylammonium iodide, for the selective transport of gallium from aqueous iron solutions into a toluene organic phase. The mode of action was probed by UV-Visible spectroscopy, ^{71}Ga NMR, electrospray ionisation mass-spectrometry and slope analysis. These techniques show that the iodide counter-ion is crucial in preventing the formation, and hence competitive transport, of $FeCl_4^-$ by reduction of Fe(III) to Fe(II), while Ga(III) is extracted as $GaCl_4^-$ forming a simple ion pair with the hydrophobic quaternary ammonium group.

Acknowledgements

First and foremost, thanks to my principal supervisor Professor Jason Love for his support and encouragement. I am particularly grateful for his enthusiasm for trying new ideas in the lab and all the advice while drafting papers, posters, talks and this thesis. I'm sure he will be glad to stop cringing at my casual (and at times deliberate) anthropomorphism of ligands or metals 'liking' things during group meetings! Thanks also to my co-supervisors Professor Carole Morrison and Professor Bryne Ngwenya for their guidance and productive discussions along the way; our chats were particularly helpful in reminding me to see the 'big picture' and their constant reassurance and positive feedback helped tremendously.

Much of the work in this thesis would not be possible without the technical help from staff within the school of chemistry. Special thanks to Dr Lorna Eades for her help with training, troubleshooting and maintenance on the ICP-OES, without it my thesis would be a bit thin! Thanks also to Dr Gary Nichol for X-Ray crystallography and to Dr Logan Mackay and Dr Faye Cruickshank for their help with Mass Spectrometry. Special thanks also to Lloyd Mitchell from the electrical workshop for his continued interest in my PhD and for going out of his way to find some 'high-quality' e-waste for me to chop up and dissolve. This allowed me to put some of the chemistry I'd developed to the ultimate test and laid the groundwork for me being able to make an engagement ring partially out of electronic waste – something that I'm so proud of and grateful for.

During my time at Edinburgh, one of my goals of the PhD was to simply have fun doing it. Despite a global pandemic getting in the way, I can safely say I have achieved that goal and massive thanks are owed in no small part to the following people for helping me realise it: Dr Rebecca Nicolson and Dr Jamie Hunter for being such fantastic colleagues, mentors and friends and for helping me learn the ropes of all things metal recovery. Thanks for putting up with my constant questions, both intellectual and obtuse (insert fishing bait emoji here)! Thanks also to my talented co-workers Andrew Carrick, Joseph O'Connell-Danes, Susanna Vance, Lotte van Rees, Tom Obey and Dr Abhijit Nag for the great conversations, sense of humour and for putting up with me for so long! Thanks also to Tom Lambert, Jay Gaston, Weronika Gruska and Annie Rae for being such fantastic people I'm proud to call friends and for all the hilarious chats involving all things politics, crosswords, porridge/soup/cereal, etc.

Thanks also to the 3rd year inorganic teaching lab technicians, Jen Anderson and Craig Ross, for putting up with me as a demonstrator for the past few years. Teaching was a fantastic and at times humbling experience but I absolutely loved the experience and the constant supply of biscuits and laughs was always a welcome distraction from research life.

Cheers to my close friends, Jonny and Jake for all of the distractions away from PhD and lockdown life, and to James, Henry, Ewan and Cameron (The Quaff) too. Many thanks to my family, specifically my parents for their unwavering support throughout everything I've done and to my aunt Fionna who inspired me to study chemistry in the first place.

Finally, to Debs. I can't put into words how much your love and support has helped me over the years. Thanks for your patience, your empathy, and for saying "Of course!" Thanks for always keeping me grounded and for all of the adventures we've been on. I can't wait for what's next.

Work presented in this thesis

Publications

Chapter 2

- "Evaluation of Simple Amides in the Selective Recovery of Gold from Secondary Sources by Solvent Extraction"
  E. D. Doidge, L. M. M. Kinsman, Y. Ji, I. Carson, A. J. Duffy, I. A. Kordas, E. Shao, P. A. Tasker, B. T. Ngwenya, C. A. Morrison, J. B. Love, ACS Sustainable Chem. Eng., 2019, 7, 15019-15029.

Chapter 3

- "Tuneable separation of gold by selective precipitation using a simple and recyclable diamide"
  L. M. M. Kinsman, B. T. Ngwenya, C. A. Morrison, J. B. Love, Nat. Commun**.,** 2021**,** 12, 6258.
- "Method of selective precipitation of metals using amide compounds"
  L. M. M. Kinsman, C. A. Morrison, B. T. Ngwenya, J. B. Love, 2021**,** UK Patent Application PE961477GB.
- "Exploring structure-activity relationships of diamides for selective metalate precipitation"
  L. M. M. Kinsman, S. Vance, R. Mao, J. Wang, G. S. Nichol, B. T. Ngwenya, C. A. Morrison, J. B. Love, Manuscript in preparation.

Chapter 4

- "Tantalum recycling by solvent extraction: chloride is better than fluoride"
  L. M. M. Kinsman, R. A. M. Crevecoeur, A. Singh-Morgan, B. T. Ngwenya, C. A. Morrison, J. B. Love, Metals, 2020, 10, 346.

Chapter 5

- "Reducing the competition: A dual purpose ionic liquid for the extraction of gallium from iron chloride solutions"
  L. M. M. Kinsman, C. A. Morrison, B. T. Ngwenya, J. B. Love, Molecules, 2020, 25, 4047.

Work contained within Chapter 2 was assisted by Yiran Ji and Chapter 4 by Rosa Crevocoeur and Amrita Singh-Morgan (final year undergraduate students) while under the supervision of the author. Work contained within Chapter 3 was assisted by Jungyang Wang and Ruizhe Mao (postgraduate taught students) while under the supervision of the author. Computational work in Chapter 3 was carried out by Professor Carole Morrison and Ms Susanna Vance. X-ray crystallographic data were collected by Dr Gary Nichol or Ms Karlotta Van Rees and solved by the author or by Dr Gary Nichol.

Conferences

- Universities of Scotland inorganic conference 2019, Glasgow, UK – 27th - 28th August 2019: Poster presentation (Evaluation of Simple Amides in the Selective Recovery of Gold from Secondary Sources by Solvent Extraction)

Prizes

- Best poster prize at Universities of Scotland inorganic conference 2019
- Co-recipient of the 2020 Anders Gustaf Ekeberg Tantalum Prize

Contents

Terms and abbreviations

δ	chemical shift
°C	degree centigrade
°	degrees
< >	less than, greater than
%	percent
~	approximately
[L]	ligand concentration
[M]	metal concentration
µ	micro
Å	angstrom
aq	aqueous
$CDCl_3$	deuterated chloroform
C_6D_6	deuterated benzene
CSD	Cambridge structural database
d	doublet (NMR)
DBC	dibutyl carbitol
DCM	dichloromethane
DFT	density functional theory
DMSO-d_6	deuterated dimethylsulfoxide
DOSY	Diffusion-ordered spectroscopy
e.g.	for example
ESI	electrospray ionisation (MS)
EXAFS	extended X-ray absorption fine structure
FT	fourier transform
g	gram
h	hour
HCl	hydrochloric acid
HNO_3	nitric acid
H_2SO_4	sulfuric acid
i.e.	that is
ICP-OES	inductively coupled plasma optical emission spectroscopy
K	kelvin
kJ mol^{-1}	kilojoules per mole
L	Ligand/extractant, litre
m	milli, metre
M	Moles per litre (molar), metal
MD	molecular dynamics
Me	methyl
MHz	frequency (NMR)
MIBK	Methyl isobutyl ketone
mg	milligram
min	minute
mL	millilitre
mmol	millimole
mol	mole
MS	mass spectrometry
m/z	mass to charge ratio
NMR	nuclear magnetic resonance
org	organic
PGMs	platinum group metals
pH	$-\log_{10}[H^+]$
pls	pregnant leach solution
ppm	parts per million
q	quartet (NMR)
s	singlet (NMR), seconds
SX	Solvent extraction
t	triplet (NMR)
T	temperature
^{t}Bu	tertiary butyl
TBP	tributyl phosphate
TOA	trioctylamine
tert	tertiary
THF	tetrahydrofuran
UV-VIS	Ultraviolet-Visible
via	by way of
vs	versus
WEEE	Waste Electrical and Electronic Equipment

Chapter 1

Introduction

1 Introduction

1.1 The urban mine(field)

Metals are finite resources which are essential to modern life, featuring heavily in consumer technologies, infrastructure, transport, catalysis and pharmaceuticals. Of the 30 or so chemical elements that make up a typical smartphone, natural sources of over half of these are becoming increasingly scarce in supply, six of which are due to run out in the next 100 years at current rates of consumption.[1] This is due to a growth in demand that is driven by global population growth, a larger proportion of people entering a wealthier middle class, and increasing consumer pressures for advances in design and functionality. As consumer technologies become more advanced, many old devices with a single purpose become superseded by devices with multiple functionalities, rendering the former obsolete. This has inadvertently resulted in large volumes of out-dated devices, or waste electrical and electronic equipment (WEEE, also referred to as electronic waste or e-waste). WEEE has become one of the fastest growing waste categories worldwide, increasing from 41.8 Mt being generated in 2014,[2] to 53.6 Mt in 2019 and is predicted to exceed 74 Mt by 2030.[3] In order to meet the future demand for these metals, resource critical elements must be sourced sustainably through a circular economy approach requiring more advanced metal recovery methods. Recycling of e-waste is beneficial in many ways. Recycling slows the exhaustion of natural resources; it avoids the creation of more waste products from mining and land scarring; recycling of e-waste will slow the rate at which landfill space is filled; and reportedly uses up to 90% less energy than metal-from-ore production.[4]

E-waste can be a lucrative secondary source of gold, with concentrations reaching up to 350 g ton^{-1} of gold depending on the type of e-waste; in contrast, 'natural' gold is found in ores and in the presence of other PGMs at around 1-2 g ton^{-1}.[5,6] In 2017, the value of gold in e-waste alone was estimated to be almost €19bn (table 1.1),[7] offering huge potential for the recycling industry to recover metals from secondary resources, otherwise known as the "urban mine". Indeed, it was found that metal recovery from secondary resources is gradually becoming more cost-effective than virgin mining,[8] especially as the volume of e-waste is projected to increase substantially; over the next few decades, new technologies become cheaper and more accessible, driving up the rate of device obsolescence.

Table 1.1 – Estimated value of selected raw materials from waste electronics.[7]

Material	Kilotons (kt)	Value (Million €)
Iron	16,283	3,582
Plastics	12,230	15,043
Aluminium	2,472	3,585
Copper	2,164	9,524
Silver	1.6	884
Gold	0.5	18,840
Palladium	0.2	3,369

Despite increased societal pressure to shift towards a more circular economy and the attractive financial opportunities that urban mining can present, significant challenges are present. Firstly, e-waste contains a much wider range of elements compared with conventional ores, where enormous effort is put into the design and composition of the device circuitry and that composition can be extremely variable depending on the type of e-waste. That is, the metal content from a mobile phone will be very different to that of a television and this will be further complicated by any residual plastics, ceramics or glass pieces that will also vary from device to device.[5,6] This variability in metal content must be accounted for by collecting large volumes of e-waste and then dismantling, shredding or pulverising it prior to any leaching steps; a challenge in and of itself given that only 17% of global electronic waste was properly recycled in 2019.[3] Speciality metals present in e-waste such as tantalum, indium and gallium are also used in small amounts, yet are less valuable than the precious metals and so the economic incentive to develop specific recovery methods for these metals from complex waste streams is lower despite their extreme risk to future supply. Even though the precious metals make up most of the value in PCBs, and are still a much more concentrated source of metal than ores, the base metals and plastics dominate in terms of weight. Therefore, any new methods developed with the aim of recovering these valuable metals from WEEE must be extremely selective and be able to tolerate a wide range of metal compositions. Furthermore, any separation methods designed to recover the less valuable yet supply-critical metals (e.g., Ta, Ga, or In) must not only be selective but also low cost and operationally simple to maximise economic viability.

This thesis will focus on tackling the complexity of e-waste recycling through the development of efficient and selective separation techniques for the various metals present. Extractive metallurgy is the primary method in which metals are refined from their ores into a purer form, and can, in principle,[6,9,10] also be applied to the recycling of metals from electronic waste.

1.2 Extractive Metallurgy

Extractive metallurgy relates to the recovery of metals from an ore or secondary source (such as WEEE) by metallurgical processes such as pyrometallurgy or hydrometallurgy. This process comprises four stages: concentration; separation; reduction; refinement.[11,12] Pyrometallurgy is historically the most common metal purification process, separating metals from their ores through the use of high temperatures and carbon reductants. This energy intensive process usually requires high grade ores to produce the desired metal in addition to large volumes of harmful emissions such SO_2 which are detrimental to the environment.

Hydrometallurgy processes ores or secondary sources *via* aqueous solutions to recover the target metals (figure 1.1). The initial step involves dissolving the metal source with a mineral acid or base to form a pregnant leach solution (PLS) that contains a mixture of metals. The following stages comprise a variety of separation and concentration techniques such as precipitation, crystallisation, distillation, ion-exchange, adsorption or solvent extraction.[12] These methods may be used successively in a particular process to give each metal in a single pure aqueous solution, which can then be reduced to its zero oxidation state for further use.

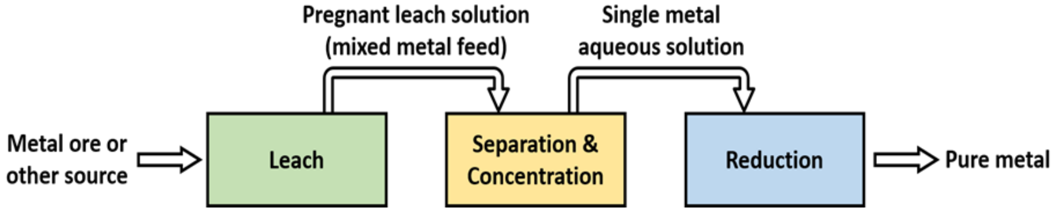

Figure 1.1 – Typical operations in hydrometallurgical processes.

1.3 Solvent extraction

Originally developed during the Manhattan Project for the separation of radioisotopes of uranium,[13] solvent extraction is well established for the purification of rare-earth elements, platinum group metals, and base metals such as copper, nickel and cobalt.[11,14] The aqueous mixed-metal feed is contacted with a water-immiscible organic solvent that contains a receptor or ligand (the extractant) that transports the desired metal from the aqueous phase to the organic phase as a lipophilic complex (figure 1.2). The organic solvent may be a high boiling point hydrocarbon such as kerosene, in which the metal complex is soluble. The two phases are separated manually and the metal-loaded organic phase treated with a stripping agent to return the metal into a fresh aqueous phase. The stripped extractant is regenerated for reuse in further cycles and the highly concentrated single-metal aqueous phase can be reduced to its metallic state, typically by electrowinning or through the addition of a reducing agent. Selective metal transport can be achieved by exploiting differences in the chemical/physical properties of the target metal, such as its propensity to form coordination complexes with a certain ligand due to, for example, atomic radii, preferred geometries or oxidation states.

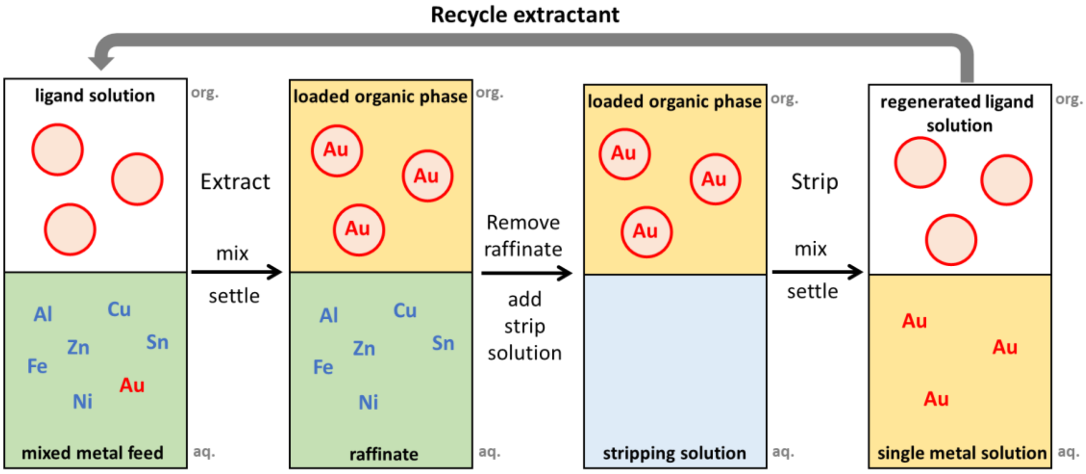

Figure 1.2 – Schematic diagram of the steps involved in a solvent extraction process.

Solvent extraction generally occurs at ambient temperature and can be suitable for large-scale continuous processing, which can result in good materials balances. However, for this to be achieved efficiently, the extractant must not degrade under the operating conditions of the process, *i.e.* the extractant must be stable to acid if the aqueous phase is strongly acidic. The extractant, and by extension any metal complex formed, must be highly soluble in the organic phase and have very low solubility in the aqueous phase in order to achieve significant separation. This is why most extractants feature long, branched alkyl chains to improve their hydrophobicity and solubility in the organic diluent.

1.4 Modes of metal recognition and separation

The underlying molecular chemistry behind many hydrometallurgical metal separation processes such as solvent extraction or precipitation is underpinned by coordination and supramolecular chemistry.[14,15] Often colloquially described as "chemistry beyond the molecule", supramolecular chemistry concerns the assembly of complex molecular systems held together by non-covalent interactions such as electrostatics, hydrogen bonding and hydrophobic interactions.[16] Host-guest chemistry is a particular branch of supramolecular chemistry pertinent to metal separation processes where the receptor molecule (the 'extractant') selectively interacts with the guest molecule (in this case, the target metal) to produce a 'host-guest' complex either by coordinate bonds, non-covalent interactions or a combination of both. The type of receptors used to separate metals in this way generally depends on the aqueous speciation of the target metal, and may be split into three different classes: cation extraction, metal-salt extraction, and anion or metalate extraction.[14] A brief overview of each is discussed, but more attention on metalate recognition is given as this is the focus of this Thesis.

1.4.1 Metal cation extraction

Cation-exchange reagents involve acidic ligands that deprotonate and bind to a target metal cation to form a charge-neutral complex that is soluble in the organic phase. As the ligand deprotonates and subsequently binds to the metal cation, protons are transferred into the aqueous phase resulting in an equilibrium process that can be controlled by pH (equation 1.1). Stripping is then achieved by contacting the loaded organic phase with an aqueous phase at a lower pH, regenerating the protonated extractant.[14,17]

$$M^{n+}{}_{(aq)} + nLH_{(org)} \rightleftharpoons [ML_n]_{(org)} + nH^{+}{}_{(aq)} \qquad (1.1)$$

Phenolic oximes are one example of this class of extractant and are used extensively in the separation and purification of copper, accounting for *ca.* 25% of world production.[14,18] Incorporating electron-donating or electron-withdrawing groups within the ligand results in altering the acidity of the ligand and therefore the strength of these reagents, and hence the stability of the resulting complexes can be controlled.[19–21]

The strength and selectivity for base-metal extraction generally follows the Irving-Williams order of stability and can be tuned by controlling the feed pH.[22] Additionally, the strong outer-sphere hydrogen bonding between the phenolic oxime ligands forms a pseudo-macrocyclic structure that results in a cavity appropriate for metal cations that adopt square planar geometries, such as Cu(II) (figure 1.3). It is for this reason that metals which preferentially adopt tetrahedral geometries, such as Zn(II), are less efficiently extracted by this particular reagent.

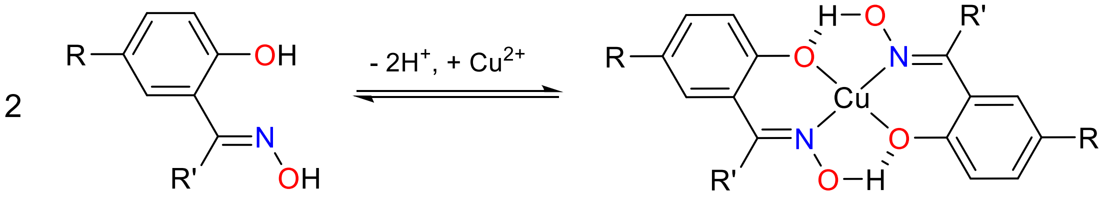

Figure 1.3 – *Pseudo*-macrocycle formation of phenolic oxime with the metal cation in a square-planar arrangement, stabilised by outer-sphere hydrogen bonding.[14]

Selectivity for 1st row, transition-metal dications favouring tetrahedral geometries is instead found by organophosphorus(V) acids, such as di-(2-ethylhexyl)phosphoric acid (D2EHPA) or Cyanex 272.[23] This is thought to be due to the characteristic of forming stable, dimeric, hydrogen-bonded structures in non-polar solvents. When extraction occurs, one of the strong intermolecular hydrogen bonds is retained and the formation of 8-membered hydrogen bonded pseudo-chelate rings provides a good fit for tetrahedral first-row dications (figure 1.4), accounting for the extensive use of D2EHPA in Zn(II) hydrometallurgical circuits and the selectivity for Co(II) over Ni(II) shown by Cyanex 272.[18,24]

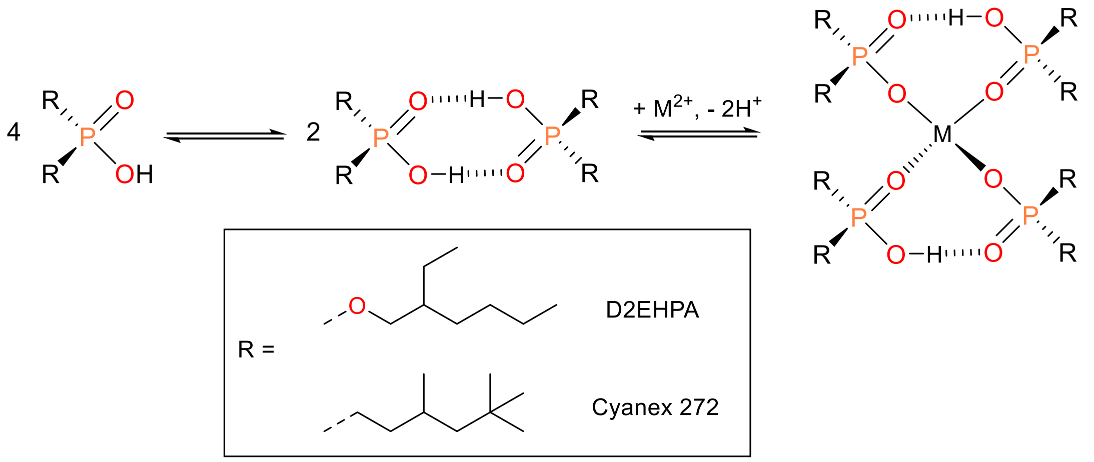

Figure 1.4 – Complex formation of phosphinic acid with the cation in a tetrahedral geometry, showing retention of the inter-ligand hydrogen bonding upon complex formation.

It is not difficult to imagine that these cation extractants can therefore be exploited to recycle base metals from e-waste given the very high concentrations of copper present. Indeed, proof-of-concept studies by several research groups have outlined potential hydrometallurgical routes for the recycling of base metals from waste PCBs using cation extractants.[25–27]

1.4.2 Metal salt extraction

Metal salt extraction involves transporting the metal cation or anion and its associated counterion(s) as a salt, MX_n, into the water-immiscible phase using a solvating agent. Perhaps the most commercially relevant example of metal salt extraction is the PUREX process in which spent nuclear fuel is dissolved in nitric acid and an organophosphorus extractant, tri-n-butylphoshate (TBP, figure 1.5, left) coordinates to U(VI) or Pu(IV) nitrates (figure 1.5, right).[28,29] The process is controlled by an ‘anion-swing’ mechanism, whereby increased uranyl loadings in the organic phase can be achieved at higher nitrate concentrations (equation 1.2). The uranyl ion may then be stripped back into the aqueous phase by contact with a more dilute nitrate solution.[18]

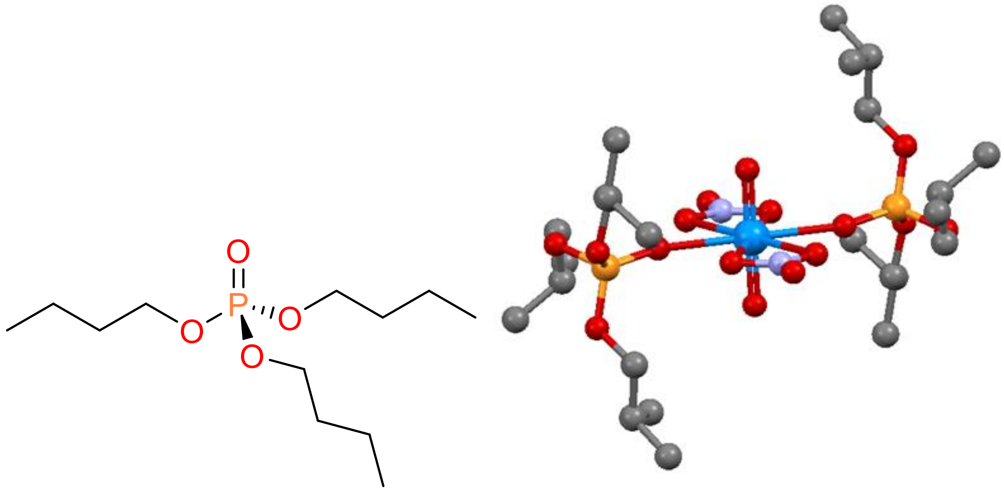

Figure 1.5 – Left: Structure of tri-n-butylphosphate, TBP. Right: X-ray structure of $[UO_2(NO_3)_2(\text{iso-TBP})_2]$.[30]

$$M^{n+}{}_{(aq)} + nX^{-}{}_{(aq)} + yL_{(org)} \rightleftharpoons [ML_yX_n]_{(org)} \qquad (1.2)$$

Metal salt extracting reagents such as TBP and diglycolamides can transport significant quantities of water into the organic phase and results in the formation of reverse-micelles in the organic phase.[31–34] Reverse-micelle formation can be key to facilitating transport of metals to the organic phase, where the metal salt is accommodated within a water 'pool' that is then solvated by polar head group of the extractant, and the lipophilic tails pointing outwards into the bulk of the non-polar solvent. Reverse-micelle formation however often results in poor metal selectivity as the water 'pool' can often incorporate multiple anions and cations with little discrimination and may also lead to poor phase disengagement or emulsion formation.

A more pertinent example of metal salt recognition to the work in this thesis involves the selective recognition and precipitation of the metal salt $KAuBr_4$ by α-cyclodextrin (α-CD, a 6-membered macrocycle of glucose) as a one-dimensional outer-sphere coordination polymer from pH-neutral aqueous solutions.[35] In this case, channels of hydrogen-bonded α-CD dimers form to incorporate $AuBr_4^-$ and $K(OH_2)_6^+$ in an alternating fashion through myriad C-H···Br-Au hydrogen bonds from the interior α-CD dimer cavities and O-H···Br-Au hydrogen bonds from the solvating water molecules of the K^+ ion (figure 1.6).

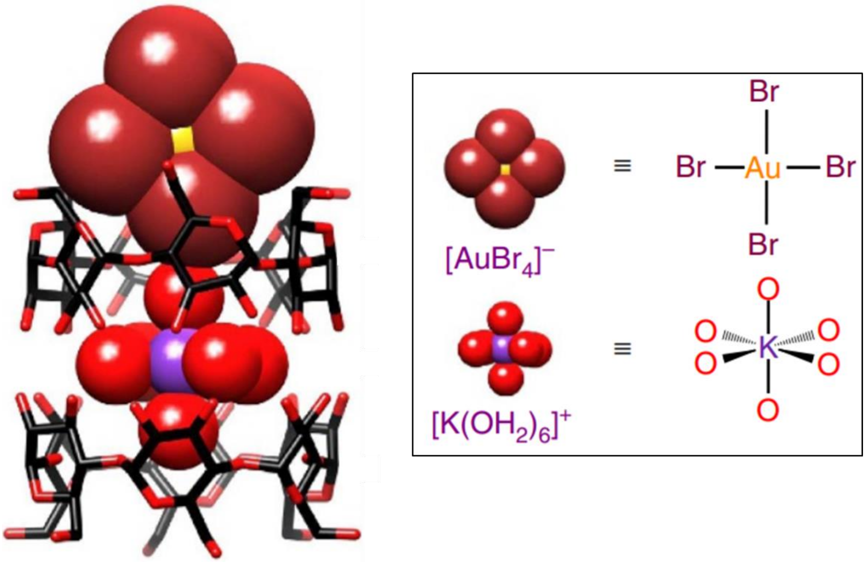

Figure 1.6 –Part of the x-ray crystal structure of $[K(OH_2)_6][AuBr_4]\subset(\alpha\text{-CD})_2$.[35]

Interestingly, co-precipitation was not observed upon switching from $AuBr_4^-$ to $AuCl_4^-$ due to a lack of O-H···Cl-Au hydrogen bonds resulting from the smaller size of $AuCl_4^-$. Furthermore, spontaneous co-precipitation was only observed between α-CD and $KAuBr_4$; the phenomenon was not observed with the larger β- or γ-cyclodextrins. Analysis of their X-ray structures revealed that the outer-spheres of $K(OH_2)_6^+$ and AuX_4^- were now coordinatively unsaturated, resulting in an increased exposure of K^+ to solvation from the bulk water and therefore impeding precipitation. A follow-up study confirmed that α-CD is highly selective for $KAuBr_4$.[36] Varying the cation (Na^+, K^+, Rb^+, or Cs^+), anion ($AuCl_4^-$ or $AuBr_4^-$) and host size (α-, β-, or γ-CD) resulted in co-precipitation occurring in only 3 out of the 24 possible permutations ($KAuBr_4$, $RbAuBr_4$, or $CsAuBr_4$ all with α-CD) with $KAuBr_4$ and α-CD co-precipitating in the highest yield. All other combinations remained in solution highlighting that subtle differences in cation, anion or host size can significantly impact the formation and stability of supramolecular assemblies driven by outer-sphere non-covalent interactions. Selectivity for $AuBr_4^-$ against other transition metals including square-planar PdX_4^{2-} and PtX_4^{2-} (X = Cl, Br) was also demonstrated, and the process has now been implemented in the commercial recovery of gold from ores by Cycladex.[37,38]

1.4.3 Metalate extraction

Metals that form the kinetically stable MCl_x^{n-} complexes under chloride conditions can vary in charge, shape and size (figure 1.7); therefore in some cases it is not practical to use cation exchange reagents. Instead, positively charged ligands can form neutral assemblies, or ion pairs, through non-covalent interactions such as electrostatics and hydrogen-bonds with metalates via the outer coordination sphere.[14,17]

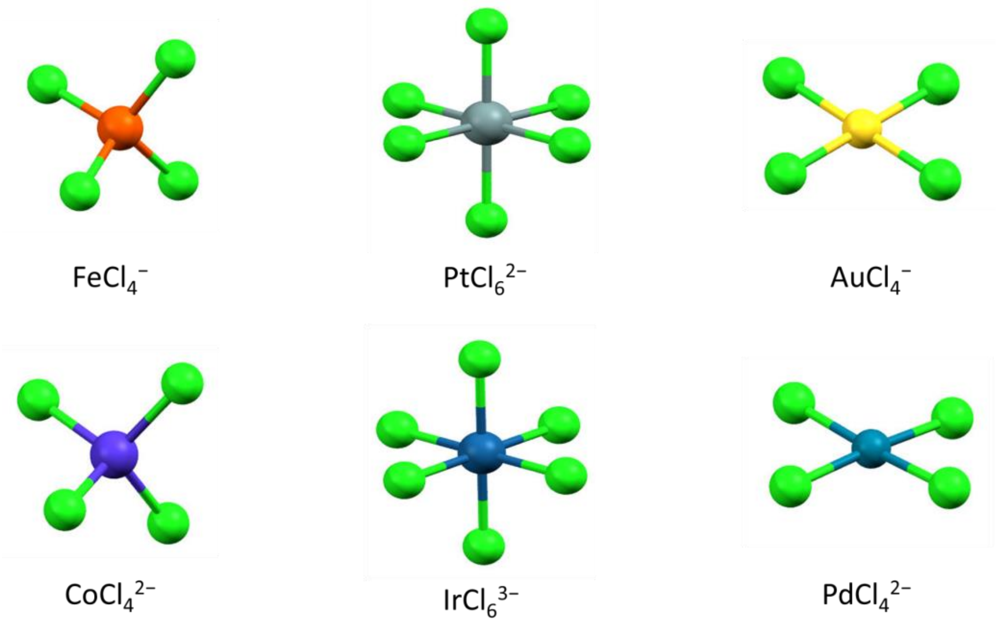
$FeCl_4^-$ $PtCl_6^{2-}$ $AuCl_4^-$

$CoCl_4^{2-}$ $IrCl_6^{3-}$ $PdCl_4^{2-}$

Figure 1.7 – Example metalates of different shapes and charges that may be present in a HCl solution.

Control of the metalate extraction equilibrium can be achieved by either varying the pH in cases where the receptor must first be protonated prior to any complexation (equation 1.3), or varying the anion concentration such that the target metal exists as the desired metalate species (equation 1.4). Conversely, contacting the metal-loaded organic phase with a fresh aqueous phase with a lower anion (or acid) concentration will back-extract the metal to the aqueous phase.

$$[MX_m]^{n-}{}_{(aq)} + nL_{(org)} + nH^+{}_{(aq)} \rightleftharpoons [MX_m][LH]_{n\ (org)} \tag{1.3}$$

$$M^{m+}{}_{(aq)} + nX^-{}_{(aq)} \rightleftharpoons [MX_n]^{(n-m)-}{}_{(aq)} \tag{1.4}$$

This strategy is only possible for metals which can readily form a metalate anion, and in significant quantities. If the metalate speciation changes across a range of chloride concentrations or over time, such as rhodium,[39] it becomes challenging to design an extractant for a given species. In addition, the high anion concentrations (e.g. chloride) required to facilitate metalate formation can lead to selectivity issues depending on the aqueous feed composition, or may lead to the anion out-competing the target metalate anion for extraction. Also, if the aqueous solution comprises many different metals, a wider assortment of metalates may be available for extraction, therefore increasing competition and decreasing selectivity.

The anion receptors used in metalate extraction are generally basic, such as amides,[40–42] amines,[43,44] ureas,[42] amidoethers,[45] and amidoamines[45–47] which can be protonated under the acidic conditions typical of leach solutions. Alternatively, quaternary ammonium salts, or ionic liquids, such as methyl trioctylammonium chloride can be used, exploiting the permanent positive charge on the ammonium group and exchanging the ‘hard’ chloride anion for a ‘softer’ more lipophilic metalate anion such as $AuCl_4^-$.[48]

N,N-dialkylsubstituted monoamides have been shown to be strong and selective extractants for gold over other PGMs and base metals.[9,49,50] Under acidic conditions, these weakly basic reagents form protonated dimeric-like units that can interact with the outer-sphere of charge-diffuse metalates through electrostatic and ‘soft’ C-H interactions. However, it can be difficult to strip the gold from the organic phase into a fresh aqueous solution, requiring additional reagents that affect the mass balance. These amide-gold assemblies can occasionally present solubility issues resulting in undesired third phase formation or phase disengagement issues. Third phase formation (also known as phase splitting) is an undesired yet common phenomenon in solvent extraction processes where an additional, distinct phase forms upon extraction that is insoluble in either the aqueous or organic phase.[51] Not only does it complicate phase separation, but it can result in loss of extraction efficiencies, ligand recycling issues and in some cases presents serious safety problems.[52]

Amidoamine receptors have been shown to have strong selectivity for the charge-diffuse $PtCl_6^{2-}$ metalate over chloride, in contrast to the tertiary amine trioctylamine which performs poorly in the high chloride concentrations typical of PGM refining circuits.[45–47,53] Protonation of the amidoamine results in a strong intramolecular proton-chelate forming between the protonated tertiary amine and the neighbouring amido oxygen group. This results in array of positively polarised C-H and N-H groups that are involved in hydrogen bonding to the faces and edges of the metalate (figure 1.8). Computational modelling calculations showed that multiple C-H···$PtCl_6^{2-}$ interactions were found to make a significant contribution to anion binding despite being weaker than individual N-H···$PtCl_6^{2-}$ interaction.[45]

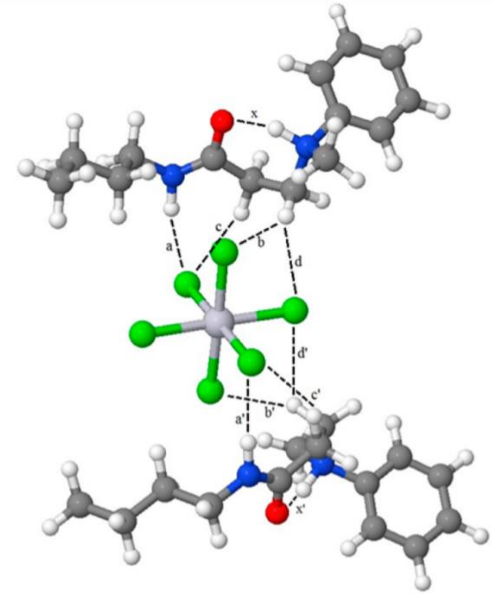

Figure 1.8 – Energy minimised structure of an amidoamonnium-$PtCl_6^{2-}$ complex featuring the key C-H···Pt and N-H···Pt interactions (annotated as a – c) and the intramolecular “proton chelate” (annotated as x).[45]

These outer-sphere interactions play an integral part in the selectivity of the larger, charge-diffuse metalates over the excess of ‘hard’ chloride anions which is reflected in the Hofmeister series.[54] The Hofmeister series states that small, charge-dense anions such as fluoride are more strongly hydrated than larger, charge-diffuse anions such as iodide which are less strongly hydrated and more hydrophobic in nature (figure 1.9).

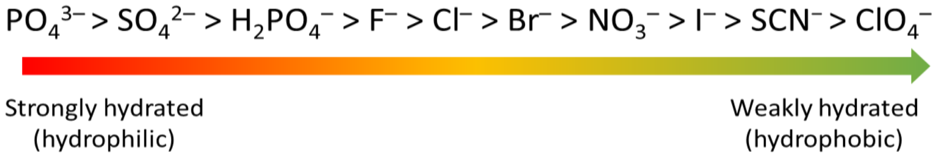

Figure 1.9 – The Hofmeister series of anion hydrophobicity.[54]

This principle of anion hydrophobicity can be extended to metalates, such that the charge diffuse species $AuCl_4^-$ will be extracted more readily than a more charge-dense metalate such as $IrCl_6^{3-}$ or a smaller, 'harder' anion such as Cl^-. More highly charged anions will therefore have a greater hydration enthalpy, and so more energy is required to displace any solvating water molecules prior to complex formation. PGMs in hydrochloric acid readily form chloridometalates at relatively low chloride concentrations. On the other hand, first-row transition metals such as iron and cobalt are more labile than the PGMs,[55,56] and therefore require higher chloride concentrations to form chloridometalates. Metalate extraction is therefore an excellent strategy to separate the valuable metals such as gold that are present in electronic waste at low concentrations from those in higher concentrations such as copper, tin or aluminium.

1.5 Thesis aims

The aim of this thesis is to investigate the extraction and separation of resource-critical metals present in e-waste by either solvent extraction or precipitation using simple ligands that can selectively recognise chloridometalate anions.

Chapter 2 appraises simple primary, secondary, and tertiary monoamides as reagents that selectively transport gold from aqueous to organic phases in a solvent extraction experiment. While the secondary and tertiary amides more efficiently extract gold from single metal solutions than primary amides, they are ineffective at gold transport from mixed-metal solutions of concentrations representative of e-waste due to the formation of a dense third phase which traps the gold thereby preventing transport into the organic phase. The identities of the species that reside in the organic and third phases have been studied by a range of methods, and strategies to overcome these issues are presented.

Chapter 3 builds on the insights gained from chapter 2 to develop a simple diamide reagent for the selective precipitation of gold from e-waste solutions, entirely avoiding the use of organic solvents. Selective and recyclable precipitation processes have become the focus of much attention lately as they can prevent the use of organic solvents and can provide many benefits over traditional single-use precipitants. Factors affecting metalate selectivity and precipitation efficiency are explored and insights into the mode of anion binding gained from X-ray crystallographic analyses.

Chapter 4 presents an alternative, fluoride-free route to extracting the conflict metal tantalum by using the simple primary amide studied in chapter 2, and comparing its solvent extraction performance of $TaCl_5$ versus the TaF_5 under chloride conditions. Despite little to no reports of $TaCl_5$ extraction in the literature, this chapter shows that extraction from chloride media is also possible by the primary amide and is more efficient than when the fluoride complex is used.

Chapter 5 concerns the separation of gallium from iron by a solvent extraction process. Under high chloride conditions, both metals exist in solution as the tetrahedral metalates, $FeCl_4^-$ and $GaCl_4^-$, rendering their discrimination by outer-sphere cationic receptors difficult. The selective separation of gallium from iron in HCl solution was achieved using methyltrioctylammonium iodide, with the reduction of Fe(III) to Fe(II) by iodide found central to inhibiting Fe transport.

Chapter 2

Evaluation of simple amides in the selective recovery of gold from secondary sources by solvent extraction

2 Evaluation of simple amides in the selective recovery of gold from secondary sources by solvent extraction

2.1 Overview

Historically used in jewelleries, arts and currencies due to its lustre, ductility and corrosion resistance, gold is a valuable and important metal. Modern applications of gold include medicines, chemical catalysis and as investments, but arguably the most important contemporary usage of gold lies in consumer electronics. Its malleability, chemical inertness and excellent electrical conductivity makes it a key component in printed circuit boards (PCBs) where it is typically electroplated on to other metals in connecting wires and strips.

The “urban mine” of electronic waste offers a significantly richer source of gold than can be found in primary ores, but due to the complex nature of e-waste, sophisticated yet simple separation methods to recycle these valuable and often critical metal resources are necessary.

In this chapter, current practices for gold recovery are outlined, and the use of simple primary, secondary and tertiary amides as reagents for the selective transport of gold from aqueous HCl solutions to organic phases is discussed. While the secondary and tertiary amides more efficiently extract gold from single-metal solutions, they are ineffective at gold transport from mixed-metal solutions of concentrations representative of electronic waste due to the formation of a dense third phase, which traps the gold thereby preventing transport into the organic phase for metal recovery. The identities of the species that reside in the organic and third phases are investigated by a combination of mass spectrometry, NMR spectroscopy, X-ray crystallography and ICP-OES methods with a view to better understand what triggers 3rd phase formation. Some strategies to overcome this issue are then demonstrated.

2.2 Current recovery methods of gold

2.2.1 Cyanidation of gold

The main method of gold recovery from primary sources (i.e. ores) by industry is the cyanidation process,[57,58] accounting for approximately 90% of gold production worldwide.[59] Part of this process involves spraying dilute sodium cyanide over low grade ores, in the presence of atmospheric oxygen to bring gold into solution as $Au(CN)_2^-$ (also known as 'heap leaching', equation 2.1). This redox process oxidises gold from Au(0) to Au(I) while reducing O(0) to O(2-). Cyanide binds to the gold ions to form an aqueous soluble complex that can be separated from the remaining solid residues.

$$4\ Au^0 + 8\ CN^- + O_2 + 2\ H_2O \rightleftharpoons 4\ Au(CN)_2^- + 4\ OH^- \qquad (2.1)$$

Elemental gold is then later precipitated by a sacrificial reducing agent, typically zinc powder, *via* a further redox reaction (equation 2.2) in a process known as 'cementation'.

$$2\ Au(CN)_2^- + Zn^0 \rightarrow 2\ Au^0 + Zn(CN)_4^{2-} \qquad (2.2)$$

The cementation technique has now been largely replaced by more selective adsorption processes where gold as $Au(CN)_2^-$ from the leach solution is selectively adsorbed on to activated carbon, a technique known as carbon-in-pulp.[60] Gold loaded particles are removed by filtration and then the gold complex can be stripped from the activated carbon by an energy intensive elution step, typically involving high temperatures, pressures, and large volumes of concentrated hydroxide or cyanide eluents.[61–63] Milder stripping protocols are being developed. Stoddart and co-workers recently demonstrated that α-cyclodextrin (α-CD) could strip $Au(CN)_2^-$ from activated carbon at room temperature by stirring a suspension of Au-loaded activated carbon with aqueous solutions of α-CD.[64] The cavity of α-CD is a good fit for the linear $Au(CN)_2^-$ molecule, and the resulting supramolecular adduct, $Au(CN)_2^- \subset \alpha$-CD, is stabilised by multiple non-covalent C-H···π and C-H···anion interactions.

The use of cyanide poses extreme toxicity hazards to personnel and the surrounding environment.[65,66] Even though the cyanide concentration is dilute, it must be kept above pH 10.5 to prevent the formation of hydrogen cyanide.[18] This is of utmost importance to minimise any industrial accidents and irreversible damage to the environment. Cyanide reagents are cheap and are therefore still widely used despite the well-documented safety and environmental concerns; however, some countries have started banning the use of cyanide and therefore alternative leaching techniques are required.

2.2.2 Alternatives to cyanide leaching

Alternatives to cyanide leaching include acidic solutions of thiocyanate, thiourea, and thiosulfate reagents;[67–70] however, despite being relatively inexpensive and considerably less toxic than cyanide, they are all less efficient and can require additional oxidising agents such as hydrogen peroxide.[6]

Mercury amalgamation is a technique widely used by small-scale and artisanal gold miners (often illegally) in developing nations.[71] The method is operationally simple and does not require complex machinery. Low-grade gold ores are crushed and contacted with mercury to form an amalgam that can be readily removed from the solids. The mercury is then distilled off to leave behind gold metal. Despite the operational simplicity and low cost of this method, exposure to mercury vapours is a major hazard to human health and the environment resulting in it being banned under the Minamata convention.[72]

More recently, approaches based on combinations of organic solvents and reactive ligands have been investigated as potential metal lixiviants.[73,74] Gold dissolution in organic media has been reported using synergistic mixtures of the strongly oxidising N-bromosuccinimide (NBS) and the coordinating solvent pyridine to produce a neutral $AuBr_3(py)$ complex via $AuBr_4^-$ formation.[75] Other methods mainly involve S-donor ligands such as pyridinethiol,[76] tetraethylthiuram disulfide,[77] or dithiobiuret;[78] each requiring the presence of an oxidant such as hydrogen peroxide, iodine or dilute aqua-regia mixtures.

2.2.3 Chloride leaching

It is well known that mineral acids such as hydrochloric and nitric acid cannot dissolve gold when used alone, but a 3:1 mixture of these two acids (known as aqua regia) can.[6,9] Mixing concentrated HCl and HNO_3 together results in several reactions that result in gold metal dissolution to form hydrogen tetrachloroaurate, $HAuCl_4$ (equations 2.3 and 2.4).

$$Au_{(s)} + 3\ HNO_{3\,(aq)} + 4\ HCl_{(aq)} \rightleftharpoons AuCl_4^-{}_{(aq)} + 3\ NO_{2\,(g)} + H_3O^+{}_{(aq)} + 2\ H_2O_{(l)} \tag{2.3}$$

$$Au_{(s)} + HNO_{3\,(aq)} + 4\ HCl_{(aq)} \rightleftharpoons AuCl_4^-{}_{(aq)} + NO_{(g)} + H_3O^+{}_{(aq)} + H_2O_{(l)} \tag{2.4}$$

While aqua regia is a reagent of choice among amateur gold refiners and hobbyists, mixtures of HCl and chlorine gas are used commercially for PGM refining circuits where gold and other PGMs are dissolved as their chloridometalates, MCl_x^{y-}.[9,18,79] In this process, $AuCl_4^-$ can be readily and selectively recovered from other chloridometalates by solvent extraction due to the Hofmeister bias, resulting in gold being recovered very early on in industrial flowsheets.[18]

2.2.4 Chloridometalate solvent extraction

Some of the most widely used reagents used commercially to recover $AuCl_4^-$ from HCl matrices by solvent extraction include methyl isobutylketone (MIBK) used by Johnson-Matthey and dibutyl carbitol (DBC) by INCO (figure 2.1).[14,80]

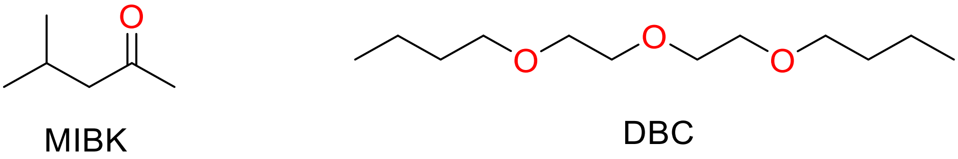

Figure 2.1 – Structures of MIBK and DBC.

DBC and MIBK are strong and selective extractants for gold over other PGMs, but which also co-extract other metals present from primary and secondary resources such as iron, tin and tellurium.[80] Large volumes of solvent are required, since the reagents must be used neat in order to maximise gold loading, which also brings safety concerns due to their volatilities. These reagents also face mass-balance and recyclability problems; when contacted with concentrated HCl solutions, the reagents are partly lost to the aqueous phase, which reduces extraction efficiency in further cycles. In some cases, the gold loaded reagent is simply incinerated to recover gold rather than employ basic reagents such as ammonia or urea to strip gold in to a fresh aqueous phase and regenerate the extractant.

Gold(III) can be extracted from HCl solution by solvent extraction with an extremely wide variety of other reagents with varying degrees of efficiency and selectivity, including but not limited to phosphinic acids, phosphonic and phosphoric acids,[81] phosphine oxides,[82–84] tertiary amines,[43,85] quaternary ammonium salts,[86] and even vacuum pump oil;,[87] however, this chapter will focus solely on amides.

2.3 Solvent extraction of $AuCl_4^-$ by simple monoamides

Previous work found that the simple primary amide, L^1, (figure 2.2) can transport gold and other chloridometalates from HCl solutions into an organic phase through an outer-sphere mechanism similar to that which may operate for other amide systems.[40,45,88] A 0.1 M toluene solution of primary amide L^1 recovered more than 90% of gold from 2–6 M HCl solutions. As the acid concentration increases, a greater proportion of L^1 is protonated and can therefore interact with anions such as $AuCl_4^-$ to form hydrophobic charge-neutral assemblies of the form described in equation 2.5. The amount of gold extracted into the organic phase decreases as the HCl concentration increases beyond 6 M, due to increasing competition of $[HL^1]^+$ between the metalate anions and the chloride ion.

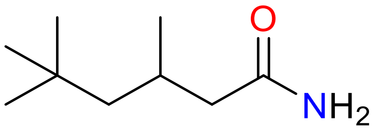

Figure 2.2 – Structure of the primary amide, L^1.

$$2\,L^1{}_{(org)} + H^+{}_{(aq)} + AuCl_4^-{}_{(aq)} \rightleftharpoons [AuCl_4(L^1H)(L^1)]_{(org)} \qquad (2.5)$$

The propensity for L^1 to extract metals other than gold was then studied in order to assess the potential for selective extraction (figure 2.3). It was found that at higher HCl concentrations, other metals such as Fe(III) and Ga(III), which form the tetrahedral metalates $FeCl_4^-$ and $GaCl_4^-$ respectively, are also efficiently extracted. Other metals such as Sn(IV) and Pt(IV) are extracted to a lesser extent, since they form the octahedral dianionic metalates $SnCl_6^{2-}$ and $PtCl_6^{2-}$ which are more negatively charged. These anions have higher hydration enthalpies compared with the monoanions and therefore are more difficult to transport into an organic phase in accordance with the Hofmeister bias. Some metals will only form chloridometalate anions at concentrations in which competitive chloride extraction dominates, while other metals do not form metalates at any HCl concentration and so are not extracted by L^1. Other more negatively charged metalates such as $IrCl_6^{3-}$ are much more highly hydrated and so the energetic penalty to desolvate and transfer them into the organic phase is too great. Selectivity for gold extraction over other metals was therefore optimal at 2 M HCl (figure 2.3). At this concentration only Au(III) was extracted to a significant extent (>90%), with only Sb(V) being a potential competitor.

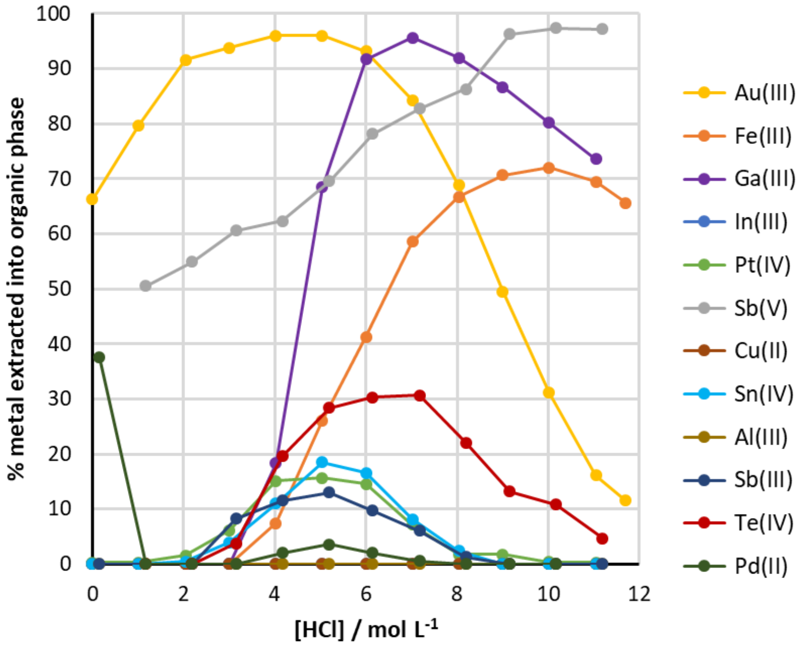

Figure 2.3 – Extractions from single metals (0.01 M) in aqueous HCl of varying concentrations into toluene using 0.1 M primary amide L^1 at a concentration of 0.1 M.[40]

Nearly 90% Au stripping from L^1 was achieved using water; in contrast, stripping from solutions derived from MIBK and DBC is more challenging, requiring ammonia or thiourea to drive back-transfer of the metalate.[12,79] Back-transfer of Au from other tertiary monoamides was also poor with water and so thiourea-HCl solutions were necessary to facilitate complete stripping.[49,50]

The identity of the Au/L^1 species in the organic phase was evaluated using a variety of experimental, spectroscopic, and computational techniques. Positive-ion electrospray ionisation mass spectrometry (ESI-MS) revealed the dominant gold-containing species as the ion pair $[(HL^1)(L^1)(AuCl_4)]$, though higher order species such as $[(HL^1)(HL^1)_2(AuCl_4)_2]$ and $[(HL^1)(HL^1)_3(AuCl_4)_3]$ were also present. This concurred with slope analysis, which found a non-integer ligand to gold ratio of 2.5-3:1, suggesting multiple gold-containing complexes were present in the organic phase. Density functional theory (DFT) corroborated the speciation seen by ESI-MS; the protonated diamide $(HL^1)(L^1)^+$ was found to be almost 90.4 kJ mol^{-1} more favourable than the protonated mono-amide $(HL^1)^+$. The resulting assembly, $[(HL^1)(L^1)(AuCl_4)]$ (figure 2.4, right), was 53.5 kJ mol^{-1} more favourable than equivalent monomeric assembly (figure 2.4, left).[40]

$(L^1)H(AuCl_4)$ $(L^1)_2H(AuCl_4)$

Figure 2.4 – Gaussian DFT geometry-optimised structures of $[(AuCl_4)(HL^1)]$ and $[(AuCl_4)(HL^1)(L^1)]$.[40]

Insights into the assembly of supramolecular clusters in the organic phase were also gained from classical molecular dynamics calculations. It was found that the $AuCl_4^-$ anions were bridged through $(HL)^+$, $(HL)(L)^+$, and $(HL)(L_3)^+$ amides with no short Au···Cl or Au···Au interactions (figure 2.5); these latter observations were consistent with EXAFS measurements which showed that only inner-sphere Au-Cl interactions were present.[40]

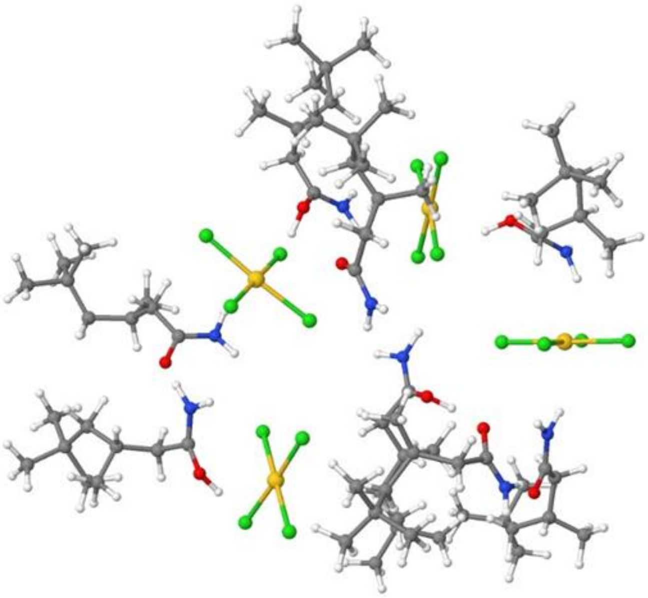

Figure 2.5 – Example geometry of an assembly of $AuCl_4^-$, L^1 and $(HL^1)(L^1)^+$ units obtained from a molecular dynamics simulation.[40]

With these results in mind, it is clear that gold is not extracted by a simple ion pair mechanism by L^1. Instead, hydrogen-bonding and electrostatic interactions appear central to the transport of gold into the organic phase by forming complex supramolecular assemblies.

When applied to a mixed-metal solution representative of WEEE,[89] L^1 showed excellent selectivity for gold compared with the commercial gold extractants (figure 2.6). Unlike the commercial reagents which were only optimal at extracting gold when used neat, L^1 could be used as a 0.1 M solution in toluene, and was highly selective for gold despite the competitive environment.[88]

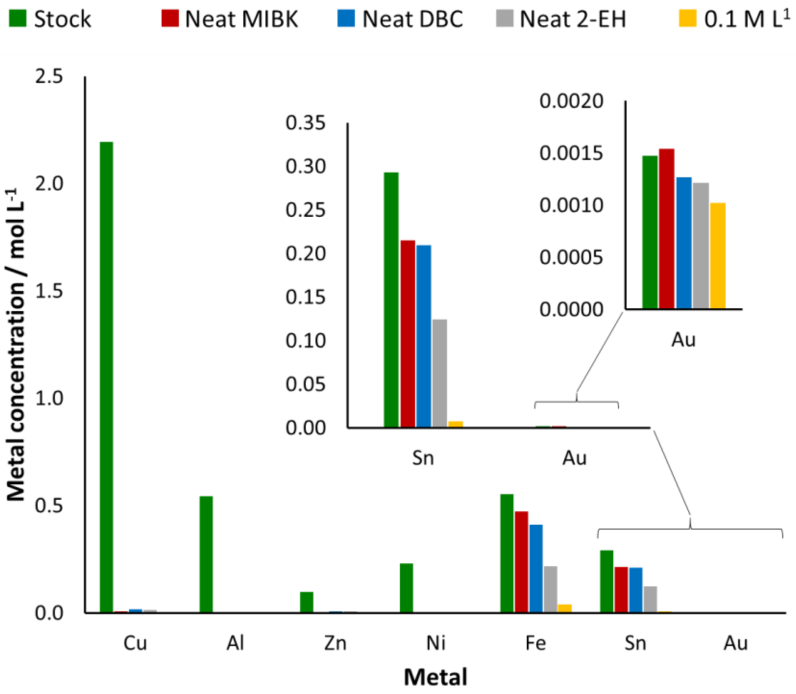

Figure 2.6 – Concentrations of metals extracted from a 2 M HCl mixed-metal feedstock (containing Cu 2.37, Al 0.57, Zn 0.11, Ni 0.24, Fe 0.61, Sn 0.28, Au 0.0012 M) representative of WEEE into toluene by neat commercial reagents (MIBK, DBC and 2-EH) and 0.1 M primary amide L^1.[88]

Contrary to primary amides, secondary and tertiary amides have been studied extensively in solvent extraction processes for PGM separation;[9,45,49,50] however, third phase formation during the solvent extraction process, compounded by challenging back-extraction conditions has led to their lack commercial uptake. Secondary and tertiary analogues of the primary amide L^1, L^2 and L^3 (figure 2.7), were subsequently synthesised to explore if similar problems arose.[88]

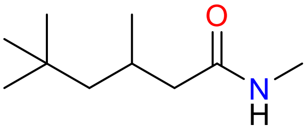
L^2

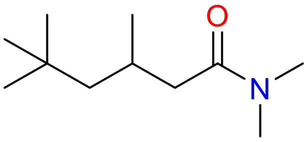
L^3

Figure 2.7 – Structures of the secondary and tertiary amides, L^2 and L^3.

It was found that L^2 and L^3 were stronger extractants than L^1 for the monoanions, $AuCl_4^-$, $FeCl_4^-$ and $GaCl_4^-$ from single-metal solutions, following the order $L^3 > L^2 > L^1$ (figures 2.8 and 2.9). This was rationalised by DFT calculations suggesting competitive chloride transport became increasingly less favourable from L^1 to L^3, and so the extraction efficiency could be maintained over a wider range of HCl concentrations than for L^1. Despite L^2 and L^3 more effectively extracting Fe and Ga at lower HCl concentrations than L^1, selectivity for tetrachloroaurate over the other monoanions could still, in principle, be maintained at 2 M HCl. Furthermore, based on these single-metal extraction experiments, L^2 and L^3 were potentially even more selective for the monoanions than L^1, with the dianionic metalates $SnCl_6^{2-}$ or $PtCl_6^{2-}$ being transported into the organic phase to a lesser extent, in contrast with L^1. As with L^1 and in contrast to other secondary and tertiary amides studied, back extraction of gold could be achieved by contacting the organic phase with water.

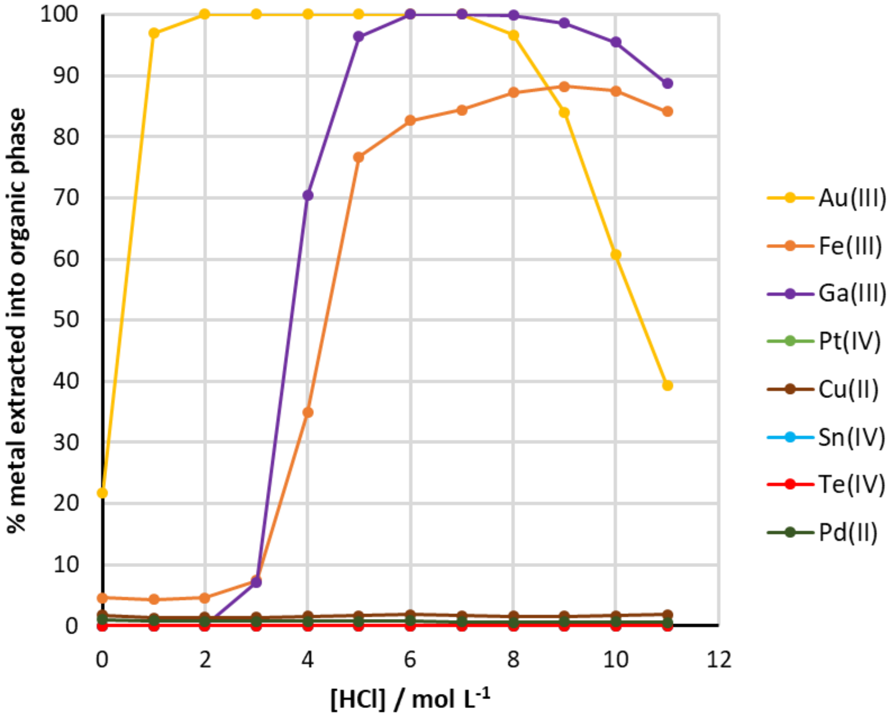

Figure 2.8 – Extractions from single metals (0.01 M) in aqueous HCl of varying concentrations into toluene using 0.1 M L^2.[88]

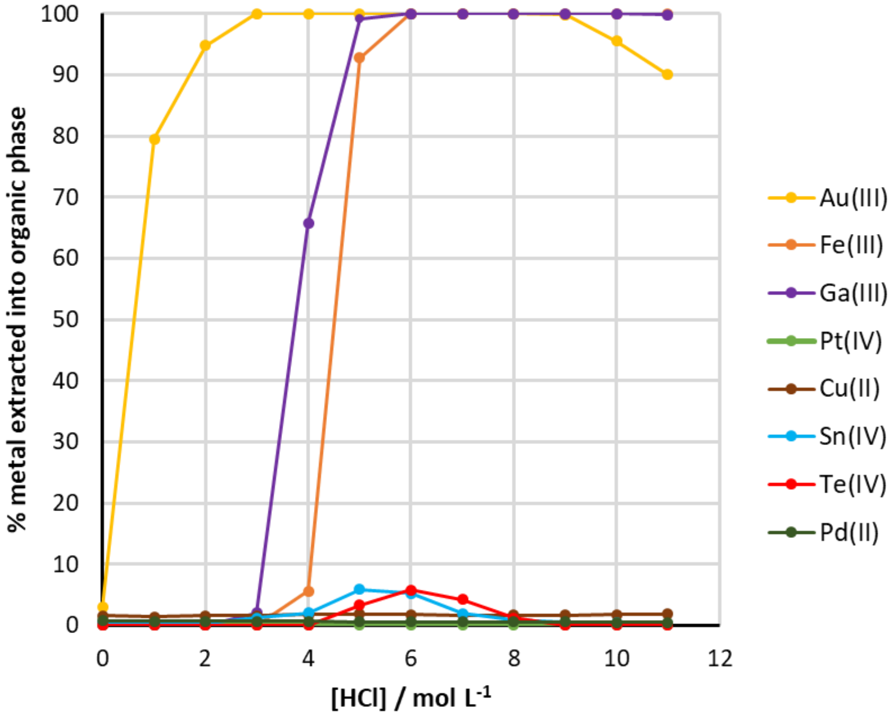

Figure 2.9 – Extractions from single metals (0.01 M) in aqueous HCl of varying concentrations into toluene using 0.1 M L^3.[88]

The identity of the gold containing complexes formed in the organic phase by L^2 and L^3 was investigated by positive-ion ESI-MS. Previously for L^1, the positive ESI-MS spectrum revealed the presence of ions of the general formula $[(AuCl_4)_n(HL^1_2)(HL^1)_{n-1}]H^+$, up to n = 4, comprising a basic unit of $(AuCl_4)(HL^1_2)H^+$, with each subsequent ion a stepwise addition of $(AuCl_4)(HL^1)$.[40]

Mass spectra of gold-loaded solutions of L^2 and L^3 were similar to those of L^1; gold-containing ions of the form $[(AuCl_4)_n(HL_2)(HL)_{n-1}]H^+$ are seen for L^2 and L^3, although clustered units containing more than one metalate were significantly less abundant than for L^1.[90] This suggested that the secondary and tertiary amides are less able to form large supramolecular aggregates with $AuCl_4^-$ than L^1 which is consistent with the removal of potential N-H hydrogen-bond donors, limiting the hydrogen-bonding interactions between the metalate and the amide receptors.

Classical molecular dynamics simulations were also used to further probe the interactions between L^2 and L^3 and $AuCl_4^-$. In similar behaviour to L^1 (figure 2.5), all simulations with L^2

and L^3 showed bridging hydrogen-bonding interactions seen between amides and multiple $AuCl_4^-$ anions, leading to the formation of supramolecular assemblies in which multiple metalates are close each other. Further analysis of the total count of amide N atoms found within a 4 Å distance from at least one chlorine atom over the course of the final 5 ns of MD production runs, expressed as a percentage of the maximum number of possible N···Cl interactions, were calculated (Table 2.1). These data showed that L^1 tends to reside closer to the metalate for longer than L^2 which in turn resides close to the metalate for longer than L^3. This can be explained by N-H···Cl interactions, of which there are fewer total interactions possible for L^2 than L^1, and are not possible with L^3. Overall the simulations suggested that the clusters formed by L^2 and L^3 are smaller and more dynamic than the clusters formed by L^1 and may help to rationalise the reduction in intensity of the ions formed from higher order assemblies in the mass spectra for gold transport by L^2 and L^3 compared with L^1.

Table 2.1 – The percentage of amide nitrogen atoms located within a distance of 4 Å from at least one chloride atom, expressed with respect to the theoretical maximum number, over the course of three molecular dynamics simulations.[91]

Reagent	Simulation 1	Simulation 2	Simulation 3
L^1	66.0	66.2	62.5
L^2	47.9	43.3	43.0
L^3	9.6	13.2	13.1

When L^2 and L^3 were used in tests to evaluate their ability to selectively recover gold from model e-waste solutions comprising a mixture of metals, both were surprisingly ineffective (figure 2.10), in stark contrast to the single metal experiments.

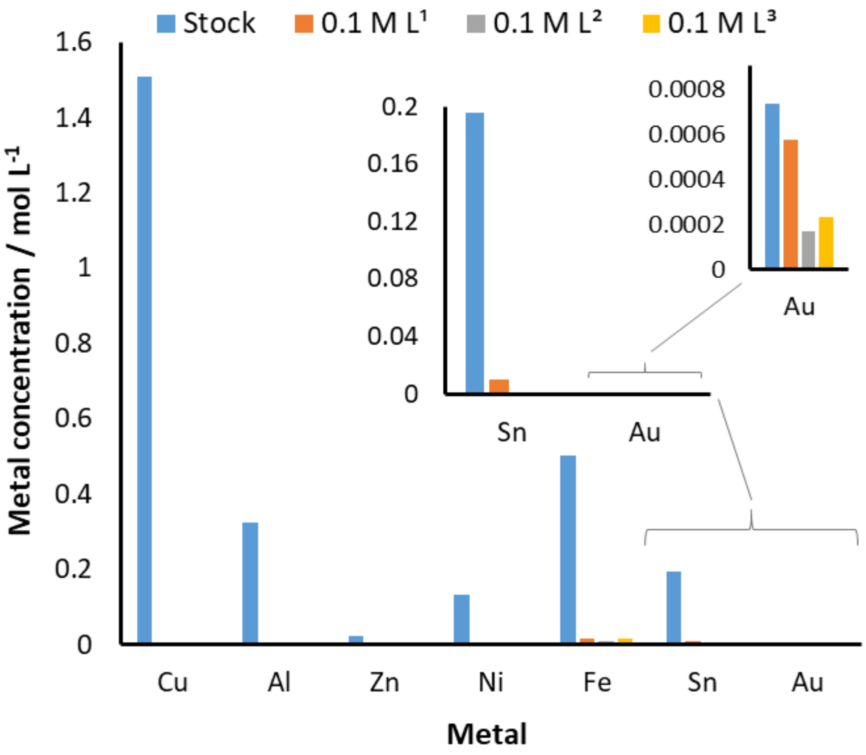

Figure 2.10 – Concentration of metals transported into a toluene solution of L^1, L^2 or L^3 from a mixed-metal aqueous solution. Conditions: Solution of L (0.1 M) in toluene (2 mL) stirred (500 rpm) with mixed-metal solution (2 M HCl, 2 mL) for 1 h at RT.

The marked decline in the concentration of gold in the organic phases of L^2 and L^3 after contact with the mixed metal feed solution was unexpected, given the expected enhanced recovery of gold by the 2° and 3° amides over the 1° amide based on the single-metal experiments discussed above (figures 2.8 and 2.9). However, inspection of the gold concentration in the model WEEE raffinate showed that 76% and 81% of gold had been successfully removed from the mixed-metal feed by L^2 and L^3, respectively. Given this mass-balance discrepancy, 'third phases' were suspected to be forming, preventing transport of gold to the organic phase, but such a phase was not seen in the small-scale solvent extraction experiments (2 mL) carried out previously.

The third phase will usually form at the aqueous-organic interface, but in some (usually rare) cases its location can vary. One such example is the extraction of Ce(IV) from nitric acid solutions in 20% (v/v) TBP in *n*-dodecane,[92] in which the density of third phase was dependent on the initial Ce(IV) concentration in the aqueous phase. Initially, no third phase formation occurred until [Ce(IV)] was 0.20 M, at which a third phase at the aqueous-organic interface formed. Raising the Ce(IV) concentration to 0.25 M resulted in a much denser 3rd phase that sunk to the bottom of the vial as spherical drops comprising multinuclear species of Ce(IV), TBP, H_2O and HNO_3, as identified by ICP-OES, IR, potentiometric titrations and Karl Fischer titrations. This dense 3rd phase remained until the Ce(IV) concentration reached 0.65 M at which point the third phase reappeared at the aqueous-organic interface.

The precise mechanism of 3rd phase formation varies from system to system and can depend on factors such as temperature,[52,93] diluent concentration,[42] diluent polarity,[94–96] acid concentration,[31,97] metal concentration,[92,95,98] or the type of aliphatic branching on the extractant.[45,99,100] These wide range of factors makes understanding this phenomenon at the molecular level extremely complicated, particularly if third phase formation occurs as a result of more than one variable.

The work in this chapter aims to understand why the performance of L^2 and L^3 in a mixed-metal stream was so poor in comparison with L^1 and to the single-metal conditions. The results presented herein do not attempt to explain the precise mechanism for 3rd phase formation in this system; instead, this chapter explores which factors do cause 3rd phase formation and the composition of the 3rd phases, with a view to address these issues and better understand the modes of action of these extractants.

2.4 Results and discussion

2.4.1 Third phase formation by L^2 and L^3

In order to quantify and characterise any 3rd phases, the mixed-metal extractions with L^1, L^2 and L^3 were scaled up (20 mL:20 mL aqueous:organic). In contrast to L^1, where no 3rd phase is observed, approximately 1 mL of a well-defined, viscous 3rd phase forms at the aqueous/organic interface (figure 2.11) from extractions with L^2 and L^3. The lighter organic phases of L^2 and L^3 are also a slightly paler in colour, consistent with gold being present in the organic phase at lower concentrations than in L^1.

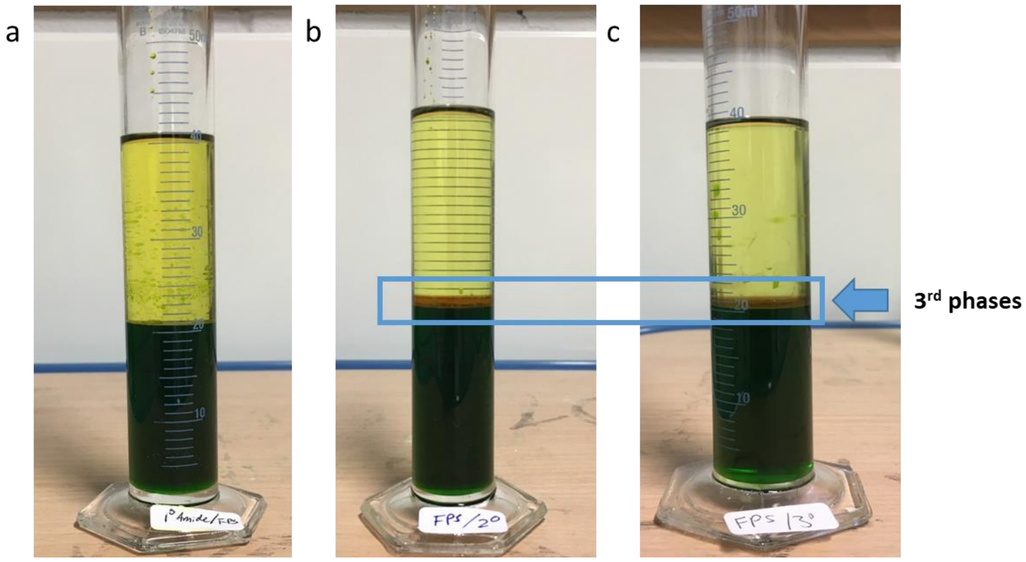

Figure 2.11 – Photographs of the disengagement of organic (upper), 3rd phase (middle) and aqueous (lower) phases after contact of a 2 M HCl mixed-metal solution with 0.1 M toluene solutions of (a) L^1, (b) L^2 and (c) L^3.

2.4.2 Third phase composition and analysis

2.4.2.1 ICP-OES analysis

Each 3rd phase was isolated and a portion diluted in 1-methoxy-2-propanol for ICP-OES analysis. The 3rd phase for L^2 comprises Au (2.8 %), Fe (87.6 %), and Sn (9.6 %), representing almost 60% of the total Au available, but only 3% and 1% of total Fe and Sn, respectively. In contrast, the 3rd phase formed when using L^3 comprises Au (1.4 %) and Fe (98.6 %) only, with all Sn remaining in the aqueous phase (figures 2.12 and 2.13).

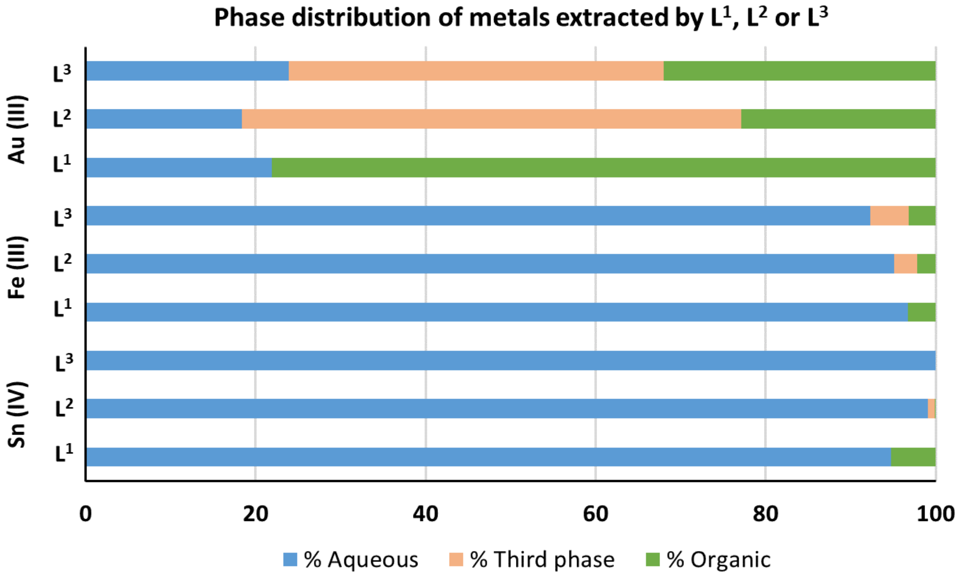

Figure 2.12 – Percentage breakdown of metals transported by L^1, L^2 or L^3 into the 3rd phase, organic phase, or remaining in the aqueous phase.

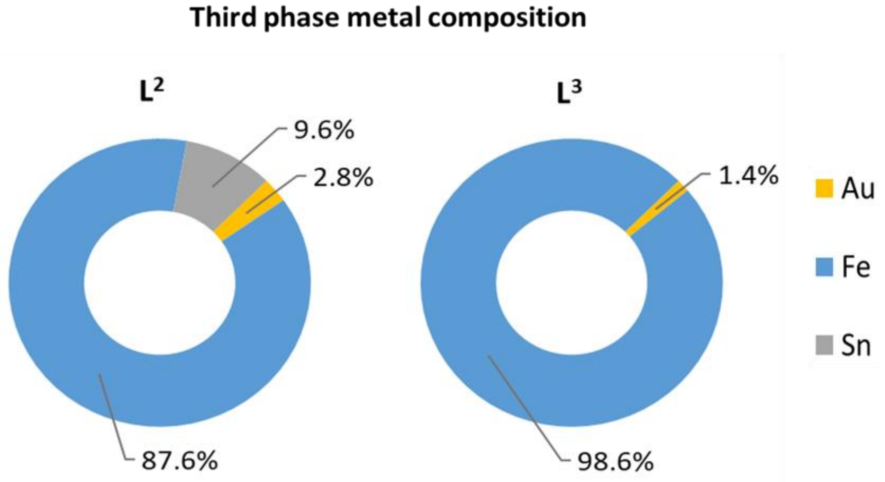

Figure 2.13 – Breakdown of metal composition in the 3rd phases formed by L^2 and L^3.

2.4.2.2 Removing 'problematic' metals from the mixed-metal solution.

As Fe comprised the major constituent of these 3rd phases, an iron-absent mixed-metal aqueous solution was prepared to investigate if it was the sole contributor to 3rd phase formation. Indeed, it is found that this Fe-free feed solution no longer forms a liquid 3rd phase with L^3 and 99% of the gold is transported to the organic phase with minimal co-extraction of tin (figure 2.14). However, it was found that a 3rd phase remained in experiments with L^2, and comprised tin and gold, now with 92% of the gold being transported into the 3rd phase, in addition to 15% of tin being co-extracted.

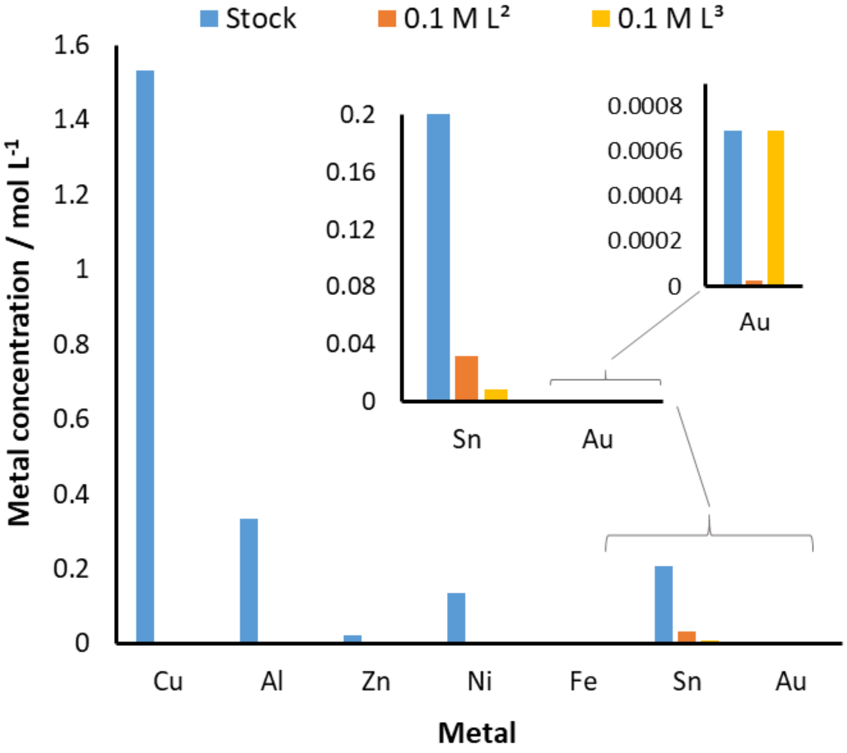

Figure 2.14 – Concentration of metals transported into a toluene solution of L^2 or L^3 from a mixed-metal aqueous solution that does not contain Fe(III). Conditions: Solution of L (0.1 M) in toluene (2 mL) stirred (500 rpm) with mixed-metal solution (2 M HCl, 2 mL) for 1 h at RT.

Removal of both tin and iron from the mixed-metal feed still results in 3rd phase formation by L^2. This new 3rd phase comprises Zn, Cu, and Au, which is surprising given that zinc and copper metalates were not found to be extracted to any significant extent from single-metal aqueous solutions with any of the amides. Solvent extraction experiments between L^2 or L^3 and a gold-absent mixed-metal aqueous solution also result in 3rd phase formation with each amide.

2.4.2.3 The effect of ligand concentration on third phase formation

Given that there are significant differences in metal concentration going from single-metal experiments to the model e-waste experiments, the overall ligand:metal ratio is now much lower. To rule out that the 3rd phase was forming as a result of a limiting concentration of L, extractions using 0.5 M L^2 and L^3 were undertaken, resulting in approximately five times more volume of third phase formed at the aqueous-organic interface than 0.1 M experiments (figure 2.15).

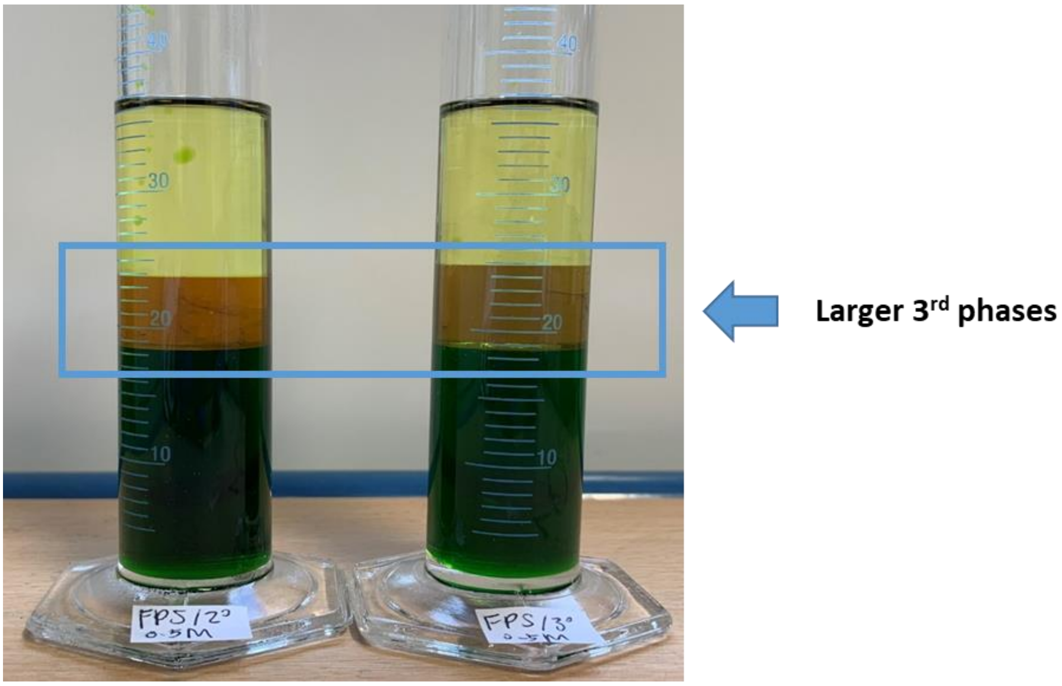

Larger 3rd phases

Figure 2.15 – Photographs of the phase disengagement after contact of toluene solutions of 0.5 M L^2 (left) and L^3 (right) with a 2 M HCl mixed-metal solution.

Concurring with 0.1 M ligand extraction experiments, only gold, iron and tin were transported from the aqueous phase into these larger 3rd phases of L^2 and L^3. Interestingly, at these higher concentrations of amide, more than 90% of the gold is extracted to the third phases, whilst 0.1 M L^2 and L^3 extractions resulted in 44% and 59% of gold in the 3rd phases respectively, with 32% and 23% of gold in the L^2 and L^3 organic phases. In addition, significantly more iron is transported with the majority present in the lighter organic phases (23% and 58% transported by L^2 and L^3 respectively), and only small quantities in the 3rd phases (figure 2.16). The secondary amide L^2 also extracted more tin into the 3rd phase when the amide concentration was increased to 0.5 M. While 0.5 M $L^{2/3}$ is still a limiting concentration of L relative to the total metal concentration, it is clear that simply adding more $L^{2/3}$ to the organic phase only exacerbates 3rd phase formation rather than abating it. Further investigations into the propensity of a metal to be transported into the denser or lighter organic phases was considered to be beyond the scope of this work.

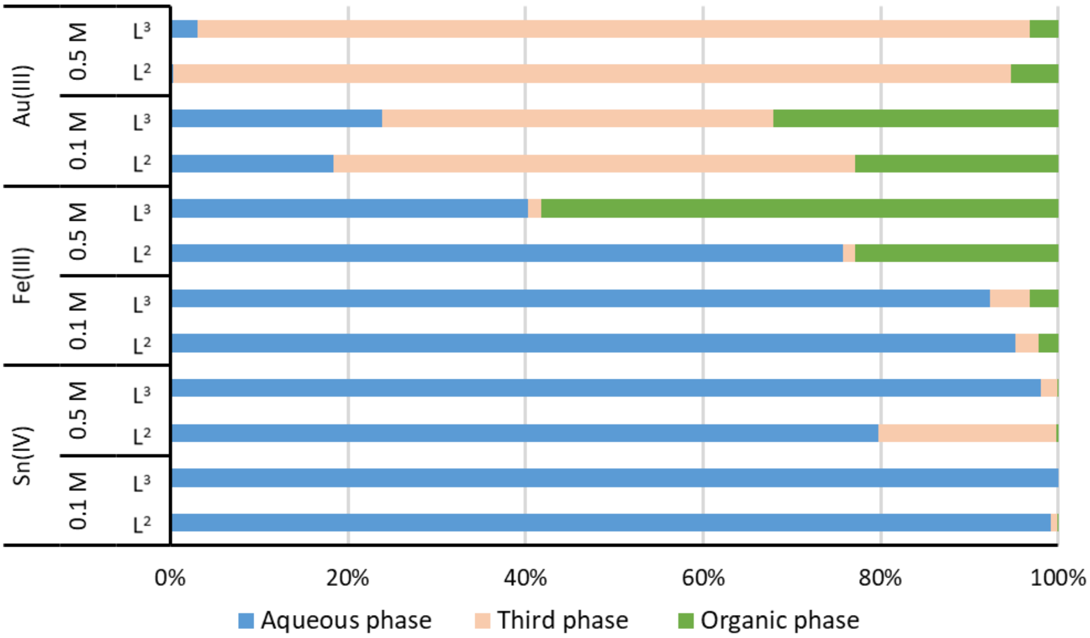

Figure 2.16 – Comparison of the performance of the extractants L^2 and L^3 at different concentrations. Conditions: 0.1 M or 0.5 M L in toluene (20 mL) stirred (500 rpm) with a mixed-metal feed in 2 M HCl (20 mL) for 1 h at RT.

Contacting L^2 or L^3 with each metal separately at the concentrations used in the model e-waste solutions in 2 M HCl does not result in the formation of a 3rd phase; nor does a combination of 0.5 M Fe, 0.15 M Sn and 0.001 M Au in 2 M HCl. It is therefore likely that, in this instance, 3rd phase formation is partly due to the nature of the model e-waste solution; this highly concentrated solution of very high ionic strength and the total chloride concentration exceeding 8 M will probably result in Fe and Sn existing in aqueous solution as their metalates and thus be co-extracted with gold at 2 M HCl. Single-metal experiments at HCl concentrations where Fe is extracted by L^2 or L^3 (see figures 2.8 and 2.9) did not form 3rd phases, although it may be that there is a limiting organic phase concentration (LOC) for iron (and/or tin) that, when exceeded, results in organic-phase splitting. This is a well-documented factor in extraction systems such as TBP and N,N,N,N Tetraoctyl Diglycolamide (TODGA),[96,101–103] where the high metal concentrations in the organic phase are unstable and split into two phases. However, this fails to account for why L^1 does not form any 3rd phases with the model e-waste solution. One reason may be that the reduced clustering of L^2 and L^3 around $AuCl_4^-$ compared with L^1 is a key factor in 3rd phase formation when subjected to complex aqueous matrices (as identified by MD simulations discussed in section 2.4, table 2.1).

2.4.2.4 X-Ray crystallography

During the mixed metal experiments involving L^3 in the absence of Fe, although there was no liquid third phase formation, colourless crystals formed at the aqueous/organic interface and were isolated and studied by X-ray diffraction. The crystal data solve and refine as the octahedral dianionic metalate, $SnCl_6^{2-}$, charge-balanced by two protonated diamides $[(HL^3)(L^3)]^+$ (figure 2.17, top). In contrast to previous studies where five-, six-, and seven-membered "proton chelate" rings form during metal extraction,[17,104–106] this system instead chelates a proton intermolecularly, via the amide O-donor atoms (O1-H1 1.24(4) Å; O1-H1 1.21(4) Å), thus enabling six polarised C-H groups to interact with the charge diffuse $SnCl_6^{2-}$ octahedron (figure 2.17, bottom).

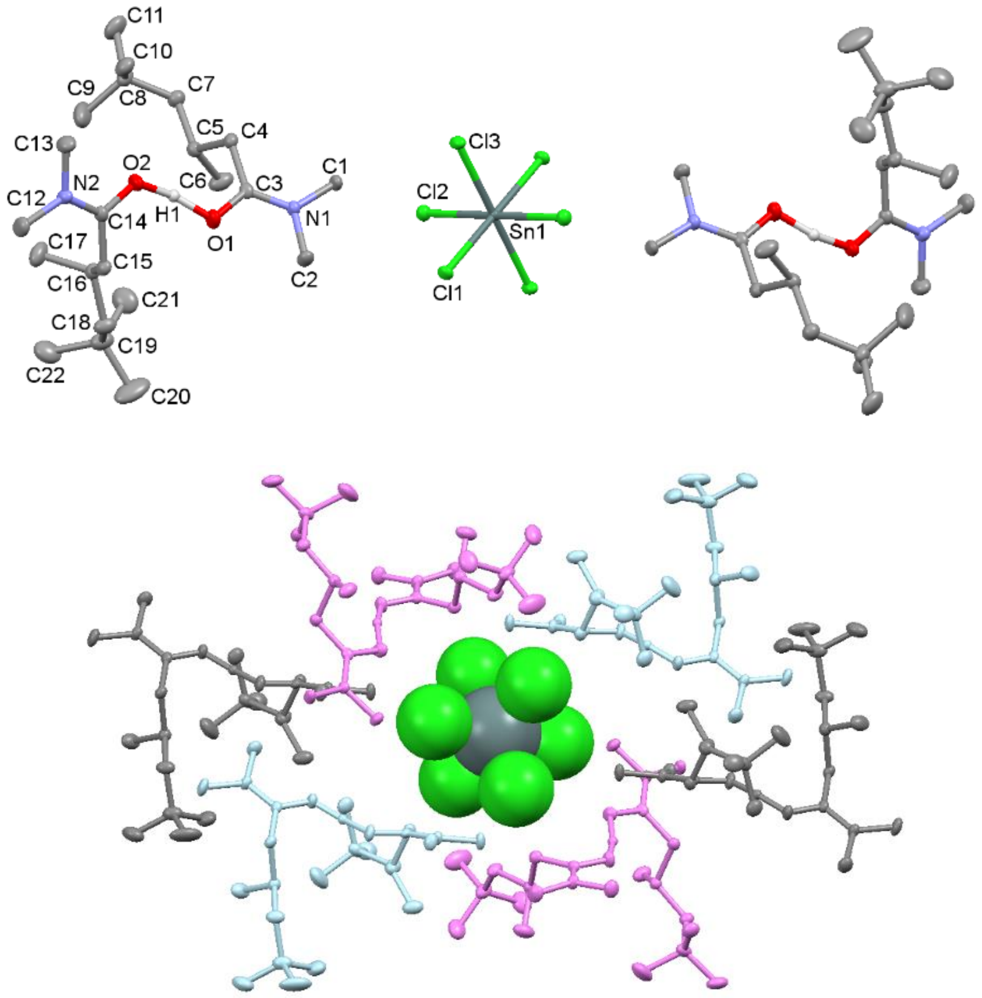

Figure 2.17 – Solid-state structure of $[H(L^3)_2]_2[SnCl_6]$. Top: $SnCl_6^{2-}$ charge-balanced by two $[(HL^3)(L^3)]^+$ units. For clarity, all hydrogen atoms are omitted except H1 (displacement ellipsoids are drawn at 50% probability). Bottom: Space-filling model of $SnCl_6^{2-}$ encapsulated by six protonated diamides through C(H)···Cl interactions (colours show equivalent symmetries). Close contact distances (Å): Cl1-C2 3.670(4); Cl1-C15 3.791(2); Cl2-C11 3.774(3); Cl3-C1 3.404(2); Cl3-C1’ 3.628(2); Cl3-C4 3.863(2). Total of 6 C(H)···Cl interactions below 4.0 Å.

2.4.2.5 ^{1}H NMR spectroscopy

Interactions between the metalate and the diamide cation $[(HL^3)(L^3)]^+$ can also be observed by NMR spectroscopy when the Sn-containing precipitate is dissolved in $CDCl_3$ (figure 2.18, bottom) and compared with a solution of L^3 in $CDCl_3$ (figure 2.18, top). All signals are shifted downfield upon interaction with the metalate, with the α-CH_2 and NCH_3 protons being shifted most strongly, indicating they are more stongly deshielded due to non-covalent interactions with the metalate. Indeed, upon inspection of the X-ray structure of $[(HL^3)(L^3)]_2[SnCl_6]$, 5 out of 6 close contact distances below 4.0 Å are from α-CH_2 or NCH_3 protons, with the 6th contact coming from a CH_3 of the terminal ${}^tBu$ group. Additionally, the NCH_3 signal has now fully coalesced into a broad singlet, consistent with the C-N bond now having less double bond character and therefore rotating more easily. The proton chelated by two L^3 molecules in the tin complex (H1 in figure 2.17, top) is seen at 10.5 ppm as a very broad singlet with an integration of approximately 0.5, consistent with the formula $[(HL^3)(L^3)]^+$.

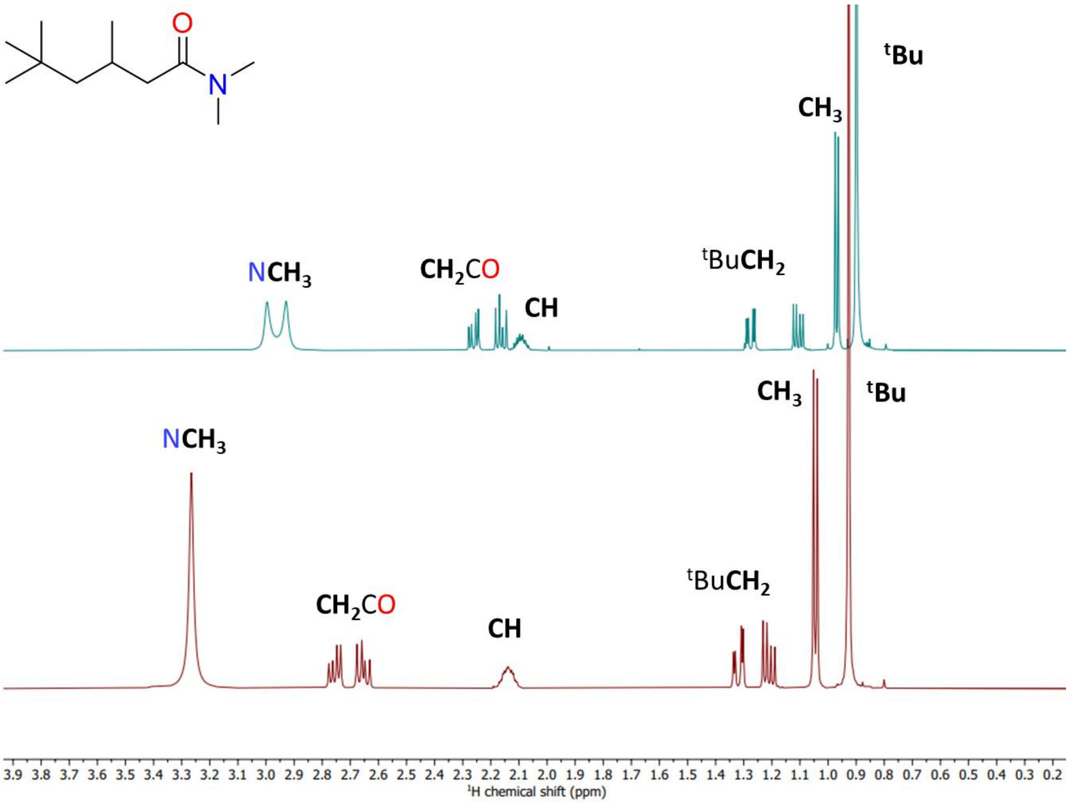

Figure 2.18 – ${}^1H$ NMR spectrum of L^3 (top) and $[(HL^3)(L^3)]_2[SnCl_6]$ (bottom) dissolved in $CDCl_3$.

2.4.2.6 Electrospray Ionisation Mass Spectrometry

Attempts to characterize the liquid 3rd phases proved more difficult; endeavors to obtain additional crystal structures were unsuccessful, and ESI-MS studies show ions of complex clusters comprising "FeCl" units with varying proportions of $L^{2/3}$ (figures 2.19 and 2.20). Rather than these species existing in solution they are more likely derived from clusters of varying proportions of $[HL^{2/3}]^+$, $L^{2/3}$, and $FeCl_4^-$, but are more unstable compared with the gold clusters for $L^{1\text{-}3}$ that could be observed by ESI-MS.[40]

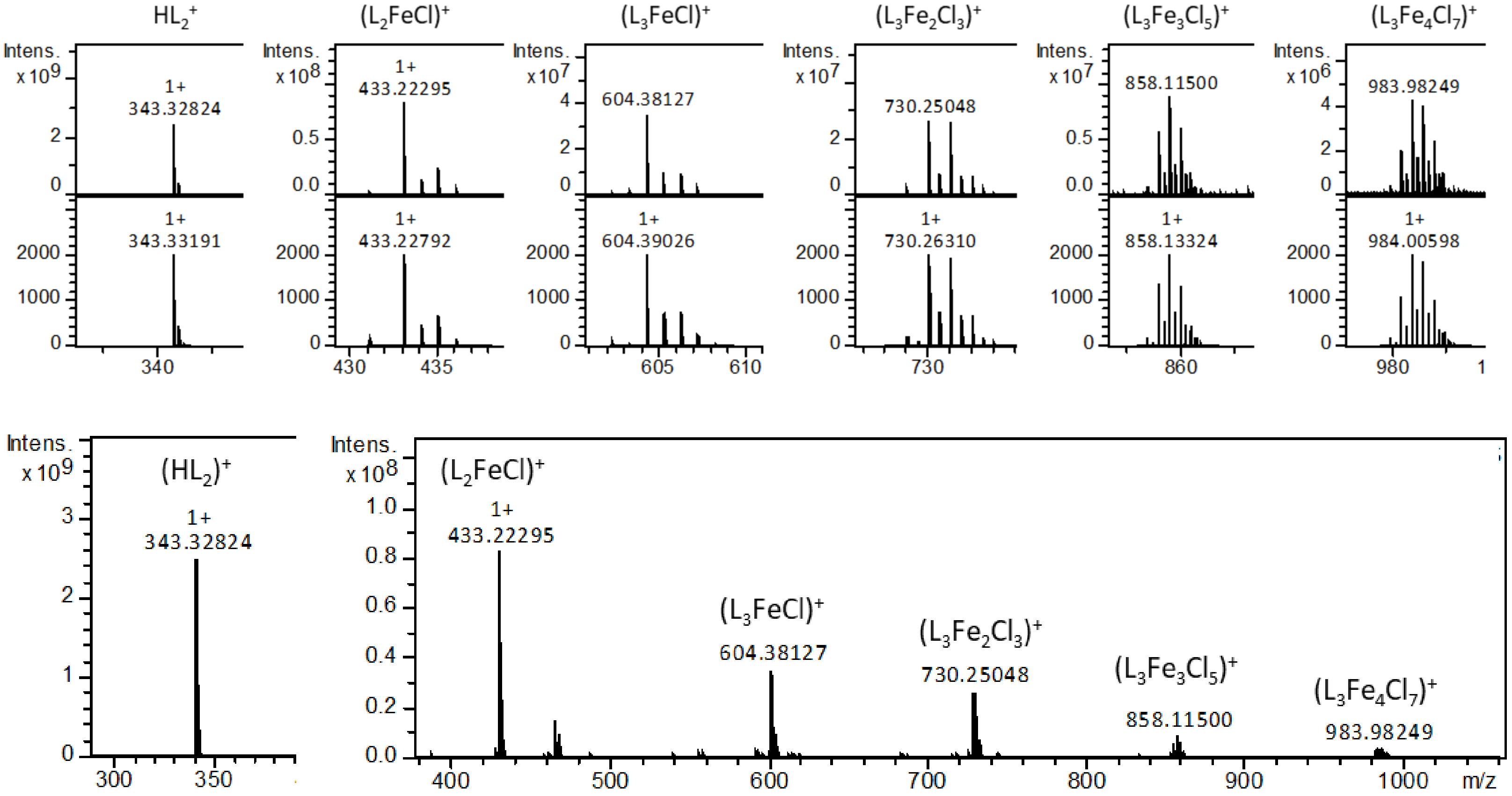

Figure 2.19 – Positive ion ESI-MS of a mixed-metal loaded L^2 toluene solution diluted in CH_3CN. Each of the assigned peaks is focused on, with the real (upper) and predicted (lower) isotopic distribution pattern shown.

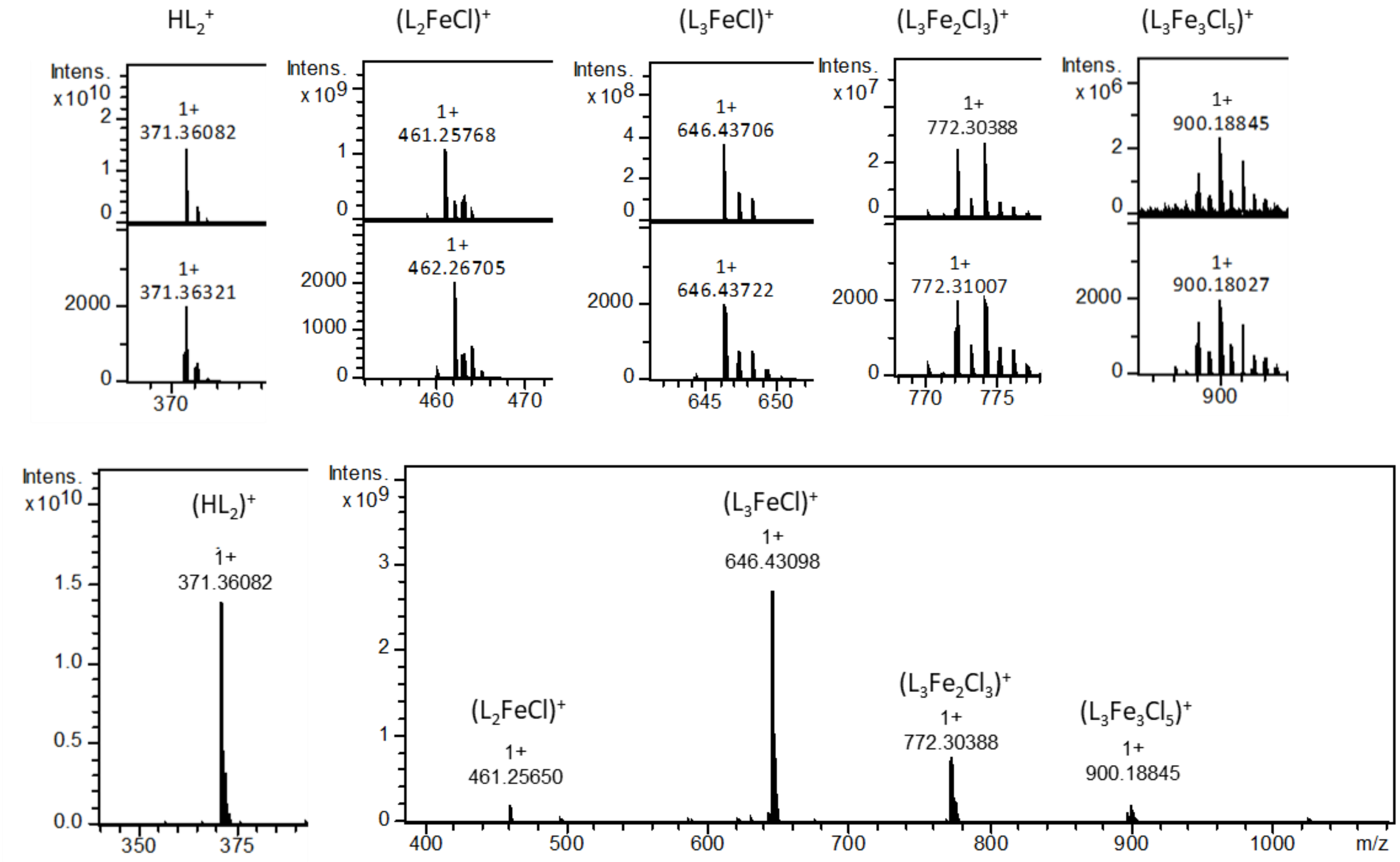

Figure 2.20 – Positive ion ESI-MS of a mixed-metal loaded L^3 toluene solution diluted in CH_3CN. Each of the assigned peaks is focused on, with the real (upper) and predicted (lower) isotopic distribution pattern shown.

2.4.2.7 ^{1}H DOSY NMR analysis of the third phase formed by L^2

Since the 3rd phases contain iron (which is paramagnetic), simple NMR experiments proved inconclusive. However, diffusion-ordered spectroscopy (DOSY) ^{1}H NMR analysis of the third phase formed between 0.1 M L^2 (in d$_6$-benzene) and the Fe absent mixed-metal feed (all other transported metals were diamagnetic) was undertaken to gain an insight into the relative size of the species present within the third phase compared to those in the lighter organic phase.

A broad peak correlating to the L^2 alkyl chain with a diffusion rate much slower than benzene solvent is observed in the 3rd phase (figure 2.21a); this is consistent with the presence of a viscous, potentially polymeric aggregate. On the other hand, all loaded organic phases display similar DOSY spectra to their analogous uncontacted organic phases, diffusing faster than the third phase, so likely being more molecular in their identity. Sampling the 3rd phase into more polar solvents such as deuterated methanol results in a DOSY spectrum (figure 2.21c) akin to the uncontacted ligand (figure 2.21d) and the organic phase (figure 2.21b), suggesting the more polar solvents are disrupting an extensive aggregation.

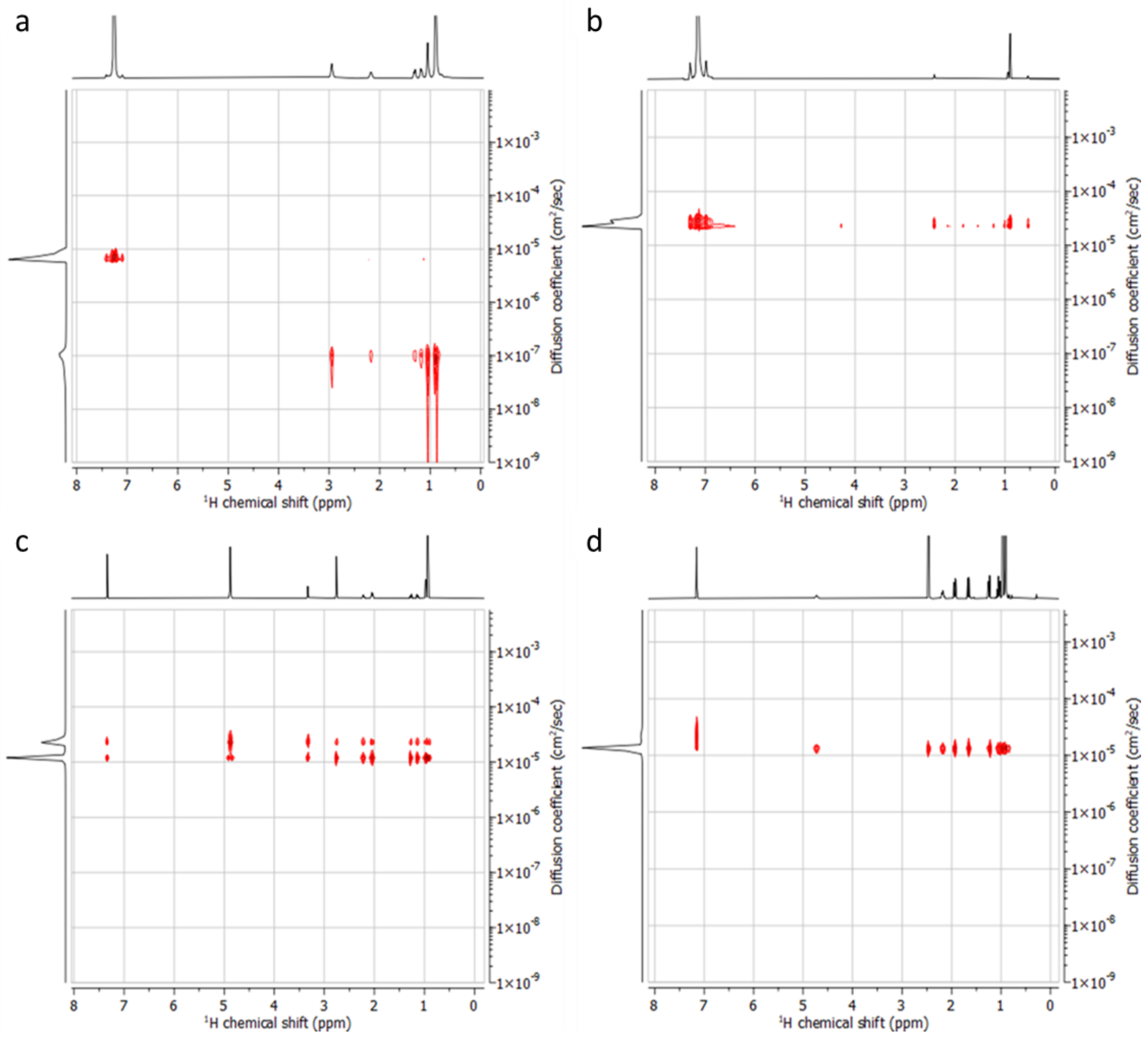

Figure 2.21 – ^{1}H DOSY NMR spectra of a) Mixed-metal loaded L^2 3rd phase in C_6D_6; b) Mixed-metal loaded L^2 lighter organic phase in C_6D_6; c) Mixed-metal loaded L^2 3rd phase diluted in MeOD; d) uncontacted L^2 in C_6D_6.

2.4.2.8 Karl Fischer water concentration determination

The concentrations of water in the 3rd phases were determined by Karl-Fischer analyses and compared with those of the organic phases (table 2.2). The water content in an organic phase of L^1 loaded from the mixed-metal feed was ca. 300 ppm higher than that seen for an organic phase loaded solely from a single Au solution.[40]

Table 2.2 – Concentrations of amide and water determined for organic and third phases following contact with the model e-waste solution. [a] Samples taken from amide solutions in deuterated benzene. [b] Determined by ^1H NMR concentration using 1,4-dioxane as an internal standard; for amide concentrations the metal-loaded organic phase was back-extracted with H_2O prior to NMR analysis to avoid interference by paramagnetic Fe(III). [c] Determined in triplicate by volumetric Karl-Fischer titration.

Sample[a]	**Amide (mol L^{-1})[b]**	**Water (ppm)[c]**	**Water (mol L^{-1})[c]**
Uncontacted organic phase L^1	0.10	209	0.012
Loaded organic phase L^1	0.07	746	0.041
Uncontacted organic phase L^2	0.10	273	0.015
Loaded organic phase L^2	0.03	456	0.025
3rd phase L^2	1.67	1064	0.059
Uncontacted organic phase L^3	0.11	202	0.011
Loaded organic phase L^3	0.04	453	0.025
3rd phase L^3	1.15	993	0.055

The metal-loaded 3rd phases contain around five times more water than the metal-loaded organic phases, which may also explain the lack of solubility of the third phase. The concentrations of amide reagents in the 3rd phases were also determined by quantitative ^1H NMR spectroscopy using 1,4-dioxane as an internal standard. In these cases, it is found that the approximate concentration of the amide L^3 in a water-stripped 3rd phase is 1.15 mol L^{-1} whereas the loaded organic phase is just 0.04 mol L^{-1} (table 2.2), i.e. the 3rd phase incorporates a significant quantity of the amide reagent. Loss of the amides into the 3rd phase points to potential aggregation between $L^{2/3}$, Fe(III) and Au(III) and water. As described earlier, diminished clustering by L^2 and L^3 compared with L^1 (which does not form a 3rd phase) may result in hydrogen-bonded clusters which are more porous, and hence are more able to aggregate into more extended, denser structures.[92,107]

2.4.3 Overcoming the third phase problem

With the exception of removing Fe from the solvent extraction experiment using L^3, omission of any other metal failed to negate 3rd phase formation using either L^2 or L^3 due to the complex composition of the mixed-metal solution. As aggregation is not observed by DOSY NMR spectroscopy when sampling the 3rd phase in more polar solvents, solvent extraction experiments with 0.1 M L^2 or L^3 solutions in chloroform or 10% (v/v) 1-octanol in toluene were carried out. In these cases, no 3rd phase formation is seen with almost quantitative transport of Au into the organic phase occurring for both L^2 and L^3, albeit with a loss of selectivity compared with L^1 with increased amounts of Sn (6-8%) and Fe (11-16%) extracted (figures 2.22 and 2.23). It is likely that the enhanced polarity and hydrogen-bonding ability of these solvents compared with toluene are deconstructing the aggregates formed in the 3rd phase.

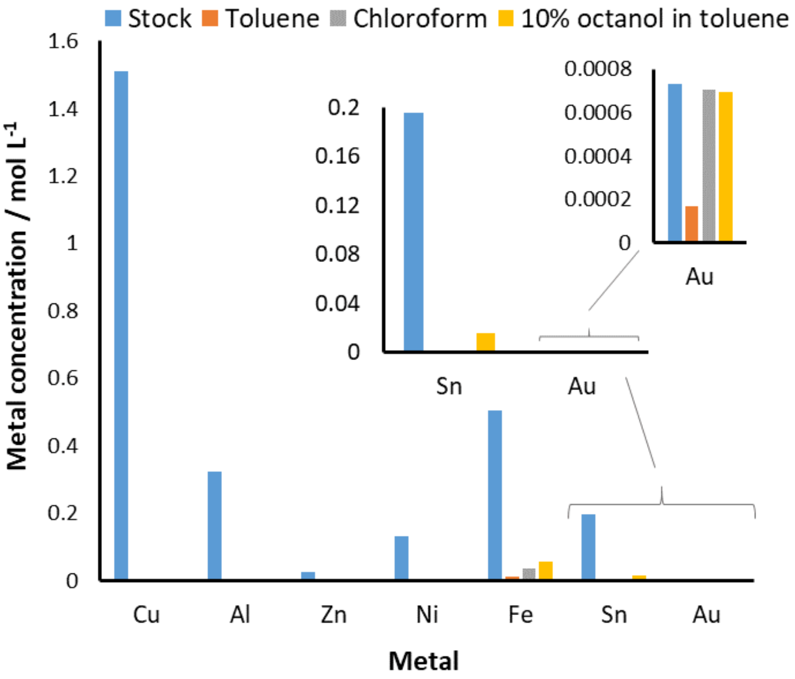

Figure 2.22 – Concentration of metals loaded into 0.1 M solutions of L^2 in toluene, chloroform, or toluene/octanol (10%) organic phases from a mixed-metal aqueous solution (blue bars). Conditions: 0.1 M L in 10%(v/v) octanol in toluene (2 mL) or chloroform (2 mL) stirred (500 rpm) with a mixed-metal feed in 2 M HCl (2 mL) for 1 h at RT.

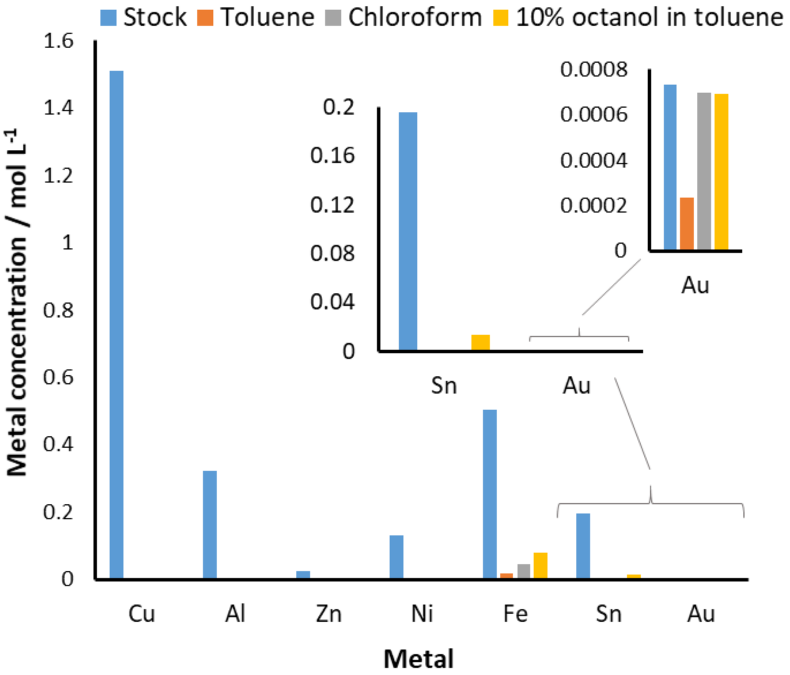

Figure 2.23 – Concentration of metals loaded into 0.1 M solutions of L^3 in toluene, chloroform, or toluene/octanol (10%) organic phases from a mixed-metal aqueous solution (blue bars). Conditions: 0.1 M L in 10%(v/v) octanol in toluene (2 mL) or chloroform (2 mL) stirred (500 rpm) with a mixed-metal feed in 2 M HCl (2 mL) for 1 h at RT.

2.5 Conclusions

The identification of a 3rd phase has accounted for the ‘poor’ extraction performance of L^2 and L^3 when using a mixed-metal feed, despite their enhanced performance over L^1 when extracting metals from single-metal solutions. It has been shown that L^2 and L^3 do indeed transport gold from the aqueous phase to a good extent, although the formation of a gold-concentrated 3rd phase makes these extractants undesirable for a potential commercial process when iron (for L^3), and iron and tin (for L^2) are present in high concentrations.

Various analytical techniques have demonstrated that the 3rd phase is potentially a polymer-like aggregated species that is insoluble in either the aqueous or the organic phase. The 3rd phases were found to contain significantly more water than the loaded organic phases, suggesting that water could be playing a role towards 3rd phase formation. The ability of the primary amide to promote the formation of molecular hydrophobic assemblies through the better availability of hydrogen-bond donors and acceptors appears crucial to its success in metalate separation by solvent extraction. These groups are diminished in the secondary and tertiary amides and could be a contributing factor towards third-phase formation.

Ideally an extractant should not show any third phase formation during solvent extraction, although it is common in some industrial processes to add modifiers to reduce third phase formation and aid phase disengagement.[98,102,108,109] In the case of L^2 and L^3, addition of 1-octanol as a modifying agent obviates 3rd phase formation but at the expense of extraction selectivity. Otherwise, using secondary and tertiary amides to effectively recover gold from e-waste feed solutions will be highly dependent on the composition and complexity of the feed solutions.

Chapter 3

Simple diamides for selective metalate precipitation

3 Simple diamides for selective metalate precipitation

3.1 Overview

Selective precipitation techniques are becoming more common in metal separations strategies as they can circumvent the use of environmentally harmful organic solvents associated with solvent extraction processes. This chapter examines a simple tertiary diamide that precipitates gold efficiently and selectively from aqueous acidic solutions. The tuneable selectivity of the diamide towards various metalates under different aqueous matrices is demonstrated, with straightforward recycling of the diamide being achieved using just water. Factors governing the strength, selectivity and efficiency of precipitation were then explored by synthesising and testing derivatives of the tertiary diamide with differing structural and electronic properties.

3.2 Introduction

Precipitation and adsorption methods that are selective and recyclable are becoming increasingly popular in gold and other metal separations, providing significant advantages over traditional, single-use precipitants.[110–114] Pre-formed porous network materials such as metal-organic frameworks (MOFs),[115,116] covalent-organic frameworks (COFs),[117] porous porphyrin polymers,[118] and electroactive materials[119–121] have been shown to selectively adsorb gold over other metals. These materials typically exploit the accessible reduction potential of gold to deposit metallic gold within the porous cavities and are particularly effective towards complex mixtures in which gold is present in low concentrations. Molecular recognition processes involving cyclodextrins,[35,36] and cucurbit[*n*]urils (*n* = 5-8)[122–124] exploit the curvature and donor-group decoration of these capsular guest molecules to host selectively both alkali-metal cations and tetrachloridoaurate anions within superstructures that ultimately precipitate gold from aqueous acidic solutions. This feature has also been applied in the separation of platinum from palladium and rhodium by precipitation in which the cucurbitural displays a preference for the hexachloroplatinate(IV) dianion.[125] Cationic cyclophanes have also been reported to capture and precipitate the square planar metalates $AuCl_4^-$, $PdCl_4^{2-}$ and $PtCl_4^{2-}$ from solution through C-H···Cl host/guest interactions.[126–128] More simple acyclic durene-based diamides act as receptors for tetrachloroaurate upon protonation through interactions between square planar $AuCl_4^-$ and the electron-rich arene present within the supramolecular extended network;[129] in these cases, no selectivity for gold over other metals was explored. The simple biomolecule niacin, a pyridine carboxylic acid, has been shown to form extended supramolecular networks upon protonation and selectively precipitates $HAuCl_4$ from acidic solutions consisting of Au, Ni, Cu, Zn, alkali- and alkaline-earth metals;[130] in this case, protonated niacin molecules assemble through hydrogen-bonding to form an extended supramolecular structure.

3.3 Simple diamides for solvent extraction

Chapter 2 investigated the performance of three simple monoamides, L^{1-3}, and found that despite L^2 and L^3 being stronger gold extractants than L^1 under single-metal conditions, undesired third phases were formed that comprised most of the gold, along with iron and tin in solvent extraction experiments with model e-waste solutions. The observation that L^3 could precipitate tin as the diamide complex $[(L^3)_2H]_2[SnCl_6]$, suggested that changes in the amide structure resulted in variability in solvent extraction performance with, in some cases, precipitation being favoured. As such, the simple diamides L^{4-6} (figure 3.1) were prepared with the assumption that L^4 and L^5 may extract gold in a similar manner to L^{1-3}, whereas selective precipitation may occur by L^6 by the formation of insoluble, infinitely extended structures.

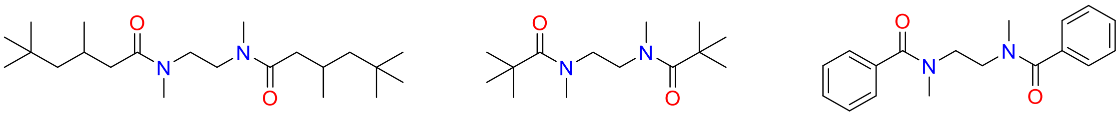

L^4 L^5 L^6

Figure 3.1 – Structures of diamides L^{4-6} used in initial solvent extraction studies.

The diamides are prepared in a single step by reacting commercially available N,N’-dimethylethylenediamine with the appropriate acid chloride and are isolated as a colourless oil (L^4) or solids (L^5 and L^6). Initially, 0.1 M solutions of the diamides in toluene or chloroform were screened as reagents for the transport of $HAuCl_4$ from 0-6 M HCl solutions by solvent extraction (Figure 3.2).

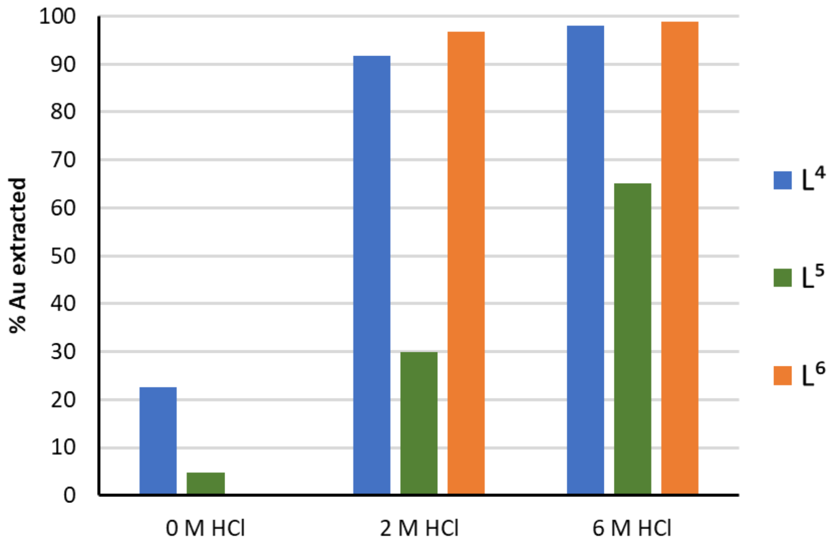

Figure 3.2 – Percentage of Au extracted by 0.1 M toluene solutions of L^4, L^5 or 0.1 M chloroform solution of L^6. Conditions: solution of $L^{4\text{-}6}$ (0.1 M, 2 mL) stirred (500 rpm) with 0.01 M $HAuCl_4$ (2 M HCl, 2 mL) for 24 h at RT.

Diamide L^4 behaves similarly to monoamide L^1 at 2 M and 6 M HCl showing almost quantitative gold extraction, whereas truncating the alkyl substituents to *tert*-butyl groups in L^5 reduces extraction efficiency and results in poor phase disengagement. Solvent extraction experiments using L^6 dissolved in chloroform (as L^6 is insoluble in toluene) result initially in fast gold transport at 2 M and 6 M HCl to form a yellow organic phase, but in contrast to the other amides a yellow precipitate forms. Analysis of both aqueous and organic solvent phases by ICP-OES shows that near quantitative gold precipitation occurs. It is evident that modifying the identities of the diamide substituents from $CH_2CH(Me)CH_2Bu^t$ in L^4 to Ph in L^6 promotes gold precipitation over gold extraction.

3.4 L^6 as a precipitant in the absence of organic solvents

The diamide L^6 was therefore evaluated as a precipitant in the absence of the organic solvent. Adding 0.2 mmol of solid L^6, the equivalent in moles used in the SX experiments (i.e., a 10-fold excess), to a 0.01 M $HAuCl_4$ solution in 2 M or 6 M HCl results in colourless supernatants and yellow solids which incorporate >99 % of the gold. Furthermore, complete gold precipitation using L^6 is also seen from solutions of $HAuCl_4$ in 20 or 100 % aqua regia or 2 M H_2SO_4 in the presence of chloride or bromide (table 3.1), indicating that the separation process should be suited for a range of acidic leaching conditions. On the other hand, α-CD only precipitates $AuBr_4^-$ between pH 2 – 5 when K^+ is present,[35] and the efficiency of $AuCl_4^-$ precipitation by cucurbit[*6*]uril was found to decrease from 96.4% at 2 M HCl to 3.3% at 10 M HCl.[124]

Table 3.1 – Precipitation experiments with Au dissolved in various aqueous matrices. Conditions: 2 mL Au solution contacted with 0.059 g L^6 for 24 hours, room temperature. Solution filtered and diluted 1000 x in 2% HNO_3 prior to ICP-MS analysis * Au^0 added to sulfuric acid and NaCl or NaBr solution with a few drops of 30% hydrogen peroxide added to aid dissolution of Au. All experiments performed in triplicate.

Aqueous matrix	**Initial Au concentration (mg L^{-1})**	**Au concentration after contact with L (mg L^{-1})**	**% Precipitated**
0.01 M $HAuCl_4$ in 2M HCl	2536	5.88	99.8
0.01 M $HAuCl_4$ in 6 M HCl	2228	2.32	99.9
0.01 M $HAuCl_4$ in 100 % Aqua regia	1920	6.00	99.7
0.01 M $HAuCl_4$ in 20 % Aqua regia	1920	4.00	99.8
2 M H_2SO_4 and 2 M NaCl *	1940	12.2	99.4
2 M H_2SO_4 and 2 M NaBr *	1930	9.00	99.5

3.4.1 Recovery of Au and reuse of L^6

Importantly, the release of gold from the isolated solids is achieved by multiple washes with deionised water, resulting in dissolution of $HAuCl_4$ into solution and the recycling of L^6 (table 3.2) as a solid. This contrasts with other precipitants such as α-CD or cucurbit[*6*]uril, which must be recovered by recrystallisation following a direct reduction of Au(III) to Au(0) with sodium metabisulfite or hydrazine.[35,124]

Table 3.2. Precipitation of $HAuCl_4$ by L^6 from 2 M HCl followed by its release from L^6 as $HAuCl_4$ using deionised water. All solutions were diluted 100x prior to ICP-OES analysis.

Sample	Au concentration (mg L^{-1})	% Precipitation	% Stripping (cumulative)
0.01 M $HAuCl_4$ in 2 M HCl (feed solution)	1940	-	
2 M HCl solution after contact with L^6	8.00	99.6 %	
Deionised water after contact with $[HL^6][AuCl_4]$ solids (2 mL) 1st wash	103	-	5.3
Deionised water after contact with $[HL^6][AuCl_4]$ solids (2 mL) 2nd wash	605	-	36.6
Deionised water after contact with $[HL^6][AuCl_4]$ solids (2 mL) 3rd wash	826	-	79.3
Deionised water after contact with $[HL^6][AuCl_4]$ solids (2 mL) 4th wash	147	-	86.9
Deionised water after contact with $[HL^6][AuCl_4]$ solids (2 mL) 5th wash	139	-	94.1

The recycled diamide can be used in further gold load/strip cycles showing 87 % loading efficacy after three cycles (table 3.3); this decrease from the initial 99% gold precipitation after three cycles is likely due sampling errors while handling milligram quantities of the diamide.

Table 3.3 – Cycling of L^6 through three load/strip phases.

Cycle	**1**	**2**	**3**
% Au Precipitated	97.7 %	90.7 %	87.3 %

3.4.2 Metal precipitation dependence on acid concentration

The precipitation of gold and other metals from varying [HCl] solutions by L^6 was evaluated (figure 3.3).

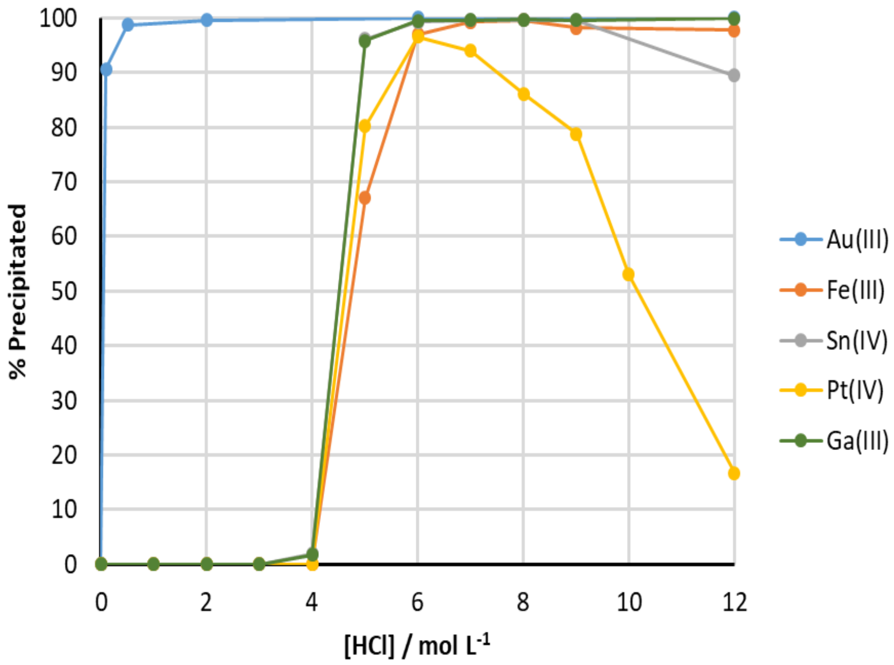

Figure 3.3 – Precipitation of Au(III), Fe(III), Ga(III), Sn(IV) and Pt(IV) by L^6. Conditions: 0.2 mmol L^6 contacted with 2 mL 0.01 M metal in 0 – 12 M HCl for 1 hour at RT, 500 rpm.

Gold is most readily precipitated by L^6 from HCl concentrations as low as 0.1 M and, in contrast to solvent extraction conditions with L^{1-3}, continues to be precipitated as the HCl concentration reaches 12 M. In a similar trend as in solvent extraction experiments with L^{1-3}, iron and gallium are precipitated when the HCl concentration increases sufficiently (4 M) such that they exist in solution as the metalates $FeCl_4^-$ and $GaCl_4^-$; these metals also continue to be precipitated up to 12 M HCl. With Sn(IV) and Pt(IV), in contrast to L^{1-3} where extraction was poor (or resulted in 3rd phase formation), L^6 effectively precipitates tin and platinum at concentrations above 5 M HCl. Interestingly, tin continues to be precipitated up to 12 M HCl whereas platinum precipitation peaks at 6 M HCl before decreasing with increasing [HCl], potentially due to chloride competition, or an increased solubility of $[HL]_2[PtCl_6]$ as the HCl concentration is increased. Spot tests between L^6 and other metals such as aluminium, copper, nickel and zinc at 6 M HCl did not show any significant precipitation (<5%) and so were not investigated further. Single crystals for X-ray diffraction of each metal precipitate were obtained and the bulk composition confirmed by elemental analysis and PXRD (PXRD for [HL^6][AuCl$_4$] only, see section 3.4.7.2).

3.4.3 Tuning the selectivity of metal precipitation

The selectivity of L^6 under mixed-metal conditions was evaluated by initially adding an 0.2 mmol of solid L^6 to a 2 mL mixed-metal solution comprising 0.01 mol L^{-1} each of Al(III), Au(III), Cu(II), Fe(III), Ni(II), Pd(II), Pt(IV) and Sn(IV) in either 2 M or 6 M HCl. In this case, L^6 is in a tenfold excess with respect to any one metal. This experiment was then repeated using a stoichiometric amount of L^6 with respect to any one metal (i.e. 0.02 mmol) (figure 3.4).

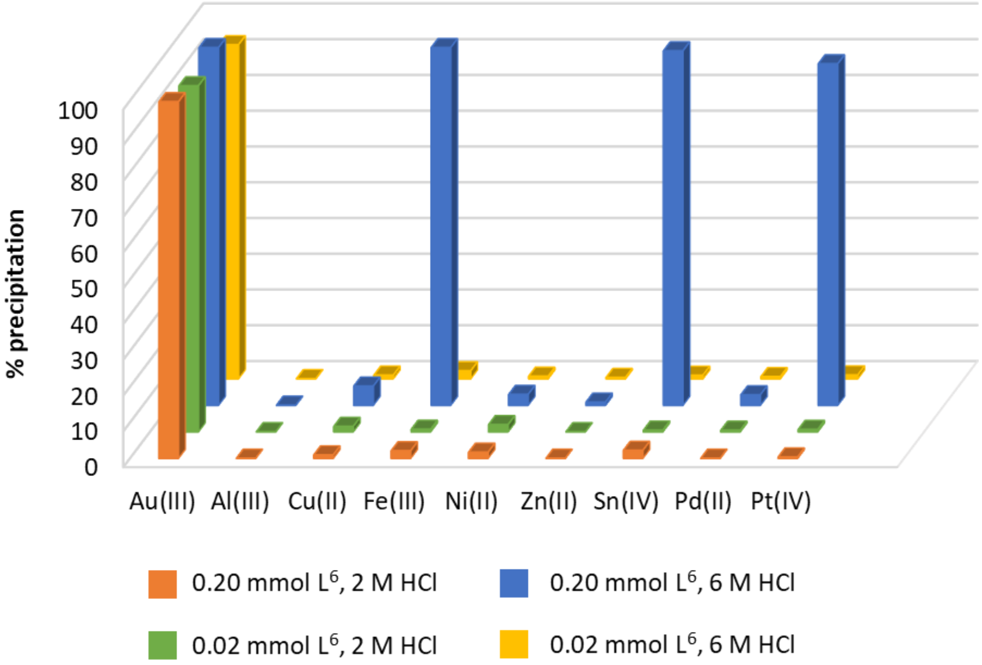

Figure 3.4 – Percentage metal(s) removed by precipitation from a 0.01 M mixed-metal solution in 2 M (orange and green bars) or 6 M (blue and yellow bars) HCl following the addition of either 0.2 mmol L^6 (10-fold excess L^6 relative to metal, orange and blue bars) or 0.02 mmol L^6 (equimolar, green and yellow bars).

The addition of excess L^6 to the 2 M HCl mixed-metal solution results in near quantitative precipitation of Au, with minimal co-precipitation of other metals (<5%, figure 3.4, orange bars). Interestingly, using one equivalent of L^6 (i.e., 0.02 mmol) results in gold uptake only (figure 3.4, green bars) which contrasts with SX conditions where an excess of extractant is required, thus highlighting the enhanced atom economy of this precipitation method. At 6 M HCl using excess L^6, complete uptake of Fe, Sn, and Pt is also seen, alongside Au, from the above mixture of metals (figure 3.4, blue bars). Using stoichiometric L^6, however, a return to selective gold uptake is seen (figure 3.4, yellow bars), which shows that a process could be designed to sequentially precipitate Au then, depending on the feed stream, Fe, Sn, or Pt. This is significant as leach solutions from gold ores (typically pyrite or arsenopyrite) are rich in iron, while those derived from e-waste have high concentrations of tin.[131] Furthermore, the selectivity shown between Pt(IV) and Pd(II) at 6 M HCl is notable as this separation is integral to precious metal refining processes currently based on SX.[132] The selectivity seen under stoichiometric conditions also suggests that the preference for gold precipitation is not wholly dependent on the ease of formation of $HAuCl_4$ compared with other chloridometalates, but that the chemical structures of the precipitates also define the sequence of separation.

3.4.4 Selective stripping of metals

The selective uptake of Au at 2 M HCl compared with the requirement for 6 M HCl to load Fe, Sn, and Pt permits a selective stripping process to be undertaken. As such, loading L^6 with Au, Fe, Pt, and Sn at 6 M HCl (figure 3.5, blue bars), followed by a wash with 2 M HCl results in re-dissolution of Fe, Sn, and Pt only, with Au retained on the solids (figure 3.5, green bars). Washing the isolated solids with DI water releases the Au into solution and recycles L^6 (figure 3.5, yellow bars).

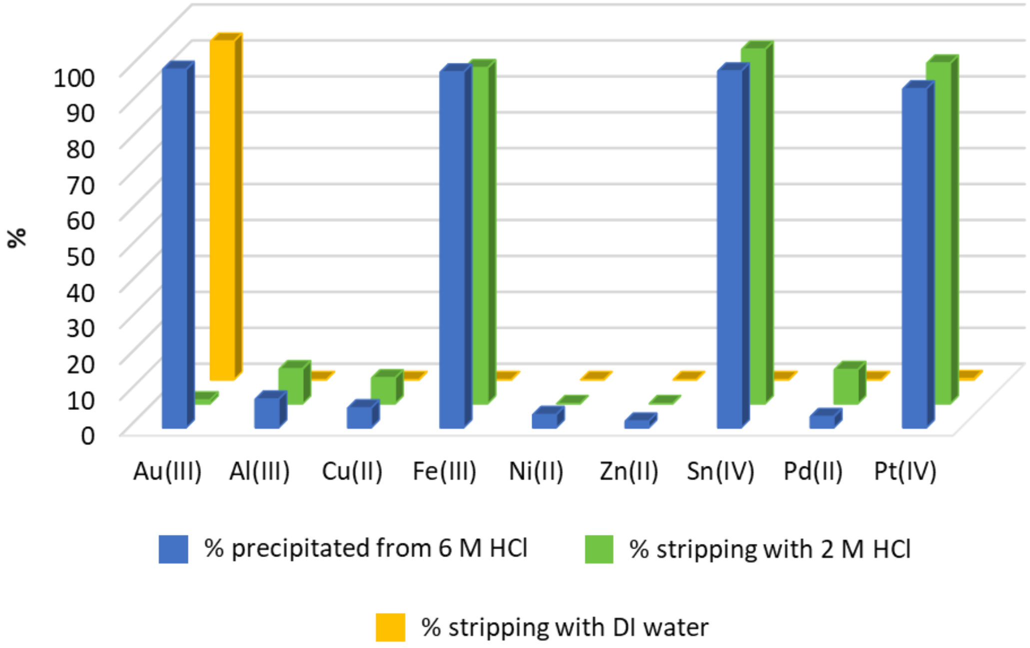

Figure 3.5 – Selective metal precipitation and stripping sequence.

3.4.5 Selectivity for other metals

The selectivity of L^6 for Au uptake was evaluated further by adding an excess to mixed-metal ICP-OES standard solutions (diluted in 2 M or 6 M HCl), comprising 29 metals at 100 or 10 ppm concentrations. Analysis of the concentrations of metals that remain in solution reveals that even in this competitive environment, L^6 is highly selective for gold, with 70% uptake after 24 h (figure 3.6, blue bars). Raising the concentration of HCl to 6 M increases the uptake of Au to >99% after 1 hour but decreases selectivity, with Tl (95%), Ga (>99%), and Fe (70%) also precipitated (figure 3.6, orange bars); however, these metals could in principle be removed from the precipitate by a 2 M HCl wash (see figure 3.5). Interestingly, no Pt uptake is seen in these experiments which is due to it being present as Pt(II) (i.e., square planar $PtCl_4^{2-}$) and not Pt(IV) (i.e., octahedral $PtCl_6^{2-}$). To confirm this, spot tests contacting excess L^6 with solutions of 0.01 M K_2PtCl_4 (i.e., Pt(II)) at 2, 6, or 10 M HCl did not result in any Pt(II) precipitation, showing that the charge and structure of the chloridometalate is important to the precipitation process. The precipitation of thallium was assumed to be as the species $TlCl_4^-$; however further investigation into thallium separation and recovery was considered to be beyond the scope of this thesis.

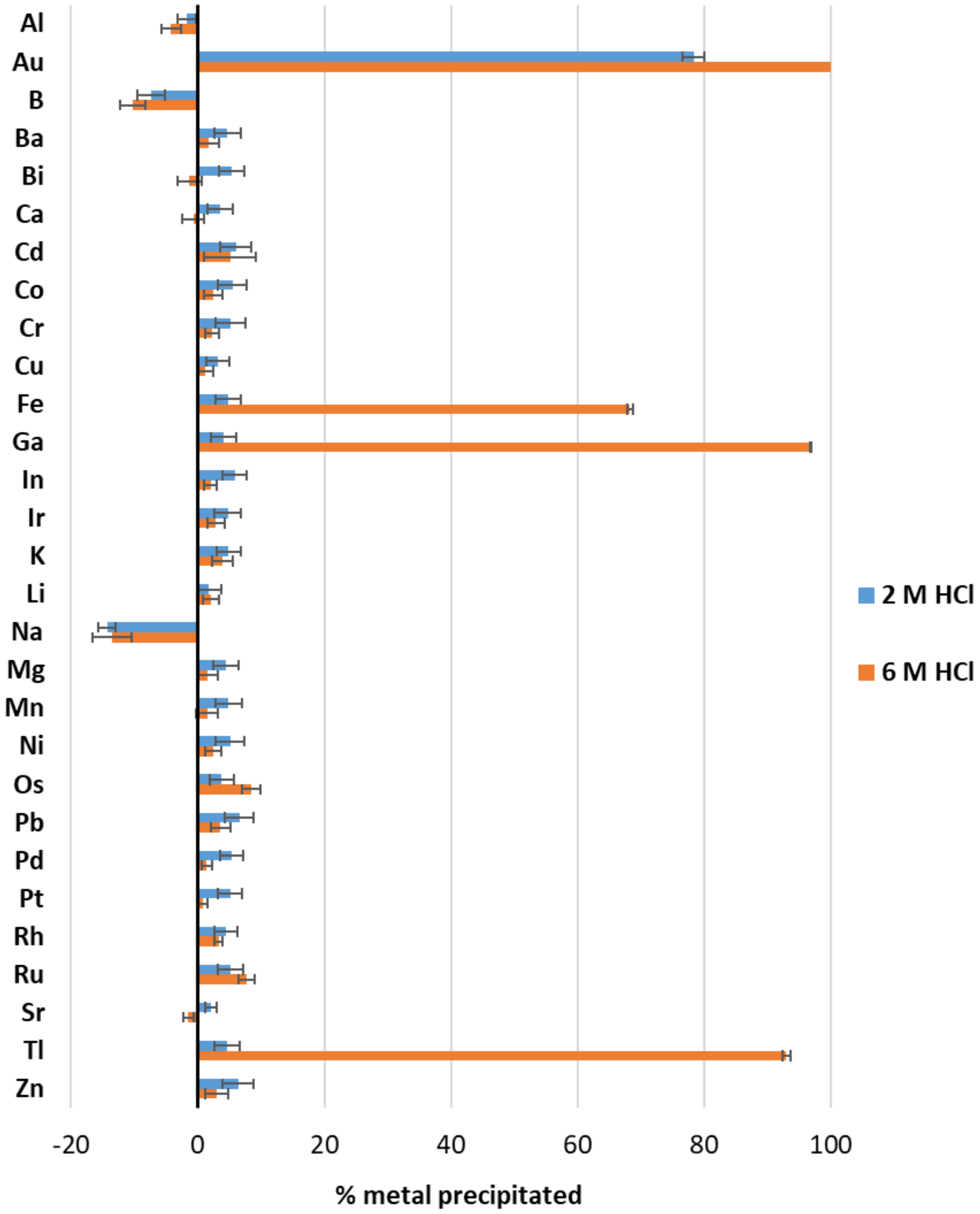

Figure 3.6 – Selectivity for gold in the presence of 28 other elements from ICP-MS standard solutions. * The negative precipitation efficiencies of some of the metals above are considered to be due to contamination of the samples from elements commonly present in water and on the experimental tools. Error bars are the standard deviation of three replicate experiments

3.4.6 Recovery of gold from real e-waste

Finally, gold was selectively separated from end-of-life printed circuit boards dissolved in aqua regia (diluted to 40%), with 98% Au precipitation after 1 h and no co-precipitation of any of the other elements present (table 3.4 and figure 3.7).

Table 3.4 – Selective precipitation of $HAuCl_4$ from a 40% aqua regia mixed-metal solution derived directly from waste printed circuit boards. See also figure 3.7.

Sample	Au (mg/L)	Cu (mg/L)	Ni (mg/L)	Pb (mg/L)	Sn (mg/L)
Feed solution	180	15400	105	818	1650
Feed solution after contact with L^6	3.45	15400	108	829	1660
% metal precipitated	98.1	0	0	0	0

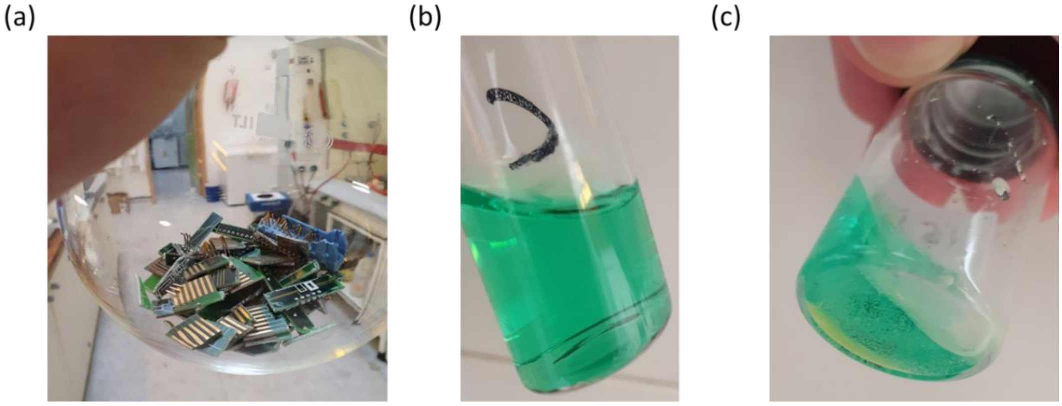

Figure 3.7 – (a) Photograph of e-waste pieces (b) photograph of aqua-regia solution after dissolution of e-waste and dilution to 40 % in deionised water (c) Photograph of $[HL^6][AuCl_4]$ precipitate from e-waste solution.

3.4.7 Characterisation of precipitates

3.4.7.1 Single-crystal X-ray structures of metal precipitates

Layering a solution of 0.01 M $HAuCl_4$ in 2 M HCl on a 0.1 M chloroform solution of L^6 results in controlled crystallisation. The X-ray crystal structure (figure 3.8) shows a chemical formula of $[HL^6][AuCl_4]$ in which the unique proton H1 is bound between adjacent amide O-atoms O1 and O1a (O1···O1a = 2.420(3) Å), forming an intermolecular proton chelate between amide units that assemble into an infinite supramolecular chain motif; a similar structure is seen for $[HL^6][AuBr_4]$ (figure 3.9).

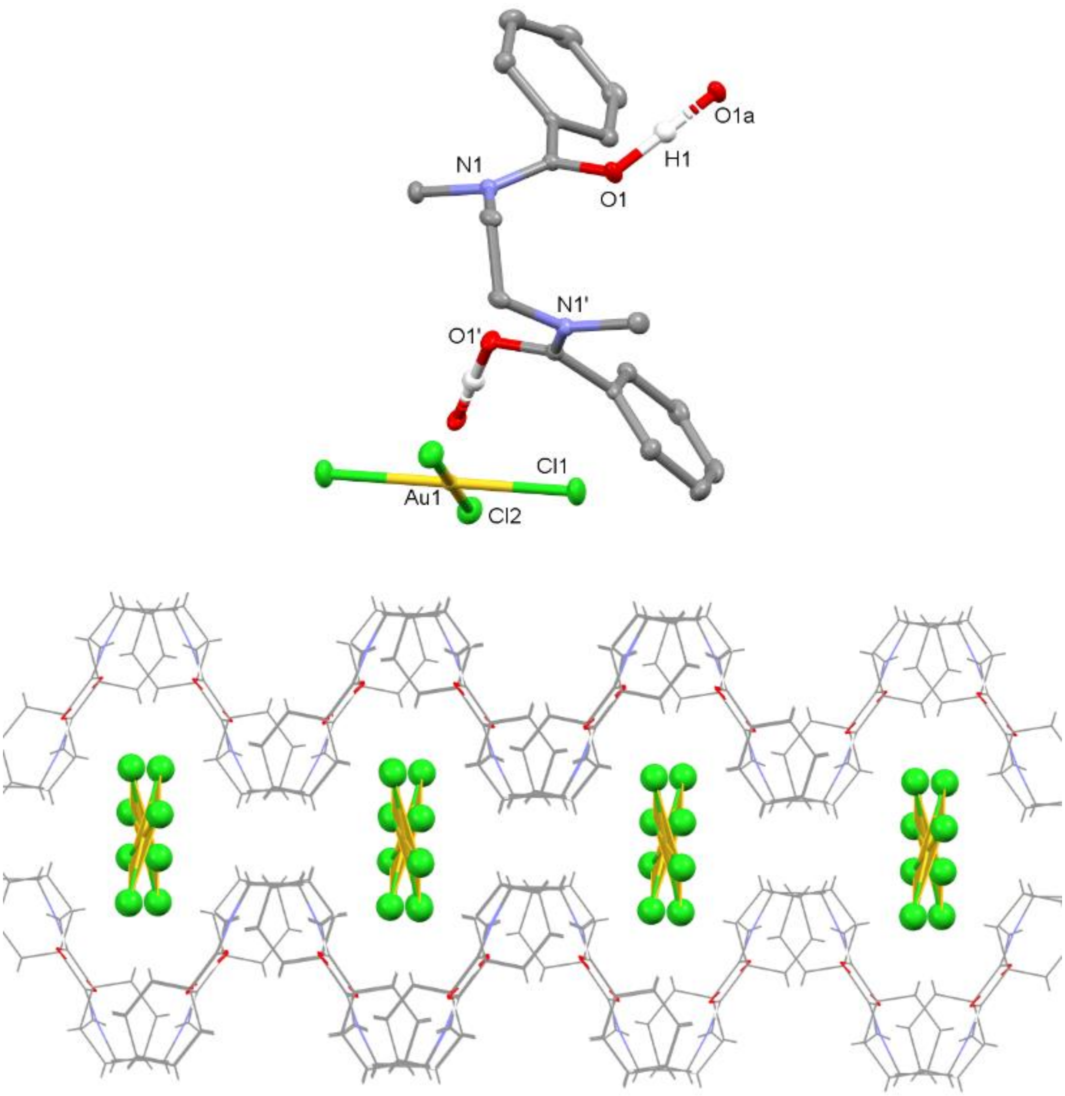

Figure 3.8 – X-ray crystal structure of [HL^6][AuCl$_4$]. Top: Asymmetric unit. Bottom: A view of the intermolecular proton-chelate structure and the arrangement of AuCl$_4^-$ within the cavity derived from the infinite chain of protonated diamides. C(H)···Cl(Au) 3.43-3.76 Å; N1-C3-C3′-N1′ 54.9(3)°. For clarity, all hydrogens except those involved in hydrogen bonding are omitted (displacement ellipsoids are drawn at 50% probability).

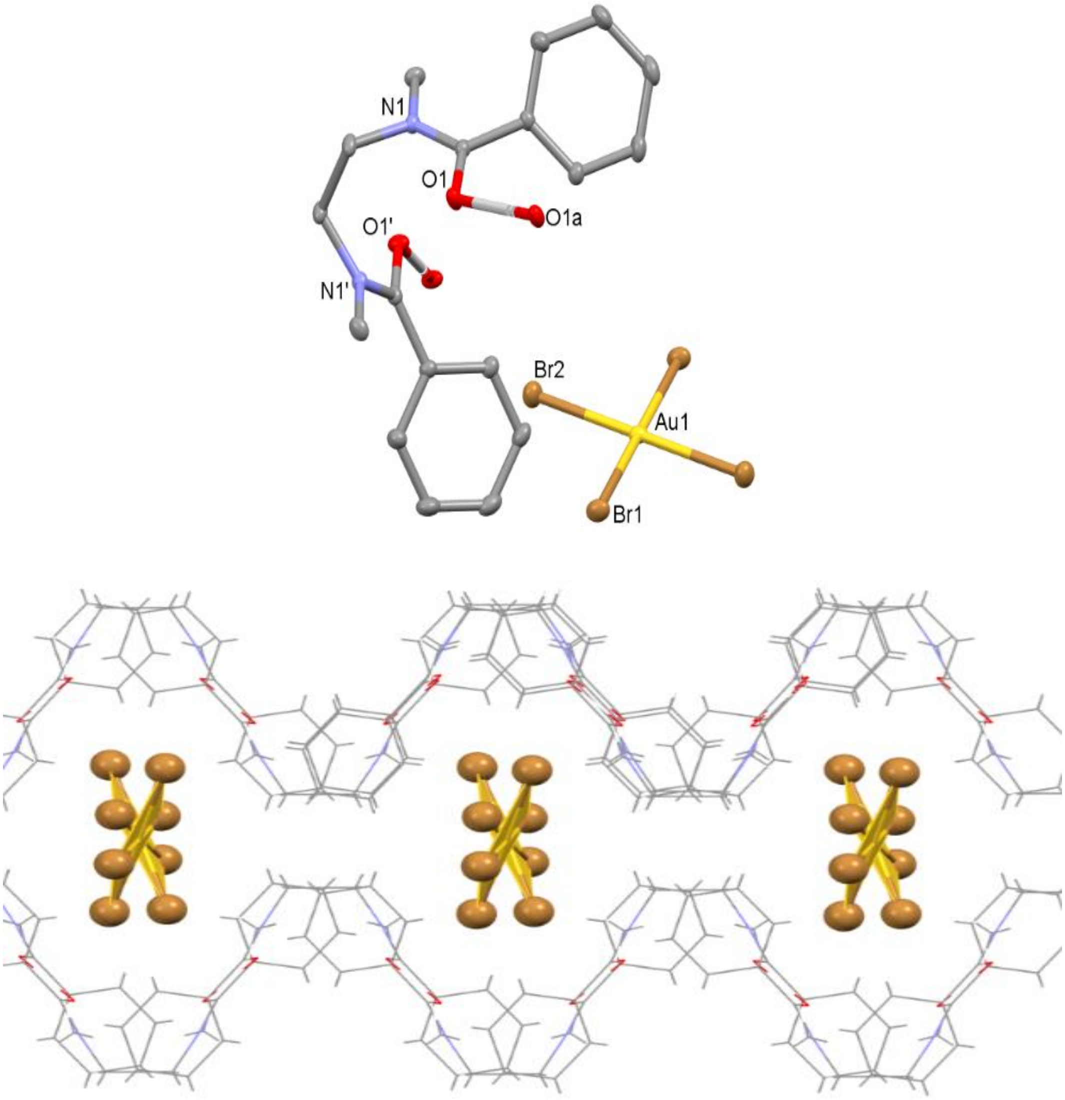

Figure 3.9 – X-ray crystal structure of [HL^6][AuBr$_4$]. Top: Asymmetric unit. Bottom: A view of the intermolecular proton-chelate structure and the arrangement of $AuBr_4^-$ within the cavity derived from the infinite chain of protonated diamides. C(H)···Br(Au) 3.79-3.92 Å; N1-C3-C3′-N1′ 55.4(2)°. For clarity, all hydrogens except those involved in hydrogen bonding are omitted (displacement ellipsoids are drawn at 50% probability).

While the linking of the diamides in [HL^6][AuCl$_4$] is similar to that seen for HAuCl$_4$ complexes of the diamidodurene R'C(O)N(R)CH$_2$(C$_6$Me$_4$)CH$_2$N(R)C(O)R',[129] the positioning of the AuCl$_4^-$ anions is different. In the latter example, the π-rich aryl group interacts strongly through face-to-face π-bonding with the planar AuCl$_4^-$ anion, whereas for [HL^6][AuCl$_4$] the phenyl and methyl substituents within the ribbon-like structure of the protonated diamides provide rhombohedral clefts that host the AuCl$_4^-$ guest and interact through non-covalent electrostatic interactions (figure 3.12).

Crystallisations of [HL^6][FeCl$_4$], [HL^6][GaCl$_4$], [HL^6]$_2$[SnCl$_6$], and [HL^6]$_2$[PtCl$_6$] were also achieved (figures 3.10, 3.11, 3.15 and 3.16, respectively). All four complexes are structurally similar, adopting a ribbon motif of [HL^6]$^+$ with an intermolecular proton chelate analogous to that seen for [HL^6][AuCl$_4$]. The N–C–C–N torsion angle of the diamide bridge varies according to the metalate and is significantly smaller for Au (54.0°) than the other metals (Fe: 81.0/88.2; Ga: 83.9°; Sn: 80.0; Pt: 80.6°); this feature may have consequences on the crystal packing and interactions between the metalate and cation host.

The X-ray structures of [HL^6][FeCl$_4$] and [HL^6][GaCl$_4$] are very similar, with each metalate being accommodated in a similar cavity to that of [HL^6][AuCl$_4$].

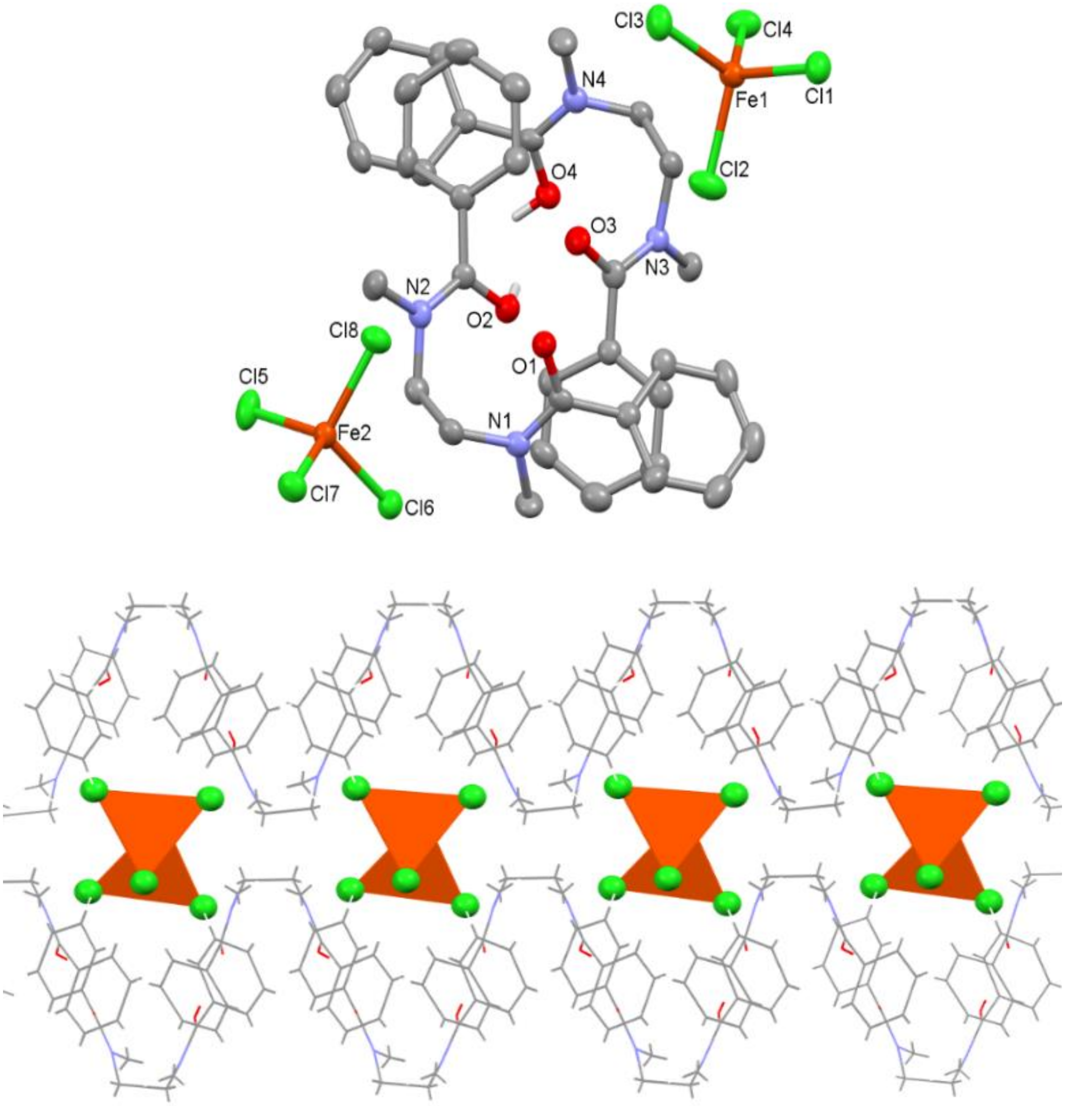

Figure 3.10 – X-ray crystal structure of [HL^6][FeCl$_4$]. Top: Asymmetric unit. For clarity, all hydrogens except those involved in hydrogen bonding are omitted (displacement ellipsoids are drawn at 50% probability). Bottom: A view of the intermolecular proton-chelate structure and the arrangement of FeCl$_4^-$ within the cavity derived from the infinite chain of protonated diamides. C(H)···Cl(Fe) 3.45-3.89 Å; N1-C9-C10-N2 88.2(8)°; N3-C27-C28-N4 81.0(8)°.

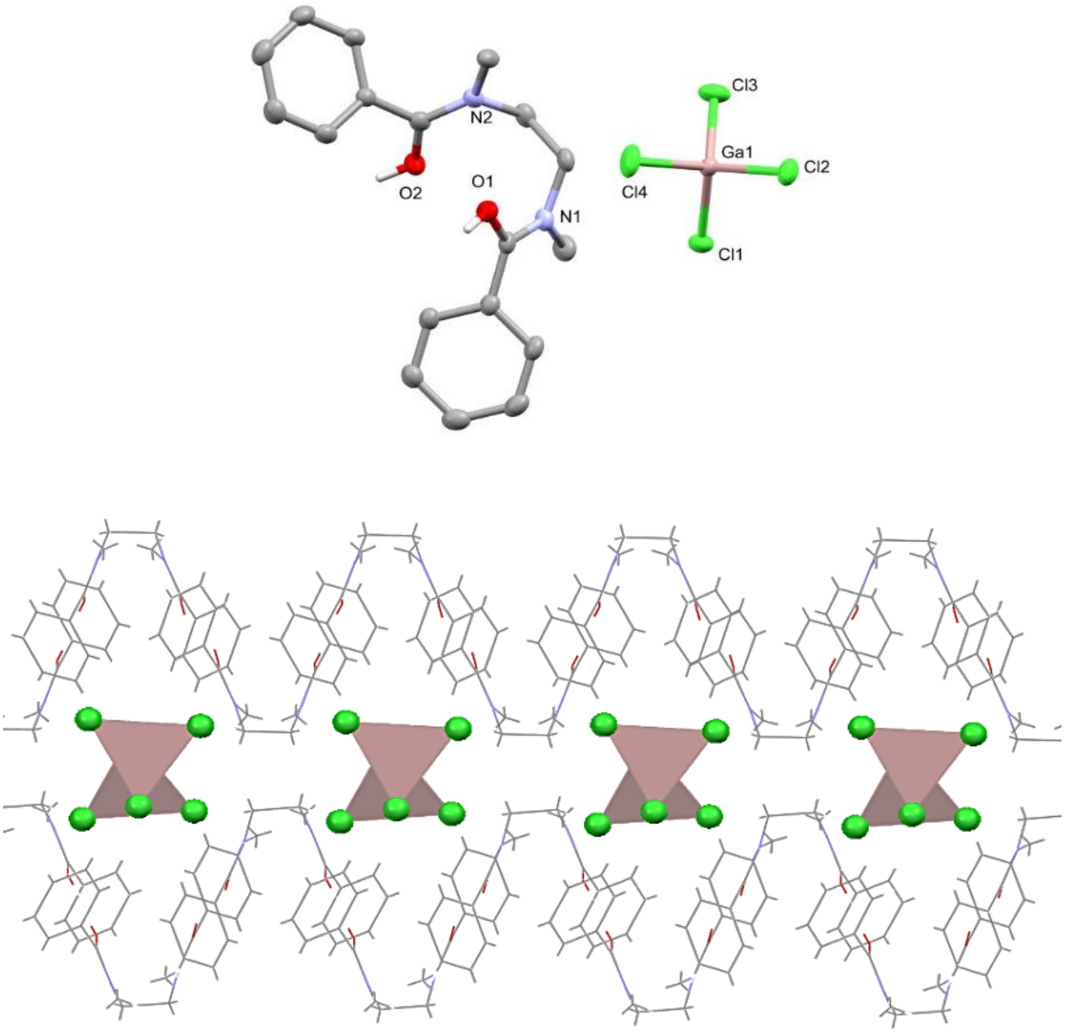

Figure 3.11 – X-ray crystal structure of [HL^6][GaCl$_4$]. Top: Asymmetric unit. For clarity, all hydrogens except those involved in hydrogen bonding are omitted (displacement ellipsoids are drawn at 50% probability). Bottom: A view of the intermolecular proton-chelate structure and the arrangement of GaCl$_4^-$ within the cavity derived from the infinite chain of protonated diamides. C(H)···Cl(Ga) 3.49-3.75 Å; N1-C9-C10-N2 83.9(4)°.

To visualise the location of the interactions between the metalates and $[HL^6]^+$, non-covalent interaction (NCI) analysis was undertaken by Professor Carole Morrison and Ms Susanna Vance (see section 7.5.1). Low-gradient isosurfaces (s = 1 a.u) of each complex are displayed to highlight the non-covalent interactions. The isosurfaces are coloured on a blue-green-red scale where blue indicates strong attractive interactions (such as hydrogen bonding) and red indicates strong non-bonding interactions (such as steric repulsion). Green colours are indicative of weaker interactions such as Van der Waals interactions.

A non-covalent interaction (NCI) plot of $[HL^6][AuCl_4]$, $[HL^6][FeCl_4]$ and $[HL^6][GaCl_4]$ (figures 3.12 – 3.14) shows the ligand clefts provide stabilising van der Waals interactions predominantly through multiple C-H···Cl contacts from aryl CH groups and NCH_3 groups, alongside.

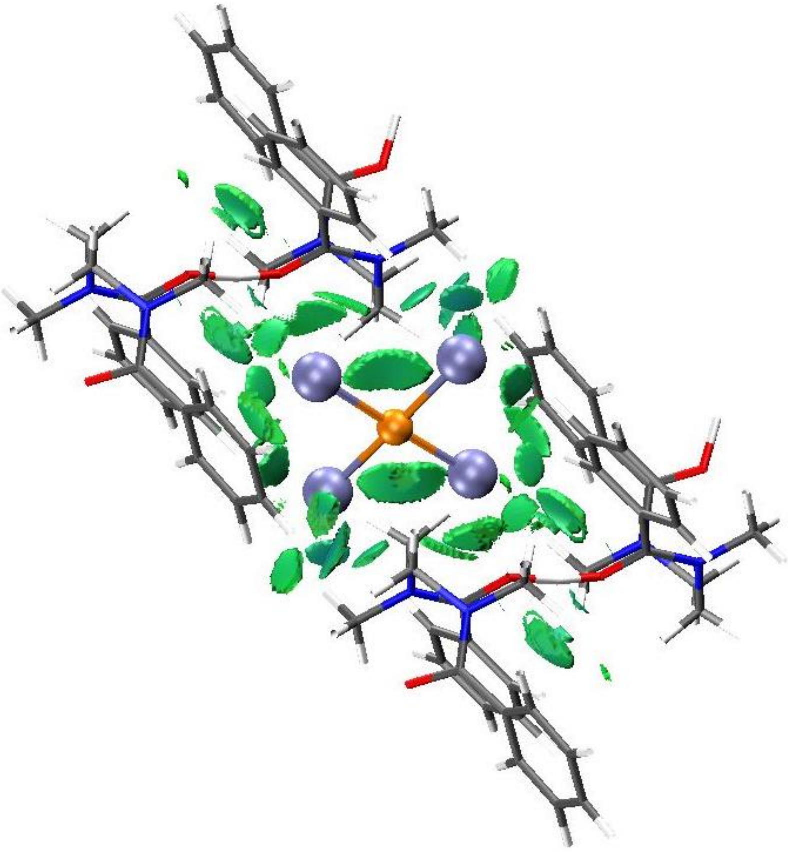

Figure 3.12 – Non-covalent interaction (NCI) analysis of $[HL^6][AuC_4]$ undertaken by Professor Carole Morrison and Ms Susanna Vance. Non-covalent bonding interactions 3D isosurface plots (s = 0.5 au, 0.05) (dark blue scale) < ρ < 0 (green scale) au). Atom colours: dark grey = C, red = O, dark blue = N; purple = Cl; white = H; Orange = Au.

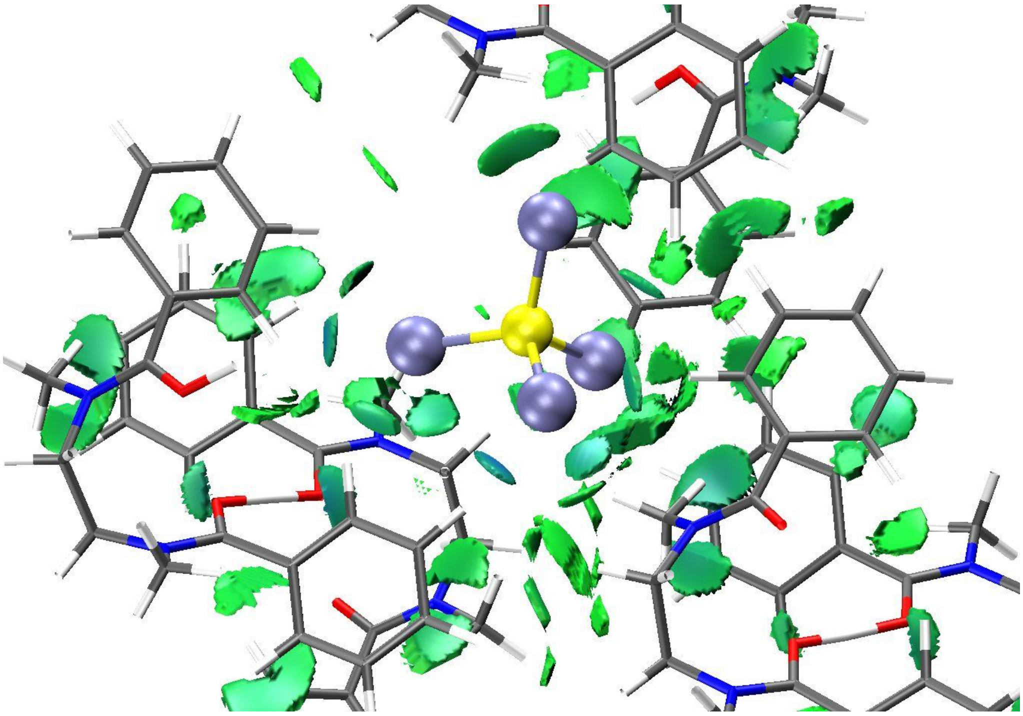

Figure 3.13 – Non-covalent interaction (NCI) analysis of [HL^6][FeCl$_4$] undertaken by Professor Carole Morrison and Ms Susanna Vance. Non-covalent bonding interactions 3D isosurface plots (*s* = 0.5 au, 0.05) (dark blue scale) < ρ < 0 (green scale) au). Atom colours: dark grey = C, red = O, dark blue = N; purple = Cl; white = H; yellow = Fe.

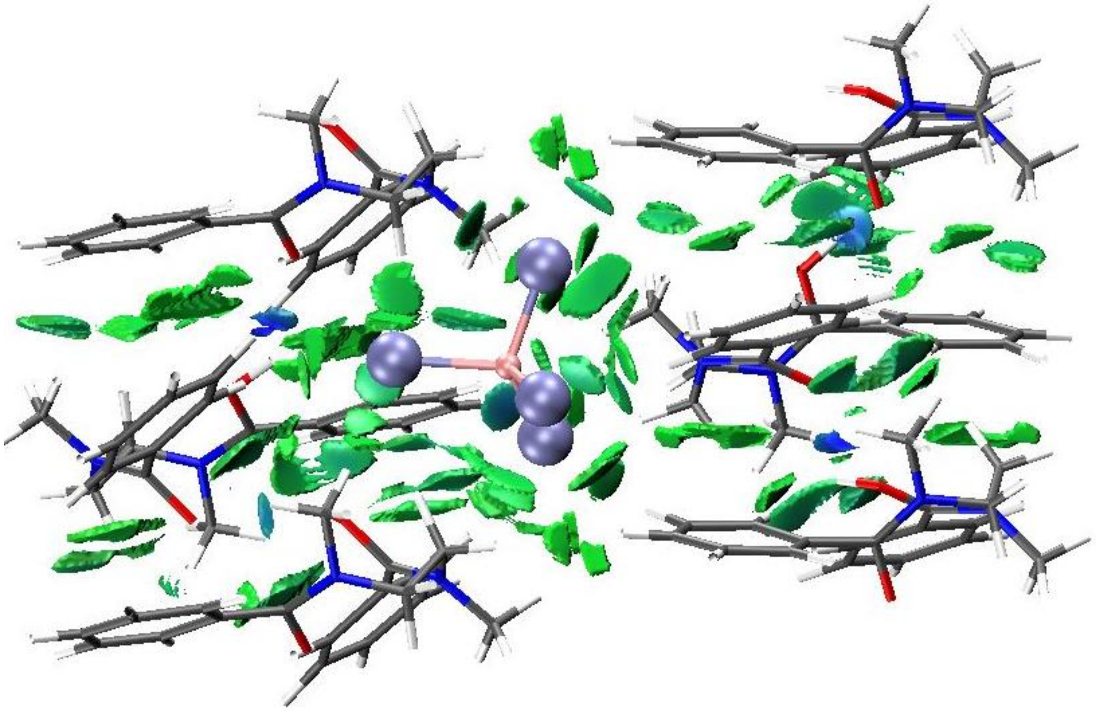

Figure 3.14 – Non-covalent interaction (NCI) analysis of [HL^6][GaC$_4$] undertaken by Professor Carole Morrison and Ms Susanna Vance. Non-covalent bonding interactions 3D isosurface plots (s = 0.5 au, 0.05) (dark blue scale) < ρ < 0 (green scale) au). Atom colours: dark grey = C, red = O, dark blue = N; purple = Cl; white = H; pink = Ga.

The X-ray structures of [HL^6]$_2$[SnCl$_6$], and [HL^6]$_2$[PtCl$_6$] are isostructural, comprising the same ribbon motif but with the octahedral metalates residing in slightly offset cavity that also includes one molecule of water. The NCI plots (figures 3.17 and 3.18) reveal that similar C-H···Cl host–guest interactions, with the water molecule in the [HL^6]$_2$[SnCl$_6$] and [HL^6]$_2$[PtCl$_6$] structures providing additional non-classical hydrogen-bonding to both the ligand and metalate ions.

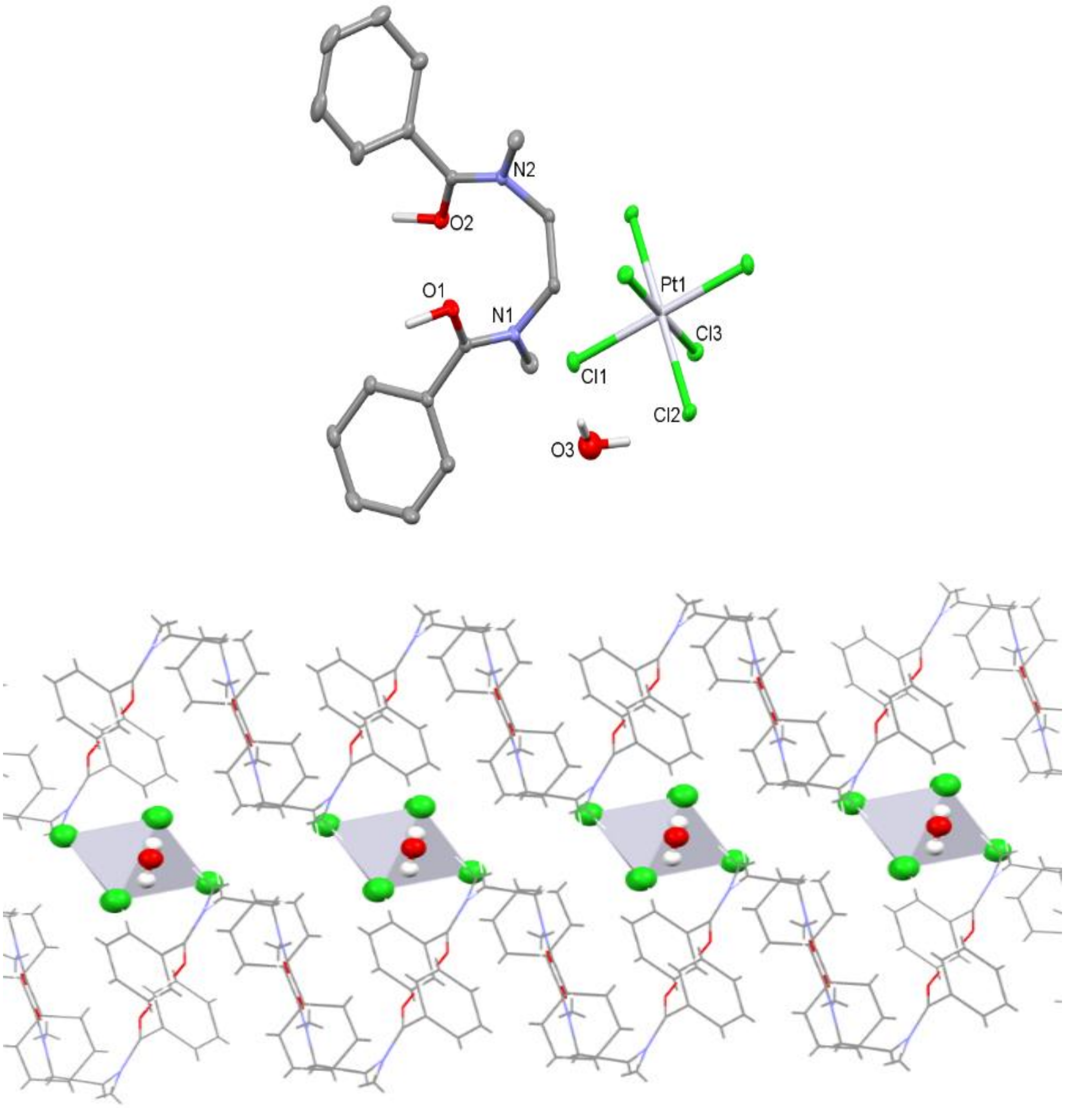

Figure 3.15 – X-ray crystal structure of $[HL^6]_2[PtCl_6](H_2O)$. Top: Asymmetric unit. For clarity, only one of the two $[HL^6]$ cations is shown and all hydrogens except those involved in hydrogen bonding are omitted (displacement ellipsoids are drawn at 50% probability). Bottom: A view of the intermolecular proton-chelate structure and the arrangement of $PtCl_6^{2-}$ within the cavity derived from the infinite chain of protonated diamides. C(H)···Cl(Pt) 3.44-3.62 Å; N1-C9-C10-N2 80.6(1)°.

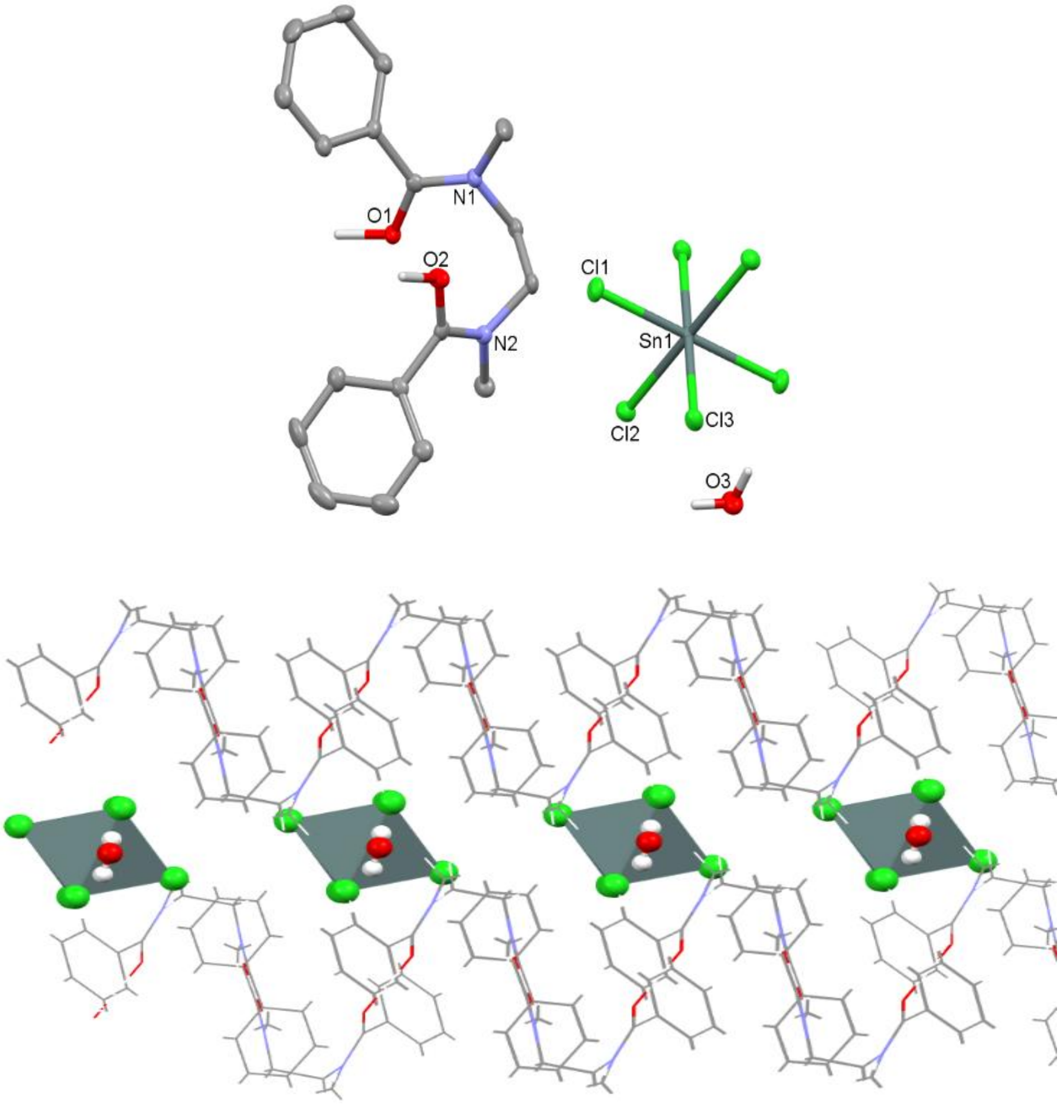

Figure 3.16 – X-ray crystal structure of $[HL^6]_2[SnCl_6](H_2O)$. Top: Asymmetric unit. For clarity, only one of the two $[HL^6]$ cations is shown and all hydrogens except those involved in hydrogen bonding are omitted (displacement ellipsoids are drawn at 50% probability). Bottom: A view of the intermolecular proton-chelate structure and the arrangement of $SnCl_6^{2-}$ within the cavity derived from the infinite chain of protonated diamides. C(H)···Cl(Sn) 3.45-3.63 Å; N1-C9-C10-N2 80.0(3)°.

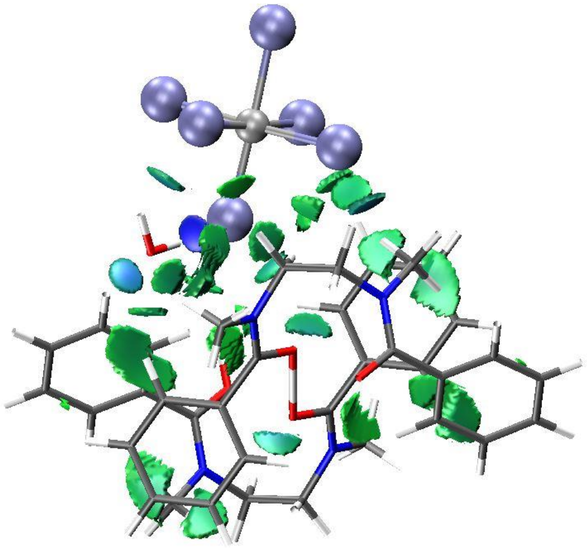

Figure 3.17 – Non-covalent interaction (NCI) analysis of $[HL^6]_2[PtC_6]$ undertaken by Professor Carole Morrison and Ms Susanna Vance. Non-covalent bonding interactions 3D isosurface plots (*s* = 0.5 au, 0.05) (dark blue scale) < ρ < 0 (green scale) au). Atom colours: dark grey = C, red = O, dark blue = N; purple = Cl; white = H; light grey = Pt.

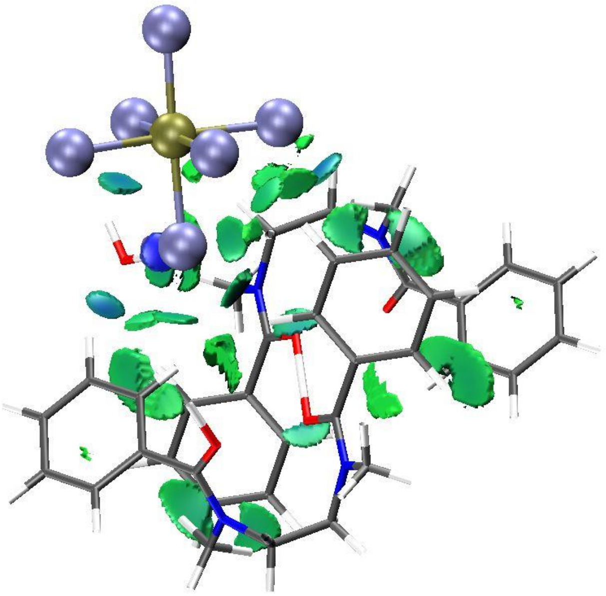

Figure 3.18 – Non-covalent interaction (NCI) analysis of $[HL^6]_2[SnC_6]$ undertaken by Professor Carole Morrison and Ms Susanna Vance. Non-covalent bonding interactions 3D isosurface plots (*s* = 0.5 au, 0.05) (dark blue scale) < ρ < 0 (green scale) au). Atom colours: dark grey = C, red = O, dark blue = N; purple = Cl; white = H; tan = Sn.

Metals such as cobalt and zinc are not precipitated by L^6. However, at 10 M HCl, a concentration at which L^6 is completely soluble, some crystallisation occurs and the X-ray crystal structures show the formation of $[HL^6][H_3O(H_2O)_2][CoCl_4]$ (figure 3.19) and $[HL^6][H_3O(H_2O)_2][ZnCl_4]$ (figure 3.20). In both cases, $[HL^6]^+$ forms an infinite intermolecular proton-chelated motif similar to all other structures with N–C–C–N torsional angles of 72.5 and 72.6° for Co and Zn, respectively. In contrast to the metal complexes that are readily precipitated by L^6, protonated water clusters $[H_3O(H_2O)_2]^+$ are found instead of a second $[HL^6]^+$, resulting in well-defined layers of $[H_3O(H_2O)_2]^+/[MCl_4]^{2-}$ interleaved with $[HL^6]^+$. The NCI plots (figure 3.21 and 3.22) again support C-H···Cl host/guest interactions, bridged with non-classical hydrogen-bonding from the protonated hydrogen bonded water clusters. This provides a distinct structural difference between the complexes that readily precipitate, which have one or no waters of crystallisation, compared with those that do not that have more than one water of crystallisation.

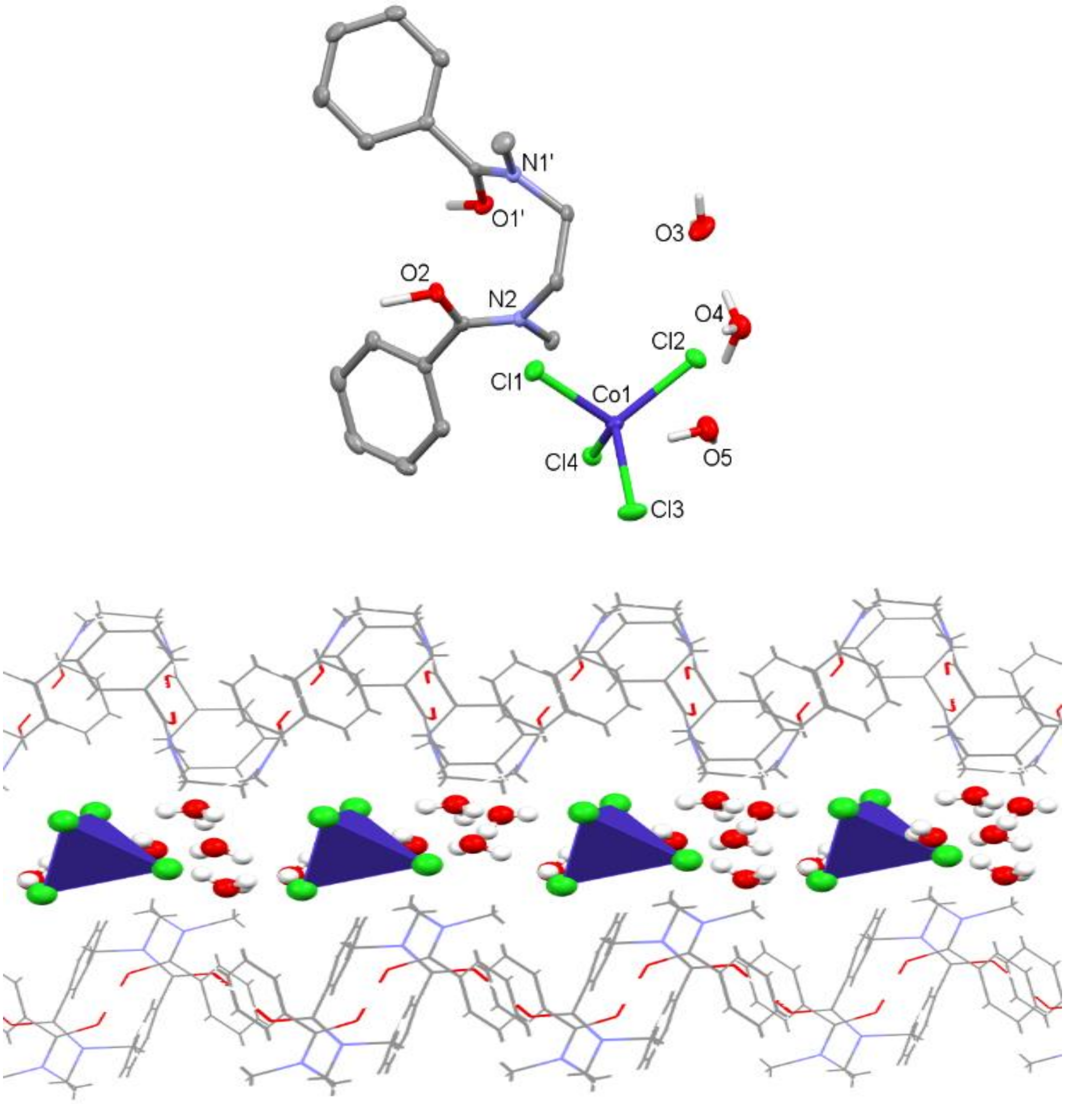

Figure 3.19 – X-ray crystal structure of [HL][$H_3O(H_2O)_2$][$CoCl_4$]. Top: Asymmetric unit. For clarity, all hydrogens except those involved in hydrogen bonding are omitted (displacement ellipsoids are drawn at 50% probability). Bottom: A view of the intermolecular proton-chelate structure and the arrangement of $CoCl_4^{2-}$ within the cavity derived from the infinite chain of protonated diamides. C(H)···Cl(Co) 3.57-3.87 Å; N1-C9-C10-N2 72.5(2)°.

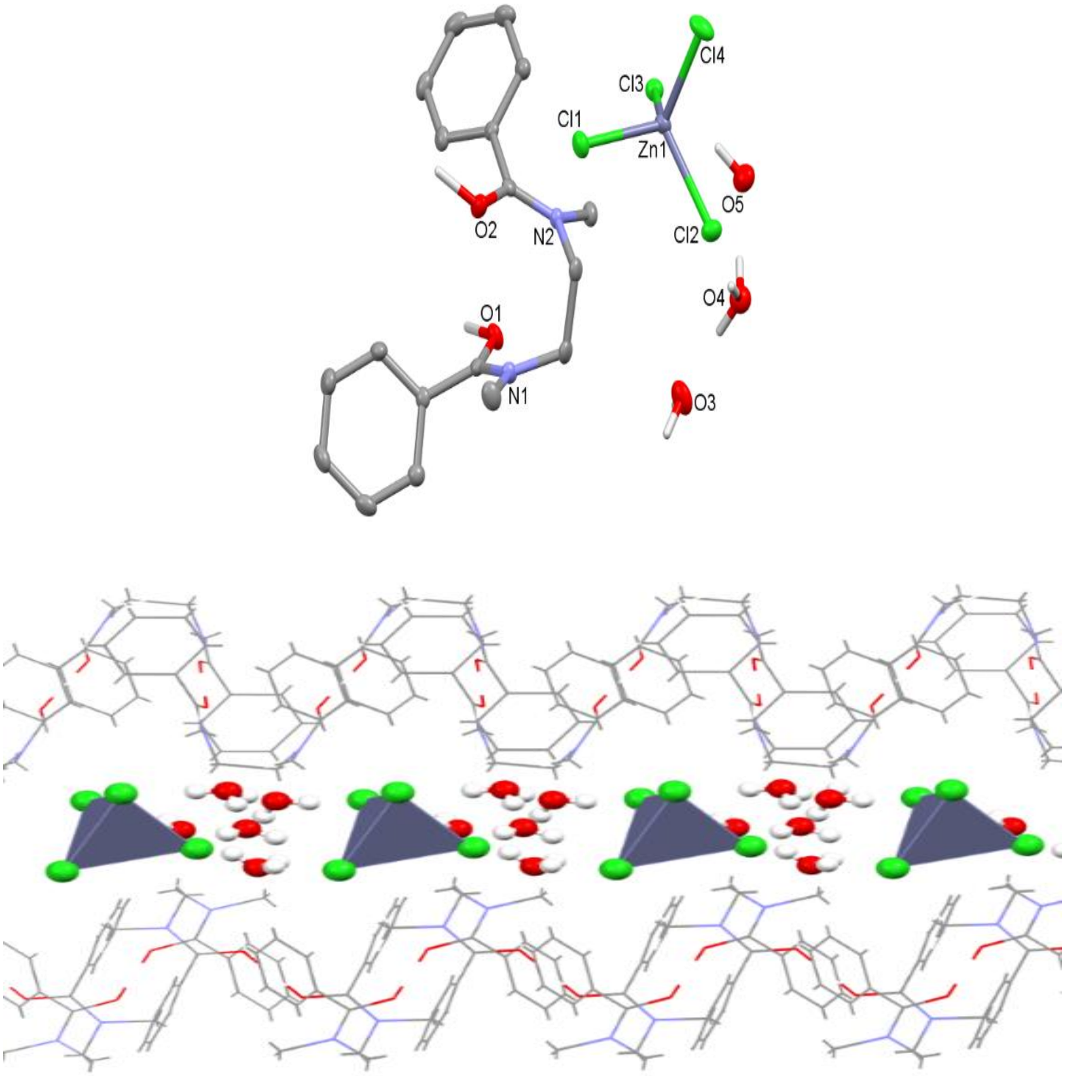

Figure 3.20 – X-ray crystal structure of $[HL][H_3O(H_2O)_2][ZnCl_4]$. Top: Asymmetric unit. For clarity, all hydrogens except those involved in hydrogen bonding are omitted (displacement ellipsoids are drawn at 50% probability). Bottom: A view of the intermolecular proton-chelate structure and the arrangement of $ZnCl_4^{2-}$ within the cavity derived from the infinite chain of protonated diamides. C(H)···Cl(Zn) 3.57-3.81 Å; N1-C9-C10-N2 72.6(3)°.

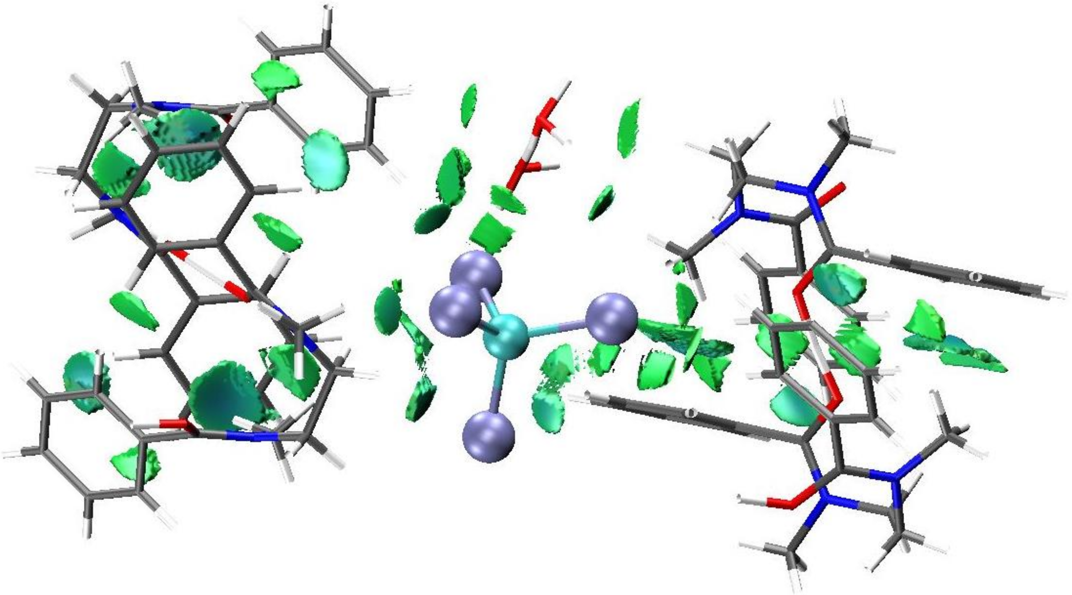

Figure 3.21 – Non-covalent interaction (NCI) analysis of [HL][$H_3O(H_2O)_2$][$CoCl_4$]. undertaken by Professor Carole Morrison and Ms Susanna Vance. Non-covalent bonding interactions 3D isosurface plots (*s* = 0.5 au, 0.05) (dark blue scale) < ρ < 0 (green scale) au). Atom colours: dark grey = C, red = O, dark blue = N; purple = Cl; white = H; cyan = Co.

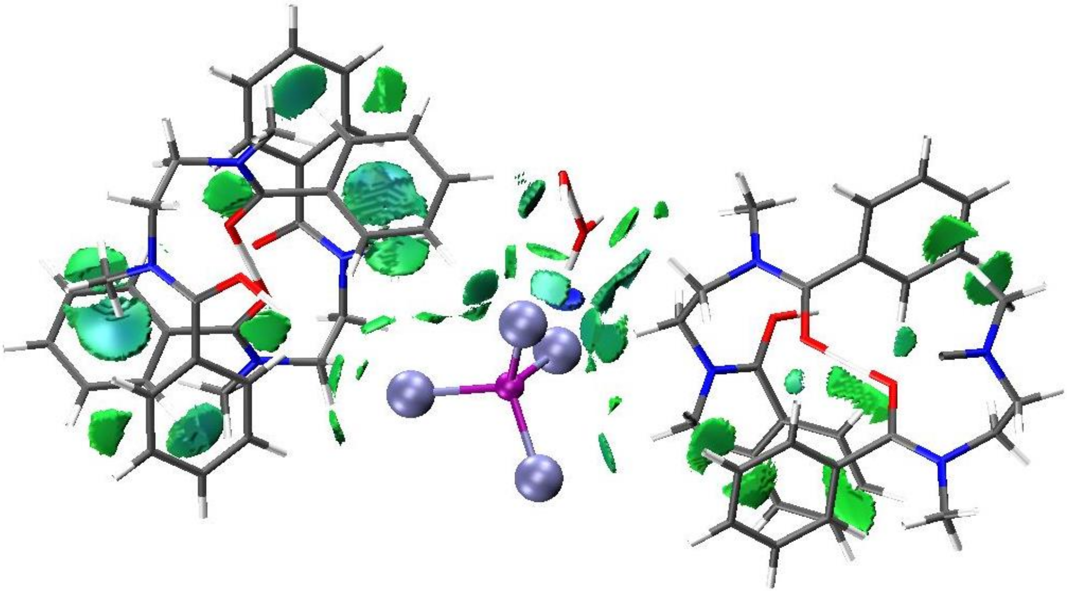

Figure 3.22 – Non-covalent interaction (NCI) analysis of [HL][$H_3O(H_2O)_2$][$ZnCl_4$]. undertaken by Professor Carole Morrison and Ms Susanna Vance. Non-covalent bonding interactions 3D isosurface plots (*s* = 0.5 au, 0.05) (dark blue scale) < ρ < 0 (green scale) au). Atom colours: dark grey = C, red = O, dark blue = N; light purple = Cl; white = H; dark purple = Zn.

3.4.7.2 Powder X-ray diffraction

To confirm that the [HL^6][AuCl$_4$] precipitate had the same structure as those determined by single crystal X-ray diffraction, the precipitate from the addition of 0.02 mmol of L^6 to a solution of 0.01 M HAuCl$_4$ in 6 M HCl was analysed by powder X-ray diffraction (figure 3.23, data collection, refinement, and analysis undertaken by Dr. Caroline Kirk) and showed the presence of two phases commensurate with a mixture of microcrystalline [HL^6][AuCl$_4$] and L^6. Refinement of the unit cell parameters in space group I2/a (a = 12.216(1) Å, b = 17.099(5) Å, c = 16.721 (3) Å, β = 142.79 (1) °) showed a close match with those of the single-crystal X-ray data for [HL^6][AuCl$_4$] (a = 12.0848(7) Å, b = 16.9574(2) Å, c = 16.5644(10) Å, β = 142.07(1) °).

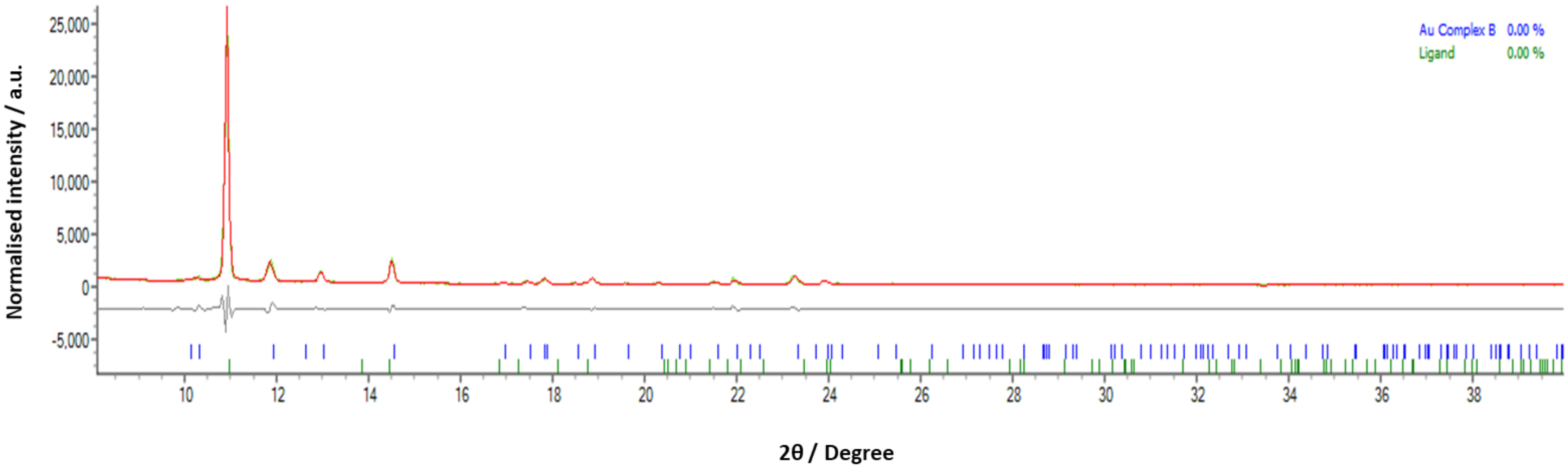

Figure 3.23 – Powder X-ray diffraction of the [HL^6][AuCl$_4$] precipitate from a mixture of L^6 (0.02 mmol) and HAuCl$_4$ (0.01 M) in 6 M HCl showing the observed data (green), the profile calculated from unit cell parameters of a combination of [HL][AuCl$_4$] and L^6 (red), and the difference profile (grey). Blue tick marks are associated with [HL^6][AuCl$_4$] whereas green tick marks are associated with L^6.

3.4.7.3 Single Crystal X-Ray Structures of halide salts of L^6

L^6 does not precipitate HCl from aqueous solution but instead HCl facilitates the dissolution of L^6, with increasing [HCl] resulting in increased L^6 being dissolved. While attempts to isolate the simple salt $[HL^6][Cl]$ from aqueous solution were unsuccessful, immersing a vial of L^6 dissolved in chloroform within a vial of concentrated HCl solution resulted in the formation of colourless crystals within the chloroform vial of $[HL^6][H_3O][H_2O][Cl][ClHCl]$ (figure 3.24). This structure still comprises the $[HL^6]^+$ ribbon motif as before, with a N–C–C–N torsional angle of 76.8°. Between these ribbons are hydrogen-bonded networks of $ClHCl^-$, water, hydronium and chloride molecules. Crystals of protonated L^6 were also obtained by vapour diffusion of 2 M HCl/Et_2O in to a $CHCl_3$ solution of L^6 (figure 3.25). In this case, the same formulation is seen but the structure is different with a discrete ‘channel’ of $ClHCl^-$ anions above one ribbon of $[HL^6]^+$ and a ‘channel’ of chloride and hydronium clusters beneath. The N–C–C–N torsional angles are also similar at 72.8 and 75.4°. Addition of these crystals to fresh HCl solutions results in dissolution and attempts to re-grow these crystals by the solvent layering technique instead of vapour diffusion were unsuccessful, suggesting that these chloride salts of L^6 are aqueous soluble and may take this form (among others) in solution.

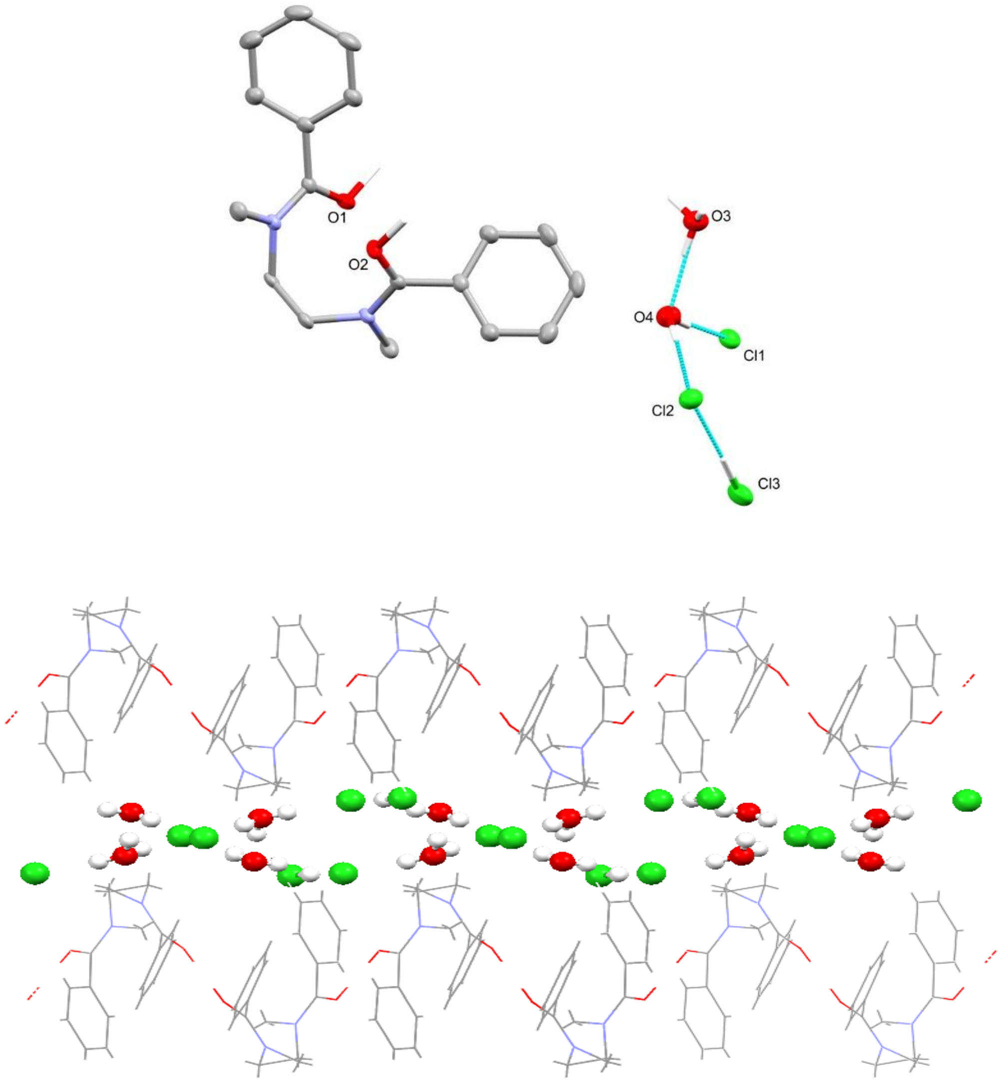

Figure 3.24 – X-ray crystal structure of [HL^6][H$_3$O][H$_2$O][Cl][ClHCl]. Top: Asymmetric unit. For clarity, all hydrogens except those involved in hydrogen bonding are omitted (displacement ellipsoids are drawn at 50% probability). Bottom: A view of the intermolecular proton-chelate structure and the arrangement of hydrogen bonded networks of $ClHCl^-$, water, hydronium and chloride molecules within the cavity derived from the infinite chain of protonated diamides. C(H)···Cl 3.51-3.84 Å; N1-C9-C10-N2 76.8(2)°.

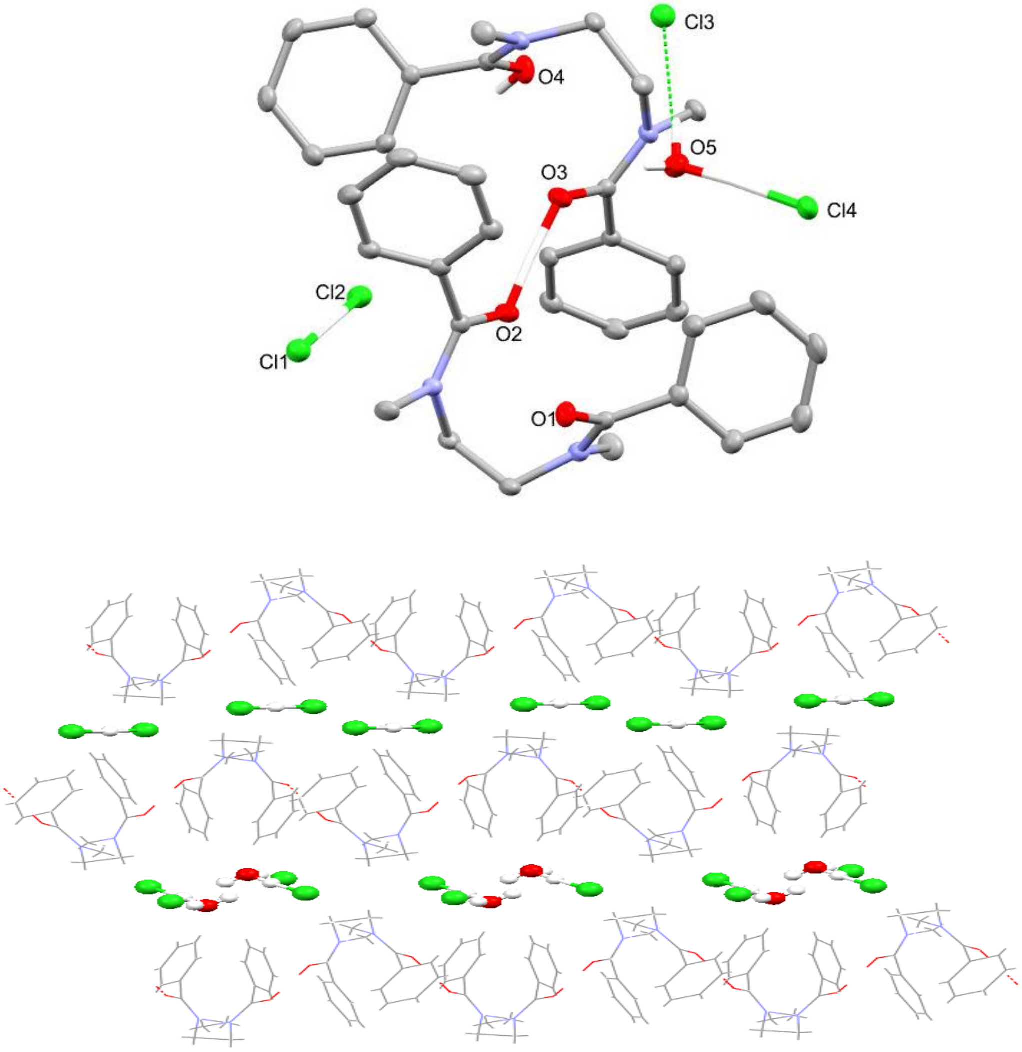

Figure 3.25 – X-ray crystal structure of $[HL^6]_2[H_3O][Cl]_2[ClHCl]$. Top: Asymmetric unit. For clarity, all hydrogens except those involved in hydrogen bonding are omitted (displacement ellipsoids are drawn at 50% probability). Bottom: A view of the intermolecular proton-chelate structure and the arrangement of hydrogen bonded networks of $ClHCl^-$, water, hydronium and chloride molecules within the cavity derived from the infinite chain of protonated diamides. C(H)···Cl 3.54-3.89 Å; N1-C9-C10-N2 -72.8(1)°; N3-C27-C28-N4 75.4(1)°.

During the growth of [HL^6][AuBr$_4$] crystals (figure 3.9) which were dark red, smaller yellow crystals were also found and their X-ray crystal structure was determined, being solved and refined as [HL^6]$_2$[Br$_2$][Br$_3$]$_2$[CHCl$_3$] (figure 3.26). However, it was noticed by the crystallographer upon initially collecting X-ray diffraction data on [HL^6][AuBr$_4$] data, that the yellow crystals were no longer present after another day and instead more dark red crystals of [HL^6][AuBr$_4$] had formed, suggesting that the bromine/tribromide crystals may be a kinetic product of crystallisation.

These observations suggest that the mode of action of precipitation proceeds by initial dissolution of L^6 to form aqueous soluble [HL^6][Cl] (or [HL^6][Br]) species, which then undergo ion-exchange with AuCl$_4^-$ (or other metalates), which are insoluble and so precipitate out of solution. This process is investigated further in section 3.4.8.

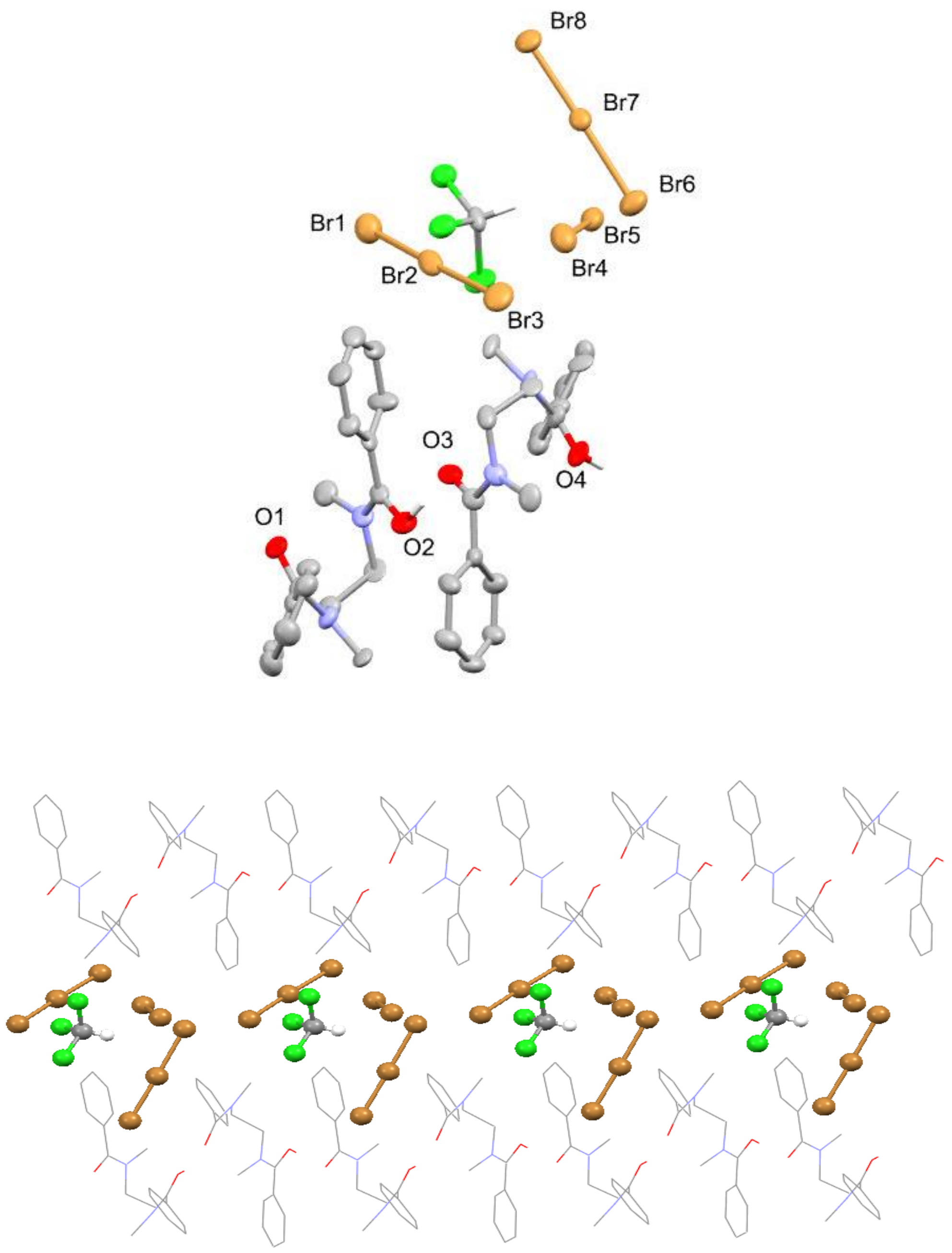

Figure 3.26 – X-ray crystal structure of $[HL^6]_2[Br_2][Br_3]_2[CHCl_3]$. Top: Asymmetric unit. For clarity, all hydrogens except those involved in hydrogen bonding and the on the chloroform molecule are omitted (displacement ellipsoids are drawn at 50% probability). Bottom: A view of the intermolecular proton-chelate structure and the arrangement of Br_2/Br_3^- molecules within the cavity derived from the infinite chain of protonated diamides. C(H)···Br 3.51-3.96 Å; N1-C10-C11-N2 -72(2)°; N3-C28-C29-N4 80(2)°.

3.4.8 Precipitation mode of action

That full uptake of gold from solution occurs using a stoichiometric amount of L^6 suggests that a dissolution-precipitation, not a surface-deposition mechanism, is occurring. After stirring a 2 M HCl solution with solid L^6, it is apparent (from visual inspection of the vial) that the majority of L^6 remains undissolved. To try and determine how much L^6 is dissolved by 2 M HCl, quantitative ^{1}H NMR spectroscopy was undertaken using *tert*-butanol as an internal standard. A suspension of L^6 in 2 M HCl/D_2O was prepared such that the concentration of L^6 would be 0.1 M if it dissolved completely; analysis of the ^{1}H NMR data showed dissolution to be minimal at 0.6 mM. Increasing the concentration of HCl to 6 M resulted in a 15-fold increase to 8.7 mM at 300 K after briefly shaking the NMR tube. Due to the high concentrations of acid and H_2O present in the samples, there were difficulties with sample tuning and locking and so further quantitative NMR experiments at higher concentrations of HCl were not undertaken.

In contrast to the 2 M HCl tests, continuous stirring of L^6 with 6 M HCl results in an almost colourless solution after 15 – 20 minutes, with few undissolved solids remaining. Interestingly, unprotonated L^6 and not the expected $[HL^6][Cl]$ was found to re-crystallise from 6 M HCl when the vial was left undisturbed over 2-3 days. When the HCl concentration is increased to 12 M HCl, L^6 rapidly and completely dissolves; dilution of this solution with water also causes unprotonated L^6 to crystallise from solution.

Solutions of $HAuCl_4$ in various concentrations of HCl were then contacted with solid L^6, and the concentration of gold remaining in solution measured by ICP-OES after various time points (figure 3.27). The time taken for gold uptake by L^6 decreases with increasing [HCl], reflecting the increasing solubility of L^6 in higher concentrations of HCl. At 2 M HCl, gold is completely precipitated after 30 minutes, compared with almost 95% of Au precipitated after 1 minute when the experiment was repeated at 6 M HCl. Addition of $HAuCl_4$ to a solution of L^6 in 12 M HCl results in the immediate precipitation of $[HL^6][AuCl_4]$.

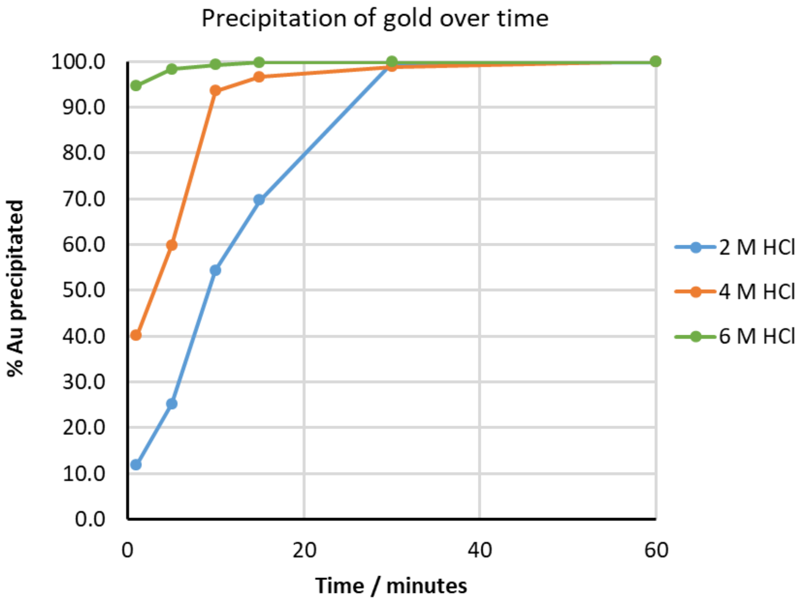

Figure 3.27 – Percentage of gold precipitated from 2, 4 or 6 M HCl solutions of 0.01 M $HAuCl_4$ over time. Conditions: 0.02 mmol L^6 stirred at 500 rpm with 2 mL $HAuCl_4$ in 2, 4 or 6 M HCl at 20 °C.

Despite the longer time taken to precipitate Au at lower HCl concentrations, L^6 could still efficiently precipitate Au from HCl concentrations as low as 0.01 mol L^{-1} after 1 hour (figure 3.28).

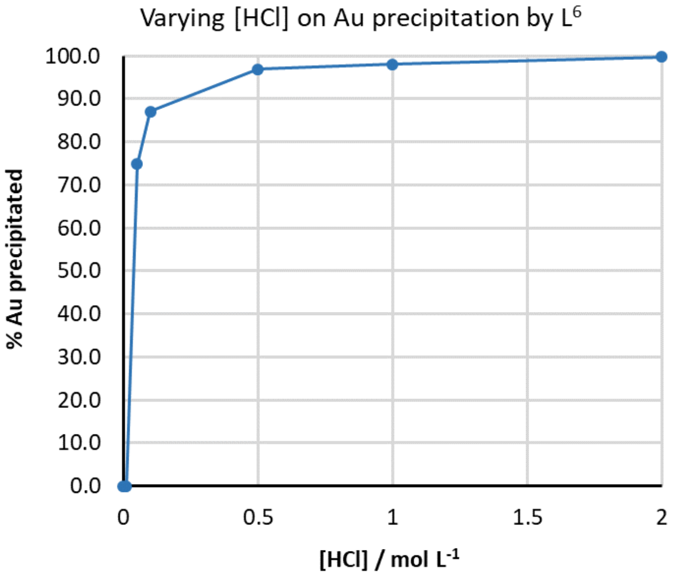

Figure 3.28 – Percentage of gold precipitated from 0-2 M HCl solutions of 0.01 M $HAuCl_4$. Conditions: 0.02 mmol L^6 stirred at 500 rpm with 2 mL $HAuCl_4$ in 0-2 M HCl solutions for 1 h at 20 °C.

To further confirm that L^6 must first be dissolved by HCl, a 2 M HCl solution of $HAuCl_4$ was pre-heated to 40 or 80 °C and then contacted with L^6 for 5 minutes at that temperature. It is found that the quantity of $[HL^6][AuCl_4]$ precipitate almost doubles as the temperature is increased from 20 to 40 °C and from 40 to 80 °C (figure 3.29).

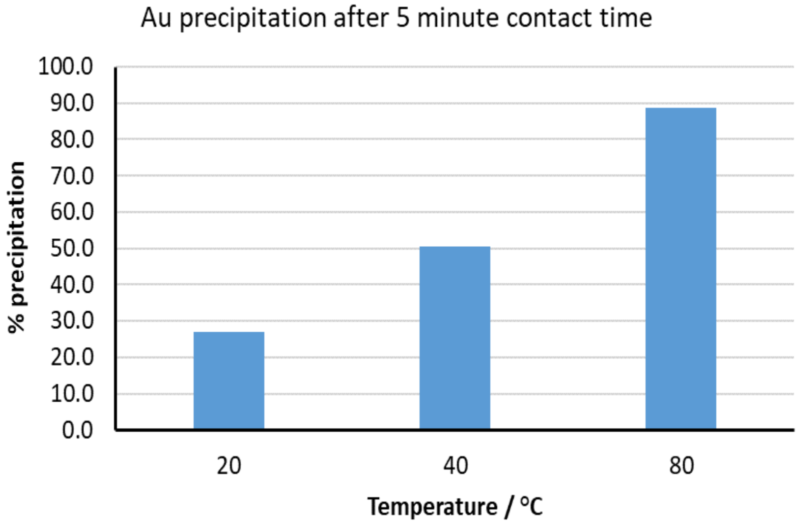

Figure 3.29 – Percentage of gold precipitated after 5 minutes from 2 M HCl solutions of 0.005 M $HAuCl_4$ at varying temperatures. Conditions: 0.02 mmol L^6 stirred at 500 rpm with 2 mL $HAuCl_4$ in 2 M HCl solutions for 5 minutes at 20, 40, and 80 °C.

3.4.9 Direct competition selectivity experiments

From the selectivity experiments in section 3.4.3 above, it is clear that L^6 is primarily selective for gold over any of the other metals that may also be precipitated. Given that Au, Fe, Ga, Pt and Sn are all precipitated at 6 M HCl under single metal conditions, it was of interest to determine if there was any further selectivity of L^6 towards some of the other target metals. This was done by contacting one molar equivalent of L^6 with 6 M HCl solutions comprising equimolar mixtures of either: $FeCl_3$ and $GaCl_3$; $FeCl_3$ and $SnCl_4$; or $SnCl_4$ and Na_2PtCl_6 (i.e., $L^6:M_1:M_2$ = 1:1:1).

3.4.9.1 Iron vs Gallium

At 6 M HCl, iron and gallium are both present in solution as monoanionic tetrahedral metalates, $FeCl_4^-$ and $GaCl_4^-$. It was therefore surprising that from 2 °C to 40 °C that L^6 was 4-

5x more selective for gallium over iron (figure 3.30). Little insight into this selectivity can be taken from the X-ray crystal structures of both precipitates (figures 3.10 and 3.11) as both structures are nearly identical. Repeating the experiment at 80 °C for 1 hour or 24 hours led to a decrease in selectivity suggesting any thermodynamic preference for Ga over Fe would be very subtle and so instead the selectivity for gallium may be under kinetic control.

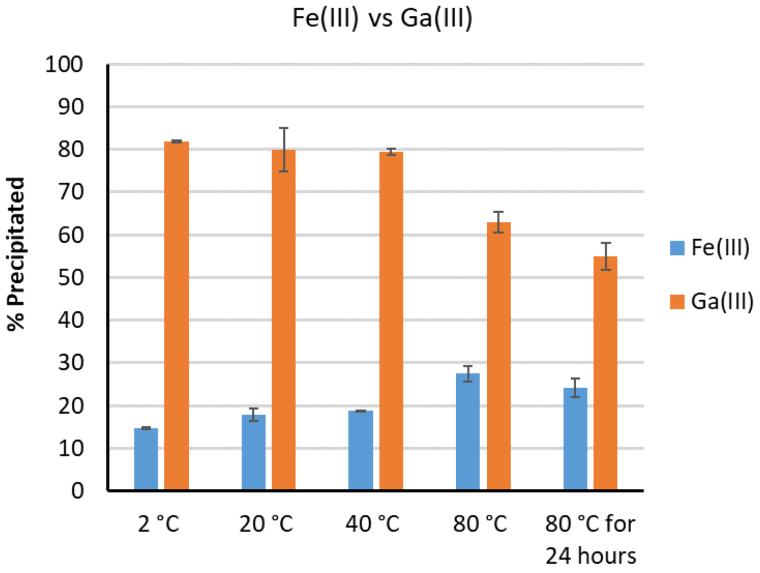

Figure 3.30 – Percentage of Fe(III) and Ga(III) precipitated by L^6 under competitive conditions. Conditions: 0.02 mmol L^6 contacted with 2 mL of $FeCl_3$ and $GaCl_3$ (0.01 M each) in 6 M HCl for 1 hour. In duplicate.

3.4.9.2 Iron vs Tin

At 20 °C, approximately 25% of Fe and Sn is precipitated by L^6. In contrast, heating the solution to 40 °C and 80 °C, L^6 almost exclusively precipitates iron over tin (figure 3.31), suggesting that precipitation of $FeCl_4^-$ is more thermodynamically favourable than $SnCl_6^{2-}$ and that $SnCl_6^{2-}$ precipitation may be more kinetically favourable, possibly because $SnCl_6^{2-}$ is a larger, more charge-diffuse anion than $FeCl_4^-$. Indeed, repeating the experiment at 2 °C results in the selectivity being reversed, with $SnCl_6^{2-}$ now being selectively precipitated over $FeCl_4^-$ indicating that the precipitation of tin proceeds under kinetic control. Sampling the solution heated to 80 °C that has been allowed to cool for 24 hours shows that a small amount of tin precipitates; this may be due an increased solubility of $[HL^6]_2[SnCl_6]$ upon heating or increased thermodynamic competition with chloride, given that complete precipitation does not occur.

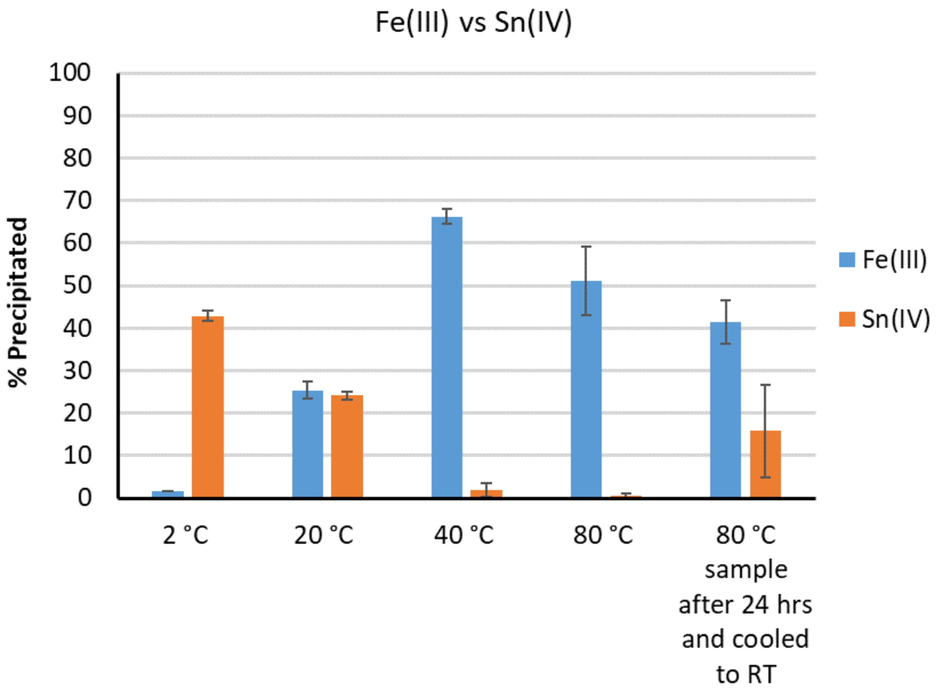

Figure 3.31 – Percentage of Fe(III) and Sn(IV) precipitated by L^6 under competitive conditions. Conditions: 0.02 mmol L^6 contacted with 2 mL of $FeCl_3$ and $SnCl_4$ (0.01 M each) in 6 M HCl for 1 hour. In duplicate.

3.4.9.3 Tin vs Platinum

With Sn(IV) and Pt(IV), both are present in solution as the dianionic octahedral metalates $SnCl_6^{2-}$ and $PtCl_6^{2-}$, and the crystal structures of each complex with L^6 are almost identical, with the only major difference being the size of $SnCl_6^{2-}$ being slightly larger than $PtCl_6^{2-}$ (the spherical diameter of $SnCl_6^{2-}$ is 4.85-4.89 Å whereas $PtCl_6^{2-}$ is 4.65-4.66 Å). The size of the metalate may be the reason behind the observed selectivity for tin from 2 °C to 40 °C, whereas at 80 °C no precipitates are observed, perhaps because both complexes are now soluble (figure 3.32) or because of increased thermodynamic competition with chloride. Indeed, sampling the solutions that were heated to 80 °C and allowed to cool for 24 h results in some tin precipitating from solution with the majority of platinum remaining in solution.

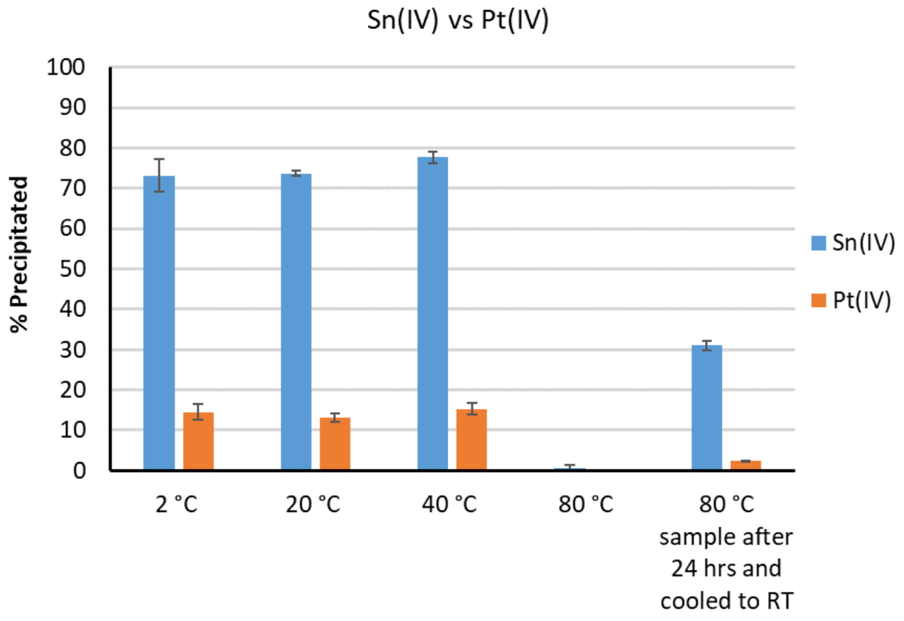

Figure 3.32 – Percentage of Sn(IV) and Pt(IV) precipitated by L^6 under competitive conditions. Conditions: 0.04 mmol L^6 contacted with 2 mL of $SnCl_4$ and Na_2PtCl_6 (0.01 M each) in 6 M HCl for 1 hour. In duplicate.

3.5 Precipitation performance of related simple diamides

As changing the diamide substituents from a branched aliphatic group in L^4 to a phenyl group in L^6 resulted in a switching from solvent extraction to precipitation, it was of interest to understand the effects (if any) that modifying the L^6 motif may have on the selectivity and efficiency of gold precipitation. To investigate this, a variety of derivatives of L^6 were prepared; this included altering the electronic effects by changing the substitution on the phenyl ring, varying the diamide axle length and shape, and inverting the amide C-N orientation. Precipitation experiments with various aqueous acidic metal solutions were then conducted to assess their suitability for precipitation.

3.5.1 Electronic effects

3.5.1.1 Spot tests with $FeCl_3$

Diamides $L^{7\text{-}10}$ (figure 3.33) were prepared to investigate how the efficiency of metal precipitation may change with different electron-donating or electron-withdrawing groups on the aromatic ring of the diamide. Initially, an excess of each diamide was contacted with a 6 M HCl solution of $FeCl_3$ for 24 hours to assess if any precipitation of $[HL^n][FeCl_4]$ occurred at all. From this spot test it was assumed that if Fe(III) was precipitated, then it was likely Au(III) would also precipitate, based on the selectivity shown for L^6 above.

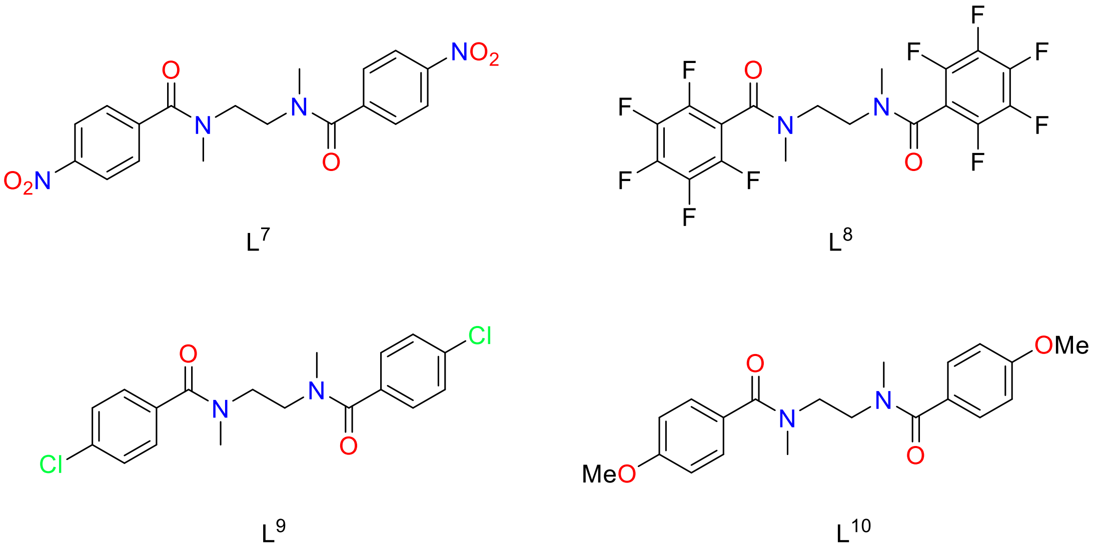

L^7 L^8

L^9 L^{10}

Figure 3.33 – Chemical structures of $L^{7\text{-}10}$.

The diamides L^7 and L^8 did not precipitate any Fe(III) at 6 M HCl after 24 h, whereas L^9 and L^{10} did efficiently precipitate Fe(III); these precipitates were subsequently confirmed by X-ray crystallography to be $[HL^9][FeCl_4]$ and $[HL^{10}][FeCl_4]$, respectively (section 3.5.1.3). As the substituent groups on the aromatic ring from L^7 to L^{10} varies from electron-withdrawing to electron-donating, the amide oxygen atoms become increasingly more basic and therefore the diamide is more easily protonated and hence formation of $[HL][FeCl_4]$ is more favourable. Spot tests with L^7 and L^8 with a solution of $HAuCl_4$ in concentrated HCl solutions also showed minimal to no Au precipitation after 24 h, and so these were not investigated further.

3.5.1.2 Metal precipitation dependence on acid concentration

Diamides L^9 and L^{10} were then tested in metal precipitation experiments in the same way as L^6 in section 3.4.2. Data for L^9 is shown in figure 3.34 and data for L^{10} is shown in figure 3.35. An alternative view of these data is provided in figure 3.36 for comparison with L^6.

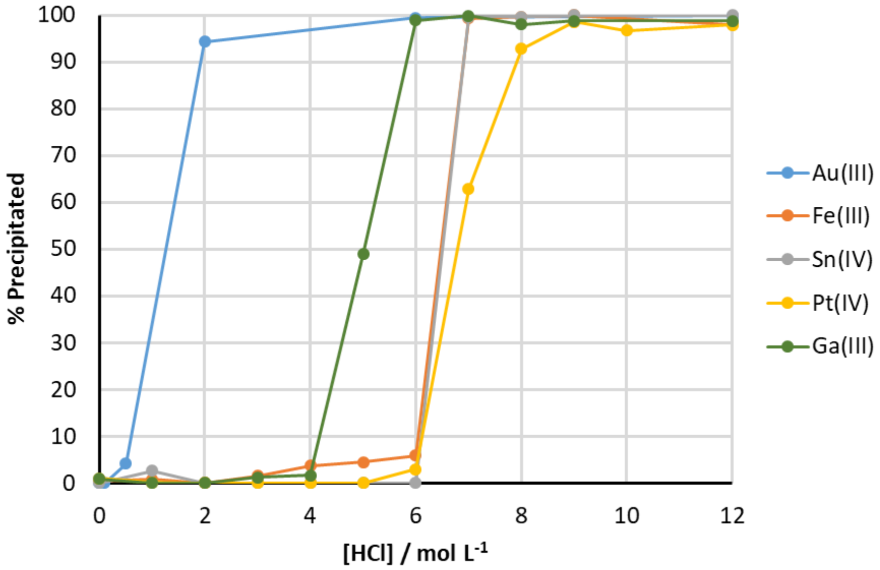

Figure 3.34 – Precipitation of Au(III), Fe(III), Ga(III), Sn(IV) and Pt(IV) by L^9. Conditions: 0.2 mmol L^9 contacted with 2 mL 0.01 M metal in 0 – 12 M HCl for 1 hour at RT, 500 rpm.

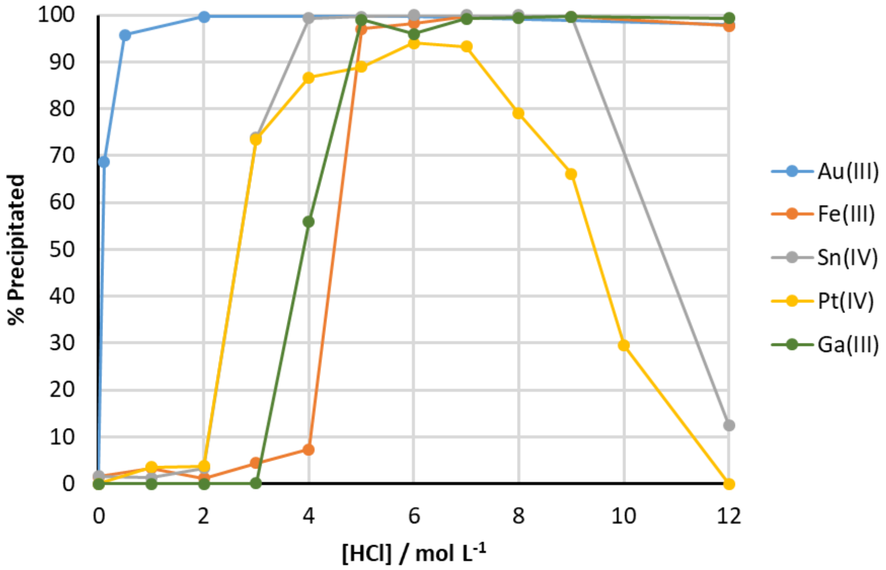

Figure 3.35 – Precipitation of Au(III), Fe(III), Ga(III), Sn(IV) and Pt(IV) by L^{10}. Conditions: 0.2 mmol of solid L^{10} contacted with 2 mL 0.01 M metal in 0 – 12 M HCl for 1 hour at RT, 500 rpm.

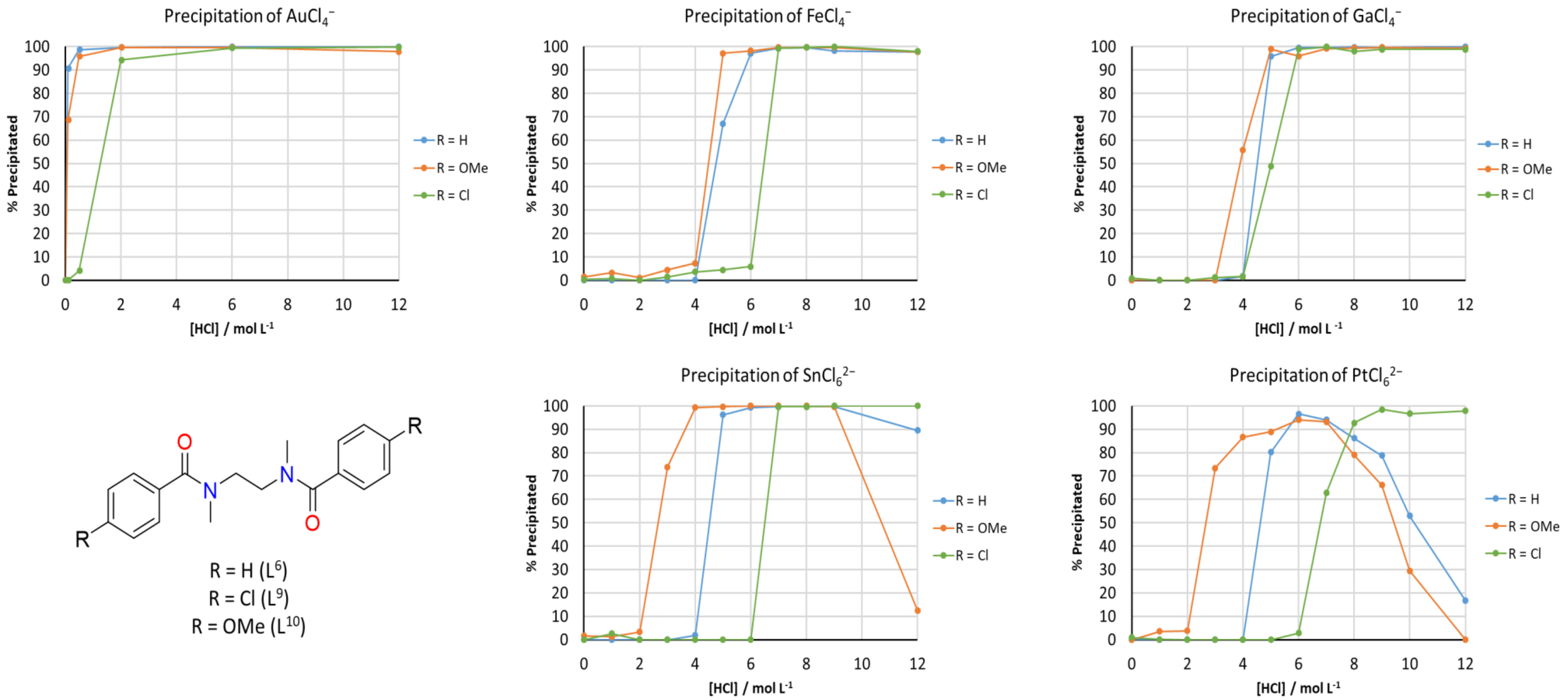

Figure 3.36 – Precipitation of Au(III), Fe(III), Ga(III), Sn(IV) and Pt(IV) by L^6, L^9 or L^{10}. Conditions: 0.2 mmol of solid L^6, L^9 or L^{10} contacted with 2 mL 0.01 M metal salt solution in 0 – 12 M HCl for 1 hour at RT, 500 rpm.

L^9 does not efficiently precipitate Au(III) at low HCl concentrations, in contrast with L^6 and L^{10}, and only begins to quantitatively precipitate the other metals tested from 6-7 M HCl, reflecting the weaker basicity of L^9 compared to L^6 and L^{10}. On the other hand, the diamide bearing electron-donating substituents, L^{10}, readily precipitates Au(III) at low HCl concentrations, and other metals are also precipitated at lower HCl concentrations than L^6. This trend is consistent for each metal tested; Fe(III) and Ga(III) are precipitated by one fewer mol L^{-1} of HCl for L^{10} than for L^9 with each metal continuing to be precipitated as [HCl] increases further. The difference in HCl concentration required for precipitation is more pronounced for the octahedral dianionic metalates; Sn(IV) is quantitatively precipitated by L^{10} at 4 M HCl, whereas L^9 did not precipitate any tin until 7 M HCl. A similar trend is also found for Pt(IV) with ~90 % precipitation at 4 M and 7 M HCl for L^{10} and L^9, respectively. However, in contrast to the other metals, as the HCl concentration increases beyond 7 M, the precipitation of Pt(IV) declines, whereas L^9 continues to effectively precipitate Pt(IV) at 12 M HCl. This may be a result of increasing competition between $PtCl_6^{2-}$ and Cl^- with L^6 and L^{10}, whereas L^9 remains selective for $PtCl_6^{2-}$ over Cl^-. A similar effect with Sn(IV) is also observed at 12 M HCl, although it is less pronounced than for Pt(IV) which is commensurate with the findings in section 3.4.9.3 that L^6 was more selective for Sn(IV) than Pt(IV).

3.5.1.3 Structural characterisation of precipitates

Crystallisations of $[HL^9][AuCl_4]$ (figure 3.37), $[HL^9][FeCl_4]$ (figure 3.38), $[HL^{10}][AuCl_4]$ (figure 3.39) and $[HL^{10}][FeCl_4]$ (figure 3.40) were achieved by layering HCl solutions of either metal on solutions of L^9 or L^{10} in $CHCl_3$.

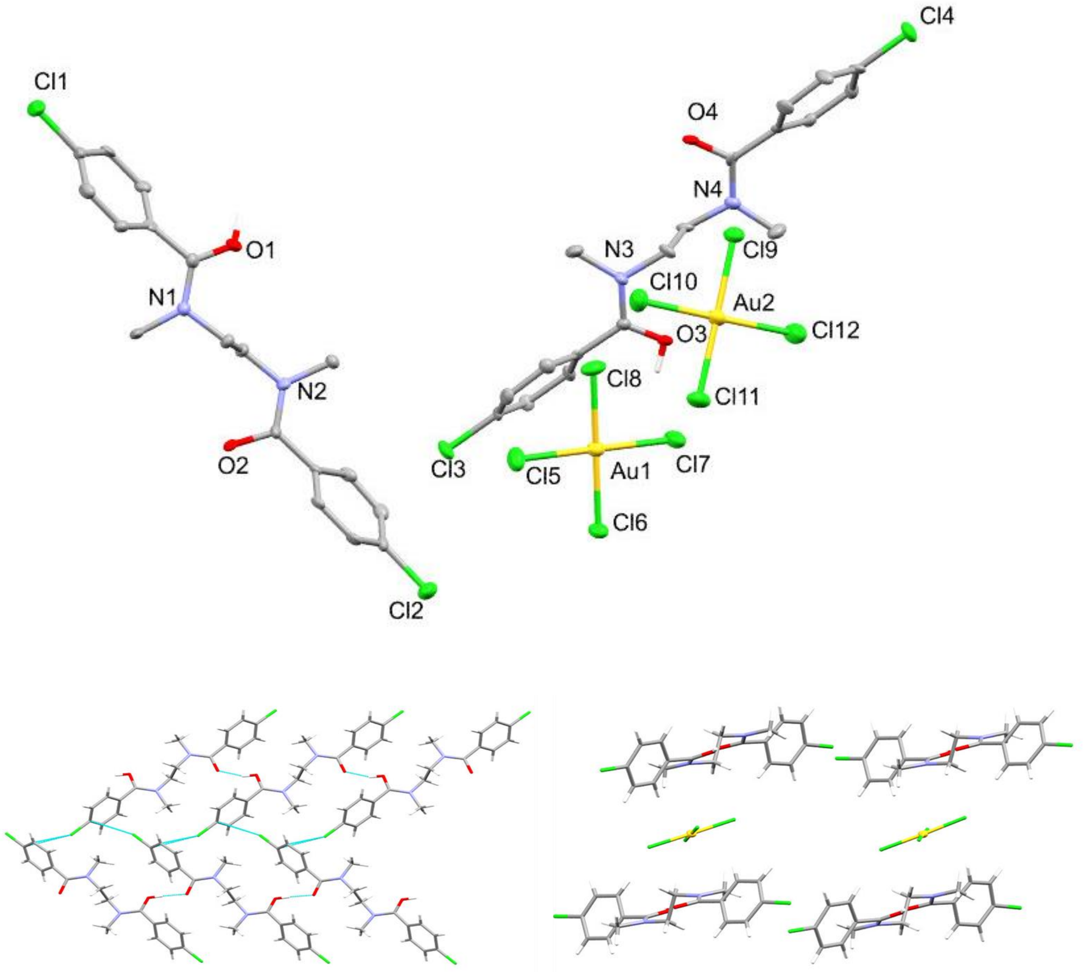

Figure 3.37 – X-ray crystal structure of $[HL^9][AuCl_4]$. Top: Asymmetric unit. For clarity, all $CHCl_3$ solvent molecules and hydrogens except those involved in hydrogen bonding are omitted (displacement ellipsoids are drawn at 50% probability). Bottom left: A view of the Cl···π interaction between of pairs of $[HL^9]^+$ molecules (for clarity, solvent and $AuCl_4^-$ molecules are omitted). Bottom right: A view along the crystallographic a-axis to illustrate where the $AuCl_4^-$ metalate is positioned between sheets of $[HL^9]^+$ (for clarity, solvent is omitted). C(H)···Cl(Au) 3.44-3.78 Å; N1-C9-C10-N2 177.4(2)°; N3-C27-C28-N4 177.6(2)°;

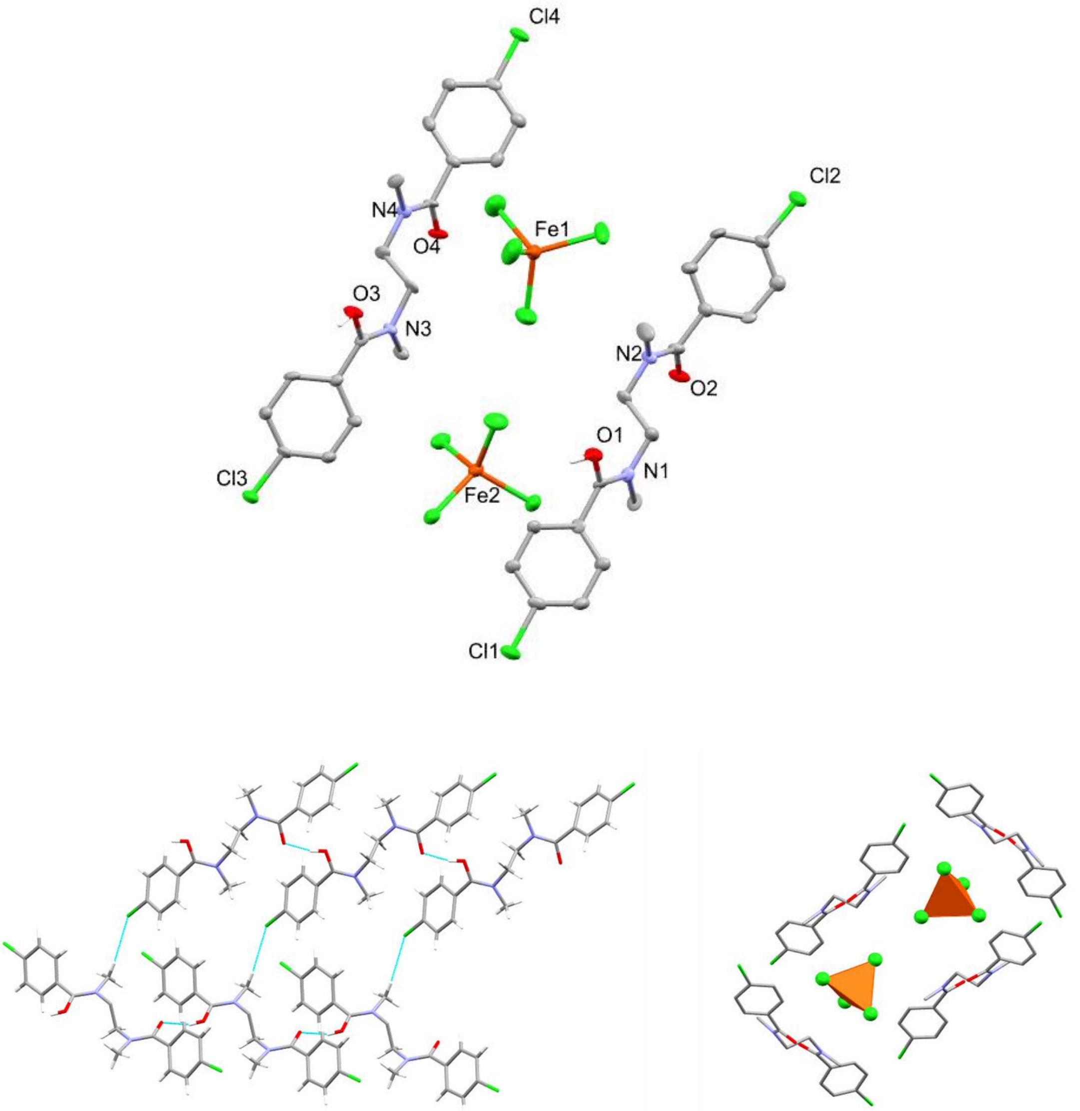

Figure 3.38 – X-ray crystal structure of $[HL^9][FeCl_4]$. Top: Asymmetric unit. For clarity, only two of the four $[HL^9]$ cations and two of the four $FeCl_4^-$ metalates are shown, $CHCl_3$ solvent is omitted and all hydrogens except those involved in hydrogen bonding are also omitted (displacement ellipsoids are drawn at 50% probability). Bottom Left: A view of the $Cl\cdots H_3C$-N interaction between of pairs of $[HL^9]^+$ molecules (for clarity, solvent and $FeCl_4^-$ molecules are omitted). Bottom right: A view along the crystallographic a-axis to illustrate where the $FeCl_4^-$ metalates are positioned between sheets of $[HL^9]^+$ (for clarity, solvent and all hydrogens are omitted). C(H)···Cl(Fe) 3.34-3.87 Å; N1-C9-C10-N2 179.9(7)°; N3-C27-C28-N4 -172.9(2)°; N5-C45-C46-N6 -178.8(8)°; N7-C83-C64-N8 176.3(8)°.

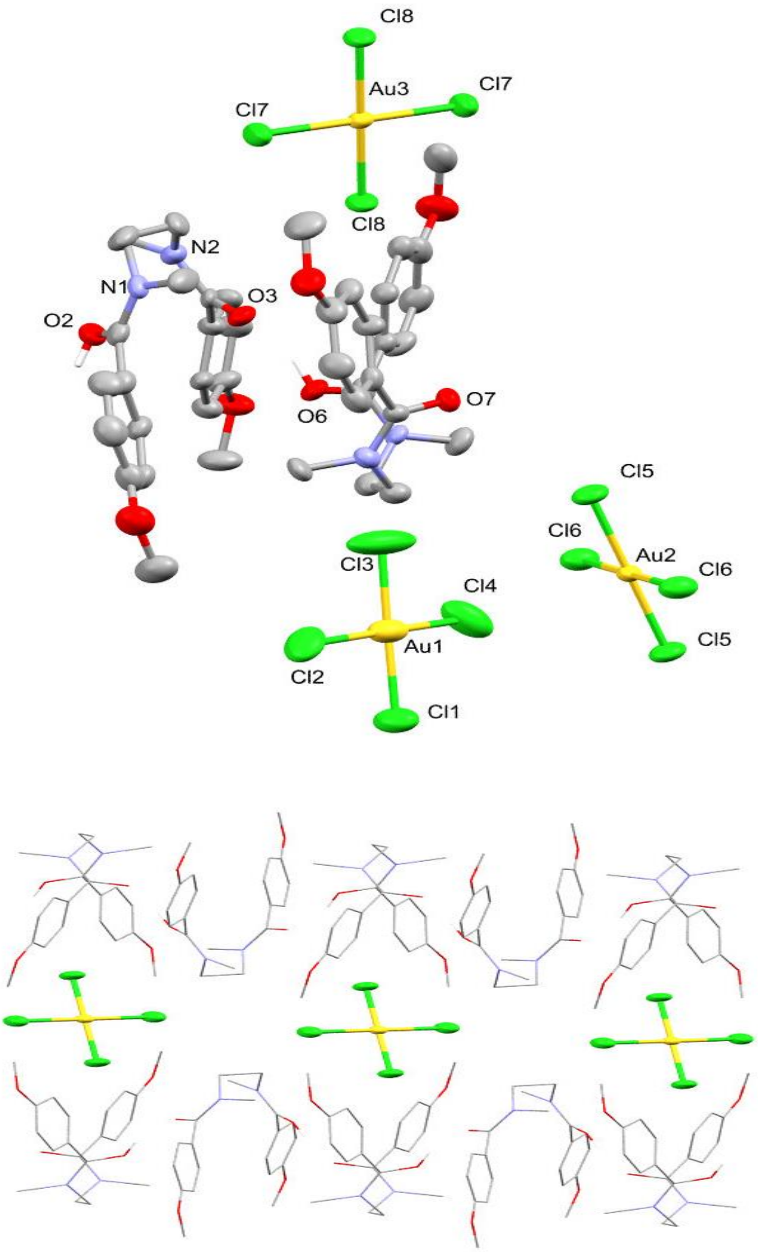

Figure 3.39 – X-ray crystal structure of [HL^{10}][$AuCl_4$]. Top: Asymmetric unit. For clarity, all $CHCl_3$ solvent molecules and hydrogens except those involved in hydrogen bonding are omitted (displacement ellipsoids are drawn at 50% probability). Bottom: A view of the intermolecular proton-chelate structure and the arrangement of $AuCl_4^-$ within the cavity derived from the infinite chain of protonated diamides (for clarity, solvent is omitted). C(H)···Cl(Au) 3.40-3.67 Å; N1-C10-C11-N2 75.4(2)°; N3-C30-C31-N4 79.4(2)°.

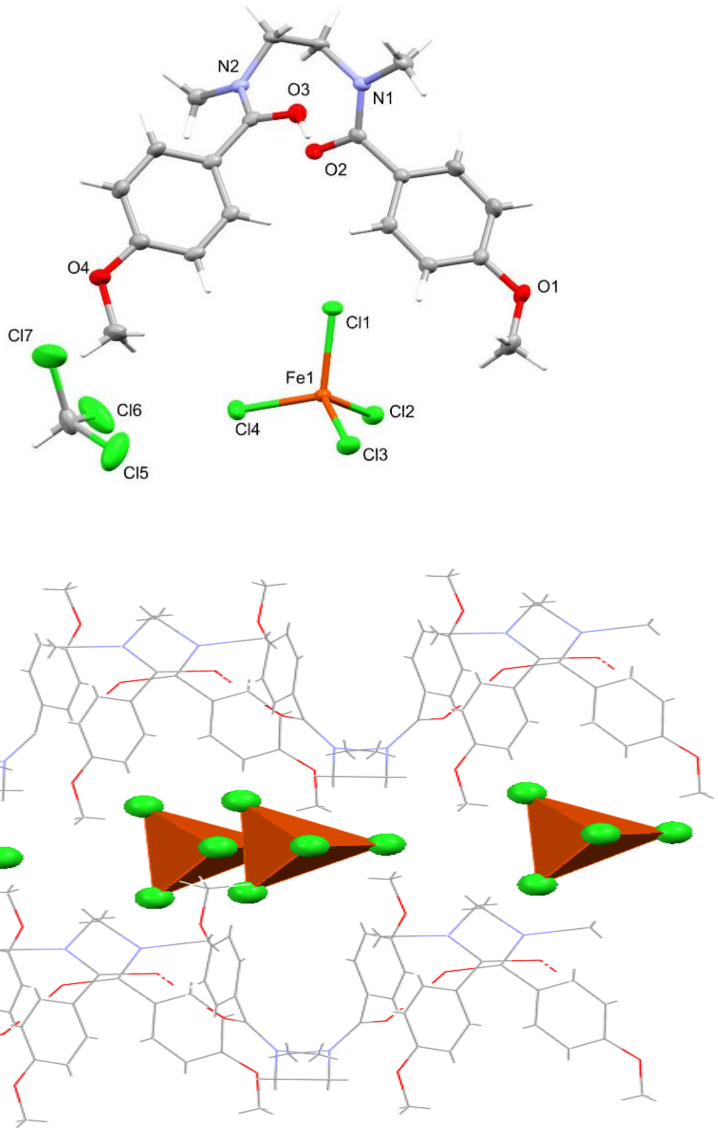

Figure 3.40 – X-ray crystal structure of [HL^{10}][FeCl$_4$]. Left: Asymmetric unit (displacement ellipsoids are drawn at 50% probability). Right: A view of the intermolecular proton-chelate structure and the arrangement of FeCl$_4^-$ within the cavity derived from the infinite chain of protonated diamides (for clarity, solvent is omitted). C(H)···Cl(Fe) 3.51-3.81 Å; N1-C10-C11-N2 76.2(3)°.

The X-Ray structures of [HL^{10}][FeCl$_4$] and [HL^{10}][AuCl$_4$] adopt a similar motif to those with L^6, with a helical-like infinite chain of [HL^{10}]$^+$ cations and AuCl$_4^-$ or FeCl$_4^-$ metalates residing within the resulting cavity. In either case, the metalate sits between the methoxy groups of a diamide, with close contacts from the aryl groups from one diamide and then additional close contacts from the methyl group of another diamide. The N–C–C–N torsion angle of the diamide bridges are slightly different to the L^{6} congeners, with $[HL^{10}][AuCl_4]$ having torsion angles of 75° and 79°, whereas $[HL^{10}][FeCl_4]$ is 65.2°.

In contrast, and while L^{9} still forms an infinite chain of $[HL^{9}]$ cations, the N–C–C–N torsion angles are close to 180° and so the metalates reside within $[HL^{9}]^{+}$ 'sheets' featuring additional non-covalent interactions between the chlorine atoms of L^{9} and the π-system of another L^{9} in the case of $[HL^{9}][AuCl_4]$, or NCH_3 groups in the case of $[HL^{9}][FeCl_4]$.

In each of these structures, a molecule of chloroform from the solvent is also present and so it is unlikely that these structures are completely representative of how Au and Fe are precipitated from aqueous solution by L^{9} or L^{10}. Attempts to grow crystals of $[HL^{9/10}][FeCl_4]$ or $[HL^{9/10}][AuCl_4]$ suitable for X-ray diffraction directly from an aqueous solution were unsuccessful.

3.5.2 Diamide hinge

3.5.2.1 Alkyl spacer length

The type and length of spacer between each amide functionality within the diamide was investigated. Initially, a 2° diamide analogue of L^{6} (L^{11}, figure 3.41) was synthesised and tested. In contrast to L^{6}, L^{11} was surprisingly ineffective at precipitating gold or iron after contacting L^{11} with 6 M HCl solutions for 24 hours.

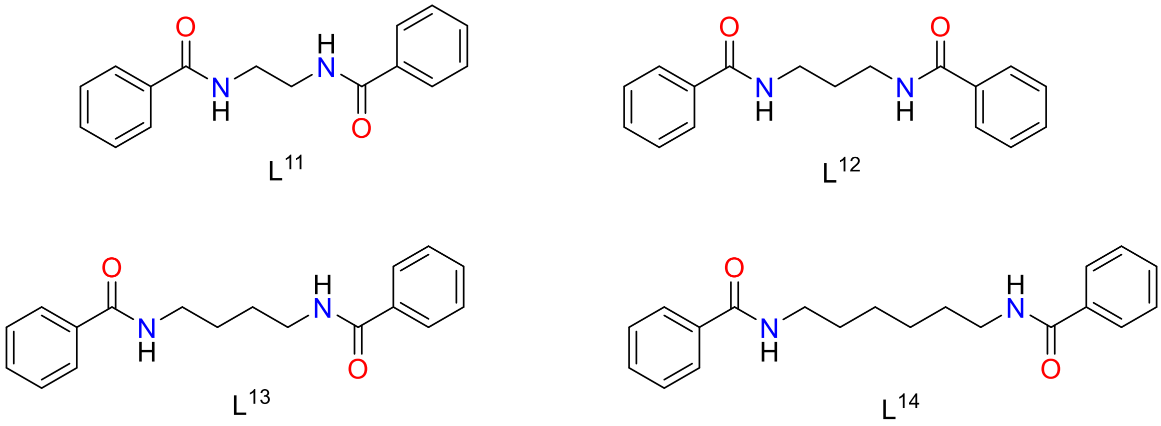

Figure 3.41 – Chemical structures of $L^{11\text{-}14}$.

As the length of the alkyl spacer is varied from 2 carbons to 6 ($L^{12\text{-}14}$, figure 3.41), Fe(III) precipitation occurs more readily than L^{11}, although still not as readily as L^{6} (figure 3.42).

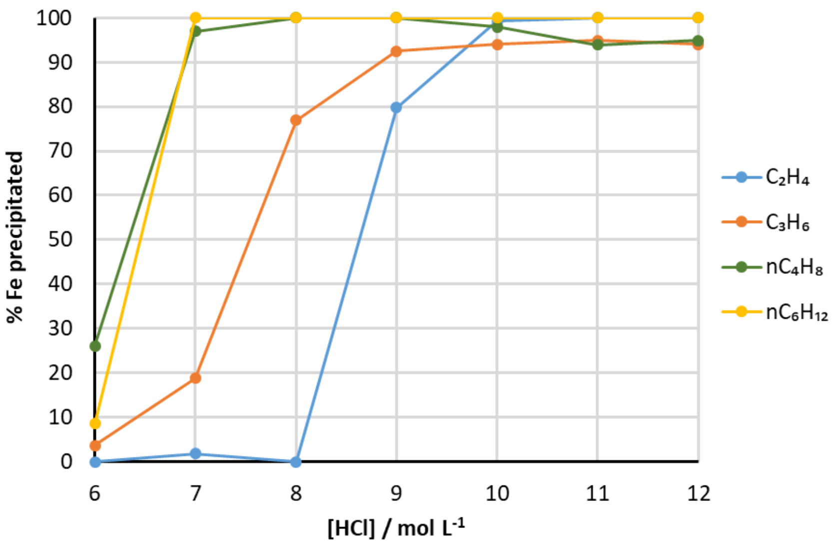

Figure 3.42 – Precipitation of Fe(III) by L$^{11-14}$. Conditions: 0.2 mmol L$^{11-14}$ contacted with 2 mL 0.01 M $FeCl_3$ in 6 – 12 M HCl for 24 hours at RT, 500 rpm.

Additional spot tests with L$^{11-14}$ and solutions of $HAuCl_4$ in 2 M HCl show little to no Au precipitation after 24 hours, again in contrast to L^{6}. Some Au precipitation was observed by L^{13} and L^{14} when the HCl concentration was increased to 6 M HCl after 3 – 4 hours, which also contrasts with L^{6}, which quantitatively precipitated Au at 6 M HCl in minutes.

3.5.2.2 Aryl spacers

Aryl spacers with different substitution patterns were also investigated. Each of the secondary diamides (L$^{15-17}$, figure 3.43) fail to precipitate any Fe(III) from solution from 6 – 12 M HCl after 24 hours (figure 3.44). From these data it was assumed that it would be unlikely that Au, Sn, Pt or Ga would precipitate either. Tertiary diamide derivatives of L^{15} and L^{16} were synthesised by methylation of the secondary amides with iodomethane, (L^{18,19}, figure 3.43) and are found to precipitate Fe(III) from 7 M HCl onwards; however, the precipitates formed rapidly discolour and degrade into brown, intractable solids, rendering further characterisation difficult. Methylation of L^{17} to form L^{20} was unsuccessful and so this tertiary diamide was not tested.

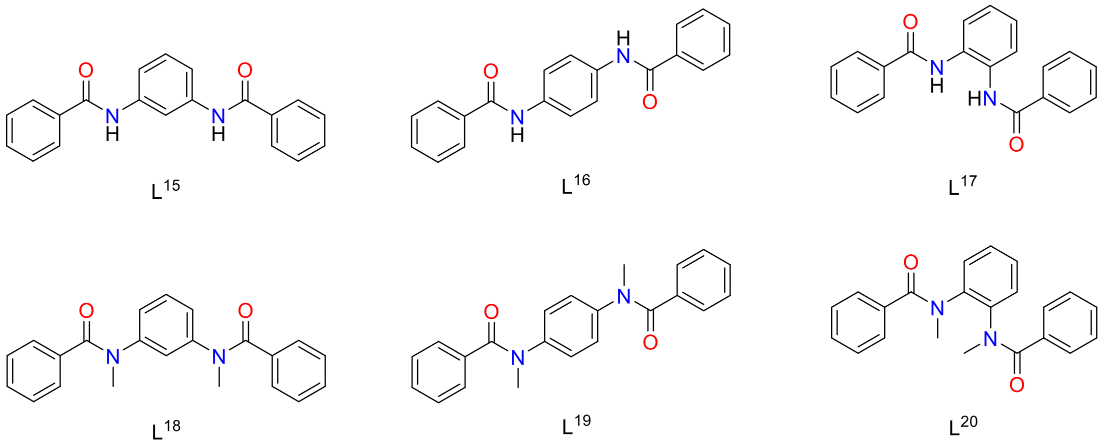

Figure 3.43 – Chemical structures of L$^{15-20}$. The synthesis of L^{20} was unsuccessful.

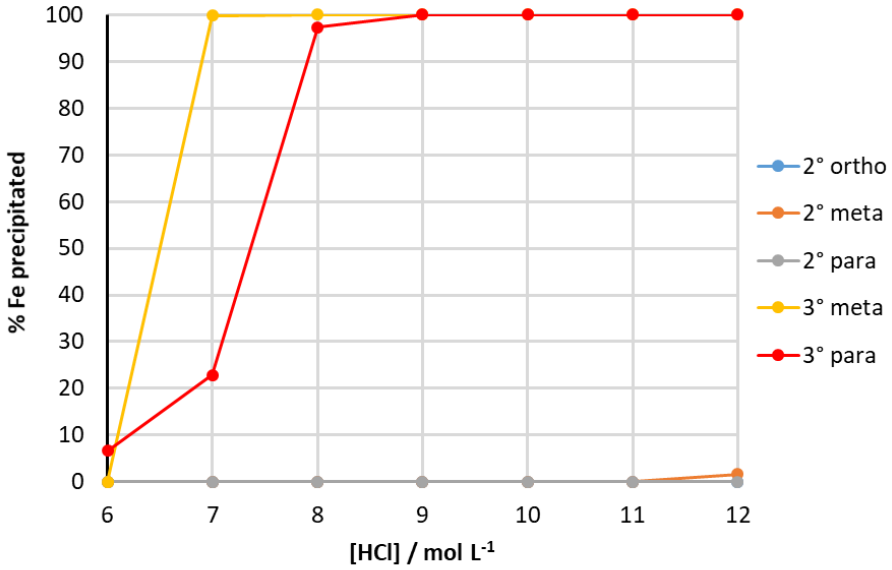

Figure 3.44 – Precipitation of Fe(III) by L$^{15-19}$. Conditions: 0.2 mmol L$^{11-14}$ contacted with 2 mL 0.01 M $FeCl_3$ in 6 – 12 M HCl for 24 hours at RT, 500 rpm.

From these data, it is clear that the presence of NCH_3 groups on the diamide are a key factor in efficient metal precipitation. It is unclear whether these groups are necessary to help with solubility, provide additional non-covalent interactions, or a combination of both. The insolubility of the secondary diamides in acid is likely to be a result of strong intermolecular hydrogen bonding between NH and CO groups of adjacent amides, which is not present in tertiary amides. Because of the poor performance of metal precipitation by these amides with iron, a more in-depth exploration into the precipitation of other metals was not undertaken.

3.5.2.3 Inverted amide

This section includes results obtained by Ms Susanna Vance at the University of Edinburgh that were not undertaken by the author, although the concept was originally conceived by the author and his supervisors. The results described are included with Ms Vance's permission which is gratefully acknowledged.

The final variation of the hinge of L^6 that was tested was one in which the orientation of the amide functional group is inverted, L^{21} (figure 3.41). This diamide was previously studied for Pt(IV) solvent extraction, although investigations into Au(III) solvent extraction (or its use as a precipitant) were not reported.[133]

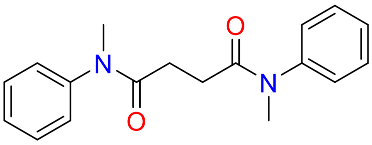

L^{21}

Figure 3.45 – Chemical structure of L^{21}.

Initial tests with Fe(III) in 6 M HCl found that 97% of the iron was precipitated after one hour but if the solution and precipitate were left to stir for 24 hours, only 62% of the total iron was precipitated, suggesting either re-dissolution of the precipitate or degradation of L^{21} and therefore subsequent re-dissolution of $FeCl_4^-$.

When undertaking precipitation experiments with $HAuCl_4$ and L^{21}, the amount of Au precipitated remained the same over a 24 hour period and re-dissolution of Au was not observed (figure 3.46).

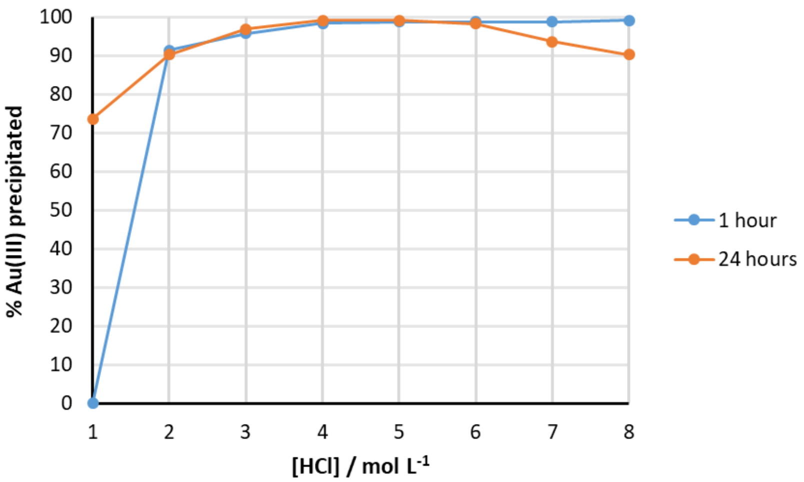

Figure 3.46 – Precipitation of Au(III) by L^{21}. Conditions: 0.2 mmol L^{21} contacted with 2 mL 0.01 M $HAuCl_4$ in 1 – 8 M HCl for 1 or 24 hours at RT, 500 rpm.

Interestingly, when the Au-containing precipitate from solutions above 6 M HCl were allowed to sit in the supernatant for several days, the formation of gold nanoparticles is observed (figure 3.47). When left over the course of a week, solid gold flakes form. The ^{13}C NMR spectrum of the supernatant from which gold nanoparticles had formed shows resonances consistent with succinic acid, these were confirmed by spiking the sample with additional succinic acid. Contacting a solution of L^{21} in $CHCl_3$ with a solution of $HAuCl_4$ in 6 M HCl results in the solvent extraction of $AuCl_4^-$ into the chloroform phase after a few minutes, but when left stirring for several days, the organic phase turned from a yellow colour characteristic of $AuCl_4^-$ to a purple colour, consistent with gold nanoparticles, which were subsequently characterised by UV-Vis spectroscopy. Furthermore, colourless single crystals grew from the $CHCl_3$ solution and the unit cell parameters match succinic acid (CCDC refcode SUCACB03).[134]

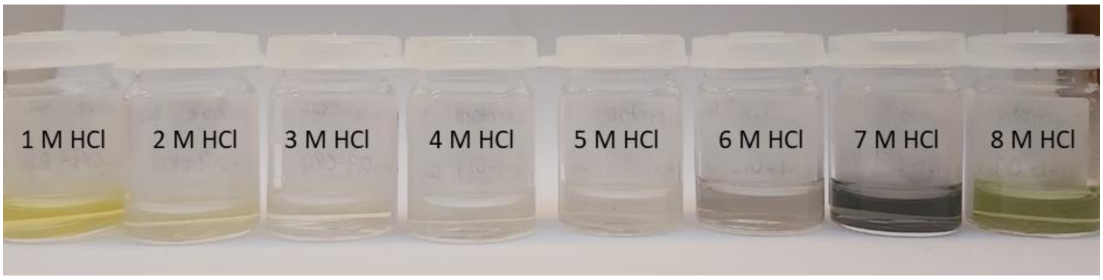

Figure 3.47 – Photograph of the supernatants resulting from L^{21} contacted with 0.01 M $HAuCl_4$ in 1 – 8 M HCl.

Unlike L^{21}, metalate precipitates from L^6 such as $[HL^6][AuCl_4]$ or $[HL^6][FeCl_4]$ do not re-dissolve in HCl and no gold nanoparticle formation or degradation of L^6 is observed. Consequently, the degradation of L^{21} in the presence of acid raises recyclability concerns and so would be unsuitable in a metal separation process.

The precise mechanism into the degradation of L^{21} in the presence of $HAuCl_4$ and HCl, and the subsequent formation (and additional characterisation) of gold nanoparticles is currently the subject of further investigation by Ms Vance.

3.5.3 Alkyl substituted diamides as precipitants

As discussed in section 3.3, solutions of the tert-butyl substituted diamide L^5 in toluene extract $AuCl_4^-$ by solvent extraction, and the resulting organic phase remains stable. As L^5 is a solid, it was briefly tested as a precipitant, in the same manner as L^6. The cyclohexyl-substituted diamide L^{22} (figure 3.48) was also prepared and tested in the same manner. At 2 M HCl after 1 hour, L^5 precipitates only 20% Au from solution, whereas L^{22} precipitates 92 % Au. Increasing the HCl concentration to 6 M HCl results in 82 % Au precipitation by L^5, and 99% by L^{22}. Despite the good precipitation efficiency, the precipitates formed by L^5 and L^{22} have an almost gel-like consistency which stuck to the stirrer bar; these contrast to most other diamides tested which precipitate the metals as 'free-flowing', microcrystalline solids. A similar consistency of material is observed in spot tests with $FeCl_3$ at 6 M HCl, where most of the iron is removed from solution.

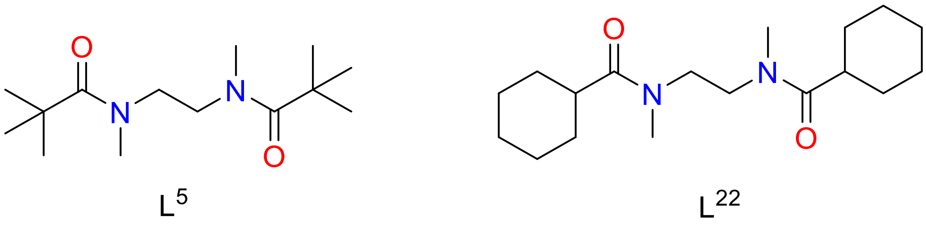

L^5 L^{22}

Figure 3.48 – Chemical structures of L^5 and L^{22}.

Crystals of the Au precipitate formed by L^5 were grown by addition of solid L^5 to a solution of $HAuCl_4$ in 6 M HCl without stirring and leaving the vial in the fridge. After three weeks, single crystals suitable for X-ray diffraction were obtained alongside amorphous solids. In contrast to most other X-ray structures in this chapter, L^5 does not form the same highly ordered, polymeric infinite chain of $[HL]^+$ cations, but instead a $H_5O_2^+$ cation is hydrogen bonded to four diamide molecules forming a cluster-like species (figure 3.49). The $AuCl_4^-$ interacts with L^5 through non-covalent interactions of the NCH_3 and *tert*-butyl groups.

Solvent extraction experiments of L^5 or L^{22} in toluene or chloroform contacted with gold solutions result in stable organic phases (i.e. no precipitation is observed) unlike the previously mentioned diamides bearing aryl groups which do precipitate from chloroform. As a result, these alkyl-substituted diamides are more suitable as solvent extractants rather than precipitants.

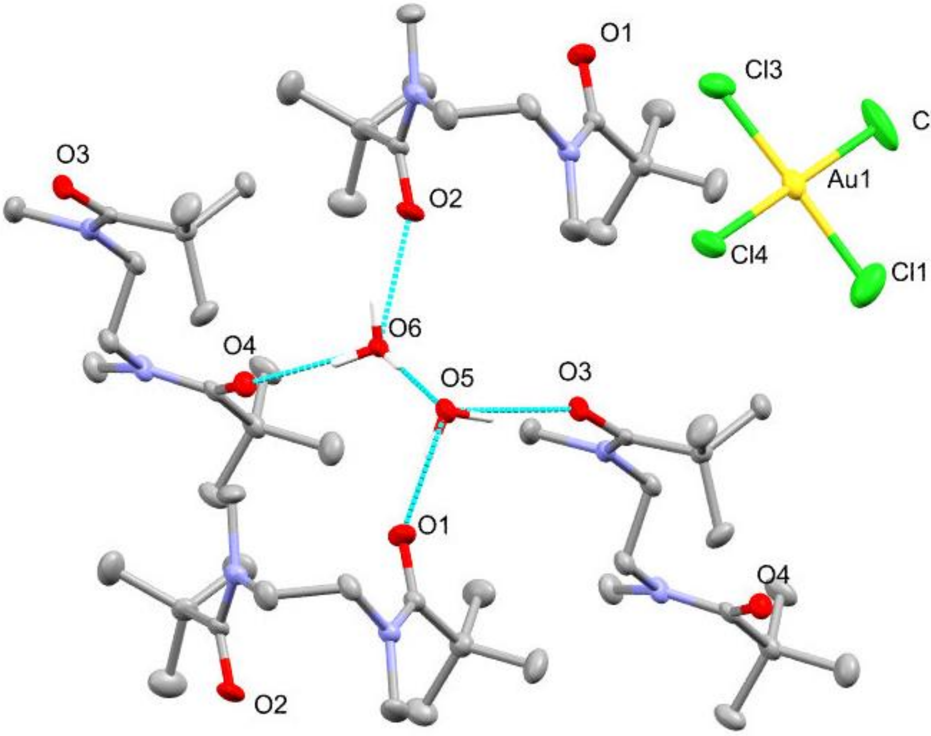

Figure 3.49 – X-ray crystal structure of $[L^5]_2[H_3O][H_2O][AuCl_4]$. For clarity, all hydrogens except those involved in hydrogen bonding are omitted (displacement ellipsoids are drawn at 50% probability). The asymmetric unit contains two amide molecules rather than the four depicted in the image. C(H)···Cl(Au) 3.46-3.79 Å; N1-C7-C8-N2 -60.9(6); N3-C22-C23-N4 168.0(4)°.

3.6 Conclusions

The simple diamide L^6 quantitatively and selectively precipitates gold from a wide range of acidic mixed-metal solutions through a dissolution – co-precipitation mechanism. The need for organic solvents is therefore prevented and only stoichiometric amounts of L^6 are necessary, resulting in reduced waste generation when compared with traditional solvent extraction processes for which large volumes of organic solvent and excess extractant are required.

Upon dissolution in acid, the diamide assembles into an infinite chain of $[HL^6]^+$ cations, formed by the chelation of the proton by two amide oxygens from adjacent diamide molecules. The resulting rhombohedral cavity created by the phenyl and methyl groups in $[HL^6]^+$ enables $AuCl_4^-$ to be hosted through electrostatic and non-covalent interactions.

At higher concentrations of HCl, co-precipitation of other metals such as Fe and Sn with Au can occur when excess L^6 is used. Even so, Au separation can be achieved by washing the precipitates with dilute HCl prior to releasing $HAuCl_4$ with deionised water and recycling L^6 for further use.

There is a clear preference for one metal over the other when a limiting number of moles of L^6 is used, and (in the case of iron vs tin) when temperature is varied. It can be tentatively concluded that the order of selectivity may follow Au(III) > Ga(III) > Fe(III) ≥ Sn(IV) > Pt(IV), which follows the rationale behind the Hofmeister bias in which more charge-diffuse anions more readily salt-out of solution. It is interesting that out of all of the metals tested, L^6 requires higher concentrations of HCl to precipitate Pt(IV). Both Au(III) and Pt(IV) exist in HCl solution as their respective metalates at lower HCl concentrations than Fe(III), Ga(III) and Sn(IV), which do not exist in aqueous solution as their metalates to an appreciable extent until around 4-5 M. It may be expected that L^6 should be capable of precipitating $PtCl_6^{2-}$ at 2 M HCl, given that it exists in solution at that HCl concentration, but as demonstrated in figure 3.5 in section 3.4.4, contacting $[HL]_2[PtCl_6]$ with 2 M HCl results in stripping of $PtCl_6^{2-}$ back into solution. Other solvent extraction and precipitation methods have reported previously that Pt(IV) solvent extraction or precipitation occurs at 2 M HCl.[125,135] Evidently, the selectivity of L^6 for a given metal does not lie solely on the speciation of the metal, but perhaps also on the resulting stability and solubility of the particular $[HL^6]_n[MCl_y]$ complex. Further experiments measuring the thermodynamics of precipitation by isothermal calorimetry may help to understand the observed selectivity.

As discussed in chapter 1, the success of Au precipitation by α-CD is almost entirely dependent on the aqueous matrix; a 'Goldilocks combination' of K^+ and $AuBr_4^-$ appear to be crucial to its success as a gold precipitatant.[36] Other Au precipitants such as cucurbit[*n*]urils,[122–124] cyclophanes[126–128] and other acyclic amides[112,129] have also shown promise but further studies into their selectivity under different aqueous matrices or with non-precious metals are lacking. In contrast, this work has shown that L^6 displays highly tuneable selectivity towards various metalates by careful modulation of the stoichiometry, HCl concentration or even temperature. This makes this simple diamide a very versatile precipitant and could be used in several different hydrometallurgical separation processes relevant to electronic waste or primary metal sources.

By synthesising structurally similar analogues of L^6 it was found that the structure of the diamide can influence the efficiency of metalate precipitation. Modifying substituents on the phenyl groups has shown that the relative ease of metalate precipitation can be regulated by changing the substituent from an electron-withdrawing group to an electron-donating group. On the other hand, switching from aryl to alkyl substituents results in the molecular structure of precipitates changing from highly ordered chains of $[HL]^+$ to more cluster-like species that are stable in hydrophobic solvents and are therefore more suited as solvent extractants rather than precipitants.

Using secondary diamides instead of tertiary diamides severely hinders metalate precipitation due to their lower solubility and so very high concentrations of HCl are required to permit $FeCl_4^-$ precipitation; however, extending the carbon chain length of the amide N-C-C-N 'hinge' can lower the HCl concentration threshold for $FeCl_4^-$ precipitation.

Switching the orientation of the amide moiety in L^6 to L^{21} also affects the efficiency of metalate precipitation and the observation that precipitates resulting from L^{21} and $AuCl_4^-$ decompose to form gold nanoparticles and succinic acid has implications for the recyclability of L^{21} in a potential metal separation process.

Chapter 4

Solvent extraction of tantalum with a primary amide

4 Solvent extraction of tantalum with a primary amide

4.1 Overview

The recycling of tantalum is becoming increasingly important due to its criticality of supply from a conflict mineral. It is used extensively in modern electronics, such as in capacitors, and so electronic waste is a potential secondary source. However, the recycling of Ta is difficult, particularly through issues of leaching and subsequent separation from other components. This chapter demonstrates that Ta halides such as $TaCl_5$ and TaF_5, in principle derived from Ta metal, can be recovered by solvent extraction from chloride solutions using a simple primary amide reagent. The need for fluoride-free tantalum recycling processes is briefly discussed. The extraction of $TaCl_5$ and TaF_5 from chloride media by the primary amide is compared and the probable mode of action is explored.

4.2 Introduction

The third-row transition metal element tantalum is critical to modern consumer technologies, with approximately 40 % of the world tantalum production being used as a component in capacitors for the microelectronics industry.[136] Tantalum capacitors consist of porous tantalum metal as an anode, coated with a thin sheet of Ta_2O_5 as an insulating layer, which is then surrounded by an electrolyte as a cathode such as manganese dioxide. The high surface area of the tantalum metal enables these capacitors to store large amounts of electrical charge (capacitance) per volume and weight. This, along with tantalum's resistance to high temperatures and inertness has resulted in it being widely used in portable electronic devices. Despite its pervasive use in this application, the end-of-life recycling rate of tantalum capacitors is limited to only 1 %.[136]

The primary source of tantalum is from Coltan ore, a combination of the chemically similar minerals columbite (dominant in niobium) and tantalite (dominant in tantalum) that also contain other elements such as iron and manganese. It is extensively mined in the Democratic Republic of Congo resulting in it being classed as a conflict resource.[137] The status of tantalum as a metal derived from a conflict mineral, combined with its low abundance in the earth's upper crust (0.7 ppm) means there is a need to design an ethical and sustainable closed-loop process to recycle tantalum from waste capacitors.

Tantalum and niobium metals (and their oxides) have very low solubilities in typical mineral acids like HCl, H_2SO_4, and HNO_3 (and combinations thereof) compared with other d-block elements, and current hydrometallurgical processes involve the use of concentrated HF, combined with H_2SO_4 or HCl in order to generate soluble anionic metalates such as TaF_6^- and TaF_7^{2-} that are stable in acidic aqueous solutions.[138–142] Ta is then separated from the acidic leach solutions using an organic solvent, most commonly methylisobutylketone (MIBK).[140] The main disadvantages of this process are the hazards associated with the reagents used, particularly on large scales; HF is extremely corrosive and toxic, and MIBK is a highly flammable and volatile solvent which has some aqueous solubility raising recyclability issues and generating toxic waste. As such, it is evident that there is a need to develop more sustainable processes which can not only efficiently recycle tantalum from secondary sources but do so using milder reagents.[143] Niobium is processed in a similar manner to tantalum with subtle differences in aqueous phase speciation.

Efforts towards fluoride-free tantalum and niobium recovery processes have focused on highly alkaline matrices to generate the aqueous soluble polyoxometalate (e.g. $Ta_6O_{19}^-$) by melting Ta_2O_5 or Nb_2O_5 with NaOH or KOH at temperatures of greater than 300 °C.[144–147] The resulting polyoxometalate readily dissolves in water and is subsequently separated from impurities (such as Ti, Fe and Na) by solvent extraction using the quaternary ammonium salt Aliquat® 336. The mode of action of extraction was determined to be based on an anion exchange mechanism between the chloride anions of the quaternary ammonium and the hexatantalate or hexaniobate ions.[148,149] In this system, the quaternary ammonium salt does not discriminate between Ta or Nb species and so both are co-extracted. Niobium was selectively stripped by a mixture of 0.5 M oxalic acid, 0.3 M HNO_3 and 0.15 M NH_4NO_3, followed by Ta stripping with 0.5 M HNO_3 and 0.5 M NH_4NO_3. Further discussion of the separation of niobium from tantalum is considered beyond the scope of this chapter, and as such is not explored further.

Ionic liquids (ILs) have also been investigated as potential extractants for tantalum. MIBK-derived ILs were shown to efficiently extract $[TaF_7]^{2-}$ from concentrated sulfuric acid solutions with excellent selectivity for tantalum over other, potentially interfering metals.[150] In this case, it was hypothesised that this enhanced extraction compared with MIBK alone could be due to greater solubility of water in the IL phase, overcoming the prerequisite to displace the hydration sphere prior to transport of the metalate into nonpolar solvents.

There are very few reports that describe the solvent extraction of tantalum from chloride-based media. Acids such as HCl were tested in the extraction of TaF_5 by several well-known commercial extractants such as D2EHPA, Aliquat® 336 and Alamine® 336, although in all cases optimal extraction of TaF_5 was found in H_2SO_4 solutions. When attempting the same tests with $TaCl_5$, solubility issues were seen.[151] Despite the limited speciation data available for tantalum in halide acids, previous theoretical studies have postulated that $TaCl_5$ could behave in a similar manner to TaF_5 in aqueous solution, so forming chloridometalates such as $TaCl_6^-$ in the presence of excess chloride ion.[152,153]

Previous work showed that the primary amide, L^1 (see chapter 2), forms hydrophobic supramolecular assemblies with metalates, including $AuCl_4^-$, which allows for e-waste separations using anion-swing solvent extraction processes.[40,90] This chapter describes the transport of tantalum as its chloridometalate $TaCl_6^-$ into a toluene organic phase using the simple primary amide reagent L from acidic solutions in the presence of chloride. Subsequent back extraction (stripping) of the metalate into a fresh aqueous phase is possible with water or dilute HCl.

4.3 Results and discussion

4.3.1 Solvent Extraction of Tantalum Pentachloride

The dissolution of $TaCl_5$ in HCl only occurs at high concentrations of HCl (12 M). Initial solvent extraction procedures were therefore studied by contacting a 0.1 M solution of L^1 in toluene with a 0.01 M solution of $TaCl_5$ in 12 M HCl. However, at this high HCl concentration no appreciable tantalum extraction is seen and it is likely that L^1 is instead transported into the aqueous phase (figure 4.1). Upon addition of LiCl to the $TaCl_5$ solution at 12 M HCl, the concentration of Cl^- is increased further, although this results in the outgassing of HCl from the solution. Under these conditions, low to moderate quantities (30 – 50%) of Ta are transferred to the organic phase, although L^1 is likely still lost to the aqueous phase as a result of the high acidity.

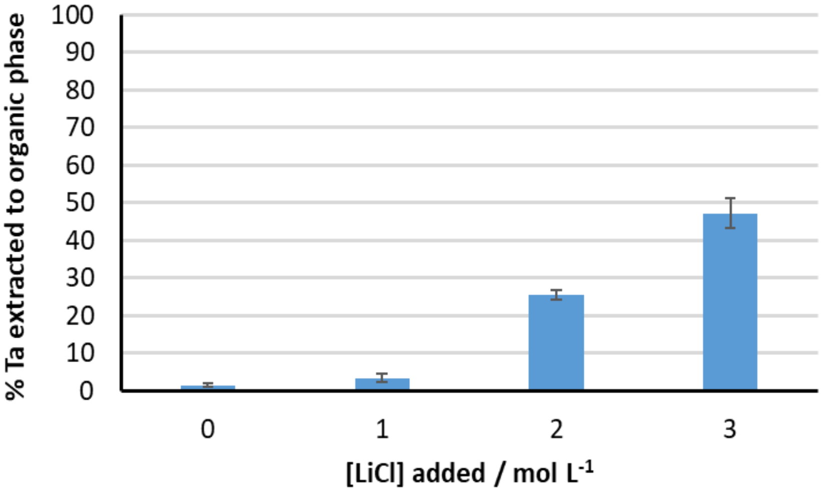

Figure 4.1 – Transport of tantalum from aqueous solutions of $TaCl_5$ in 12 M HCl with varying concentrations of LiCl into a toluene solution of **L**. Conditions: $TaCl_5$ (0.01 M) in 12 M HCl with 0 – 3 M LiCl (2 mL) stirred with **L** (0.1 M) in toluene (2 mL); phases contacted for 1 h at RT with magnetic stirring. Experiments performed in duplicate and reported as an average.

To minimise the loss of L^1 to the aqueous phase while maximising Ta transfer, the acid concentration was diluted to 1 M HCl in conjunction with varying total chloride concentration through the addition of LiCl. In extraction experiments, no loss of L^1 from the organic phase is seen (by quantitative ^1H NMR spectroscopy) and Ta is completely extracted between 7 and 11 M LiCl (figure 5.2).

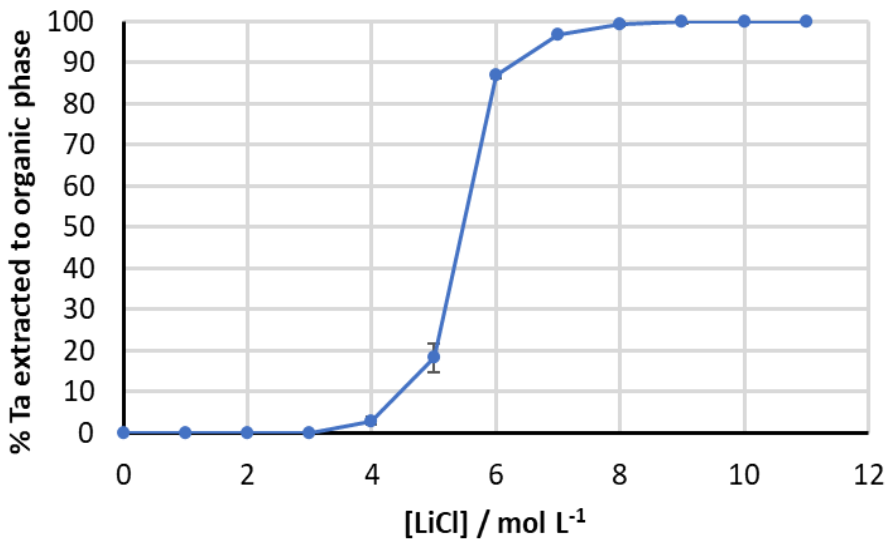

Figure 4.2 – Transport of tantalum from aqueous solutions of $TaCl_5$ in 1 M HCl with varying concentrations of LiCl into a toluene solution of **L**. Conditions: 0.01 M $TaCl_5$ diluted in 1 M HCl, 1-11 M [LiCl] (2 mL), stirred with **L** (0.1 M) in toluene (2 mL); phases contacted for 1 h at RT with magnetic stirring. Experiments performed in duplicate and reported as an average.

As tantalum begins to be extracted at 3-6 M LiCl, small quantities of a precipitate (figure 4.3) formed which was not present in experiments at higher LiCl concentrations. Control experiments showed that the formation of these solid third phases was dependent on the presence of $TaCl_5$, LiCl and L^1; any attempts to reproduce this phenomenon in the absence of any one of these variables were unsuccessful. ^1H NMR analysis of this precipitate dissolved in deuterated DMSO shows that no L^1 from the organic phase was present, despite L^1 being required to induce precipitation. Additional quantitative ^1H NMR analysis showed that the concentration of L^1 in C_6D_6 solutions remains constant as the LiCl concentration was varied, confirming no transfer of L^1 to the aqueous phase or inclusion into the precipitate. ICP-OES analysis shows the solids comprise tantalum and lithium, so is potentially $LiTaCl_6$ or a similar complex. Furthermore, L^1 does not transfer significant quantities (< 10 ppm) of Li into the organic phase as the concentrations of **L** or LiCl are varied.

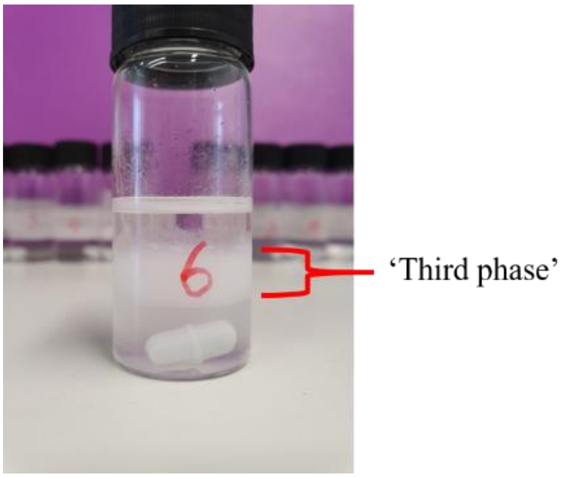

Figure 4.3 – Photograph showing the formation of a cloudy third phase (white precipitate) after contact of 0.01 M $TaCl_5$ in 1 M HCl with 6 M LiCl with solutions of 0.1 M L^1 in toluene.

Initial attempts to obtain single crystals of this precipitate suitable for X-ray diffraction were unsuccessful and since it was inferred by ^1H NMR spectroscopy that L^1 was not present, further investigations into the nature of the precipitate were considered beyond the scope of this work.

The need for high levels of LiCl to promote Ta extraction suggests that either the formation of the anion $TaCl_6^-$ is a prerequisite for transport into the organic phase or that a salting-out effect is operating. To understand this, experiments were undertaken which varied the concentration of BF_4^- (using $NaBF_4$) as a non-coordinating anion instead of Cl^- and show that negligible Ta transfer to the organic phase occurred. This confirms that $TaCl_5$ is not simply "salting-out" to the organic phase and that a source of chloride is necessary to drive $TaCl_6^-$ formation; even so, the high salt content may aid extraction by reducing the concentration of free water in the aqueous phase.[154] Importantly, Ta is readily back-extracted (~80%) from the organic phase to a fresh aqueous phase with either water or 1 M HCl; a white precipitate forms with water, indicative of hydrolysed Ta species, while no precipitate is immediately observed in the strip solution with 1 M HCl.

4.3.2 Structure Elucidation and extraction mode of action

4.3.2.1 Karl Fischer water content determination

Karl Fischer titrations were undertaken to determine the role of water in the extracted species. As the concentration of L^1 is increased, more tantalum transfers to the organic phase whereas the concentration of water remains relatively constant (figure 4.4). The trends in these data are in agreement with previous solvent extraction experiments between $AuCl_4^-$ and L^1 in toluene.[40] This suggests that L^1 is not extracting tantalum species by a reverse micelle mechanism where L^1 would act as a surfactant around a pool of water which may encapsulate the metal. However, at even higher concentrations of L^1 where the concentration of tantalum in the organic phase does not change, more water is transported across, suggesting that water transport into the organic phase is associated with the concentration of L^1.

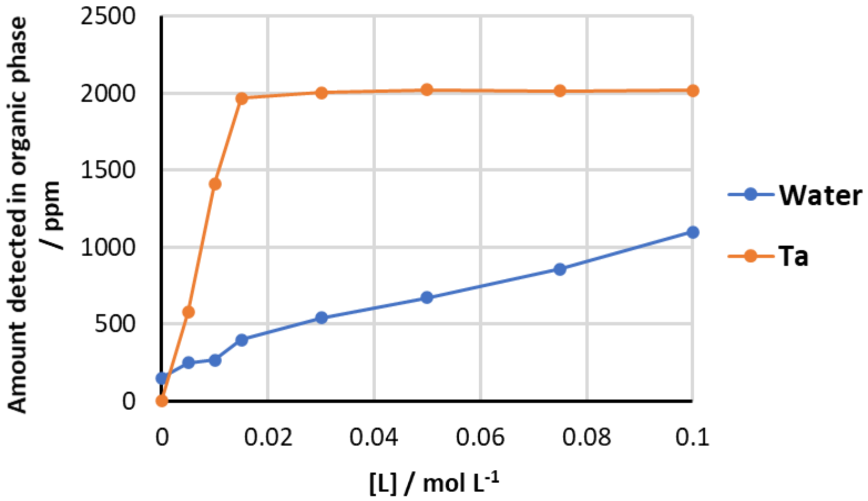

Figure 4.4 – The change in water and tantalum concentrations (determined by ICP-OES and Karl-Fischer titrations, respectively) in the organic phase with increasing concentration of L^1 dissolved in toluene. Conditions: 0.01 M $TaCl_5$ in 1 M HCl with 9 M LiCl contacted with solutions of 0 - 0.1 M L^1 in toluene.

4.3.2.2 Slope analysis

The extent of tantalum extraction into the organic phase increases as the concentration of L^1 is increased. It is therefore apparent that Ta is transported into the organic phase as a function of $[L^1]$, likely as an ion pair $[HL^1][L^1]_n[TaCl_6]$. To further probe the organic-phase speciation, slope analysis (see section 6.4.2) of Log D (D = distribution coefficient, the ratio of metal detected in the organic and aqueous phases after extraction) against Log $[L^1]$ was carried out.

A L^1:Ta ratio of approximately 2 (derived from the slope of 1.71, figure 4.5) suggests the formation of an ion pair such as $[HL^1_2][TaCl_6]$ in the organic phase. However, this analysis assumes the presence of a single species present in the organic phase. The non-integer value obtained suggests the presence of additional species in solution, such as the ion pair $[HL^1][TaCl_6]$, clusters such $[HL^1_2][L^1][TaCl_6]_2$ or even a neutral inner-sphere complex such as $TaCl_5(L)$. In addition, excess ligand that is not directly involved in Ta extraction is not considered in this analysis, despite there being the potential for surplus L^1 to associate with the outer-sphere of the extracted species.

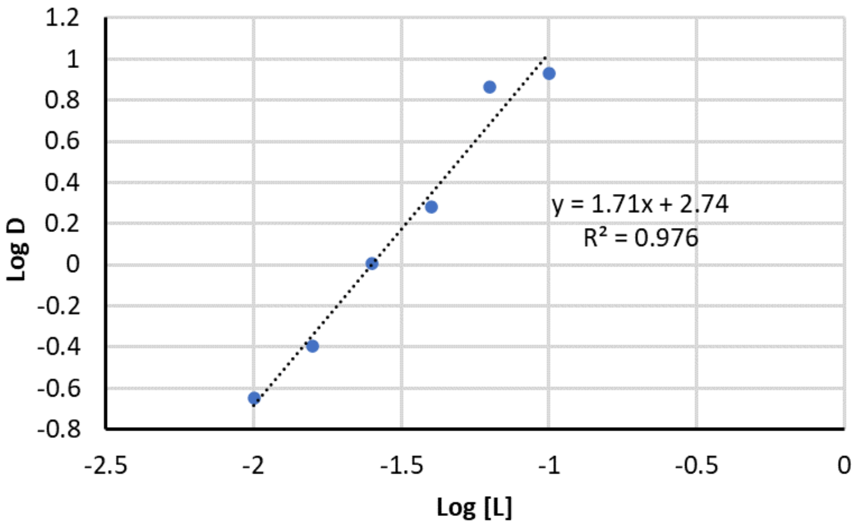

Figure 4.5 – Slope analysis for the transport of Ta with L^1. Conditions: 2 mL 0.01 M $TaCl_5$ in 1 M HCl, 11 M LiCl, contacted with 2 mL of 0.01 to 0.1 M L^1 in toluene for 1 h at RT with magnetic stirring.

This type of outer-sphere coordination behaviour is similar to that seen previously for Au extraction using L^1 in which experimental and computational analysis showed that two amides chelate a proton through the oxygen atoms to form a charge-diffuse cation that can interact with diffusely charged metalate anions through non-classical hydrogen bonds.[40,91]

4.3.2.3 Mass spectrometry

Structural characterisation of the extracted species by electrospray ionisation mass spectrometry proved inconclusive, with only HL_2^+ and LiL_2^+ ions present in the positive-ion spectrum. This contrasts with experiments between L^1 and $AuCl_4^-$ where not only the HL_2^+ species is present, but also gold containing clusters of the general formula $[(HL)_{n+1}(AuCl_4)_n]^+$. The lack of species such as $[(HL)_2][TaCl_6]^+$ may be attributed to the presence of low concentrations of LiCl salt being present in the organic phase. It has been demonstrated previously that the analysis of proteins by electrospray ionisation mass spectrometry can be hindered by the presence of inorganic salt impurities as low as 0.5 mM NaCl (10 ppm Na), resulting in suppressed ionisation of protonated proteins.[155,156] Ta solvent extraction was therefore attempted with at high concentrations of HCl (6 – 12 M HCl) that are necessary to form $TaCl_6^-$ instead of LiCl, but observation of any extracted Ta species remained elusive, presumably due to the loss of L^1 to the aqueous phase.

4.3.2.4 ^{1}H NMR spectroscopy

^{1}H NMR studies can provide an indication as to how the receptor $HL^1_2{}^+$ is interacting with the metalate (figure 4.6). As the concentration of tantalum in the organic phase increases, the two signals at 4.61 and 6.46 ppm in the ^{1}H NMR spectrum associated with the NH_2 protons of L^1 coalesce and shift downfield to 9.63 ppm. Variable temperature NMR spectra (figure 4.7) reveal an additional signal that can be attributed to associated water or hydronium, which coalesces with the amide protons upon Ta loading.

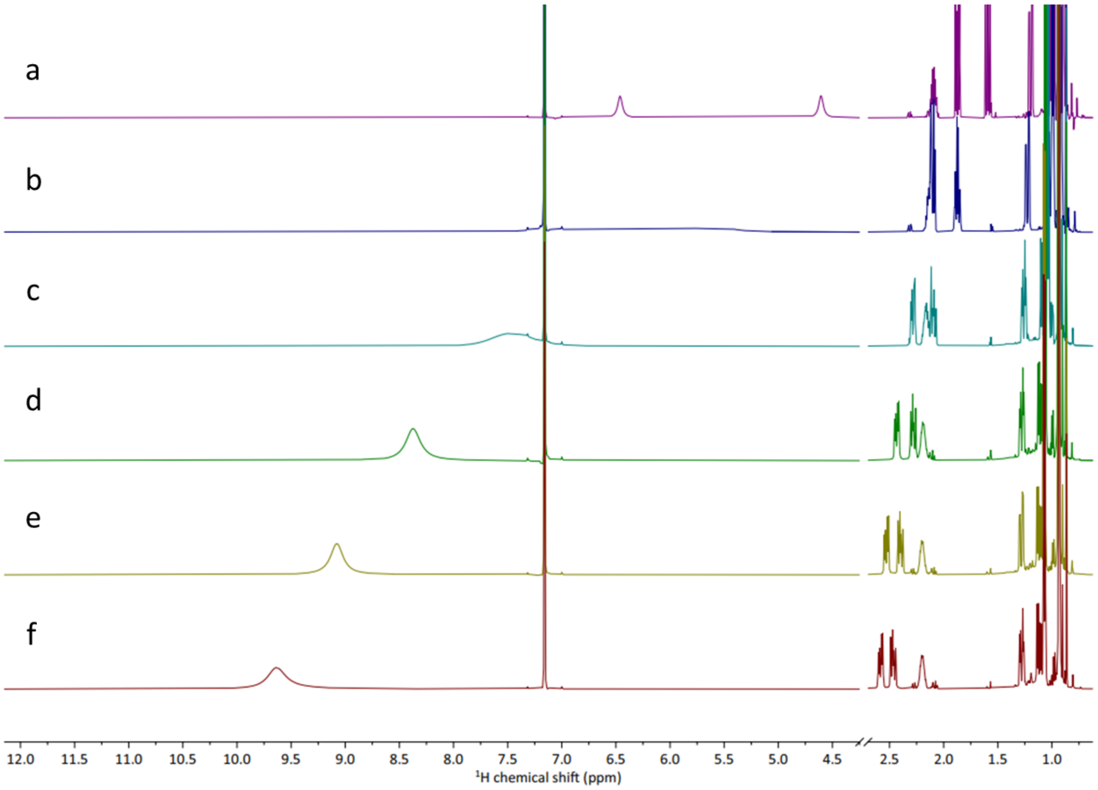

Figure 4.6 – ^{1}H NMR spectra: a) 0.1 M L^1 in C_6D_6, then 0.1 M L^1 in C_6D_6 after contact with 0.01 M $TaCl_5$ in 1 M HCl; b) 5 M LiCl; c) 6 M LiCl; d) 7 M LiCl; e) 8 M LiCl; f) 9 M LiCl.

There is also a large downfield shift of the signals at 1.59 and 1.87 ppm, associated with the diastereotopic CH_2 protons adjacent to the amide group, to 2.49 and 2.56 ppm respectively. These changes in the ^{1}H NMR spectra for Ta-loaded L^1 are like those seen for Au-loaded L^1 (figure 4.8).

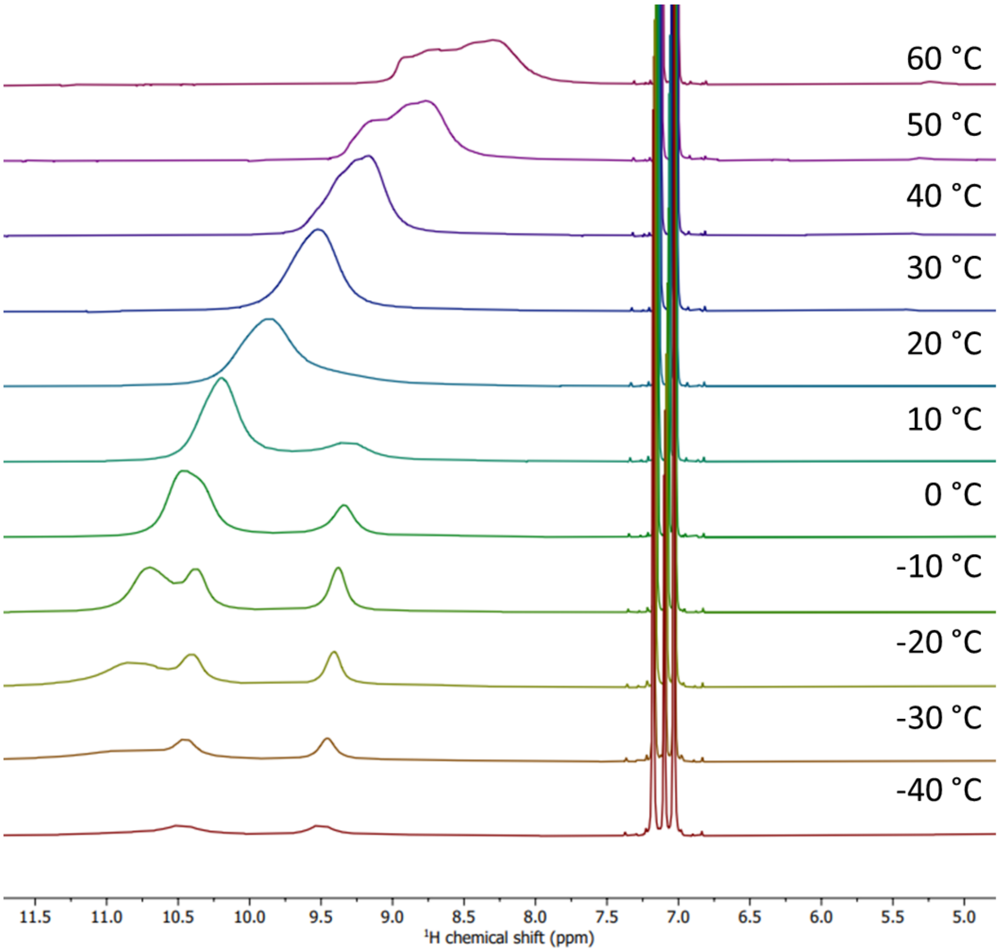

Figure 4.7 – Variable temperature ^{1}H NMR spectra of 0.1 M L^1 in Toluene-d_8 after contact with 0.01 M $TaCl_5$ in 1 M HCl and 9 M LiCl. Temperature varied from -40 °C to 60 °C.

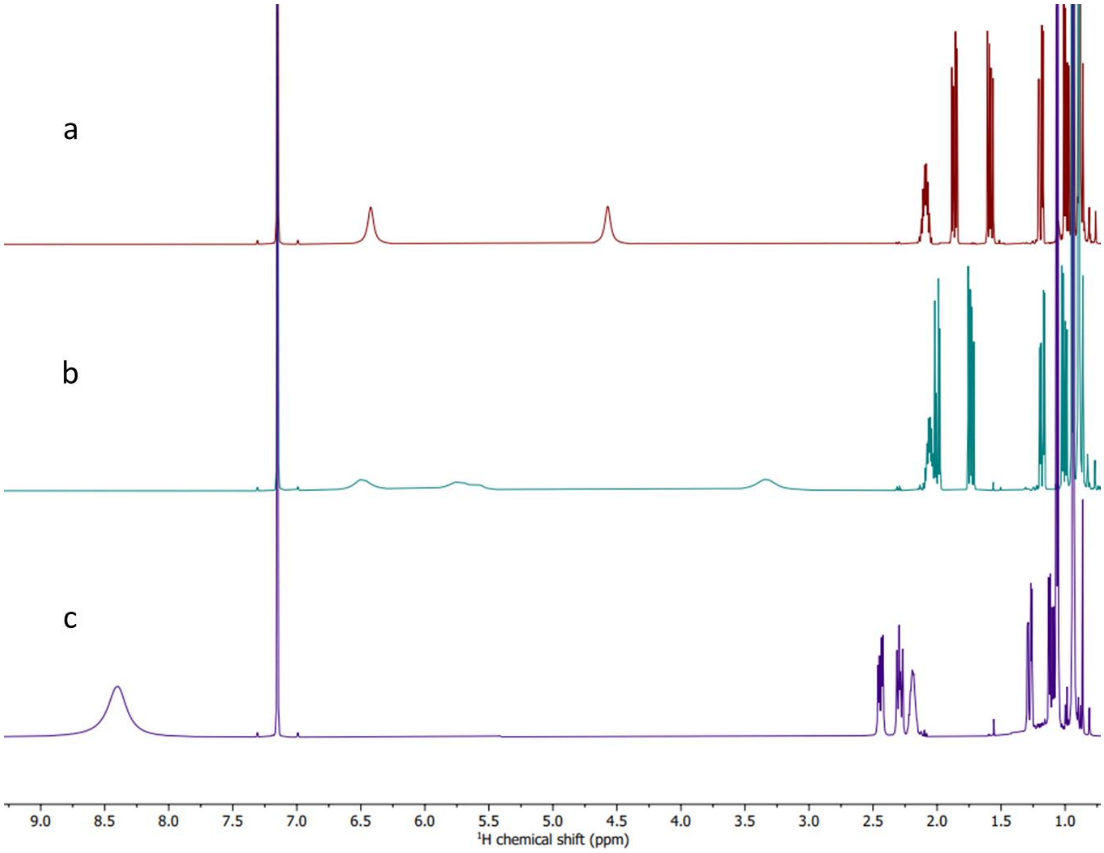

Figure 4.8 – ^{1}H NMR spectra: a) 0.1 M **L** in C_6D_6 then 0.1 M **L** in C_6D_6 after contact with b) 0.01 M $AuCl_4$ in 6 M HCl and c) 0.01 M $TaCl_5$ in 1 M HCl and 9 M LiCl..

The downfield shifts are strong evidence that the charge-diffuse cation is participating in non-classical hydrogen bonding to a tantalum metalate such as $TaCl_6^-$ in a similar manner to that previously reported for $AuCl_4^-$.[40] This can be reinforced further by drawing comparisons to the solid third phase formed between $SnCl_6^{2-}$ and the tertiary amide version of L^1 (L^3, chapter 2, figure 2.18). In this latter case, the solid-state structure showed that the two amide ligands chelate the single proton through the amide oxygen atoms, with this large cation subsequently interacting with the outer-sphere of the $SnCl_6^{2-}$ octahedron through non-classical C-H hydrogen bonds.[17,45,91]

4.3.2.5 ^{13}C NMR spectroscopy

The similarity in the ^{1}H NMR spectra for Ta/Au loaded L^1 prompted an investigation into differences in ^{13}C NMR spectra. As expected, there is also a relatively large downfield shift of the carbonyl carbon from 174 ppm to 180 ppm in the ^{13}C NMR spectrum (figure 4.9) upon Ta loading, strongly suggesting that a similar structure to Au-loaded L[1] forms in the organic phase.

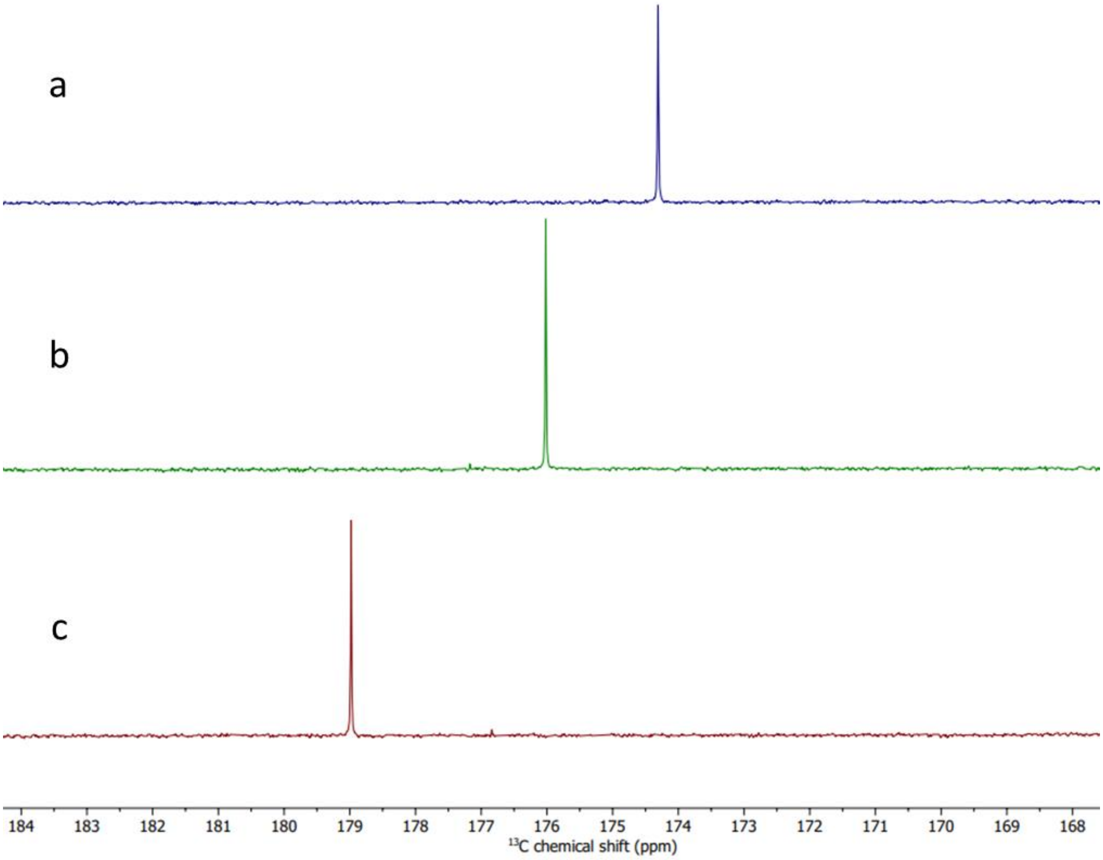

Figure 4.9 – ^{13}C NMR spectra: a) 0.1 M L^1 in C_6D_6 then 0.1 M L^1 in C_6D_6 after contact with b) 0.01 M $AuCl_4$ in 6 M HCl and c) 0.01 M $TaCl_5$ in 1 M HCl and 9 M LiCl.

In a separate study on the solvent extraction of rhodium by synergistic mixtures of L^1 and 2-ethylhexylamine, ^{1}H and ^{13}C NMR spectroscopy identified the presence of additional resonances attributed to the inner-sphere complex, $[RhCl_5(L)]^{2-}$,in which L^1 had tautomerised to its enol form and coordinated to the rhodium centre through the nitrogen atom.[157] In this case, distinct resonances attributable to $[RhCl_5(L)]^{2-}$ were observed in addition to the peaks attributed to excess L^1. In the case of Ta loaded L^1, there are no additional resonances in the ^{1}H or ^{13}C spectra, suggesting that an inner-sphere amide complex such as $TaCl_5(L^1)$ is not formed.

4.3.3 Solvent Extraction of Tantalum Pentafluoride

As current commercial processes for tantalum recovery involve the use of hydrogen fluoride to leach the metal as its fluoride salts, it is important to compare how the chloride process described above would compare with its fluoride equivalent. The extraction of TaF_5 by L^1 was therefore probed to compare its behaviour to that of $TaCl_5$. The TaF_5 salt is more soluble in water and dilute acids and so initial attempts focussed on extraction from H_2SO_4 solutions. However, all attempts to extract TaF_5 instead of $TaCl_5$ were unsuccessful, with negligible extraction seen at 0-18 M H_2SO_4 with L^1; at high acid concentrations L^1 is lost to the aqueous phase, and there is no halide source available to generate anionic metalates. Experiments using hydrofluoric acid solutions were not undertaken due to the serious hazards associated with HF. Instead, attempts to extract tantalum as TaF_6^- from potassium fluoride solutions in dilute H_2SO_4 were undertaken to minimise formation of HF. Contacting L^1 with aqueous solutions of TaF_5 dissolved in 0.1 M H_2SO_4 and 12 M KF also failed to result in any appreciable Ta extraction. It is likely that the acid concentration was too low to protonate L and therefore form ion pairs with the anionic metalates, TaF_6^- or TaF_7^{2-}; the acid concentration was kept low to minimise HF formation and so higher concentrations of H_2SO_4 were not explored.

Extraction experiments with TaF_5 in 0–12 M HCl were unsuccessful; at high HCl concentrations, L^1 is lost to the aqueous phase as [LH][Cl], whereas at low HCl concentrations it is likely that there is insufficient chloride to generate anionic metalates such as TaF_5Cl^- or $TaF_5Cl_2^{2-}$. To mitigate these issues, TaF_5 was instead dissolved in 1 M HCl solutions with varying concentrations of LiCl in the same manner as the experiments using $TaCl_5$ above.

Initially, Ta is extracted by L^1 more effectively at 5 M LiCl for TaF_5 (~45%, figure 4.10) than for $TaCl_5$ (18 %, (figure 4.2). This may be due to metalates such as TaF_5Cl^- forming more readily in aqueous solution than $TaCl_6^-$. However, as the LiCl concentration is increased further, transport of TaF_5 trends downwards whereas $TaCl_5$ transport increased and plateaued beyond 8 M HCl. In contrast to $TaCl_5$, experiments with TaF_5 and L did not form third phases or precipitates at any stage, and quantitative ^1H NMR experiments confirmed that no amide was lost to the aqueous phase as the LiCl concentration was varied. Instead, it is likely that competitive transport of chloride is occurring, with the formation of [HL][Cl] in the organic phase. This phenomenon is well documented in the chloridometalate extraction literature,[17,45] particularly at such high chloride concentrations. Alternatively, mixed halometalate species of the form $[TaF_nCl_m]^{5-n-m-}$ may predominate as chloride concentration increases; Ta adsorption on ion exchange resins from mixtures of chloride and fluoride media were previously found to decrease with increasing HCl concentrations.[158,159]

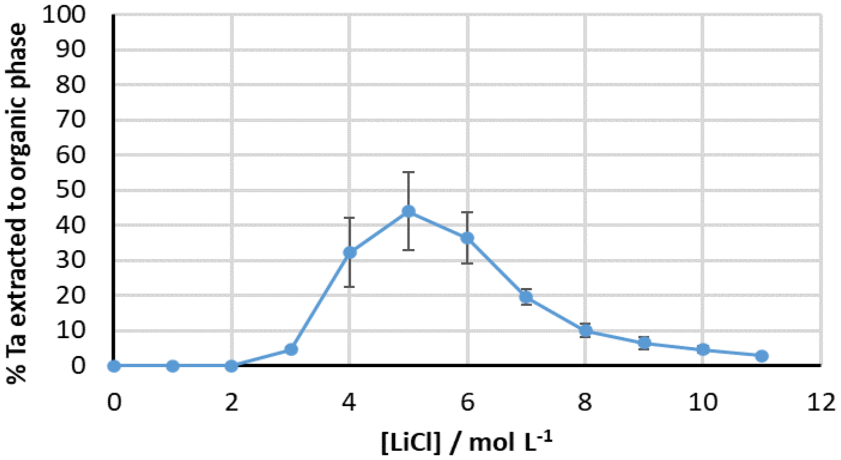

Figure 4.10 – Transport of tantalum from aqueous solutions of TaF_5 in 1 M HCl with varying concentrations of LiCl into a toluene solution of L^1. Conditions: 0.01 M TaF_5 diluted in 1 M HCl, 0-11 M [LiCl] (2 mL), stirred with L^1 (0.1 M) in toluene (2 mL); phases contacted for 1 h at RT with magnetic stirring. Experiments performed in duplicate and reported as an average.

4.3.4 Why is chloride better than fluoride?

Charge-dense, 'harder', anions are predicted to be more difficult to transfer from aqueous matrices into non-polar, water-immiscible solvents, due to the phenomenon known as the Hofmeister bias.[54,160] These charge-dense anions are more difficult to extract as more dehydration energy is required to displace the solvating water molecules, which must be removed upon transfer.[14] The fluorine atom is smaller and more electronegative than chlorine and therefore $TaCl_6^-$ is a larger, more charge-diffuse metalate than TaF_6^-. In X-ray crystal data of these metalates, the spherical diameter of $TaCl_6^-$ is about 1 Å larger than that of TaF_6^- (figure 4.11).

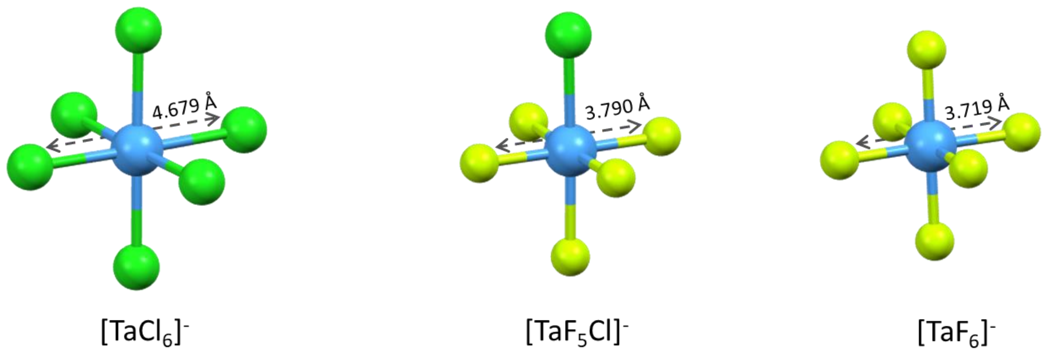

Figure 4.11 – Size comparison of different tantalum metalates found from a search of the Cambridge Structural Database. CSD ref codes KIKLOF, RUXQEI and ECANAY.[161,162] For clarity, counter ions are omitted.

Given that the size of TaF_5Cl^- is larger than TaF_6^- but smaller than $TaCl_6^-$, it would therefore be expected that TaF_5Cl^- is extracted more efficiently than TaF_6^-. This is supported by experiments using a 100 ppm standard solution of NH_4TaF_6 diluted in H_2SO_4; very limited extraction of Ta only occurred at 5 M H_2SO_4 (20 %), while at 6 M H_2SO_4 almost no L^1 remains in the organic phase, instead becoming increasingly soluble in H_2SO_4, and therefore no improvement on Ta transport is observed (figure 4.12).

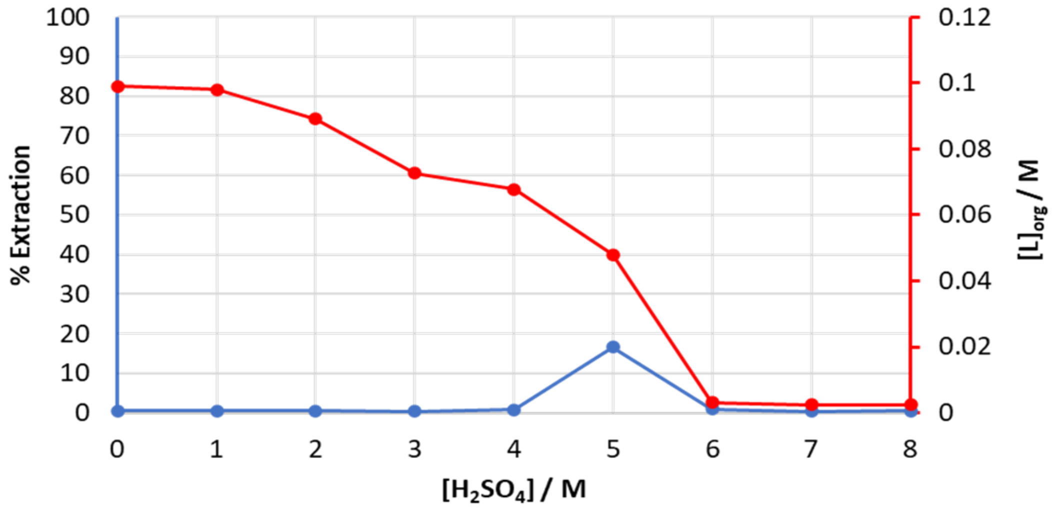

Figure 4.12 – Extraction of tantalum from aqueous solutions of 100 ppm NH_4TaF_6 in 0 – 8 M H_2SO_4 into solutions of 0.1 M L in C_6D_6 (blue) and concentration of L in the organic phase (C_6D_6) after contact with solutions of 100 ppm NH_4TaF_6 in 0 – 8 M H_2SO_4 (red).

These results contrast with a recent study using the ionic liquid N-octyl-N-ethyl-piperidinium bis(trifluoromethylsulfonyl)imide (EOPiP-NTf$_2$) which efficiently recovered Ta from mixtures of sulfuric acid and hydrofluoric acid.[163] Less than 1 % of the ionic liquid is lost to a 6 M H_2SO_4 aqueous phase containing 7 g/L tantalum and 1 M HF. While the extraction mode of action was not established, discrete cation or anion exchange mechanisms were ruled out. The ionic liquid was shown to be reusable in multiple extraction/back-extraction cycles with minimal loss in performance.

Raman spectroscopy of solutions containing mixtures of tantalum, ammonium fluoride and hydrofluoric acid have identified that at high HF concentrations TaF_6^- is the major Ta species in solution whereas TaF_7^{2-} predominates at relatively low HF concentrations.[164] Therefore, it is likely that at the lower acid concentrations where L^1 is not lost to the aqueous phase, Ta is present as the TaF_7^{2-} whereas TaF_6^- predominates at high acidity.

4.4 Conclusions

The simple primary amide, L^1, shows excellent performance for tantalum recovery by solvent extraction under high chloride conditions. While direct characterisation of the extracted species was inconclusive, the extraction mechanism was identified as similar to that seen for the recovery of gold by L^1 in which charge-diffuse protonated receptors are formed that preferentially interact with the charge diffuse monoanionic metalate $AuCl_4^-$.[40,91] ^1H and ^{13}C NMR data are consistent with an outer-sphere interaction between $[HL_2]^+$ and $TaCl_6^-$. Further work is needed to fully elucidate the solution-phase structure of the extracted species, potentially using EXAFS and/or computational modelling.

In contrast, amide L^1 is a poor reagent of choice when attempting to transport TaF_5 under high chloride conditions, likely due to a combination of competitive chloride extraction and significantly weaker interactions between $[HL_2]^+$ and more charge-dense species in the aqueous phase such as TaF_5Cl^-. This latter aspect is evident from a comparison of X-ray crystal data for $TaCl_6^-$ and TaF_6^- which shows a 1 Å decrease in the diameter of the Ta complex moving from the chloride to the fluoride. It is therefore anticipated that L^1 would be a poor extractant for Ta when used under solely fluoride conditions in which species such as TaF_6^- and even the dianion TaF_7^{2-} are dominant. Even so, the process described here represents an alternative, fluoride-free route to recycling Ta from waste electronics, using milder reagents than the current commercial methods.

Chapter 5

A dual-purpose ionic liquid for the extraction of gallium from iron chloride solutions.

5 A dual-purpose ionic liquid for the extraction of gallium from iron chloride solutions.

5.1 Overview

Discrimination between iron and gallium in chloride media is challenging because their anionic chloridometalates, $FeCl_4^-$ and $GaCl_4^-$, display similar chemical properties. This chapter describes the separation of gallium from iron by solvent extraction from chloride media using the quaternary ammonium salt, methyltrioctylammonium iodide.

The importance of gallium and the potential requirement for its recovery from alternative sources is discussed. The aqueous chemistries of iron and gallium in chloride media is briefly discussed and the performance and mode of action of this ionic liquid is then investigated.

5.2 Gallium

Gallium is an important component in materials found in modern electronic devices such as light-emitting diodes (LEDs) and solar panels,[136] and is also used in biomedical, pharmaceutical and radiopharmaceutical applications, owing to the similar chemical properties of Ga^{3+} and Fe^{3+} cations.[165,166] There are no abundant natural sources of gallium and instead it is primarily recovered as a by-product from alumina refining in which Ga is present in bauxite ore in trace amounts.[167,168] Alumina is refined from bauxite ore by the Bayer process from which 70% of the Ga present in the ore leaches into highly caustic solutions known as Bayer liquor, reaching concentrations of 100-300 ppm; the remaining 30% of Ga is left behind in red mud residues rich in iron.[169] Solvent extraction of Ga from these alkaline solutions exploits the cation extractant Kelex 100, a hydrocarbon-soluble 8-hydroxyquinoline (figure 5.1) as outlined in equation 5.1.[169,170] Washing the organic phase with 6 M HCl removes co-extracted Al and Na impurities, with the Ga remaining in the organic phase as an ion pair of $GaCl_4^-$ and protonated Kelex 100; this is finally stripped using 2 M HCl.

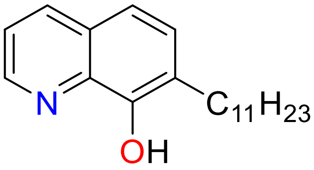

Figure 5.1 – Chemical structure of Kelex 100.

$$\mathrm{Ga(OH)_4^-}_{\,(aq)} + 3\ \mathrm{HL_{kelex\,(org)}} \rightleftharpoons \mathrm{Ga(L_{kelex})_{3\,(org)}} + \mathrm{OH^-}_{\,(aq)} + 3\ \mathrm{H_2O}_{\,(aq)} \qquad (5.1)$$

Gallium is considered to be a critical raw material by the European Commission due to a combination of the limited supply of Ga in nature and the increasing demand for it in semiconductors. This has led to efforts to recover Ga from alternative sources such as red mud, coal fly ash, or electronic waste.[167,171] In these cases however, the presence of iron poses challenging selectivity issues in its separation, for example by solvent extraction from chloride media. Under high chloride concentrations, both of these metals exist as tetrahedral metalates, $FeCl_4^-$ and $GaCl_4^-$, for which current outer-sphere cationic receptors (such as the monoamides discussed in Chapter 2) cannot efficiently discriminate. [165,166,170]

The selective recovery of Ga from iron mine tailings was recently reported.[172] Leaching of the metals using 8 M HCl generated a mixture of Ga and Fe chlorides, which were separated by reducing Fe^{3+} to Fe^{2+} using $SnCl_2$. At this oxidation state the iron was not extracted easily whereas the monoanion $GaCl_4^-$ was extracted with tributylphosphate (TBP, 10% in benzene), albeit with 20-30% co-extraction of iron. In addition, while not explored by the authors it is likely that at these high chloride concentrations, the newly oxidised Sn(IV) cation would form $SnCl_6^{2-}$ which has been reported elsewhere to be extracted by TPB or quaternary ammonium reagents,[173] therefore this approach is not wholly selective for Ga.

Solvent extraction processes that feature metalate transport largely exploit chloride media to generate chloridometalates, although processes using other aqueous halides or as counterions for ionic liquids (ILs) have been reported.[174] ILs are a class of solvent that are liquid at low temperatures (<100 °C),[175] and are an increasingly established class of extractant used either neat or diluted in a hydrophobic solvent to extract various metal ions from aqueous solutions.[14,176] ILs have been reported to enhance the solvent extraction efficiency of alkali and alkaline-earth metals by crown ethers compared to traditional solvents such as toluene or chloroform,[177,178] yet without the crown ether the ionic liquids fail to transport the metal from the aqueous phase. ILs have also been used in the direct recovery of metals from secondary sources by selective metal dissolution.[179,180] In this latter case, a trihalide IL provided both an oxidizing agent to dissolve the metal and a cation or additional complexing agent. However, current approaches using ILs do not address the challenges in selectivity for $FeCl_4^-$ and $GaCl_4^-$. ILs such as trioctylammonium chloride ([TOAH][Cl]) and methytrioctylammonium chloride ([MTOA][Cl]) have been widely reported as reagents for the recovery of gallium and iron by solvent extraction.[181–183] Phase transport is achieved through the formation of charge-neutral supramolecular assemblies such as [MTOA][$GaCl_4$], with $GaCl_4^-$ formed under high chloride conditions in the aqueous phase.

This chapter reports a combination of the selective reduction of Fe^{3+} and recovery of Ga^{3+} by solvent extraction using the dual-purpose IL methyltrioctylammonium iodide ([MTOA][I]). Mass spectrometry, NMR spectroscopy, and UV-Vis spectrophotometry confirm that the iodide functions as a reducing agent for Fe^{3+} and that the hydrophobic quaternary ammonium group forms a stable ion pair with $GaCl_4^-$ in the organic phase, facilitating phase transport and separation in one-step.

5.3 Results and discussion

5.3.1 Halide dependence on Ga(III) and Fe(III) solvent extraction: iodide vs chloride

The transport of gallium into a toluene solution of [MTOA][I] from an equimolar mixture of 0.01 M $FeCl_3$ and $GaCl_3$ in varying concentrations of hydrochloric acid solutions was tested and shows excellent selectivity for gallium between 1 and 4 M HCl (figure 5.2). The amount of iron extracted increases markedly as the concentration of HCl increases above 3 M, likely due to a greater proportion of Fe existing as $FeCl_4^-$ in solution. Similar experiments under the same conditions with [MTOA][Cl] on the other hand show that both iron and gallium are efficiently extracted at concentrations greater than 1 M HCl.

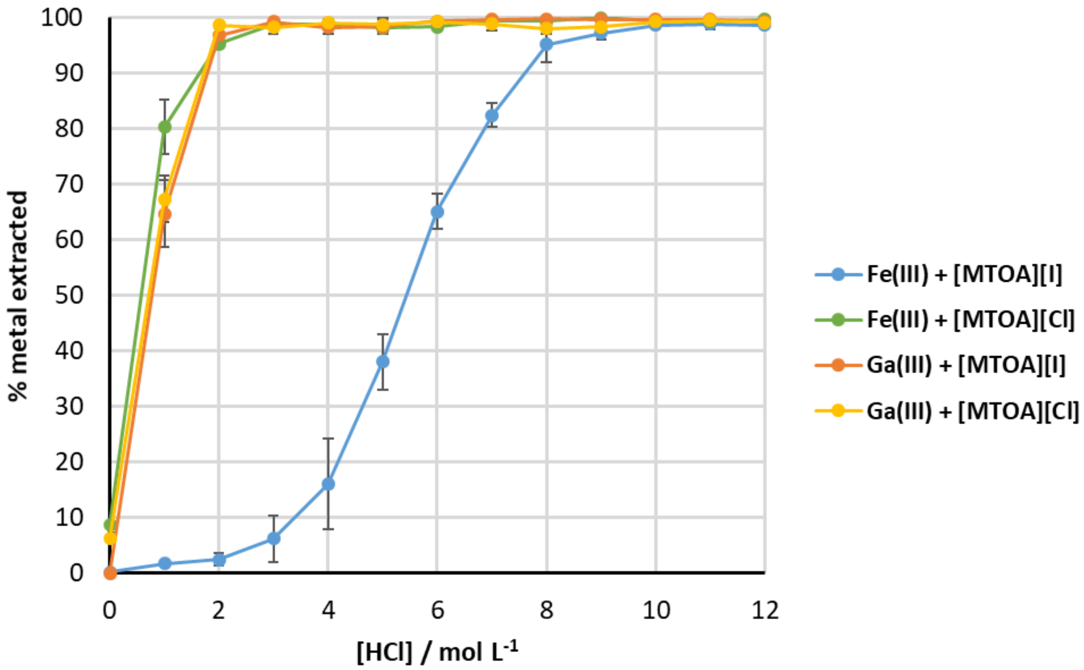

Figure 5.2 – Percentage of gallium and iron extracted by [MTOA][Cl] or [MTOA][I] at varying [HCl] from an equimolar mixture of 0.01 M $FeCl_3$ and $GaCl_3$. Experiments performed in duplicate and reported as an average.

Gallium is readily stripped from the organic phase by a fresh aqueous phase of water whereas <5 % is stripped using 2 M HCl, suggesting that hydrolysis of the chlorogallate species is occurring in water, resulting in the formation of [MTOA][Cl] in the organic phase (equation 5.2). Analysis of this contacted water solution by ^{71}Ga NMR spectroscopy shows one peak at 0.0 ppm assigned to the hexahydrate $[Ga(H_2O)_6][Cl_3]$.[184]

$$[MTOA][GaCl_4]_{(org)} + 6\ H_2O_{(aq)} \rightleftharpoons [MTOA][Cl]_{(org)} + [Ga(H_2O)_6]^{3+}_{(aq)} + 3\ Cl^-_{(aq)} \qquad (5.2)$$

5.3.2 Mode of action of gallium separation by [MTOA][I]

5.3.2.1 ^{71}Ga NMR spectroscopy of a Ga loaded organic phase

The nature of the extracted gallium species was probed by ^{71}Ga NMR spectroscopy (figure 5.3). After contact of a $GaCl_3$ solution in 2 M HCl with either 0.1 M [MTOA][Cl] or [MTOA][I] in toluene, only one signal at 250 ppm is observed for both organic phases, consistent with the formation of the $GaCl_4^-$ anion.[184] In contrast, aqueous solutions of $GaCl_3$ in 0 M to 7 M

HCl show a peak at 0.0 ppm assigned to the hydrated Ga cation. The metalate, $GaCl_4^-$, is only observed by NMR in aqueous solutions above 8 M HCl upon which the ^{71}Ga signal shifts to 250 ppm. As the metalate is not initially present at 2 M HCl in significant concentrations, it is likely that formation of chlorogallates such as $GaCl_4^-$ are occurring at the interface between the two phases, which readily forms a stable ion pair with the quaternary ammonium cation in the organic phase, shifting the equilibrium of $GaCl_4^-$ further to the right in the aqueous phase (equation 5.3).

$$Ga^{3+}_{(aq)} + 4Cl^-_{(aq)} \rightleftharpoons GaCl_4^-{}_{(aq)} \rightleftharpoons GaCl_4^-{}_{(org)} \qquad (5.3)$$

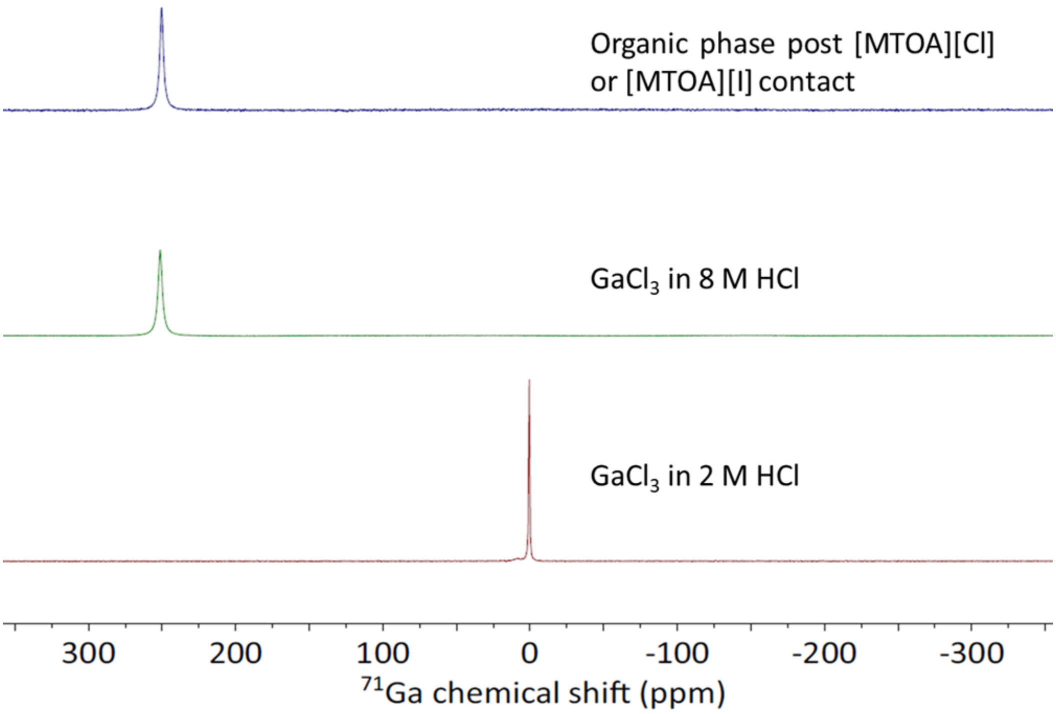

Figure 5.3 – Top: ^{71}Ga NMR spectrum of 0.1 M [MTOA][I] in toluene after contact with 0.01 M $GaCl_3$ dissolved in 2 M HCl. Middle: ^{71}Ga NMR spectrum of 0.01 M $GaCl_3$ dissolved in 8 M HCl Bottom: ^{71}Ga NMR spectrum of 0.01 M $GaCl_3$ dissolved in 2 M HCl.

5.3.2.2 Mass Spectrometry

Electrospray ionization mass spectrometry (ESI-MS) was also used to probe the organic phase speciation of extracted Ga and Fe solutions. A 0.1 M solution of [MTOA][I] in toluene after contact with an equimolar solution of $FeCl_3$ and $GaCl_3$ (0.01 M each) in 2 M HCl was diluted into CH_3CN and analysed by ESI-MS in negative and positive mode (figures 5.4 and 5.5 respectively)

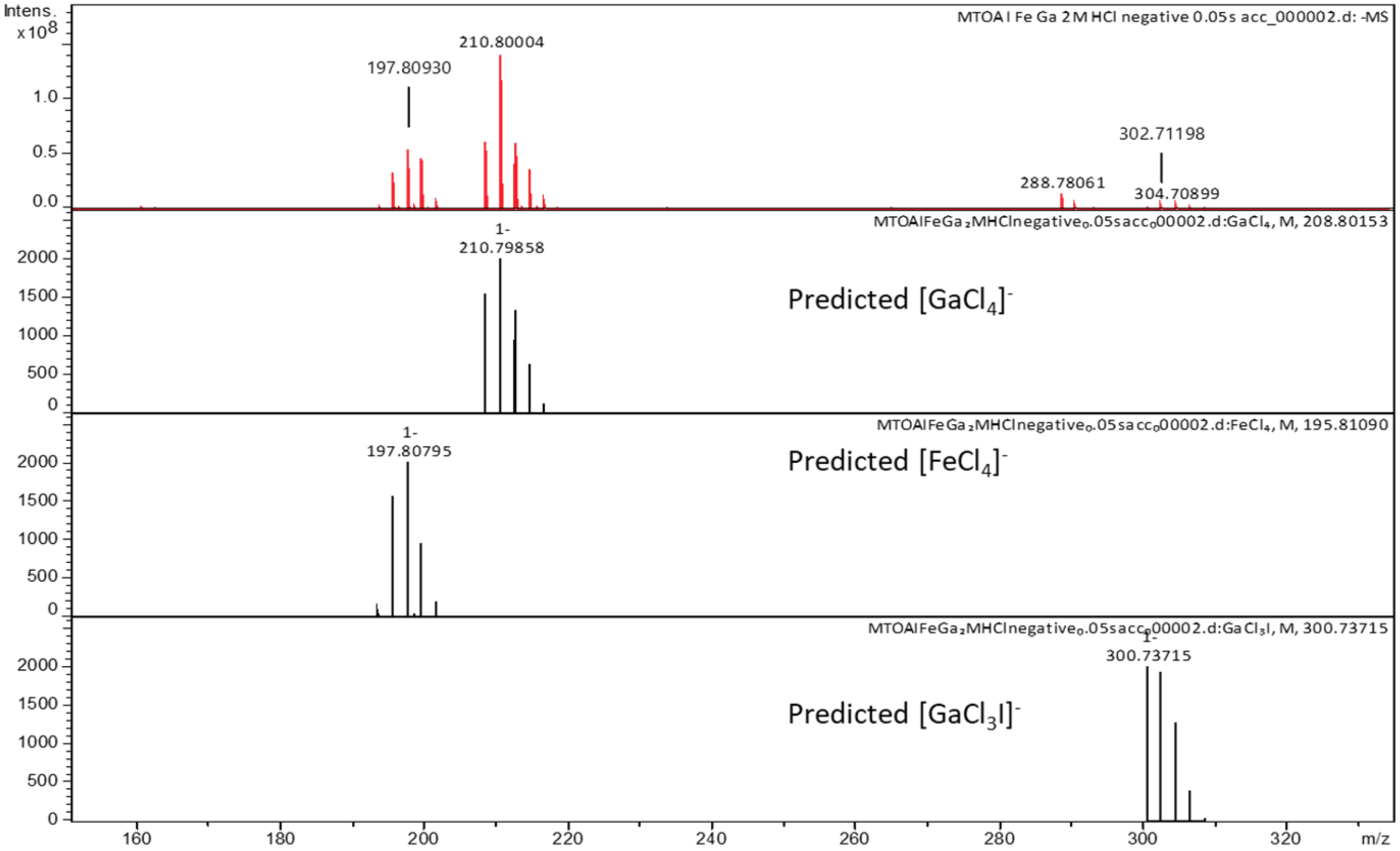

Figure 5.4 – Negative ion ESI-MS of [MTOA][I] in toluene after contact with $FeCl_3$ and $GaCl_3$ in 2 M HCl. Solution diluted in CH_3CN. Real peaks coloured in red and predicted peaks coloured black.

The negative ion ESI-MS spectra show no evidence of mixed halometalates such as $GaCl_3I^-$ or $FeCl_3I^-$; instead only the tetrachloridometalates $FeCl_4^-$ and $GaCl_4^-$ are observed (figure 5.4), suggesting the extracted species in solution are the simple ion pairs [MTOA][MCl_4]. This is also in agreement with ^{71}Ga NMR spectra where only one Ga species $GaCl_4^-$ is observed in the organic phase. The absence of anions such as $GaCl_3I^-$ again suggests that $GaCl_4^-$ is initially formed in the aqueous phase (or at the interface) prior to transport across to the organic phase, as opposed to the transport of the neutral complex $GaCl_3$ with subsequent metalate formation in the organic phase due to the presence of I^- ions.

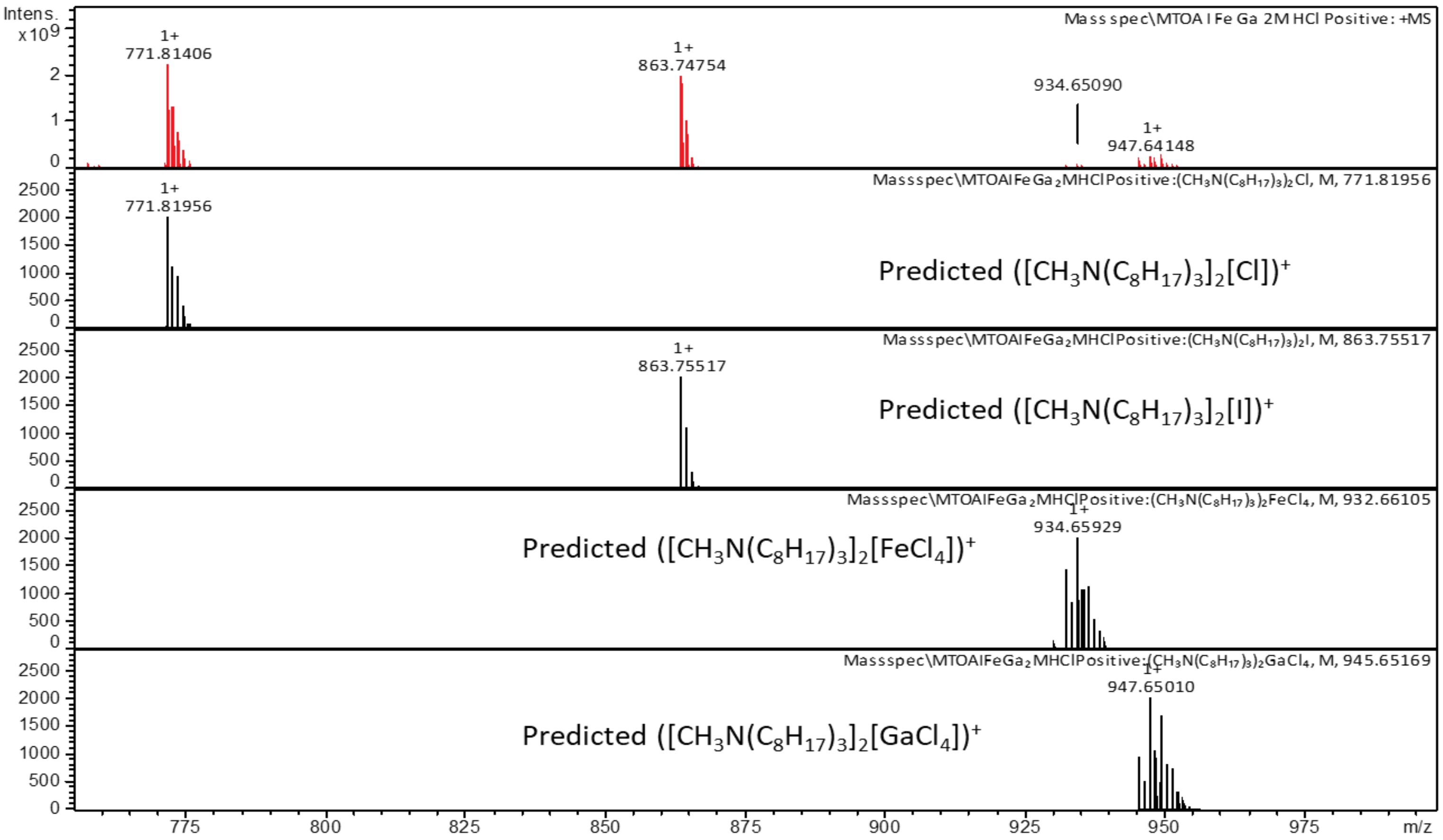

Figure 5.5 – Positive ion ESI-MS of [MTOA][I] in toluene after contact with $FeCl_3$ and $GaCl_3$ in 2 M HCl. Solution diluted in CH_3CN. Real peaks coloured in red and predicted peaks coloured black.

In the positive ion ESI-MS, the two dominant molecular ions are $([MTOA]_2Cl)^+$ and $([MTOA]_2I)^+$, suggesting some iodide has exchanged for chloride from the aqueous phase. Also present are ions consistent with the formula $([MTOA]_2[GaCl_4])^+$. There is a less intense peak commensurate with $([MTOA]_2[FeCl_4])^+$ but no mixed-halometalate ions such as $([MTOA]_2[GaCl_3I])^+$ could be assigned.

5.3.2.3 Slope Analysis

Slope analysis was carried out to confirm if H^+ was being co-extracted with $GaCl_4^-$ by varying the acid concentration with HNO_3 from 0.01 M to 1 M at 2 M NaCl and plotting log D against log $[H^+]$ (figure 5.6). The slope of almost zero indicates there is no correlation between Ga transport and $[H^+]$, ruling out transport of neutral species such as $HGaCl_4$, therefore confirming an ion-exchange extraction mechanism between I^- and $GaCl_4^-$ (equation 5.4).

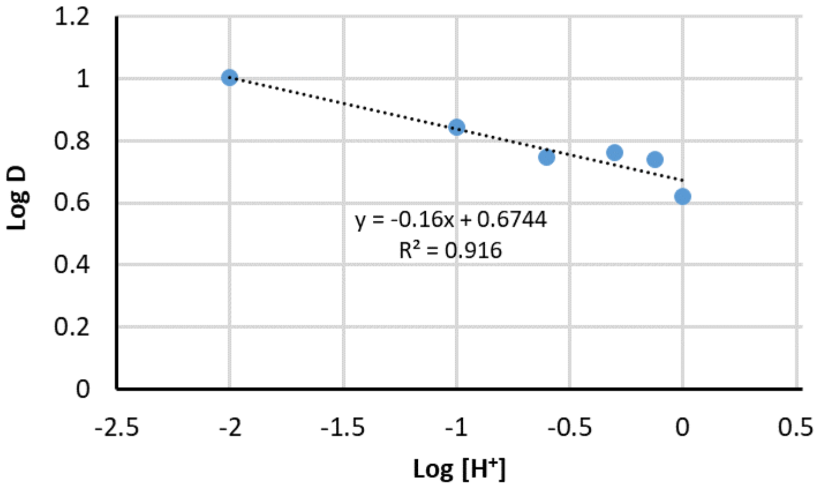

Figure 5.6 – Slope analysis for the transport of Ga by [MTOA][I] with varying $[H^+]$. Conditions: $GaCl_3$ (0.01 M) in in 2 M NaCl varying HNO_3 (0.01 M – 1 M, 2 mL), contacted with [MTOA][I] (0.1 M) in toluene (2 mL) for 1 h at RT with magnetic stirring.

$$[MTOA][I]_{(org)} + HCl_{(aq)} + GaCl_{3\,(aq)} \rightleftharpoons [MTOA][GaCl_4]_{(org)} + HI_{(aq)} \qquad (5.4)$$

In addition, slope analysis was also used to confirm the ratio of ligand:metal in the organic phase upon extraction by plotting the log D versus log [L] (figure 5.7) by varying the concentration of [MTOA][I] from 0.001 M to 0.25 M at 2 M HCl. An L:Ga ratio of approximately 1 is obtained which suggests that the simple ion pair [MTOA][$GaCl_4$] is present in the organic phase, in good agreement with the ESI-MS data above (figures 5.4 and 5.5).

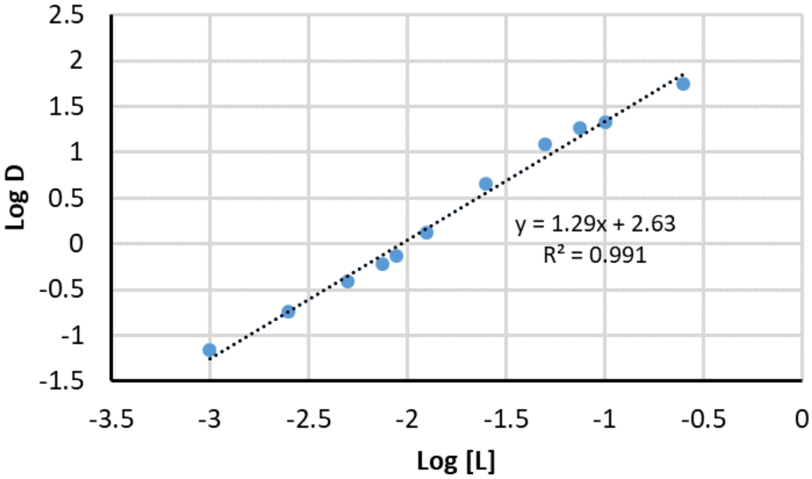

Figure 5.7 – Slope analysis for the transport of Ga with [MTOA][I]. Conditions: 2 mL 0.01 M $GaCl_3$ in 2 M HCl, contacted with 2 mL of 0.001 M to 0.25 M [MTOA][I] in toluene for 1 h at RT with magnetic stirring.

5.3.2.4 UV-Vis spectroscopy

The reduction of Fe^{3+} by I^- during extractions is apparent as the colour of the organic phase changes from bright yellow to deep red, and the initially yellow aqueous phase turns colourless. The deep red colour of the organic phase is consistent with the presence of the triiodide anion, I_3^-, which is supported by the appearance of an absorption at 375 nm in the UV-Vis spectrum of the metal-loaded organic phase (figure 5.8).[185]

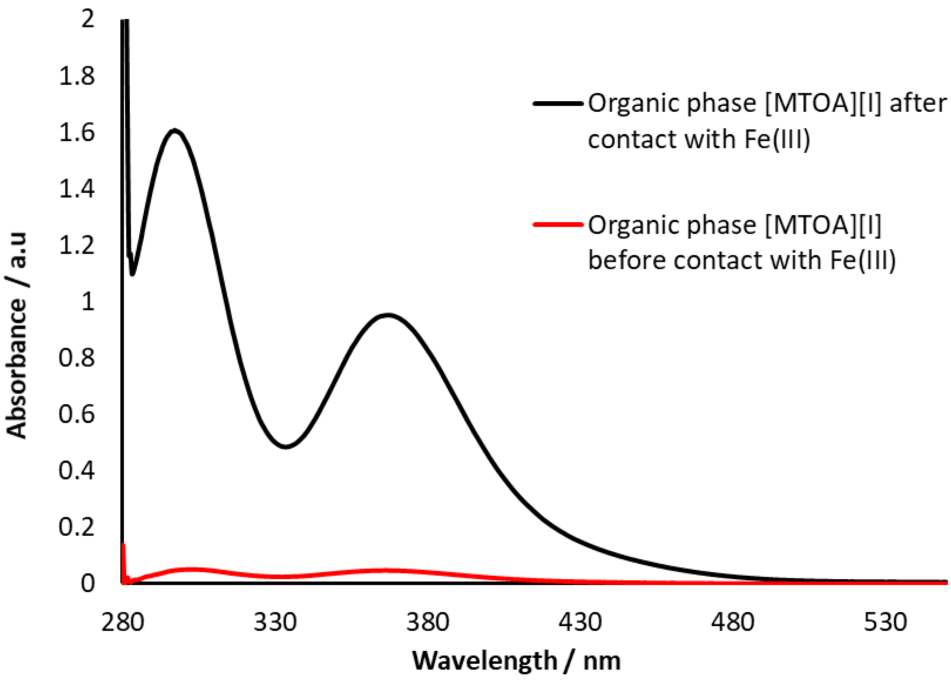

Figure 5.8 – UV-Vis spectra. (a): Toluene solutions of [MTOA][I] before (red) and after (black) contact with solutions of $FeCl_3$ in 2 M HCl. Each solution diluted 500x in toluene.

The reduction of Fe^{3+} by I^- in aqueous solution is known in the literature, and is the basis of a 'clock' reaction (equation 5.5).

$$FeCl_{3\,(aq)} + I^-_{(aq)} \rightleftharpoons FeCl_{2\,(aq)} + Cl^-_{(aq)} + \tfrac{1}{2}\, I_{2\,(aq)} \qquad (5.5)$$

In the presence of excess iodide, any iodine produced will react to form triodide (equation 5.6).

$$[MTOA][I]_{(org)} + I_{2\,(aq)} \rightleftharpoons [MTOA][I_3]_{(org)} \qquad (5.6)$$

At HCl concentrations above 4 M, the selectivity of Ga extraction is reduced and as discussed above is likely due to the increased concentration of $FeCl_4^-$ in the aqueous phase that can exchange with I^- (or I_3^-). The ion pair $[MTOA][FeCl_4]$ was detected by ESI-MS analysis as $([MTOA]_2[FeCl_4])^+$, suggesting that any excess I^- in the organic phase does not reduce $Fe^{3+}_{(org)}$ and that reduction of Fe^{3+} is only occurring in aqueous solution. Transport of I^- to the aqueous phase can occur by two possible options; either by ion exchange between I^- and $GaCl_4^-$ (equation 5.3) or by ion exchange between I^- and Cl^- (equation 5.7).

$$[MTOA][I]_{(org)} + HCl_{(aq)} \rightleftharpoons [MTOA][Cl]_{(org)} + HI_{(aq)} \quad (5.7)$$

The UV-Vis spectrum of the Fe^{3+} aqueous phase at 2 M HCl prior to contact with [MTOA][I] shows two absorption maxima at 220 nm and 336 nm which are consistent with the presence of $FeCl^{2+}$ (figure 5.9, black).[186,187] After contact with [MTOA][I], the UV-Vis spectrum of the aqueous phase shows only one absorption maximum at 225 nm due to the presence of aqueous Fe^{2+} (figure 5.9, red); Fe(II) chlorometalates, such as $FeCl_4^{2-}$, are unlikely to be present as high chloride concentrations are needed for their formation and therefore no anionic extraction of Fe(II) complexes is seen.[188,189]

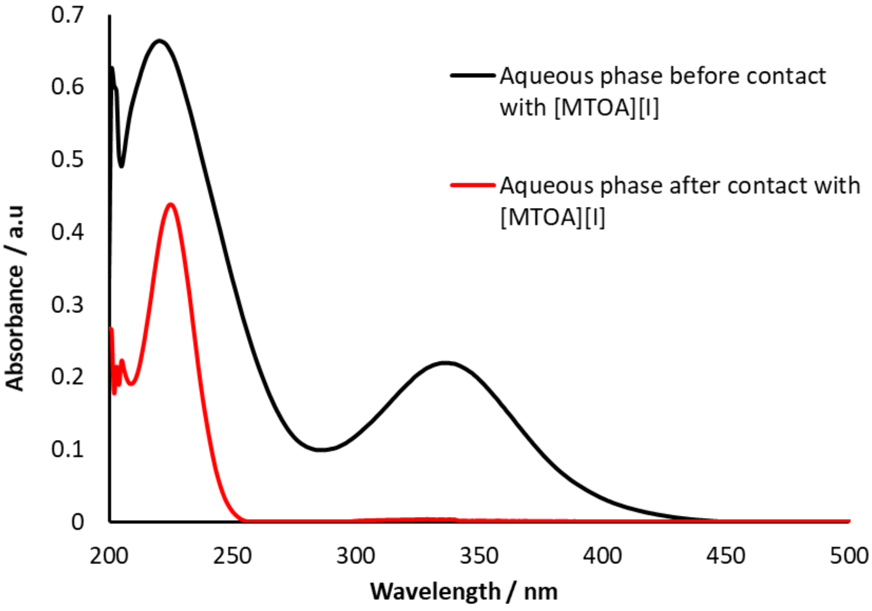

Figure 5.9 − 2 M HCl solutions of $FeCl_3$ before (black) and after (red) contact with 0.1 M [MTOA][I] in toluene. Each solution diluted 100x in 2 M HCl.

5.4 Conclusions

It is clear from this work that the quaternary ammonium salt, [MTOA][I], functions as a dual-purpose extractant, efficiently and selectively separating Ga^{3+} from Fe^{3+} in a single step between 1 – 4 M HCl by reduction of Fe^{3+} to Fe^{2+} and transport of Ga as its metalate $GaCl_4^-$ by anion exchange. This process is operationally simple, eliminating the need for external reducing agents such as Fe powder or $SnCl_2$. Under the high chloride concentrations reported previously,[172] there would be the potential for the newly oxidised Sn(IV) species to form $SnCl_6^{2-}$, which would be readily co-extracted by quaternary ammonium reagents. Back extraction of gallium from the organic phase occurs readily with water and the extractant could, in principle, be regenerated by contact with aqueous potassium iodide and a mild reducing agent, such as sodium thiosulfate.

Chapter 6

Conclusions

6 Conclusions

The primary aim of this work, to develop, investigate and apply simple chemical separation methods for the separation of resource-critical metals present in e-waste, has been achieved. This work has focussed on the recovery of metals under chloride conditions, exploiting the formation of anionic chloridometalates that can be separated from metals that do not form such species as readily or have higher hydration enthalpies.

Chapter 2 evaluated simple primary, secondary, and tertiary monoamides as reagents that selectively extract gold from model e-waste solutions by solvent extraction. Ultimately, this chapter has demonstrated that if the problem of metal recycling from e-waste is to be addressed effectively, then it is not enough to simply evaluate a reagent's extraction performance based on single metal studies alone. When highly concentrated mixed-metal solutions are used, the secondary and tertiary amides form 3rd phases which trap the gold and prevent the efficient extraction of gold, while the primary amide does not and will transport gold effectively. This contrasts with single metal experiments which demonstrated that the secondary and tertiary amides extracted gold more efficiently than the primary amide. DOSY NMR demonstrated that the 3rd phase was a highly aggregated assembly that could be broken up by the addition of more polar solvents but at the expense of selectivity.

Two 'problematic' metals that were contributing to 3rd phase formation were tin and iron, yet simply eliminating them from the solution did not necessarily prevent 3rd phase formation. Given the importance that the e-waste composition may have on extraction performance, it is therefore also not enough to simply apply a 'one-size-fits-all' approach to the leaching of metals from e-waste in to solution (i.e., leach everything from the e-waste into solution and proceed immediately to the separation step). More consideration should be given to the leaching step(s) so that issues of metal composition and concentration are minimised.

Chapter 3 reported the development of a simple diamide reagent, L^6, for the selective and quantitative precipitation of gold from e-waste solutions, entirely avoiding the use of organic solvents and by extension evading 3rd phase formation and reducing waste generation. Throughout this chapter, X-ray crystallography proved invaluable in identifying the structures of the outer-sphere complexes that precipitate out of solution. Upon dissolution in acid, an infinite chain of $[HL^6]^+$ cations is formed by the chelation of a proton by two amide oxygens from adjacent diamide molecules. The resulting rhombohedral cavity created by the phenyl and methyl groups in $[HL^6]^+$ enables metalates to be hosted through electrostatic and non-covalent interactions.

The selectivity of the diamide towards various metalates is highly tuneable. At higher concentrations of HCl, co-precipitation of other metals such as Pt, Fe or Sn with Au can occur when excess L^6 is used, yet Au separation can be achieved by washing the precipitates with dilute HCl prior to releasing $HAuCl_4$ with deionised water and recycling L^6 for further use. Alternatively, control of the diamide stoichiometry or temperature can lead to control of precipitation selectivity. Direct competition experiments demonstrated a clear preference for one metal over the other when a limiting number of moles of L^6 is used, and (in the case of iron vs tin) when temperature is varied. This flexibility makes this simple diamide a very versatile precipitant and could be used in several different hydrometallurgical separation processes relevant to electronic waste or primary metal sources. Further experiments measuring the thermodynamics of precipitation by isothermal calorimetry may help to understand the observed selectivity.

Investigating structurally similar analogues of L^6 demonstrated that the structure of the diamide can impact on the efficiency of metalate precipitation. Changing the substituent on the phenyl groups from an electron-withdrawing group to an electron-donating group regulates the relative ease of metalate precipitation, in large part due to the relative ease of protonation of the relevant diamide. When the phenyl substituent is switched to an alkyl substituent, the molecular structure of precipitates changes from the highly ordered chains of $[HL]^+$ to more cluster-like species that are stable in hydrophobic solvents and are therefore more suited as solvent extractants rather than as precipitants. On the other hand, secondary diamide analogues of L^6 are found to have much lower aqueous solubility than tertiary diamides and so higher concentrations of HCl are required to facilitate $FeCl_4^-$ precipitation. Extending the carbon chain length of the secondary amide N-C-C-N 'hinge' can lower the HCl concentration threshold for precipitation, but this threshold is still higher than that for tertiary diamides.

Chapter 4 compares the extraction efficiency of the conflict metal tantalum from $TaCl_5$ versus TaF_5 under chloride conditions and demonstrated that, despite sparse reports in the literature, extraction from chloride media is also possible by the primary amide and is more efficient than when the fluoride complex is used. The solution-phase structure of the extracted species remains elusive and requires further work potentially using EXAFS and/or computational modelling. The fluoride complex is poorly extracted by L^1 and it seems likely that, based on Hofmeister bias arguments, L^1 would be even worse under the exclusively fluoride media that current hydrometallurgical processes rely on to leach tantalum. This work has demonstrated a potential fluoride-free solvent extraction process for tantalum. Given all of hazards associated with hydrofluoric acid, it is desirable to move away from this as a leaching agent and instead develop alternative, milder reagents for tantalum leaching potentially using sources of chloride.

Chapter 5 briefly explored the separation of gallium from iron by a solvent extraction process using the dual-purpose extractant, methyltrioctylammonium iodide. Various analytical techniques showed that reduction of Fe(III) to Fe(II) by iodide is key to the success in selective transport of Ga(III) as its metalate $GaCl_4^-$ by anion exchange. Under high chloride conditions, discrimination by outer-sphere cationic receptors is difficult given that both metals exist in solution as the tetrahedral metalates, $FeCl_4^-$ and $GaCl_4^-$ and so this presents a convenient way to separate the two metals in one step. Nevertheless, the production of triiodide as a by-product requires additional reagents to then regenerate iodide for further use, which in turn affects the materials balance. It would therefore be advantageous if a system could be developed in which Ga and Fe may be separated without the need for a reduction step. Chapter 3 briefly touches on this issue, where L^6 shows promising signs of Ga selectivity over Fe, but further work is needed to fully understand why this is the case.

Chapter 7

Experimental

7 Experimental

7.1 Overview

This chapter describes general solvent extraction and precipitation protocols, synthetic procedures, treatment of data and potential sources of error.

7.2 General solvent extraction procedures

A typical solvent extraction procedure is outlined in figure 7.1.

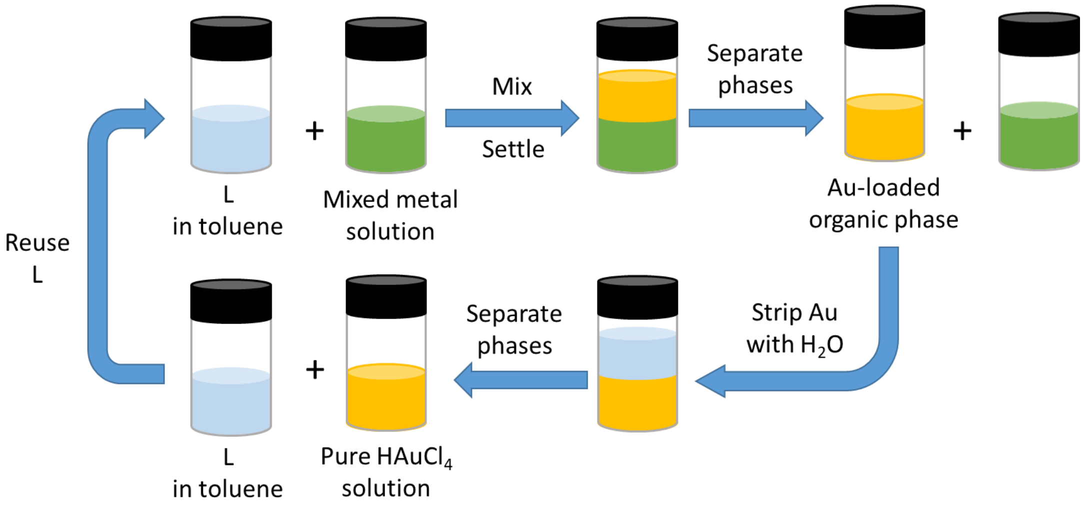

Figure 7.1 – Schematic of a selective solvent extraction process.

An organic solution of ligand L (typically in 0.1 mol L^{-1} in toluene) was mixed with a metal-containing aqueous solution in a glass screw-top vial at 500 rpm for 1 h at room temperature. After settling, the two phases (and a possible 3rd phase) were physically separated from each other. Samples from the organic phases (or 3rd phases) were diluted in 1-methoxy-2-propanol to an appropriate range (0.1 – 25 ppm) for the determination of metal concentrations by ICP-OES. Those from aqueous phases were diluted in 2 % nitric acid to similar concentration ranges. Samples from relevant phases were also withdrawn for water concentration determination, NMR analysis and MS characterisation as required.

Metal stock solutions were prepared by dissolution of the relevant metal chloride salt in varying concentrations of hydrochloric acid. Metal solutions were prepared at a standard concentration of 0.01 M for comparison with other work in the group. Ligand concentrations were set to 0.1 M in toluene by default, allowing for a sufficiently large excess of ligand present to provide at least minimal extraction. Toluene was chosen as the organic solvent as it was considered representative of typical high-boiling solvents used in industrial processes, and again allowed for comparison to previous work of other solvent extraction systems studied by the group. Solvent extraction experiments comprised 2 mL of each phase to allow for thorough mixing and enough material for additional testing (i.e., ICP-OES, NMR, MS, etc.). When 3rd phases formed, extraction experiments were scaled up to 10 or 20 mL to allow for a sufficient volume of 3rd phase to be collected.

7.2.1 Preparation of $TaCl_5$ and TaF_5 solutions

A 0.12 M stock solution of TaX_5 (X = F, Cl) was prepared in 12 M HCl. This stock solution was then diluted to 0.01 M TaX_5 in 1 M HCl with varying solutions of lithium chloride in deionised water. A white precipitate formed over several weeks in dilute HCl solutions of $TaCl_5$, and so solutions were used immediately after diluting from the 12 M HCl stock solution. A white precipitate formed overnight from stock solutions of TaF_5 in 12 M HCl, and so solutions were therefore diluted and used immediately.

7.3 Precipitation procedures

A typical precipitation procedure is outlined in figure 7.2.

To allow for comparison to solvent extraction experiments, metal concentrations were set to 0.01 M and the volume of aqueous solution was 2 mL. Therefore, experiments using excess L were always undertaken with 0.2 mmol of solid L (i.e., a 10x excess of L to metal). This allowed for a reasonable mass of L to be weighed out each time (generally 50 – 70 mg).

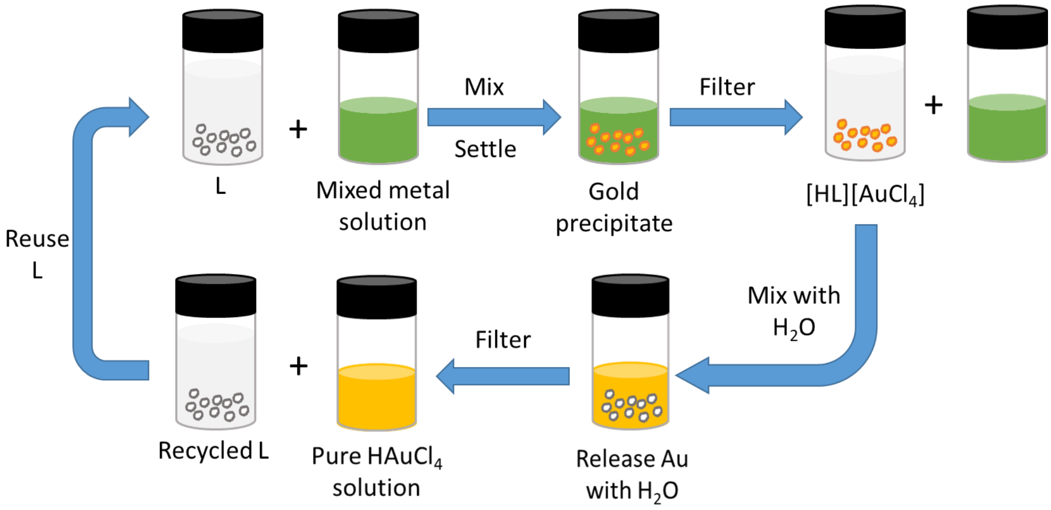

Figure 7.2 – Schematic of a selective precipitation process.

7.3.1 Precipitation procedure for 0.01 M mixed metal solutions.

Mixed-metal solutions (0.01 M) were typically prepared by dilution of 0.1 M stock solutions of each individual metal salt solution in 2 or 6 M HCl. Solid L (0.2 mmol or 0.02 mmol) was added to a vial with a magnetic stir bar and the metal-containing aqueous solution (2 mL) added. The mixture was stirred for 1 h at room temperature at 500 rpm after which the stir bar was removed and the vial centrifuged. The supernatant was decanted and samples prepared for ICP-OES analysis to measure the uptake of metal by L. Samples were diluted by 100x in 2% nitric acid prior to ICP-OES analysis. This procedure was repeated in triplicate.

7.3.2 Selective precipitation of gold from 28 other elements procedure.

The following ICP multi-element standard solutions were used: Transition metal mix 3 for ICP supplied by Sigma Aldrich comprising 100 mg L^{-1} Au, Ir, Os, Pd, Pt, Rh, Ru in 10% hydrochloric acid and ICP multi-element standard solution IV comprising 1000 mg L^{-1} Ag, Al, B, Ba, Bi, Ca, Cd, Co, Cr, Cu, Fe, Ga, In, K, Li, Mg, Mn, Na, Ni, Pb, Sr, Tl, Zn in 5% nitric acid. Each solution (1 mL) was diluted to 10 mL using either 2 M HCl or 6 M HCl, resulting in solutions of 10 mg L^{-1} Au, Ir, Os, Pd, Pt, Rh, Ru and 100 mg L^{-1} Al, B, Ba, Bi, Ca, Cd, Co, Cr, Cu, Fe, Ga, In, K, Li, Mg, Mn, Na, Ni, Pb, Sr, Tl, Zn. The solutions were filtered prior to use in precipitation experiments due to the precipitation of silver chloride, which was subsequently excluded from ICP-OES analysis. The precipitation method used for the 0.01 M mixed-metal solutions was followed.

7.3.3 Selective stripping experiments with H-tube apparatus.

Solid L (0.2 mmol) was added to one side of the H-tube (figure 7.3) with a stir bar. The metal-containing aqueous solution (2 mL) was then added to the solids and the mixture stirred for 1 h at room temperature at 500 rpm, after which it was passed through the glass frit of the H-tube with the aid of compressed air or N_2 gas. The filtrate was collected for ICP-OES analysis to determine metal uptake. The solids were subsequently washed with 2 M HCl (3 x 2 mL; for 30 mins each), with each wash solution being passed through the glass frit of the H-tube. The solids were then washed with ultrapure deionised water (5 x 2 mL) in the same manner. The use of a H-tube allows for all solids to be retained in the same vessel to minimise any loss of metal due to material transfer. This procedure was repeated in duplicate.

Figure 7.3 – Photograph of H-tube apparatus for selective stripping experiments.

7.3.4 Selective precipitation of gold from waste printed circuit boards.

End-of-life printed circuit boards were supplied by Edinburgh School of Chemistry workshop. Gold-tipped sections of the circuit boards (22.85 g) were cut off and soaked in 100 mL aqua regia for 24 hours. This solution was then diluted with deionised water to 250 mL and the metal content analysed by ICP-OES. An aliquot of the e-waste solution (2 mL) was stirred with L (0.0059 g, 0.02 mmol, excess with respect to the gold concentration) for 1 h at room temperature after which the stir bar was removed and the vial centrifuged. The supernatant was decanted and samples prepared for ICP-OES analysis to measure the uptake of metal. Samples were diluted by 1000x and 20x in 2% nitric acid prior to ICP-OES analysis. This procedure was repeated in triplicate.

7.3.5 Timed gold precipitation experiments.

Solutions of $HAuCl_4$ (0.01 M) were prepared in 2, 4 or 6 M HCl. Solid L (0.02 mmol) was added to a vial with a magnetic stir bar and the relevant aqueous metal solution (2 mL) was added. The mixture was stirred for between 1 min* and 55 mins after which the stir bar was removed and the vial centrifuged for 5 minutes. The supernatant was decanted and samples prepared for ICP-OES analysis to measure the uptake of metal. Samples were diluted by 100x in 2% nitric acid prior to ICP-OES analysis. *One-minute experiments were not centrifuged and instead stirred for 30 seconds before removing the stir bar and allowing any solids to settle for an additional 30 s. A clear 0.1 mL aliquot was then sampled immediately and prepared for ICP-OES analysis.

7.4 ICP-OES analysis

Metal content analysis was conducted by ICP-OES on a Perkin Elmer Optima 8300 Inductively Coupled Plasma Optical Emission Spectrometer. Organic samples were doped with 10 ppm ytrrium internal standard in 1-methoxy-2-propanol and taken up by peristaltic pump at a rate of 1.0 mL min^{-1} into a Gem Tip cross flow nebuliser and a Glass Cyclonic spray chamber. Argon plasma conditions were: 1500 W RF forward power, argon gas flows of 17, 1.0 and 0.5 L min^{-1} for plasma, auxiliary and nebuliser flow, respectively. Aqueous samples were diluted in 2% nitric acid and taken up at a rate of 1.3 mL min s^{-1} and the argon gas flow parameters were 12, 0.2 and 0.6 L min^{-1}, respectively. ICP-OES calibration standards were obtained from VWR International, SCP science or Sigma-Aldrich. Emission wavelengths for each element analysed are detailed in table 7.1

Table 7.1 – List of emission wavelengths used for ICP-OES analysis.

Metal	Wavelength / nm
Al	396.153
Au	267.595
B	249.772
Ba	233.527
Bi	306.766
Ca	317.933
Cd	228.802
Co	228.616
Cr	205.56
Cu	327.393
Fe	238.204
Ga	417.206
In	325.609
Ir	224.268
K	766.49
Li	610.362
Na	589.59
Mg	285.213
Mn	257.61
Ni	221.648
Os	225.585
Pb	220.353
Pd	340.458
Pt	265.945
Rh	343.489
Ru	240.272
Sr	460.733
Ta	226.230
Tl	351.924
Zn	213.857

7.4.1 Treatment of data

The basic equation to calculate percentage of metal extracted is provided in equation 7.1. The concentration of metal in the organic phase can be measured directly, or it can be inferred from the final concentration of metal remaining in the aqueous phase after extraction (assuming a third phase does not form.) In this thesis, organic-phase metal concentrations were analysed directly and compared against the initial metal concentration in the aqueous phase. Samples of the aqueous phase after solvent extraction were also measured and confirm mass balance to account for any potential third phase formation.

$$\%\,extraction = \frac{[Metal]_{Organic}}{[Metal]_{Initial\,Aq}} \times 100\% \tag{7.1}$$

This thesis preferentially reports the amount of metal extracted as percentages, however it is common in the solvent extraction literature for extraction values to be reported in terms of the distribution coefficient (D, the ratio of metal detected in each phase after extraction, equation 7.2). When D = 1, 50% of the metal is extracted in to the organic phase.

$$D_M = \frac{[Metal]_{(Org)}}{[Metal]_{(Aq.)}} \tag{7.2}$$

The basic equation to calculate the percentage of metal precipitated is provided in equation 7.3. It is assumed that the amount of metal missing from the aqueous phase after contact with L is incorporated in to the resulting solids, which are subsequently removed after centrifugation.

$$\%\,precipitation = \frac{[Metal]_{Initial\,Aq.} - [Metal]_{Final\,Aq.}}{[Metal]_{Initial\,Aq}} \times 100\% \tag{7.3}$$

7.4.2 Slope analysis

This numerical analysis technique is very common in the solvent extraction literature and can be helpful in elucidating the mode of action of solvent extraction when other analytical techniques are inconclusive or unavailable.[12] This analysis is based on the equilibrium in equation 7.4, in which the mathematical expression in equation 7.5 may be derived:

$$M + aX^- + nL + nH^+ \rightleftharpoons [MX_a(LH)_n] \tag{7.4}$$

$$K = \frac{[MX_a(LH)_n]}{[M][X^-]^a[L]^n[H^+]^n}$$

$$D_M = \frac{[M]_{(org)}}{[M]_{(aq)}} = \frac{[MX_a(LH)_n]}{[M]}$$

$$K = \frac{D_M}{[X^-]^a[L]^n[H^+]^n}$$

$$D_M = K[X^-]^a[L]^n[H^+]^n$$

$$log\ D_M = \log K + a\log[X^-] + n\log[L] + n\log[H^+] \tag{7.5}$$

Therefore, plotting log D against log [X$^-$], log [L] or log [H$^+$] gives a straight line in which the ratio of anion, ligand or proton to metal in the extracted species can be inferred from the gradient of the line. This analysis assumes only one species being extracted, and that any excess ligand does not interact with the extracted species. Therefore non-integer gradients and deviations from linearity indicate mixtures of species.

7.4.3 Sources of error

Errors associated with instruments, measurements and systematic handling of samples and data are included in table 7.2. However, some sources of error are more difficult to quantify. There is the possibility of precipitation of metal species on dissolution of samples from the solvent extractions into 1-methoxy-2-propanol, which leads to an artificial decrease the metal concentration detected by ICP-OES. Likewise, potential evaporation of solvents during solvent extraction experiments and ICP-OES analysis can lead to artificial increases in metal concentration. These potential sources of error were kept consistent across all samples by ensuring each sample is prepared and analysed within a short timeframe (1 – 2 days) and the total volumes used in dilutions are kept constant. The pipettes used for dilutions were calibrated annually by an external company and their accuracy checked on a regular basis by lab members.

Table 7.2 – Associated errors with instruments used.

Instrument	**Associated Error**
Mass Balance	± 0.05 mg
Manual pipettes*	
Gilson 0.1 mL	± 0.5 μL
Gilson 1 mL	± 6 μL
Gilson 5 mL	± 27 μL
Eletronic Eppendorf Multipette E3x positive displacement pipette*	± 0.95 μL (dispensing 500 μL) ± 0.38 μL (dispensing 2500 μL) ± 0.23 μL (dispensing 5000 μL
5 mL volumetric flask	± 0.025 mL
10 mL volumetric flask	± 0.025 mL
25 mL volumetric flask	± 0.040 mL
100 mL volumetric flask	± 0.080 mL
ICP-OES calibration plot	$R^2 > 0.995$
ICP-OES sample data	$\sigma = \sqrt{\frac{\sum(x-\mu)^2}{n}}$ σ = standard deviation x = value of sample μ = mean of samples n = number of samples

*As documented on 2021 calibration reports.

7.5 Chemicals and instrumentation

All solvents and reagents were used as received from Sigma-Aldrich, Fisher Scientific UK, Alfa Aesar, Acros Organics or VWR International. Deionised water was obtained from a Milli-Q purification system.

All NMR spectra were recorded at 300 K unless otherwise stated. ^{1}H and ^{13}C spectra were recorded on a Bruker AVA400, AVA500 or AVA600 spectrometer operating at 399.90, 500.12, or 599.95 MHz respectively for ^{1}H, and 100.55, 125.76, or 150.83 MHz, respectively, for ^{13}C. ^{71}Ga NMR spectra were recorded on a Bruker PRO500 spectrometer at 152.55 MHz. Chemical shifts are reported in δ (ppm).

UV-Vis spectra were recorded in quartz cuvettes (1 cm^3 path length) on a Shimadzu UV-1900 UV-VIS spectrophotometer.

ESI FT-ICR MS measurements were recorded in positive-ion or negative-ion mode using the standard Bruker ESI sprayer operated in "infusion" mode coupled to a SolariX FTICR mass spectrometer. Direct infusion spectra were typically a sum of 20 acquisitions. All mass spectra were analysed using DataAnalysis software version 4.1 (Bruker Daltonics). Ions were assigned manually.

Karl Fischer analysis of the water concentration in organic phases after extraction were carried out on a Metrohm 831 KF Coloumeter with Hydranal Coulomat AG as the reagent mixture. Titrations for each sample were repeated in triplicate and the result reported as an average.

Powder X-ray Diffraction (PXRD) data were collected on a sample of $[HL^6][AuCl_4]$ precipitated by the addition of L^6 (5.9 mg, 0.02 mmol) to a solution of $HAuCl_4$ (0.01 M) in HCl (6 M) using a Bruker D2 phaser diffractometer in reflection geometry with Cu Kα radiation (λ = 1.541 Å). A LynxEye position sensitive detector was used to collect data over the 2θ range 6-65^o for 15 minutes. Sample preparation involved grinding powder samples, mixing with acetone, and depositing a thin layer on a zero-background silicon (911) substrate. The data were analysed using a Pawley fitting routine in the Topas Academic (version 6) software suite.

7.5.1 NCI calculations

Calculations were performed and analysed by Professor Carole Morrison and Ms Susanna Vance. All structures were optimised (atom-only) using CASTEP17.21,[190] with on-the-fly pseudopotentials and a plane-wave energy cut-off of 750 eV, coupled to the PBE DFT functional and TS dispersion correction scheme.[191–193] Brillouin zone sampling was 0.05 $Å^{-1}$. Geometry convergence criteria: energy tolerance = 2×10^{-5} eV $atom^{-1}$, max force = 0.05 eV $Å^{-1}$, max atomic displacement = 2×10^{-3} Å. Following geometry optimisation, charge density cube files were generated using the CASTEP2CUBE utility, and subsequently used to generate non-covalent interaction (NCI) plots using the CRITIC2 code.[194–196] The graphical output from CRITIC2 was processed using VMD1.9.3[197] and Origin2019.

7.5.2 Single Crystal X-ray diffraction

X-ray crystallographic data were collected by Dr Gary Nichol at 100 K or 120 K on an Oxford Diffraction Excalibur diffractometer using graphite monochromated Mo-K_α radiation equipped with an Eos CCD detector (λ = 0.71073 Å), or at 100 K or 120 K on a Supernova, Dual, Cu at Zero Atlas diffractometer using Cu-K_α radiation (λ = 1.5418 Å), or at 100 K on a Bruker *APEX*-II CCD diffractometer using graphite monochromated Mo-K_α radiation (λ = 0.71073 Å).

Structures were solved either by the author or by Dr Gary Nichol using ShelXT direct methods or intrinsic phasing and refined using a full-matrix least-square refinement on $|F|^2$ using ShelXL.[198–200] All programs were used within the Olex suites.[201] All non-hydrogen atoms were refined with anisotropic displacement parameters. H-atom parameters were constrained to parent atoms and refined using a riding model except H1 and H2, which where possible were located in the difference Fourier maps and refined with isotropic displacement parameters.

All X-ray crystal structures were analysed and illustrated using Mercury 4.1.0. X-ray data are presented in Appendix I.

7.6 Synthetic procedures

7.6.1 3,5,5-Trimethylhexanamide, L[1]

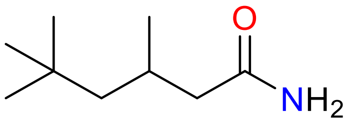

Monoamide L[1] was prepared according to a procedure from the literature.[40] 3,5,5-trimethylhexanoyl chloride (10 mL, 0.053 mol) was added dropwise to an aqueous ammonia solution (80 mL, 35 wt%) at 0°C, and the mixture was stirred at ambient temperature for 3 h to give a white precipitate. The solid was extracted into dichloromethane (80 mL) and washed with water (3 x 80 mL). The organic phase was then dried over Na_2SO_4 and the solvent was removed under reduced pressure to give the desired compound as a white solid (6.91 g, 75%).

^{1}H NMR (500 MHz, $CDCl_3$) δ = 0.93 (s, 9H, C(C*H*$_3$)$_3$), 1.01 (d, *J* = 6.5 Hz, 3H, CH(C*H*$_3$)), 1.13 (dd, *J* = 14.0, 6.4 Hz, 1H, C*H*$_2$C(CH$_3$)$_3$), 1.27 (dd, *J* = 14.0, 3.9 Hz, 1H, C*H*$_2$C(CH$_3$)$_3$), 1.99 (dd, *J* = 13.6, 8.5 Hz, 1H, C*H*$_2$CO), 2.02 – 2.10 (m, 1H, C*H*(CH$_3$)), 2.24 (dd, *J* = 14.0, 6.4 Hz, 1H, C*H*$_2$CO), 5.54(br. s, 2H, N*H*$_2$); ^{13}C{^{1}H} NMR (126 MHz, $CDCl_3$) δ = 22.54, 27.30, 30.00, 31.05, 45.86, 50.72, 175.19.

7.6.2 N,3,5,5-Tetramethylhexanamide, L[2]

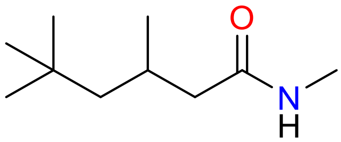

Monoamide L[2] was prepared according to a procedure adapted from the literature.[40] 3,5,5-trimethyhexanoyl chloride (47.5 mL, 0.25 mol) was added dropwise to an aqueous methylamine solution (300 mL, 40 wt%) at 0°C, and the mixture was stirred at room temperature for 3 h. The crude product was extracted into dichloromethane (300 mL) and washed with water (3 x 300 mL). The organic phase was dried over Na_2SO_4 and the solvent was removed under reduced pressure to give the desired compound as a colourless oil (36.21 g, 84%).

^{1}H NMR (600 MHz, CDCl$_3$) δ = 0.91 (s, 9H, C(C*H*$_3$)$_3$), 0.97 (d, *J* = 6.7 Hz, 3H, CH(C*H*$_3$)), 1.10 (dd, *J* = 14.0, 6.6 Hz, 1H, C*H*$_2$(CH$_3$)$_3$), 1.24 (dd, *J* = 14.0, 3.9 Hz, 1H, C*H*$_2$(CH$_3$)$_3$), 1.94 (dd, *J* = 13.5, 8.4 Hz, 1H, (C*H*$_2$CO), 2.03 – 2.09 (m, 1H, CH(C*H*$_3$)), 2.19 (dd, *J* = 13.5, 5.9 Hz, 1H, C*H*$_2$CO), 2.80 (d, *J* = 4.9 Hz 3H, N(C*H*$_3$)), 6.55 (s, 1H, N*H*); ^{13}C{^{1}H} NMR (126 MHz, CDCl$_3$) δ = 22.56, 26.08, 27.34, 29.95, 30.98, 46.39, 50.69, 173.42.

7.6.3 N,N,3,5,5-Pentamethylhexanamide, L^3

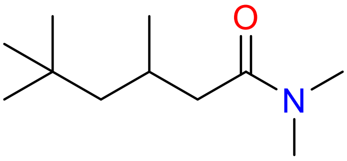

Monoamide L^3 was prepared according to a procedure adapted from the literature.[40] 3,5,5-trimethylhexanoyl chloride (47.5 mL, 0.25 mol) was added dropwise to an aqueous dimethylamine solution (300 mL, 40 wt%) at 0°C, and the mixture was stirred at ambient temperature for 3 h. The crude product was extracted into dichloromethane (300 mL) and washed with water (3 x 300 mL). The organic phase was dried over Na$_2$SO$_4$ and the solvent was removed under reduced pressure to give the desired compound as a colourless oil (28.16 g, 61%).

^{1}H NMR (500 MHz, CDCl$_3$) δ = 0.80 (s, 9H, C(C*H*$_3$)$_3$), 0.87 (d, J = 6.5 Hz, 3H CH(C*H*$_3$)), 1.00 (dd, J = 13.9, 6.5 Hz, 1H, C*H*$_2$(CH$_3$)$_3$), 1.18 (dd, J = 14.0, 3.8 Hz, 1H, C*H*$_2$(CH$_3$)$_3$), 1.94 – 2.03 (m, 1H, C*H*(CH$_3$)), 2.06 (dd, J = 14.6, 8.2 Hz, 1H, C*H*$_2$CO), 2.16 (dd, J = 14.6, 5.8 Hz, 1H, C*H*$_2$CO), 2.82 (s, 3H, N(C*H*$_3$)), 2.90 (s, 3H, N(C*H*$_3$)); ^{13}C{^{1}H} NMR (126 MHz, CDCl$_3$) δ = 22.83, 26.84, 29.95, 31.04, 35.25, 37.41, 42.72, 50.84, 172.50.

7.6.4 N,N'-(ethane-1,2-diyl)bis(N,3,5,5-tetramethylhexanamide), L^4

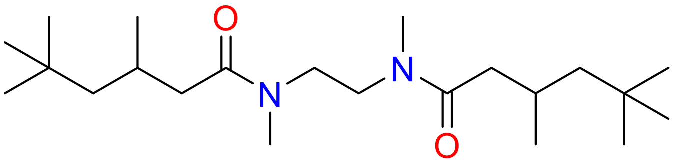

N,N'-Dimethylethylenediamine (1.08 mL, 10 mmol) was added dropwise to a solution of 3,5,5-ttrimethylhexanoyl chloride (5.7 mL, 30 mmol) and trimethylamine (4.18 mL, 30 mmol) in 40 mL dichloromethane at 0 °C and was stirred overnight at room temperature. The solids were filtered off and the filtrate was washed with dilute HCl (3 x 100 mL), brine (3 x100 mL) and water (3 x 100 mL). The organic phase was dried over Na_2SO_4 and the solvent removed under reduced pressure to yield a light-yellow oil which was purified by silica gel chromatography (20% ethyl acetate in hexanes) to provide the product as a colourless oil and a 3:1:1 mixture of diastereomers (2.72 g, 73%).

^{1}H NMR (600 MHz, $CDCl_3$): δ = 0.91 – 0.95 (m, 18H, $C(CH_3)_3$, mixture of diastereomers), 0.96 – 1.02 (m, 6H, CH_3, mixture of diastereomers), 1.14 (m, 2H, diasterotopic CH, mixture of diastereomers), 1.28 (m, 2H, diasterotopic CH, mixture of diastereomers), 2.13 (m, 4H, CH_2CO, mixture of diastereomers), 2.25 (m, 2H, C**H**CH_3, mixture of diastereomers), 2.98 (s, 6H CH_3N, minor diastereomer), 3.04 (s, 6H, CH_3N, minor diastereomer), 3.06 (s, 6H, CH_3N, major diastereomer), 3.52 (m, 4H CH_2N, mixture of diastereomers); $^{13}C\{^1H\}$ NMR (126 MHz, $CDCl_3$): δ = 22.82 (major diastereomer CH_3), 22.86 (minor diastereomer CH_3), 22.93 (minor diastereomer CH_3), 26.67 (minor diastereomer CH), 26.73 (major diastereomer CH), 27.11 (minor diastereomer CH), 30.02 (minor diastereomer C(**C**$H_3)_3$), 30.06 (major diastereomer, likely overlapped with additional minor diastereomer C(**C**$H_3)_3$), 31.13 (major diastereomer **C**(CH_3)), 31.14 (minor diastereomer **C**(CH_3)), 31.16 (minor diastereomer **C**(CH_3)), 33.71 (minor diastereomer NCH_3), 35.89 (major diastereomer NCH_3), 37.10 (minor diastereomer NCH_3), 42.14 (minor diastereomer **C**H_2CO), 49.94 (major diastereomer **C**H_2CO), 42.91 (major diastereomer **C**H_2CO), 44.57 (major diastereomer CH_2N), 47.06 (minor diastereomer CH_2N), 47.46 (minor diastereomer CH_2N), 50.85 (minor diastereomer CH_2), 50.86 (minor diastereomer CH_2), 51.04 (major diastereomer CH_2), 172.73 (minor diastereomer C=O), 172.77 (minor diastereomer C=O), 172.83 (major diastereomer C=O).

ESI Accurate Mass Analysis (ESI, m/z): Calcd. for $C_{22}H_{44}N_2O_2$ $[M+H]^+$ 369.3487; Found 369.3475

7.6.5 N,N′-(1,2-Ethanediyl)bis(2,2-dimethyl-N-methylpropanamide), L^5

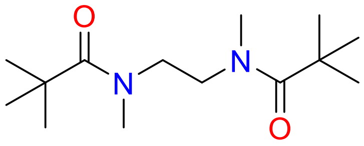

Diamide L^5 was prepared according to a procedure adapted from the literature.[202] Under argon, N,N′-dimethylethylenediamine (1.08 mL, 10 mmol) was dissolved in CH_2Cl_2 (15 mL) and 1 M sodium hydroxide solution added (20 mL). A solution of trimethylacetyl chloride (2.71 mL, 22mmol) in CH_2Cl_2 (5 mL) was slowly added and the resulting solution was stirred at r.t. for 18 h. The solution was then diluted with CH_2Cl_2 (50 mL) and washed with 1 M HCl (3 x 100 mL) and brine (3 x 100 mL). The organic layer was dried over sodium sulfate and evaporated to dryness under vacuum to yield L^5 as a white powder (1.61 g, 63%).

^1H NMR (500 MHz, $CDCl_3$): δ = 1.29 (s, 18H; CH_3), 3.18 (s, 6H; NCH_3), 3.53 ppm (s, 4H; CH_2); $^{13}C\{^1H\}$ NMR (126 MHz, $CDCl_3$): δ = 28.2, 37.9, 47.2, 177.7 ppm.

7.6.6 N,N′-(Ethane-1,2-diyl)bis(N-methylbenzamide), L^6

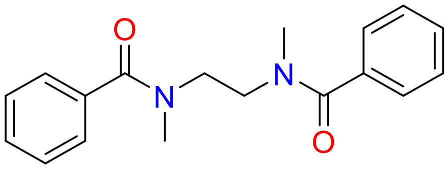

Diamide L^6 was prepared according to a procedure adapted from the literature.[202] Under argon, N,N′-dimethylethylenediamine (1.76 g, 2.15 mL, 20 mmol) was dissolved in CH_2Cl_2 (30 mL) and treated with NEt_3 (7 mL). A solution of benzoyl chloride (7.03 g, 5.81 mL, 50 mmol) in CH_2Cl_2 (20 mL) was slowly added and the resulting solution was stirred at r.t. for 18 h. The solution was then diluted with CH_2Cl_2 (50 mL) and washed with 1 M HCl (3 x 100 mL) and brine (3 x 100 mL). The organic layer was dried over sodium sulfate and evaporated to dryness under vacuum. The resulting solid was recrystalised from hot toluene to yield L^6 as a white powder (4.54 g, 77%).

^{1}H NMR (500 MHz, $CDCl_3$): δ= 2.63–3.01 (br m, 6H; NCH_3), 3.24–4.08 (br. m, 4H; NCH_2), 7.32–7.49 ppm (m, 10H; ArH); ^{13}C{^{1}H} NMR (126 MHz, $CDCl_3$): δ= 37.9, 44.5, 126.9, 128.4, 129.5, 136.3, 172.0 ppm. The NMR spectra agreed with previous reports in the literature.

7.6.7 N,N'-(Ethane-1,2-diyl)bis(N-methyl-4-nitrobenzamide), L^7

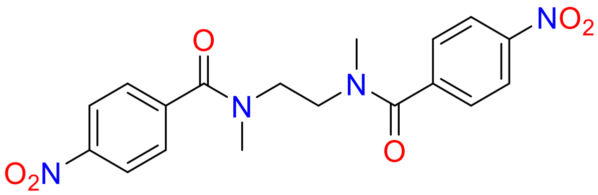

Diamide L^7 was prepared according to a procedure adapted from the literature.[202] Under argon, N,N'-dimethylethylenediamine (0.54 mL, 5 mmol) was dissolved in CH_2Cl_2 (30 mL) and treated with NEt_3 (7 mL). A solution of 4-nitrobenzoyl chloride (2.04 g, 11mmol) in CH_2Cl_2 (10 mL) was slowly added and the resulting solution was stirred at r.t. for 18 h. The solution was then diluted with CH_2Cl_2 (50 mL) and washed with 1 M HCl (3 x 100 mL) and brine (3 x 100 mL). The organic layer was dried over sodium sulfate and evaporated to dryness under vacuum. The resulting solid was recrystalised from hot toluene to yield L^7 as a light-yellow powder (0.96 g, 50 %).

^{1}H NMR (500 MHz, $CDCl_3$): δ = 3.10 (br. s, 6H; NCH_3), 3.89 (br. s, 4H; NCH_2), 7.56 (d, ^3J = 8.8 Hz, 4H; ArH), 8.24 ppm (d, ^3J = 8.7 Hz, 4H; ArH); ^{13}C{^{1}H} NMR (126 MHz, $CDCl_3$): δ = 37.8, 44.9, 123.9, 127.7, 142.3, 148.1, 170.1 ppm. The NMR spectra agreed with previous reports in the literature.

7.6.8 N,N'-(Ethane-1,2-diyl)bis(pentafluoro-N-methylbenzamide), L^8

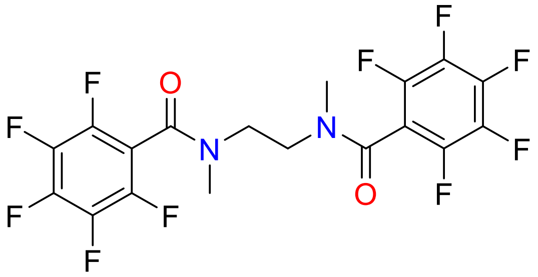

Diamide L^8 was prepared according to a procedure adapted from the literature.[202] Under argon, N,N'-dimethylethylenediamine (1.08 mL, 10 mmol) was dissolved in CH_2Cl_2 (15 mL) and treated with NEt_3 (4.18 mL). A solution of pentafluorobenzoyl chloride (3.05 mL, 22mmol) in CH_2Cl_2 (5 mL) was slowly added and the resulting solution was stirred at r.t. for 18 h. The solution was then diluted with CH_2Cl_2 (50 mL) and washed with 1 M HCl (3 x 100 mL) and brine (3 x 100 mL). The organic layer was dried over sodium sulfate and evaporated to dryness under vacuum. The resulting solid was recrystalised from hot toluene to yield L^8 as an orange powder (1.17 g, 22 %).

^1H NMR (500 MHz, $CDCl_3$): δ = 3.07 (s, 6H; NCH_3), 3.92 ppm (s, 4H; NCH_2); $^{13}C\{^1H\}$ NMR (126 MHz, $CDCl_3$): δ = 36.7, 44.9, 136.7, 138.7, 141.8, 143.8, 159.2 ppm. The NMR spectra agreed with previous reports in the literature.

7.6.9 N,N′-(Ethane-1,2-diyl)bis(4-chloro-N-methylbenzamide), L^9

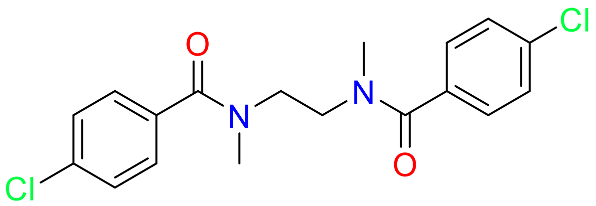

Diamide L^9 was prepared according to a procedure adapted from the literature.[202] Under argon, N,N′-dimethylethylenediamine (1.08 mL, 10 mmol) was dissolved in CH_2Cl_2 (15 mL) and treated with NEt_3 (4.18 mL). A solution of 4-chlorobenzoyl chloride (2.82 mL, 22mmol) in CH_2Cl_2 (5 mL) was slowly added and the resulting solution was stirred at r.t. for 18 h. The solution was then diluted with CH_2Cl_2 (50 mL) and washed with 1 M HCl (3 x 100 mL) and brine (3 x 100 mL). The organic layer was dried over sodium sulfate and evaporated to dryness under vacuum. The resulting solid was recrystalised from hot toluene to yield L^9 as a white powder (1.87 g, 51 %).

^{1}H NMR (500 MHz, $CDCl_3$): δ = 2.70–3.29 (br. m, 6H; NCH_3), 3.35–4.03 (br. m, 4H; CH_2), 7.10–7.36 ppm (m, 8H; ArH); ^{13}C{^{1}H} NMR (126 MHz, $CDCl_3$): δ = 37.9, 44.7, 128.3, 128.7, 135.4, 135.6, 171.0 ppm.

7.6.10 N,N′-(Ethane-1,2-diyl)bis(4-methoxy-N-methylbenzamide), L^{10}

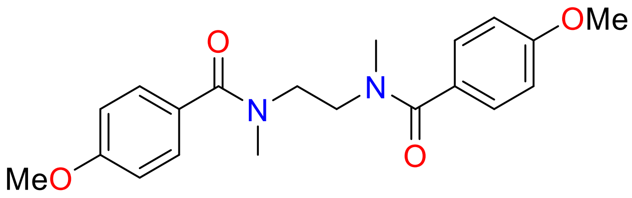

Diamide L^{10} was prepared according to a procedure adapted from the literature.[202] Under argon, N,N′-dimethylethylenediamine (1.08 mL, 10 mmol) was dissolved in CH_2Cl_2 (15 mL) and 1 M sodium hydroxide solution added (20 mL). A solution of 4-methoxybenzoyl chloride (2.98 mL, 22mmol) in CH_2Cl_2 (5 mL) was slowly added and the resulting solution was stirred at r.t. for 18 h. The solution was then diluted with CH_2Cl_2 (50 mL) and washed with 1 M HCl (3 x 100 mL) and brine (3 x 100 mL). The organic layer was dried over sodium sulfate and evaporated to dryness under vacuum. The resulting solid was recrystalised from hot toluene to yield L[10] as a white powder (1.74 g, 48%).

^{1}H NMR (500 MHz, $CDCl_3$): δ = 2.75–3.04 (br. m, 6H; NCH_3), 3.39–3.80 (br. m, 10H; NCH_2, OCH_3), 6.79 (d, ^{3}J = 6.3 Hz, 4H; ArH), 7.28–7.38 ppm (m, 4H; ArH); $^{13}C\{^{1}H\}$ NMR (126 MHz, $CDCl_3$): δ = 37.8, 44.3, 55.1, 113.3, 128.6, 128.2, 160.3, 171.6 ppm. The NMR spectra agreed with previous reports in the literature.

7.6.11 N,N'-(ethane-1,2-diyl)dibenzamide, L[11]

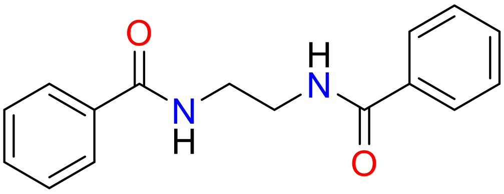

Diamide L[11] was prepared according to a procedure adapted from the literature.[203] Under argon, ethylenediamine (1.34 mL, 20 mmol) was dissolved in CH_2Cl_2 (15 mL) and treated with NEt_3 (7 mL). A solution of benzoyl chloride (5.81 mL, 50 mmol) in CH_2Cl_2 (5 mL) was slowly added and the resulting solution was stirred at r.t. for 18 h. A white suspension formed which was then filtered and the solids washed with CH_2Cl_2 (3 x 50 mL), 1 M HCl (3 x 50 mL), methanol (50 mL) and pentane (50 mL). The resulting solids were dried under vacuum to yield L[11] as a white powder (3.91 g, 73%).

^{1}H NMR (400 MHz, DMSO-d_6) δ = 3.18 (m, 4H; NCH_2), 7.40 – 7.55 (m, 6H; ArH), 7.82 – 7.88 (m, 4H; ArH), 8.62 (br. s, 2H; NH). $^{13}C\{^{1}H\}$ NMR (100 MHz, DMSO-d_6): δ = 49.1, 127.7, 128.7, 131.6, 135.0, 167.0 ppm. The NMR spectra agreed with previous reports in the literature.

7.6.12 N,N'-(propane-1,3-diyl)dibenzamide, L[12]

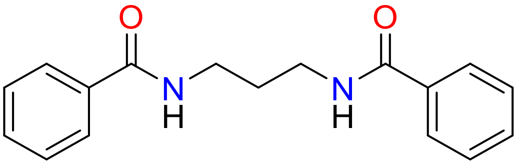

Diamide L[12] was prepared according to a procedure adapted from the literature.[203] Under argon, 1,3-diaminopropane (1.67 mL, 20 mmol) was dissolved in CH_2Cl_2 (15 mL) and treated with NEt_3 (7 mL). A solution of benzoyl chloride (5.81 mL, 50 mmol) in CH_2Cl_2 (5 mL) was slowly added and the resulting solution was stirred at r.t. for 18 h. A white suspension formed which was then filtered and the solids washed with CH_2Cl_2 (3 x 50 mL), 1 M HCl (3 x 50 mL), methanol (50 mL) and pentane (50 mL). The resulting solids were dried under vacuum to yield L[12] as a white powder (3.67 g, 65%).

^{1}H NMR (500 MHz, DMSO-d_6) δ = 1.79 (m, 2H; CH_2), 3.33 (m, 4H; NCH_2), 7.40 – 7.58 (m, 6H; ArH), 7.82 – 7.88 (m, 4H; ArH), 8.53 (br. t, 2H; NH). ^{13}C{^{1}H} NMR (126 MHz, DMSO-d_6): δ = 29.3, 37.0, 127.9, 128.7, 131.0, 135.0, 166.7 ppm. The NMR spectra agreed with previous reports in the literature.

7.6.13 N,N'-(butane-1,4-diyl)dibenzamide, L[13]

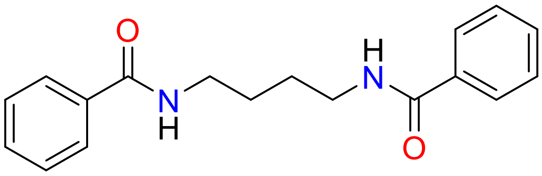

Diamide L[13] was prepared according to a procedure adapted from the literature.[203] Under argon, 1,4-diaminobutane (1.76 g, 20 mmol) was dissolved in CH_2Cl_2 (15 mL) and treated with NEt_3 (7 mL). A solution of benzoyl chloride (5.81 mL, 50 mmol) in CH_2Cl_2 (5 mL) was slowly added and the resulting solution was stirred at r.t. for 18 h. A white suspension formed which was then filtered and the solids washed with CH_2Cl_2 (3 x 50 mL), 1 M HCl (3 x 50 mL), methanol (50 mL) and pentane (50 mL). The resulting solids were dried under vacuum to yield L[13] as a white powder (2.37 g, 40%).

^{1}H NMR (500 MHz, $CDCl_3$) δ = 1.76 (m, 4H; CH_2) 3.56 (m, 4H; NCH_2), 6.52 (br. s, 2H; NH), 7.43 – 7.47 (m, 4H; ArH) 7.50 – 7.54 (m, 2H; ArH), 7.80 – 7.84 (m, 4H; ArH). ^{13}C{^{1}H} NMR (126 MHz, $CDCl_3$): δ = 27.0, 39.6, 126.9, 128.5, 131.4, 134.5, 167.7 ppm. The NMR spectra agreed with previous reports in the literature.

7.6.14 N,N'-(hexane-1,6-diyl)dibenzamide, L[14]

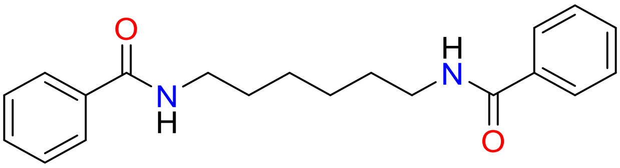

Diamide L[14] was prepared according to a procedure adapted from the literature.[203] Under argon, 1,6-diaminohexane (2.32 g, 20 mmol) was dissolved in CH_2Cl_2 (15 mL) and treated with NEt_3 (7 mL). A solution of benzoyl chloride (5.81 mL, 50 mmol) in CH_2Cl_2 (5 mL) was slowly added and the resulting solution was stirred at r.t. for 18 h. A white suspension formed which was then filtered and the solids washed with CH_2Cl_2 (3 x 50 mL), 1 M HCl (3 x 50 mL), methanol (50 mL) and pentane (50 mL). The resulting solids were dried under vacuum to yield L[14] as a white powder (4.15 g, 64%).

^{1}H NMR (400 MHz, DMSO-d$_6$) δ = 1.35 (m, 4H; CH_2), 1.54 (m, 4H; CH_2), 3.26 (m, 4H; CH_2), 7.40 – 7.55 (m, 6H; ArH), 7.80 – 7.86 (m, 4H; ArH), 8.43 (t, J = 5.6 Hz, 2H; NH). ^{13}C{^{1}H} NMR (100 MHz, DMSO-d$_6$): δ = 26.7, 29.6, 127.6, 128.7, 131.4, 135.2, 166.5 ppm. The NMR spectra agreed with previous reports in the literature.

7.6.15 N,N'-(1,3-phenylene)dibenzamide, L[15]

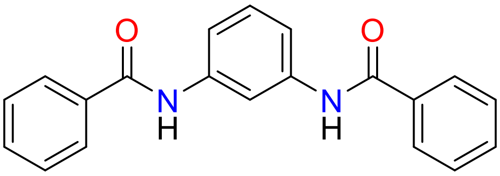

Diamide L[15] was prepared according to a procedure adapted from the literature.[204] Under argon, 1,3-phenylenediamine (2.16 g, 20 mmol) was dissolved in CH_2Cl_2 (15 mL) and treated with NEt_3 (7 mL). A solution of benzoyl chloride (5.81 mL, 50 mmol) in CH_2Cl_2 (5 mL) was slowly added and the resulting solution was stirred at r.t. for 18 h. A white suspension formed which was then filtered and the solids washed with CH_2Cl_2 (3 x 50 mL), 1 M HCl (3 x 50 mL), methanol (50 mL) and pentane (50 mL). The resulting solids were dried under vacuum to yield L[15] as a white powder (3.67 g, 58 %).

^{1}H NMR (400 MHz, DMSO-d$_6$) δ = 7.32 (m, 1H; ArH), 7.44-7.65 (m, 8H; ArH), 7.93-8.03 (m, 4H; ArH), 8.34 (m, 1H; ArH), 10.31 (s, 2H; NH). ^{13}C{^{1}H} NMR (100 MHz, DMSO-d$_6$): δ = 113.4, 116.5, 127.2, 128.2, 129.0, 132.0, 135.4, 139.8, 166.0 ppm. The NMR spectra agreed with previous reports in the literature.

7.6.16 N,N'-(1,4-phenylene)dibenzamide, L^{16}

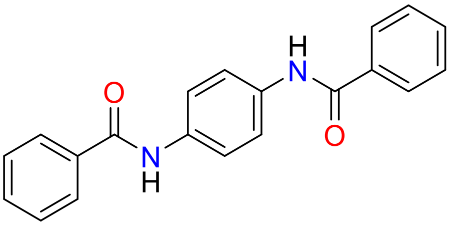

Diamide L^{16} was prepared according to a procedure adapted from the literature.[205] Under argon, 1,4-phenylenediamine (2.16 g, 20 mmol) was dissolved in CH_2Cl_2 (15 mL) and treated with NEt_3 (7 mL). A solution of benzoyl chloride (5.81 mL, 50 mmol) in CH_2Cl_2 (5 mL) was slowly added and the resulting solution was stirred at r.t. for 18 h. A white suspension formed which was then filtered and the solids washed with CH_2Cl_2 (3 x 50 mL), 1 M HCl (3 x 50 mL), methanol (50 mL) and pentane (50 mL). The resulting solids were dried under vacuum to yield L^{16} as a white powder (3.23 g, 51 %).

^{1}H NMR (400 MHz, DMSO-d$_6$) δ = 7.48-7.63 (m, 6H;ArH), 7.76 (s, 4H; ArH), 7.92-8.03 (m, 4H; ArH), 10.24 (s, 2H; NH). ^{13}C{^{1}H} NMR (100 MHz, DMSO-d$_6$): δ = 121.1, 128.1, 128.8, 131.9, 135.5, 165.7 ppm. The NMR spectra agreed with previous reports in the literature.

7.6.17 N,N'-(1,2-phenylene)dibenzamide, L^{17}

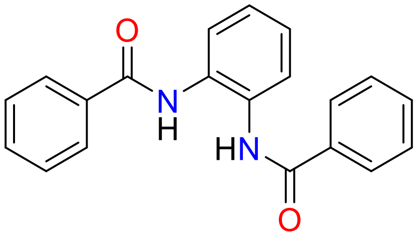

Under argon, 1,2-phenylenediamine (2.16 g, 20 mmol) was dissolved in CH_2Cl_2 (15 mL) and treated with NEt_3 (7 mL). A solution of benzoyl chloride (5.81 mL, 50 mmol) in CH_2Cl_2

(5 mL) was slowly added and the resulting solution was stirred at r.t. for 18 h. A white suspension formed which was then filtered and the solids washed with CH_2Cl_2 (3 x 50 mL), 1 M HCl (3 x 50 mL), methanol (50 mL) and pentane (50 mL). The resulting solids were dried under vacuum to yield L^{16} as a white powder (2.09 g, 33 %).

^{1}H NMR (500 MHz, DMSO-d_6,) δ = 7.32 (m, 2H; ArH), 7.48 – 7.71 (m, 8H; ArH), 7.96 (m, 4H; ArH), 10.21 (s, 2H; NH). ^{13}C{^{1}H} NMR (100 MHz, DMSO-d_6): δ = 126.0, 126.4, 127.9, 129.0, 131.8, 132.3, 134.6, 165.9 ppm.

7.6.18 N,N'-(1,3-phenylene)bis(N-methylbenzamide), L^{18}

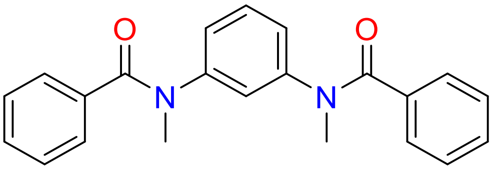

Solid diamide L^{15} (1.58 g, 5 mmol) and neat iodomethane (1.25 mL, 20 mmol) were added to a flask containing a stirred suspension of potassium hydroxide (1.12 g, 20 mmol) and dimethylformamide (DMF, 20 mL) and stirred. The mixture was stirred overnight and quenched with water (40 mL). CH_2Cl_2 (100 mL) was added and washed in succession with dilute HCl (100 mL), water (100 mL) and brine (100 mL). The organic layer was dried over sodium sulfate and evaporated to dryness under vacuum to give the product as a white solid (0.99 g, 58 %).

^{1}H NMR (500 MHz, $CDCl_3$) δ = 3.36 (s, 6H; NCH_3), 6.75-6.82 (m, 3H; ArH), 7.05 (t, J = 7.9 Hz, 1H; ArH), 7.17-7.25 (m, 8H; ArH), 7.28-7.34 (m, 2H; ArH). ^{13}C{^{1}H} NMR (126 MHz, $CDCl_3$): δ = 38.1, 124.7, 125.1, 127.9, 128.7, 129.6, 129.8, 135.7, 145.7, 170.5 ppm.

7.6.19 N,N'-(1,4-phenylene)bis(N-methylbenzamide), L[19]

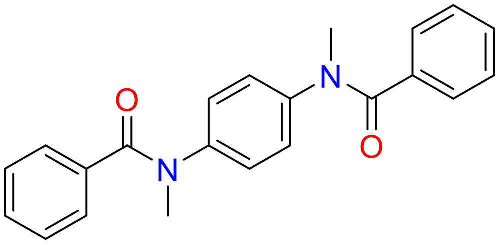

Solid diamide L[16] (1.58 g, 5 mmol) and neat iodomethane (1.25 mL, 20 mmol) were added to a flask containing a stirred suspension of potassium hydroxide (1.12 g, 20 mmol) and dimethylformamide (DMF, 20 mL) and stirred. The mixture was stirred overnight and quenched with water (40 mL). CH_2Cl_2 (100 mL) was added and washed in succession with dilute HCl (100 mL), water (100 mL) and brine (100 mL). The organic layer was dried over sodium sulfate and evaporated to dryness under vacuum to give the product as a white solid (0.99 g, 58 %).

^{1}H NMR (500 MHz, $CDCl_3$) δ = 3.45 (s, 6H; NCH_3), 6.91 (s, 4H; ArH), 7.14-7.22 (m, 4H; ArH), 7.23-7.26 (m, 4H; ArH), 7.27-7.32 (m, 2H; ArH). ^{13}C{^{1}H} NMR (126 MHz, $CDCl_3$): δ = 38.3, 127.4, 127.8, 128.7, 129.8, 135.6, 143.0, 170.5 ppm.

7.6.20 N,N'-dimethyl-N,N'-diphenylsuccinamide, L[21]

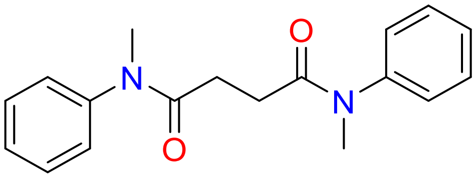

Diamide L[16] was prepared according to a procedure adapted from the literature.[206] Under argon, N-methylaniline (1.19 ml, 11 mmol) was dissolved in CH_2Cl_2 (15 mL) and 1 M sodium hydroxide solution added (20 mL). A solution of succinyl chloride (0.55 mL, 5 mmol) in CH_2Cl_2 (5 mL) was added slowly and the resulting solution was stirred at r.t. for 18 h. The solution was then diluted with CH_2Cl_2 (50 mL) and washed with 1 M HCl (3 x 100 mL) and brine (3 x 100 mL). The organic layer was dried over sodium sulfate and evaporated to dryness under vacuum. The resulting brown solid was thoroughly rinsed with cold acetone then dried under vacuum to yield L[21] as a white powder (0.47 g, 32%).

^{1}H NMR (500 MHz, $CDCl_3$) δ = 2.35 (s, 4H; NCH_2), 3.26 (s, 6H; CH_3), 7.27 (m, 6H; ArH), 7.34 (m, 2H; ArH), 7.43 (m, 4H; ArH). $^{13}C\{^1H\}$ NMR (126 MHz, $CDCl_3$): δ = 29.6, 37.3, 127.5, 127.7, 129.8, 144.7, 172.0 ppm. The NMR spectra agreed with previous reports in the literature.

7.6.21 N,N′-(Ethane-1,2-diyl)bis(N-methylcyclohexanamide), L[22]

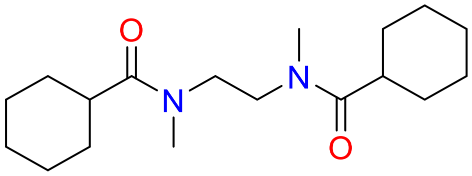

Diamide L[22] was prepared according to a procedure adapted from the literature.[202] Under argon, N,N′-dimethylethylenediamine (1.08 mL, 10 mmol) was dissolved in CH_2Cl_2 (15 mL) and 1 M sodium hydroxide solution added (20 mL). A solution of cyclohexanecarbonyl chloride (2.94 mL, 22mmol) in CH_2Cl_2 (5 mL) was slowly added and the resulting solution was stirred at r.t. for 18 h. The solution was then diluted with CH_2Cl_2 (50 mL) and washed with 1 M HCl (3 x 100 mL) and brine (3 x 100 mL). The organic layer was dried over sodium sulfate and evaporated to dryness under vacuum. The resulting solid was recrystalised from diethyl ether to yield L[22] as a white powder (1.77 g, 57%).

^{1}H NMR (500 MHz, $CDCl_3$): δ = 1.30 (m, 6H; cy-CH_2), 1.40-1.58 (m, 4H; cy-CH_2), 1.66 -1.90 (m, 10H; cy-CH_2) 2.45 (m, 2H; cy-CH) 2.90 - 3.13 (m, 6H; NCH_3), 3.45 – 3.58 ppm (m, 4H; CH_2); $^{13}C\{^1H\}$ NMR (126 MHz, $CDCl_3$): δ = 25.7, 25.8, 29.2, 35.5, 40.8, 44.6, 176.4 ppm. The NMR spectra agreed with previous reports in the literature.

7.6.22 Methyltrioctylammonium iodide, [MTOA][I]

Following a literature procedure,[207] iodomethane (4.44 g, 31 mmol) was added dropwise to a stirred solution of trioctylamine (8.85 g, 25 mmol) in THF (100 mL), and the mixture was stirred at 35 °C for 18 h under a flow of N_2. The crude mixture was concentrated under vacuum to yield a viscous light-orange oil (99%) which was diluted with toluene to form a 1.0 M stock solution.

^{1}H NMR (500 MHz, $CDCl_3$): δ = 0.89 (t, J = 6.8 Hz, 9H, CH_2CH_3), 1.43–1.23 (m, 30H, CH_2), 1.74–1.64 (m, 6H, CH_2), 3.24 (s, 3H, NCH_3), 3.41–3.35 (m, 6H, NCH_2); $^{13}C\{^1H\}$ NMR (126 MHz, $CDCl_3$): δ = 14.04, 22.43, 22.57, 26.30, 29.01, 29.10, 31.62, 48.83, 61.70. The NMR spectra agreed with previous reports in the literature.

References

1 EuChemS, Element Scarcity – EuChemS Periodic Table, https://www.euchems.eu/euchems-periodic-table/, (accessed 4 February 2022).

2 C. P. Baldé, F. Wang, R. Kuehr and J. Huisman, *The Global E-waste Monitor 2014*, 2015.

3 V. Forti, C. P. Baldé, R. Kuehr and Bel G., *The Global E-waste Monitor 2020*, 2020.

4 F. K. Crundwell, M. S. Moats, V. Ramachandran, T. G. Robinson and W. G. Davenport, in *Extractive Metallurgy of Nickel, Cobalt and Platinum Group Metals*, Elsevier, 2011, pp. 537–549.

5 C. Hagelüken and C. W. Corti, *Gold Bull.*, 2010, **43**, 209–220.

6 M. D. Rao, K. K. Singh, C. A. Morrison and J. B. Love, *RSC Adv.*, 2020, **10**, 4300–4309.

7 C. P. Baldé, V. Forti, V. Gray, R. Kuehr and P. Stegmann, *The Global E-waste Monitor 2017*, 2017.

8 X. Zeng, J. A. Mathews and J. Li, *Environ. Sci. Technol.*, 2018, **52**, 4835–4841.

9 S. Syed, *Hydrometallurgy*, 2012, **115–116**, 30–51.

10 R. M. Izatt, S. R. Izatt, R. L. Bruening, N. E. Izatt and B. A. Moyer, *Chem. Soc. Rev*, 2014, **43**, 2451.

11 F. Habashi, *A Textbook of Hydrometallurgy*, Quebec, 1994, vol. 7.

12 J. Rydberg, C. Musikas and G. Choppin, *Principles and Practices of Solvent Extraction*, Marcel Dekker, New York, USA, 1992.

13 F. Habashi, *Hydrometallurgy*, 2005, **79**, 15–22.

14 A. M. Wilson, P. J. Bailey, P. A. Tasker, J. R. Turkington, R. A. Grant and J. B. Love, *Chem. Soc. Rev.*, 2014, **43**, 123–134.

15 I. V Kolesnichenko and E. V Anslyn, *Chem. Soc. Rev.*, 2017, **46**, 2385–2390.

16 J. W. Steed and J. L. Atwood, *Supramolecular Chemistry*, John Wiley & Sons, Ltd, Chichester, UK, 2009.

17 J. R. Turkington, P. J. Bailey, J. B. Love, A. M. Wilson and P. A. Tasker, *Chem. Commun.*, 2013, **49**, 1891–1899.

18 P. A. Tasker and E. D. Doidge, in *Comprehensive Coordination Chemistry III*, Elsevier, 2021, pp. 494–557.

19 R. S. Forgan, P. A. Wood, J. Campbell, D. K. Henderson, F. E. McAllister, S. Parsons, E. Pidcock, R. M. Swart and P. A. Tasker, *Chem. Commun.*, 2007, 4940.

20 B. D. Roach, T. Lin, H. Bauer, R. S. Forgan, S. Parsons, D. M. Rogers, F. J. White and P. A. Tasker, *Aust. J. Chem.*, 2017, **70**, 556.

21 M. R. Healy, J. W. Roebuck, E. D. Doidge, L. C. Emeleus, P. J. Bailey, J. Campbell, A. J. Fischmann, J. B. Love, C. A. Morrison, T. Sassi, D. J. White and P. A. Tasker, *Dalt. Trans.*, 2016, **45**, 3055–3062.

22 H. Irving and R. J. P. Williams, *J. Chem. Soc.*, 1953, 3192.

23 D. S. Flett, *J. Organomet. Chem.*, 2005, **690**, 2426–2438.

24 P. R. Danesi, L. Reichley-Yinger, G. Mason, L. Kaplan, E. P. Horwltz and H. Diamond, *Solvent Extr. Ion Exch.*, 1985, **3**, 435–452.

25 M. D. Rao, K. K. Singh, C. A. Morrison and J. B. Love, *Sep. Purif. Technol.*, 2021, **263**, 118400.

26 Y. J. Park and D. J. Fray, *J. Hazard. Mater.*, 2009, **163**, 259–265.

27 M. M. J. Correa, F. P. C. Silvas, P. Aliprandini, V. T. de Moraes, D. Dreisinger and D. C. R. Espinosa, *Brazilian J. Chem. Eng.*, 2018, **35**, 919–930.

28 A. P. Paiva and P. Malik, *J. Radioanal. Nucl. Chem. 2004 2612*, 2004, **261**, 485–496.

29 J. Veliscek-Carolan, *J. Hazard. Mater.*, 2016, **318**, 266–281.

30 J. H. Burns, G. M. Brown and R. R. Ryan, *Acta Crystallogr. Sect. C Cryst. Struct. Commun.*, 1985, **41**, 1446–1448.

31 K. J. MacRuary, R. J. Gordon, R. A. Grant, S. Woollam, R. J. Ellis, P. A. Tasker, J. B. Love and C. A. Morrison, *Solvent Extr. Ion Exch.*, 2017, **35**, 531–548.

32 R. J. Ellis, Y. Meridiano, J. Muller, L. Berthon, P. Guilbaud, N. Zorz, M. R. Antonio, T. Demars and T. Zemb, *Chem. - A Eur. J.*, 2014, **20**, 12796–12807.

33 B. Qiao, T. Demars, M. Olvera de la Cruz and R. J. Ellis, *J. Phys. Chem. Lett.*, 2014, **5**, 1440–1444.

34 R. J. Ellis, Y. Meridiano, R. Chiarizia, L. Berthon, J. Muller, L. Couston and M. R. Antonio, *Chem. - A Eur. J.*, 2013, **19**, 2663–2675.

35 Z. Liu, M. Frasconi, J. Lei, Z. J. Brown, Z. Zhu, D. Cao, J. Iehl, G. Liu, A. C. Fahrenbach, Y. Y. Botros, O. K. Farha, J. T. Hupp, C. A. Mirkin and J. F. Stoddart, *Nat. Commun.*, 2013, **4**, 1855–1859.

36 Z. Liu, A. Samanta, J. Lei, J. Sun, Y. Wang and J. F. Stoddart, *J. Am. Chem. Soc.*, 2016, **138**, 11643–11653.

37 United States Patent and Trademark Office, US20140311297, 2014.

38 Cycladex, http://cycladex.com/home/value-proposition/, (accessed 29 January 2022).

39 E. Benguerel, G. P. Demopoulos and G. B. Harris, *Hydrometallurgy*, 1996, **40**, 135–152.

40 E. D. Doidge, I. Carson, P. A. Tasker, R. J. Ellis, C. A. Morrison and J. B. Love, *Angew. Chemie - Int. Ed.*, 2016, **55**, 12436–12439.

41 H. Narita, M. Tanaka, K. Morisaku and T. Abe, *Hydrometallurgy*, 2006, **81**, 153–158.

42 Y. Ueda, S. Morisada, H. Kawakita and K. Ohto, *Sep. 2021, Vol. 8, Page 139*, 2021, **8**, 139.

43 F. J. Alguacil and C. Caravaca, *Hydrometallurgy*, 1993, **34**, 91–98.

44 M. K. Jha, D. Gupta, J. Lee, V. Kumar and J. Jeong, *Hydrometallurgy*, 2014, **142**, 60–69.

45 I. Carson, K. J. MacRuary, E. D. Doidge, R. J. Ellis, R. A. Grant, R. J. Gordon, J. B. Love, C. A. Morrison, G. S. Nichol, P. A. Tasker and A. M. Wilson, *Inorg. Chem.*, 2015, **54**, 8685–8692.

46 K. J. Bell, A. N. Westra, R. J. Warr, J. Chartres, R. Ellis, C. C. Tong, A. J. Blake, P. A. Tasker and M. Schröder, *Angew. Chemie Int. Ed.*, 2008, **47**, 1745–1748.

47 R. J. Warr, K. J. Bell, A. Gadzhieva, R. Cabot, R. J. Ellis, J. Chartres, D. K. Henderson, E. Lykourina, A. M. Wilson, J. B. Love, P. A. Tasker and M. Schröder, *Inorg. Chem.*, 2016, **55**, 6247–6260.

48 Y. Tong, L. Han and Y. Yang, *Ind. Eng. Chem. Res.*, 2012, **51**, 16438–16443.

49 H. Narita, M. Tanaka, K. Morisaku and T. Abe, *Hydrometallurgy*, 2006, **81**, 153–158.

50 E. A. Mowafy and D. Mohamed, *Sep. Purif. Technol.*, 2016, **167**, 146–153.

51 C. Erlinger, L. Belloni, T. Zemb and C. Madic, *Langmuir*, 1999, **15**, 2290–2300.

52 T. G. Srinivasan and P. R. Vasudeva Rao, *Sep. Sci. Technol.*, 2014, **49**, 2315–2329.

53 R. J. Warr, A. N. Westra, K. J. Bell, J. Chartres, R. Ellis, C. Tong, T. G. Simmance, A. Gadzhieva, A. J. Blake, P. A. Tasker and M. Schröder, *Chem. - A Eur. J.*, 2009, **15**, 4836–4850.

54 F. Hofmeister, *Arch. für Exp. Pathol. und Pharmakologie*, 1888, **24**, 247–260.

55 H. Taube, *Chem. Rev.*, 1952, **50**, 69–126.

56 S. F. Lincoln, *Helv. Chim. Acta*, 2005, **88**, 523–545.

57 M. Adams, Ed., *Gold Ore Processing*, Elsevier, Singapore, 2nd Editio., 2016.

58 S. R. La Brooy, H. G. Linge and G. S. Walker, *Miner. Eng.*, 1994, **7**, 1213–1241.

59 B. Yarar, in *Ninth International Conference on Tailings and Mine Waste*, A A Balkema,

Fort Collins, Colorado, 2002, pp. 197–204.

60 M. D. Adams, G. J. McDougall and R. D. Hancock, *Hydrometallurgy*, 1987, **18**, 139–154.

61 S. Ubaldini, R. Massidda, F. Vegliò and F. Beolchini, *Hydrometallurgy*, 2006, **81**, 40–44.

62 M. Soleimani and T. Kaghazchi, *J. Chinese Inst. Chem. Eng.*, 2008, **39**, 9–11.

63 K. Bunney, M. I. Jeffrey, R. Pleysier and P. L. Breuer, *Mining, Metall. Explor. 2010 274*, 2010, **27**, 205–211.

64 W. Liu, L. O. Jones, H. Wu, C. L. Stern, R. A. Sponenburg, G. C. Schatz and J. F. Stoddart, *J. Am. Chem. Soc.*, 2021, **143**, 1984–1992.

65 G. Hilson and A. J. Monhemius, *J. Clean. Prod.*, 2006, **14**, 1158–1167.

66 V. M. Luque-Almagro, C. Moreno-Vivián and M. D. Roldán, *Curr. Opin. Biotechnol.*, 2016, **38**, 9–13.

67 C. Abbruzzese, P. Fornari, R. Massidda, F. Vegliò and S. Ubaldini, *Hydrometallurgy*, 1995, **39**, 265–276.

68 A. C. Grosse, G. W. Dicinoski, M. J. Shaw and P. R. Haddad, *Hydrometallurgy*, 2003, **69**, 1–21.

69 J. Zhang, S. Shen, Y. Cheng, H. Lan, X. Hu and F. Wang, *Hydrometallurgy*, 2014, **144–145**, 114–123.

70 M. Gökelma, A. Birich, S. Stopic, B. Friedrich, M. Gökelma, A. Birich, S. Stopic and B. Friedrich, *J. Mater. Sci. Chem. Eng.*, 2016, **4**, 8–17.

71 L. Wade, *Science*, 2013, **341**, 1448–1449.

72 United Nations Environment Programme, *Minamata Convention on Mercury*, United Nations, 2013.

73 X. Li and K. Binnemans, *Chem. Rev*, 2021, **121**, 4530.

74 E. Heliövaara, H. Liljeqvist, M. Muuronen, A. Eronen, K. Moslova and T. Repo, *Chem. – A Eur. J.*, 2021, **27**, 8668–8672.

75 C. Yue, H. Sun, W. J. Liu, B. Guan, X. Deng, X. Zhang and P. Yang, *Angew. Chemie - Int. Ed.*, 2017, **56**, 9331–9335.

76 M. Räisänen, E. Heliövaara, F. Al-Qaisi, M. Muuronen, A. Eronen, H. Liljeqvist, M. Nieger, M. Kemell, K. Moslova, J. Hämäläinen, K. Lagerblom and T. Repo, *Angew. Chemie Int. Ed.*, 2018, **57**, 17104–17109.

77 A. Serpe, L. Marchiò, F. Artizzu, M. L. Mercuri and P. Deplano, *Chem. – A Eur. J.*, 2013,

19, 10111–10114.

78 World Intellectual Property Organisation, WO2016168930A1, 2016.

79 T. G. Crundwell, F. K., Moats, M. S., Ramachandran, V., Robinson, T. G., Davenport, *Extractive Metallurgy of Nickel, Cobalt and Platinum Group Metals*, Elsevier Ltd, 2011.

80 R. A. Grant and V. A. Drake, in *Proceediings of the International Solvent Extraction Conference*, 2002, pp. 940–945.

81 W. D. Xing, M. S. Lee and Y. H. Kim, *J. Ind. Eng. Chem.*, 2018, **59**, 328–334.

82 M. A. Barroso, F. A. López, A. Sastre and F. J. Alguacil, *Hydrometallurgy*, 1997, **45**, 199–209.

83 T. H. Nguyen, L. Wang and M. S. Lee, *Korean J. Met. Mater.*, 2017, **55**, 247–255.

84 W. D. Xing, M. S. Lee and G. Senanayake, *Hydrometallurgy*, 2018, **180**, 58–64.

85 F. J. Alguacil, *Solvent Extr. Ion Exch.*, 2003, **21**, 841–852.

86 S. Martínez, A. M. Sastre and F. J. Alguacil, *Hydrometallurgy*, 1999, **52**, 63–70.

87 Y. Xiong, H. Kawakita, J. Inoue, M. Abe, K. Ohto, K. Inoue and H. Harada, *Solvent Extr. Res. Dev. Japan*, 2010, **17**, 151–162.

88 E. D. Doidge, The University of Edinburgh, 2018.

89 W. A. Bizzo, R. A. Figueiredo and V. F. De Andrade, *Materials*, 2014, **7**, 4555–4566.

90 E. D. Doidge, L. M. M. Kinsman, Y. Ji, I. Carson, A. J. Duffy, I. A. Kordas, E. Shao, P. A. Tasker, B. T. Ngwenya, C. A. Morrison and J. B. Love, *ACS Sustain. Chem. Eng.*, 2019, **7**, 15019–15029.

91 E. D. Doidge, L. M. M. Kinsman, Y. Ji, I. Carson, A. J. Duffy, I. A. Kordas, E. Shao, P. A. Tasker, B. T. Ngwenya, C. A. Morrison and J. B. Love, *ACS Sustain. Chem. Eng.*, 2019, **7**, 15019–15029.

92 M. R. Antonio, T. J. Demars, M. Audras and R. J. Ellis, *Sep. Sci. Technol.*, 2018, **53**, 1834–1847.

93 S. Nave, C. Mandin, L. Martinet, L. Berthon, F. Testard, C. Madic and T. Zemb, *Phys. Chem. Chem. Phys.*, 2004, **6**, 799–808.

94 P. K. Verma, P. N. Pathak, P. K. Mohapatra, V. K. Aswal, B. Sadhu and M. Sundararajan, *J. Phys. Chem. B*, 2013, **117**, 9821–9828.

95 M. R. Antonio, R. Chiarizia and F. Jaffrennou, *Sep. Sci. Technol.*, 2010, **45**, 1689–1698.

96 P. Weßling, U. Müllich, E. Guerinoni, A. Geist and P. J. Panak, *Hydrometallurgy*, 2020, **192**, 105248.

97 R. J. Ellis, M. Audras and M. R. Antonio, *Langmuir*, 2012, **28**, 15498–15504.

98 K. R. Swami, K. A. Venkatesan and M. P. Antony, *Solvent Extr. Ion Exch.*, 2019, **37**, 500–517.

99 A. Chandrasekar, N. Sivaraman, T. K. Ghanty and A. Suresh, *Sep. Purif. Technol.*, 2019, **217**, 62–70.

100 C. Berger, E. Moreau, C. Marie, D. Guillaumont, A. Beillard and L. Berthon, *Solvent Extr. Ion Exch.*, 2021, 1–22.

101 S. Tachimori, Y. Sasaki and S. Suzuki, *Solvent Extr. Ion Exch.*, 2002, **20**, 687–699.

102 L. Berthon, A. Paquet, G. Saint-Louis and P. Guilbaud, *Solvent Extr. Ion Exch.*, 2021, **39**, 204–232.

103 P. R. Vasudeva Rao and Z. Kolarik, *Solvent Extr. Ion Exch.*, 1996, **14**, 955–993.

104 R. J. Ellis, J. Chartres, D. K. Henderson, R. Cabot, P. R. Richardson, F. J. White, M. Schröder, J. R. Turkington, P. A. Tasker and K. C. Sole, *Chem. - A Eur. J.*, 2012, **18**, 7715–7728.

105 J. R. Turkington, V. Cocalia, K. Kendall, C. A. Morrison, P. Richardson, T. Sassi, P. A. Tasker, P. J. Bailey and K. C. Sole, *Inorg. Chem.*, 2012, **51**, 12805–12819.

106 M. Cokoja, I. I. E. Markovits, M. H. Anthofer, S. Poplata, A. Pöthig, D. S. Morris, P. A. Tasker, W. A. Herrmann, F. E. Kühn and J. B. Love, *Chem. Commun.*, 2015, **51**, 3399–3402.

107 R. J. Ellis, T. L. Anderson, M. R. Antonio, A. Braatz and M. Nilsson, *J. Phys. Chem. B*, 2013, **117**, 5916–5924.

108 J. M. Perera and G. W. Stevens, *Solvent Extr. Ion Exch.*, 2011, **29**, 363–383.

109 Z. Lu, S. Dourdain and S. Pellet-Rostaing, *Langmuir*, 2020, **36**, 12121–12129.

110 J. J. M. Nelson and E. J. Schelter, *Inorg. Chem.*, 2019, 58, 979–990.

111 J. J. M. Nelson, T. Cheisson, H. J. Rugh, M. R. Gau, P. J. Carroll and E. J. Schelter, *Commun. Chem.*, 2020, **3**, 7.

112 C. C. Shaffer and B. D. Smith, *Org. Chem. Front.*, 2021, **8**, 1294–1301.

113 A. Verma, R. Kore, D. R. Corbin and M. B. Shiflett, *Ind. Eng. Chem. Res.*, 2019, **58**, 15381–15393.

114 A. E. Lewis, *Hydrometallurgy*, 2010, **104**, 222–234.

115 M. Mon, J. Ferrando-Soria, T. Grancha, F. R. Fortea-Pérez, J. Gascon, A. Leyva-Pérez, D. Armentano and E. Pardo, *J. Am. Chem. Soc.*, 2016, **138**, 7864–7867.

116 D. T. Sun, N. Gasilova, S. Yang, E. Oveisi and W. L. Queen, *J. Am. Chem. Soc*, 2018, **140**, 16697–16703.

117 H. L. Qian, F. L. Meng, C. X. Yang and X. P. Yan, *Angew. Chemie - Int. Ed.*, 2020, **59**, 17607–17613.

118 Y. Hong, D. Thirion, S. Subramanian, M. Yoo, H. Choi, H. Y. Kim, J. F. Stoddart and C. T. Yavuz, *Proc. Natl. Acad. Sci.*, 2020, 16174–16180.

119 B. O. Okesola, S. K. Suravaram, A. Parkin and D. K. Smith, *Angew. Chemie Int. Ed.*, 2016, **55**, 183–187.

120 Y. Wu, Q. Fang, X. Yi, G. Liu and R.-W. Li, *Prog. Nat. Sci. Mater. Int.*, 2017, **27**, 514–519.

121 E. Lahtinen, L. Kivijärvi, R. Tatikonda, A. Väisänen, K. Rissanen and M. Haukka, *ACS Omega*, 2017, **2**, 7299–7304.

122 L. X. Chen, M. Liu, Y. Q. Zhang, Q. J. Zhu, J. X. Liu, B. X. Zhu and Z. Tao, *Chem. Commun.*, 2019, **55**, 14271–14274.

123 R.-L. Lin, Y.-P. Dong, M. Tang, Z. Liu, Z. Tao and J.-X. Liu, *Inorg. Chem.*, 2020, **59**, 3850–3855.

124 H. Wu, L. O. Jones, Y. Wang, D. Shen, Z. Liu, L. Zhang, K. Cai, Y. Jiao, C. L. Stern, G. C. Schatz and J. F. Stoddart, *ACS Appl. Mater. Interfaces*, 2020, **12**, 38768–38777.

125 H. Wu, Y. Wang, L. O. Jones, W. Liu, L. Zhang, B. Song, X. Y. Chen, C. L. Stern, G. C. Schatz and J. F. Stoddart, *Angew. Chemie - Int. Ed.*, 2021, **60**, 17587–17594.

126 C.-C. Dong, J.-F. Xiang, L.-J. Xu and H.-Y. Gong, *Tetrahedron Lett.*, 2018, **59**, 264–267.

127 W. Liu, A. G. Oliver and B. D. Smith, *J. Am. Chem. Soc.*, 2018, **140**, 6810–6813.

128 L.-L. Wang, Y.-K. Tu, H. Yao and W. Jiang, *Beilstein J. Org. Chem.*, 2019, **15**, 1460–1467.

129 C. C. Shaffer, W. Liu, A. G. Oliver and B. D. Smith, *Chem. – A Eur. J.*, 2021, **27**, 751–757.

130 A. Nag, M. R. Islam and T. Pradeep, *ACS Sustain. Chem. Eng.*, 2021, **9**, 2129–2135.

131 C. Yang, Q. Tan, L. Liu, Q. Dong and J. Li, *ACS Sustain. Chem. Eng.*, 2017, **5**, 9586–9598.

132 H. Narita, R. Kasuya, T. Suzuki, R. Motokawa and M. Tanaka, in *Encyclopedia of Inorganic and Bioinorganic Chemistry*, Wiley, 2020, pp. 1–28.

133 M. C. Costa, R. Almeida, A. Assunção, A. M. Rosa da Costa, C. Nogueira and A. P. Paiva, *Sep. Purif. Technol.*, 2016, **158**, 409–416.

134 J. L. Leviel, G. Auvert and J. M. Savariault, *Acta Crystallogr. Sect. B Struct. Crystallogr. Cryst. Chem.*, 1981, **37**, 2185–2189.

135 S. Katsuta, Y. Yoshimoto, M. Okai, Y. Takeda and K. Bessho, *Ind. Eng. Chem. Res*, 2011,

50, 12735–12740.

136 European Commission, *Critical raw materials factsheets*, 2017.

137 S. B. Young, *Int. J. Life Cycle Assess.*, 2018, **23**, 1429–1447.

138 A. Agulyansky, in *Chemistry of Tantalum and Niobium Fluoride Compounds*, Elsevier, 2004, pp. 125–134.

139 M. Nete, W. Purcell and J. T. Nel, *JOM*, 2016, **68**, 556–566.

140 Z. Zhu and C. Y. Cheng, *Hydrometallurgy*, 2011, **107**, 1–12.

141 M. J. Kabangu and P. L. Crouse, *Hydrometallurgy*, 2012, **129**–**130**, 151–155.

142 T. H. Nguyen and M. S. Lee, *Miner. Process. Extr. Metall. Rev.*, 2019, **40**, 265–277.

143 B. Debnath, R. Chowdhury and S. K. Ghosh, *Front. Environ. Sci. Eng.*, 2018, **12**, 2.

144 H. Zhou, S. Zheng and Y. Zhang, *Hydrometallurgy*, 2005, **80**, 83–89.

145 P. A. Abramov, A. M. Abramova, E. V. Peresypkina, A. L. Gushchin, S. A. Adonin and M. N. Sokolov, *J. Struct. Chem.*, 2011, **52**, 1012–1017.

146 G. J. P. Deblonde, V. Weigel, Q. Bellier, R. Houdard, F. Delvallée, S. Bélair and D. Beltrami, *Sep. Purif. Technol.*, 2016, **162**, 180–187.

147 G. J.-P. Deblonde, A. Chagnes, S. Bélair and G. Cote, *Hydrometallurgy*, 2015, **156**, 99–106.

148 G. J.-P. Deblonde, D. Bengio, D. Beltrami, S. Bélair, G. Cote and A. Chagnes, *Sep. Purif. Technol.*, 2019, **215**, 634–643.

149 G. J-P Deblonde, A. Chagnes, M.-A. Roux, V. Weigel and G. Cote, *Dalt. Trans.*, 2016, **45**, 19351.

150 R. Turgis, G. Arrachart, S. Michel, S. Legeai, M. Lejeune, M. Draye and S. Pellet-Rostaing, *Sep. Purif. Technol.*, 2018, **196**, 174–182.

151 M. J. Ungerer, D. J. Van Der Westhuizen, G. Lachmann and H. M. Krieg, *Hydrometallurgy*, 2014, **144**–**145**, 195–206.

152 M. J. Ungerer, C. G. C. E. van Sittert, D. J. van der Westhuizen and H. M. Krieg, *Comput. Theor. Chem.*, 2016, **1090**, 112–119.

153 M. J. Ungerer, C. G. C. E. van Sittert, D. J. van der Westhuizen and H. M. Krieg, *J. Phys. Chem. Solids*, 2019, **135**, 109121.

154 K. L. Nash, *Solvent Extr. Ion Exch.*, 1993, **11**, 729–768.

155 H. Metwally, R. G. McAllister and L. Konermann, *Anal. Chem.*, 2015, **87**, 2434–2442.

156 S. Karki, F. Shi, J. J. Archer, H. Sistani and R. J. Levis, *J. Am. Soc. Mass Spectrom.*, 2018,

29, 1002–1011.

157 A. I. Carrick, E. D. Doidge, A. Bouch, G. S. Nichol, J. Patrick, E. R. Schofield, C. A. Morrison and J. B. Love, *Chem. – A Eur. J.*, 2021, **27**, 8714–8722.

158 J. I. Kim, H. Lagally and H. J. Born, *Anal. Chim. Acta*, 1973, **64**, 29–43.

159 R. Caletka, R. Hausbeck and V. Krivan, *J. Radioanal. Nucl. Chem. 1989 1312*, 1989, **131**, 343–352.

160 M. C. Gurau, S.-M. Lim, E. T. Castellana, F. Albertorio, S. Kataoka and P. S. Cremer, *J. Am. Chem. Soc.*, 2004, **126**, 10522–10523.

161 G. Levasseur and A. L. Beauchamp, *Acta Crystallogr. Sect. C Cryst. Struct. Commun.*, 1991, **47**, 547–550.

162 J. Yamada, K. Fujimoto, H. Akutsu, S. Nakatsuji, H. Nishikawa and K. Kikuchi, *Synth. Met.*, 2005, **153**, 373–376.

163 C. Micheau, G. Arrachart, R. Turgis, M. Lejeune, M. Draye, S. Michel, S. Legeai and S. Pellet-Rostaing, *ACS Sustain. Chem. Eng.*, 2020, **8**, 1954–1963.

164 O. L. Keller and A. Chetham-Strode, *Inorg. Chem.*, 1966, **5**, 367–372.

165 S. A. Wood and I. M. Samson, *Ore Geol. Rev.*, 2006, **28**, 57–102.

166 W. Liu, B. Etschmann, J. Brugger, L. Spiccia, G. Foran and B. McInnes, *Chem. Geol.*, 2006, **231**, 326–349.

167 F. Lu, T. Xiao, J. Lin, Z. Ning, Q. Long, L. Xiao, F. Huang, W. Wang, Q. Xiao, X. Lan and H. Chen, *Hydrometallurgy*, 2017, **174**, 105–115.

168 Z. Sun, H. Cao, Y. Xiao, J. Sietsma, W. Jin, H. Agterhuis and Y. Yang, *ACS Sustain. Chem. Eng.*, 2017, 5, 21–40.

169 Z. Zhao, Y. Yang, Y. Xiao and Y. Fan, *Hydrometallurgy*, 2012, **125**–**126**, 115–124.

170 I. Mihaylov and P. A. Distin, *Hydrometallurgy*, 1992, **28**, 13–27.

171 J. J. M. Nelson and E. J. Schelter, *Inorg. Chem.*, 2019, **58**, 979–990.

172 K. Y. Macías-Macías, A. E. Ceniceros-Gómez, M. E. Gutiérrez-Ruiz, J. L. González-Chávez and L. G. Martínez-Jardines, *J. Environ. Chem. Eng.*, 2019, **7**, 102964.

173 Z. Li and K. Binnemans, *Ind. Eng. Chem. Res.*, 2021, **60**, 8538–8547.

174 W. Vereycken, S. Riaño, T. Van Gerven and K. Binnemans, *ACS Sustain. Chem. Eng.*, 2020, **8**, 8223–8234.

175 P. Wasserscheid and W. Keim, *Angew. Chemie*, 2000, **39**, 3772–3789.

176 J. Hunter, S. Dolezalova, B. Ngwenya, C. Morrison and J. Love, *Metals*, 2018, **8**, 465.

177 X. Han and D. W. Armstrong, *Acc. Chem. Res.*, 2007, **40**, 1079–1086.

178 A. E. Visser, R. P. Swatloski, W. M. Reichert, S. T. Griffin and R. D. Rogers, *Ind. Eng. Chem. Res.*, 2000, **39**, 3596–3604.

179 A. Van den Bossche, W. Vereycken, T. Vander Hoogerstraete, W. Dehaen and K. Binnemans, *ACS Sustain. Chem. Eng.*, 2019, **7**, 14451–14459.

180 X. Li, A. Van den Bossche, T. Vander Hoogerstraete and K. Binnemans, *Chem. Commun.*, 2018, **54**, 475–478.

181 S. Katsuta, Y. Yoshimoto, M. Okai, Y. Takeda and K. Bessho, *Ind. Eng. Chem. Res*, 2011, **50**, 12735–12740.

182 A. P. De Los Ríos, F. J. Hernández-Fernández, L. J. Lozano, S. Sánchez, J. I. Moreno and C. Godínez, *J. Chem. Eng. Data*, 2010, **55**, 605–608.

183 S. Nayak and N. Devi, *Hydrometallurgy*, 2017, **171**, 191–197.

184 Z. Černy, J. Macháček, J. Fusek, O. Křiž, B. Čásensky and D. G. Tuck, *J. Organomet. Chem.*, 1993, **456**, 25–30.

185 A. D. Awtrey and R. E. Connick, *J. Am. Chem. Soc.*, 1951, **73**, 1842–1843.

186 G. A. Gamlen and D. O. Jordan, *J. Chem. Soc.*, 1953, 1435–1443.

187 I. Persson, *J. Solution Chem.*, 2018, **47**, 797–805.

188 C. A. Heinrich and T. M. Seward, *Geochim. Cosmochim. Acta*, 1990, **54**, 2207–2221.

189 R. Zhao and P. Pan, *Can. J. Chem.*, 2001, **79**, 131–144.

190 S. J. Clark, M. D. Segall, C. J. Pickard, P. J. Hasnip, M. I. J. Probert, K. Refson and M. C. Payne, *Zeitschrift für Krist. - Cryst. Mater.*, 2005, **220**, 567–570.

191 E. R. McNellis, J. Meyer and K. Reuter, *Phys. Rev. B*, 2009, **80**, 205414.

192 J. P. Perdew, K. Burke and M. Ernzerhof, *Phys. Rev. Lett.*, 1996, **77**, 3865–3868.

193 A. Tkatchenko and M. Scheffler, *Phys. Rev. Lett.*, 2009, **102**, 073005.

194 J. Contreras-García, E. R. Johnson, S. Keinan, R. Chaudret, J.-P. Piquemal, D. N. Beratan and W. Yang, *J. Chem. Theory Comput.*, 2011, **7**, 625–632.

195 A. Otero-de-la-Roza, M. A. Blanco, A. M. Pendás and V. Luaña, *Comput. Phys. Commun.*, 2009, **180**, 157–166.

196 A. Otero-de-la-Roza, E. R. Johnson and V. Luaña, *Comput. Phys. Commun.*, 2014, **185**, 1007–1018.

197 W. Humphrey, A. Dalke and K. Schulten, *J. Mol. Graph.*, 1996, **14**, 33–38.

198 G. M. Sheldrick, *Acta Crystallogr. Sect. A Found. Crystallogr.*, 2008, **64**, 112–122.

199 G. M. Sheldrick, *Acta Crystallogr. Sect. A Found. Adv.*, 2015, **71**, 3–8.

200 G. M. Sheldrick, *Acta Crystallogr. Sect. C Struct. Chem.*, 2015, **71**, 3–8.

201 O. V Dolomanov, L. J. Bourhis, R. J. Gildea, J. A. K. Howard and H. Puschmann, *J. Appl. Cryst*, 2009, **42**, 339–341.

202 L. Kaufmann, E. V. Dzyuba, F. Malberg, N. L. Löw, M. Groschke, B. Brusilowskij, J. Huuskonen, K. Rissanen, B. Kirchner and C. A. Schalley, *Org. Biomol. Chem.*, 2012, **10**, 5954–5964.

203 L. Köring, N. A. Sitte and J. Paradies, *Synthesis (Stuttg).*, 2022, **54**, 1287–1300.

204 J. Winters, R. Bolia, W. Dehaen and K. Binnemans, *Green Chem.*, 2021, **23**, 1228–1239.

205 N. Cheng, Q. Yan, S. Liu and D. Zhao, *CrystEngComm*, 2014, **16**, 4265–4273.

206 E. M. Pasciak, A. Sengupta, M. S. Mubarak, K. Raghavachari and D. G. Peters, *Electrochim. Acta*, 2014, **127**, 159–166.

207 M. A. Ab Rani, N. Borduas, V. Colquhoun, R. Hanley, H. Johnson, S. Larger, P. D. Lickiss, V. Llopis-Mestre, S. Luu, M. Mogstad, P. Oczipka, J. R. Sherwood, T. Welton and J.-Y. Xing, *Green Chem.*, 2014, **16**, 1282–1296.

Appendix

X-ray data for chapter 2

$[HL^3]_2[SnCl_6]$

Crystal data	
Chemical formula	$(Cl_6Sn)\cdot 2(C_{22}H_{47}N_2O_2)$
M_r	1074.62
Crystal system, space group	Monoclinic, $P2_1/n$
Temperature (K)	120
a, b, c (Å)	18.1977 (5), 8.4952 (2), 19.6349 (5)
β (°)	111.389 (3)
V (Å^3)	2826.36 (14)
Z	2
Radiation type	Mo $K\alpha$
μ (mm^{-1})	0.78
Crystal size (mm)	0.51 × 0.39 × 0.07
Data collection	
Diffractometer	SuperNova, Dual, Cu at home/near, Atlas
Absorption correction	Multi-scan *CrysAlis PRO* 1.171.39.46 (Rigaku Oxford Diffraction, 2018) Empirical absorption correction using spherical harmonics, implemented in SCALE3 ABSPACK scaling algorithm.
T_{min}, T_{max}	0.771, 1.000
No. of measured, independent and observed [$I > 2\sigma(I)$] reflections	33010, 6984, 5975
R_{int}	0.035
(sin θ/λ)$_{max}$ (Å^{-1})	0.694
Refinement	
$R[F^2 > 2\sigma(F^2)]$, $wR(F^2)$, S	0.031, 0.118, 0.89
No. of reflections	6984
No. of parameters	324
H-atom treatment	H atoms treated by a mixture of independent and constrained refinement
$\Delta\rho_{max}$, $\Delta\rho_{min}$ (e Å^{-3})	0.53, −0.45

X-ray data for chapter 3

$[HL^5][AuCl_4]$

mo_jl21001_0m	
Crystal data	
Chemical formula	$0.5(AuCl_4)\cdot C_{14}H_{28}N_2O_2\cdot 0.5(H_2O)\cdot 0.5(H_3O)$
M_r	444.29
Crystal system, space group	Monoclinic, $P2_1$
Temperature (K)	100
a, b, c (Å)	9.7976 (6), 18.9668 (11), 10.3874 (6)
β (°)	90.705 (3)
V (Å^3)	1930.1 (2)
Z	4
Radiation type	Mo $K\alpha$
μ (mm^{-1})	4.13
Crystal size (mm)	0.25 × 0.16 × 0.10
Data collection	
Diffractometer	Bruker *APEX*-II CCD
Absorption correction	–
No. of measured, independent and observed [$I > 2\sigma(I)$] reflections	126928, 11756, 11485
R_{int}	0.033
$(\sin \theta/\lambda)_{\text{max}}$ (Å^{-1})	0.715
Refinement	
$R[F^2 > 2\sigma(F^2)]$, $wR(F^2)$, S	0.030, 0.078, 1.07
No. of reflections	11756
No. of parameters	426
No. of restraints	10
H-atom treatment	H atoms treated by a mixture of independent and constrained refinement
$\Delta\rho_{\text{max}}$, $\Delta\rho_{\text{min}}$ (e Å^{-3})	3.39, −1.58
Absolute structure	Flack x determined using 5388 quotients [(I+)-(I-)]/[(I+)+(I-)] (Parsons, Flack and Wagner, Acta Cryst. B69 (2013) 249-259).
Absolute structure parameter	−0.0007 (18)

$[HL^6][AuBr_4]$

JL20014x1	
Crystal data	
Chemical formula	$AuBr_4 \cdot C_{18}H_{21}N_2O_2$
M_r	813.96
Crystal system, space group	Monoclinic, $C2/c$
Temperature (K)	100
a, b, c (Å)	10.6708 (12), 16.965 (2), 12.2245 (15)
β (°)	94.415 (4)
V (Å^3)	2206.5 (5)
Z	4
Radiation type	Mo $K\alpha$
μ (mm^{-1})	13.93
Crystal size (mm)	0.22 × 0.16 × 0.06
Data collection	
Diffractometer	Bruker *APEX*-II CCD
Absorption correction	Multi-scan *SADABS2016*/2 (Bruker,2016/2) was used for absorption correction. wR2(int) was 0.1411 before and 0.0783 after correction. The Ratio of minimum to maximum transmission is 0.5986. The λ/2 correction factor is Not present.
T_{min}, T_{max}	0.447, 0.747
No. of measured, independent and observed [$I \geq 2u(I)$] reflections	80320, 4075, 3765
R_{int}	0.056
(sin θ/λ)$_{max}$ (Å^{-1})	0.780
Refinement	
$R[F^2 > 2\sigma(F^2)]$, $wR(F^2)$, S	0.020, 0.049, 1.04
No. of reflections	4075
No. of parameters	125
H-atom treatment	H atoms treated by a mixture of independent and constrained refinement
$\Delta\rho_{max}$, $\Delta\rho_{min}$ (e Å^{-3})	1.05, −1.50

[HL^6][AuCl$_4$]

jl20012_refinalized	
Crystal data	
Chemical formula	$AuCl_4{\cdot}C_{18}H_{21}N_2O_2$
M_r	636.13
Crystal system, space group	Monoclinic, $I2/a$
Temperature (K)	120
a, b, c (Å)	12.0848 (7), 16.9574 (2), 16.5644 (10)
β (°)	142.074 (13)
V (Å^3)	2086.4 (4)
Z	4
Radiation type	Mo $K\alpha$
μ (mm^{-1})	7.58
Crystal size (mm)	0.24 × 0.13 × 0.06
Data collection	
Diffractometer	Rigaku Oxford Diffraction XCalibur
Absorption correction	Multi-scan *CrysAlis PRO* 1.171.40.84a (Rigaku Oxford Diffraction, 2020) Empirical absorption correction using spherical harmonics, implemented in SCALE3 ABSPACK scaling algorithm.
T_{min}, T_{max}	0.610, 1.000
No. of measured, independent and observed [$I > 2\sigma(I)$] reflections	22821, 2669, 2397
R_{int}	0.028
(sin θ/λ)$_{max}$ (Å^{-1})	0.692
Refinement	
$R[F^2 > 2\sigma(F^2)]$, $wR(F^2)$, S	0.016, 0.030, 1.07
No. of reflections	2669
No. of parameters	129
No. of restraints	1
H-atom treatment	H atoms treated by a mixture of independent and constrained refinement
$\Delta\rho_{max}$, $\Delta\rho_{min}$ (e Å^{-3})	0.54, −0.53

$[HL^6][Br_2][Br_3]$

jl20014x2_refinalized_1a	
Crystal data	
Chemical formula	$2.667(Br_3)\cdot 2(C_{18}H_{21}N_2O_2)\cdot CHCl_3$
M_r	1353.38
Crystal system, space group	Triclinic, $P\bar{1}$
Temperature (K)	120
a, b, c (Å)	9.1268 (13), 14.0105 (17), 18.7477 (17)
α, β, γ (°)	85.493 (9), 84.475 (10), 84.065 (11)
V (Å^3)	2367.7 (5)
Z	2
Radiation type	Cu $K\alpha$
μ (mm^{-1})	10.00
Crystal size (mm)	0.12 × 0.04 × 0.02
Data collection	
Diffractometer	SuperNova, Dual, Cu at home/near, Atlas
Absorption correction	Multi-scan *CrysAlis PRO* 1.171.40.84a (Rigaku Oxford Diffraction, 2020) Empirical absorption correction using spherical harmonics, implemented in SCALE3 ABSPACK scaling algorithm.
T_{min}, T_{max}	0.385, 1.000
No. of measured, independent and observed [$I > 2\sigma(I)$] reflections	28196, 4945, 3257
R_{int}	0.205
θ_{max} (°)	50.4
$(\sin \theta/\lambda)_{max}$ (Å^{-1})	0.500
Refinement	
$R[F^2 > 2\sigma(F^2)]$, $wR(F^2)$, S	0.092, 0.261, 1.03
No. of reflections	4945
No. of parameters	510
No. of restraints	424
H-atom treatment	H-atom parameters constrained
$\Delta\rho_{max}$, $\Delta\rho_{min}$ (e Å^{-3})	1.38, −1.22

[HL^6][Cl$_2$H][Cl][H$_3$O]

mo_jl21011_0m	
Crystal data	
Chemical formula	0.5(Cl$_2$H)·0.5(Cl)·0.5(ClH$_3$O)·C$_{18}$H$_{21}$N$_2$O$_2$
M_r	378.28
Crystal system, space group	Triclinic, $P\bar{1}$
Temperature (K)	100
a, *b*, *c* (Å)	9.0297 (12), 11.5330 (15), 18.397 (2)
α, β, γ (°)	86.352 (5), 83.328 (5), 89.601 (5)
V (Å^3)	1899.0 (4)
Z	4
Radiation type	Mo *K*α
μ (mm^{-1})	0.36
Crystal size (mm)	0.34 × 0.26 × 0.10
Data collection	
Diffractometer	Bruker *APEX*-II CCD
Absorption correction	Multi-scan *SADABS2016*/2 (Bruker,2016/2) was used for absorption correction. wR2(int) was 0.1194 before and 0.0607 after correction. The Ratio of minimum to maximum transmission is 0.9528. The λ/2 correction factor is Not present.
T_{min}, T_{max}	0.711, 0.746
No. of measured, independent and observed [$I > 2\sigma(I)$] reflections	109558, 11335, 9323
R_{int}	0.050
(sin θ/λ)$_{max}$ (Å^{-1})	0.714
Refinement	
$R[F^2 > 2\sigma(F^2)]$, $wR(F^2)$, S	0.033, 0.081, 1.03
No. of reflections	11335
No. of parameters	465
H-atom treatment	H atoms treated by a mixture of independent and constrained refinement
$\Delta\rho_{max}$, $\Delta\rho_{min}$ (e Å^{-3})	0.37, −0.27

[HL^6][ClH][Cl][H_2O][H_3O]

j2116_auto	
Crystal data	
Chemical formula	$1.333(Cl)\cdot 0.667(ClH)\cdot C_{12}H_{13.667}N_{1.333}O_{1.333}\cdot 0.667(H_2O)\cdot 0.667(H_3O)$
M_r	294.17
Crystal system, space group	Triclinic, $P\bar{1}$
Temperature (K)	120
a, b, c (Å)	9.1201 (2), 10.7445 (3), 11.6223 (2)
α, β, γ (°)	82.236 (2), 85.893 (2), 86.007 (2)
V (Å^3)	1123.47 (4)
Z	3
Radiation type	Mo $K\alpha$
μ (mm^{-1})	0.43
Crystal size (mm)	0.36 × 0.25 × 0.14
Data collection	
Diffractometer	Xcalibur, Eos
Absorption correction	Analytical *CrysAlis PRO* 1.171.40.53 (Rigaku Oxford Diffraction, 2019) Analytical numeric absorption correction using a multifaceted crystal model based on expressions derived by R.C. Clark & J.S. Reid. (Clark, R. C. & Reid, J. S. (1995). Acta Cryst. A51, 887-897) Empirical absorption correction using spherical harmonics, implemented in SCALE3 ABSPACK scaling algorithm.
T_{min}, T_{max}	0.937, 0.971
No. of measured, independent and observed [$I > 2\sigma(I)$] reflections	42792, 4090, 3828
R_{int}	0.044
$(\sin \theta/\lambda)_{max}$ (Å^{-1})	0.602
Refinement	
$R[F^2 > 2\sigma(F^2)]$, $wR(F^2)$, S	0.043, 0.097, 1.16
No. of reflections	4090
No. of parameters	266
H-atom treatment	H atoms treated by a mixture of independent and constrained refinement
$\Delta\rho_{max}$, $\Delta\rho_{min}$ (e Å^{-3})	0.36, −0.33

$[HL^6][FeCl_4]$

jl20019_sadabs	
Crystal data	
Chemical formula	$Cl_4Fe\cdot C_{18}H_{21}N_2O_2$
M_r	495.02
Crystal system, space group	Monoclinic, $P2_1$
Temperature (K)	120
a, b, c (Å)	8.6282 (1), 19.0047 (3), 13.8701 (3)
β (°)	105.557 (2)
V (Å^3)	2191.04 (7)
Z	4
Radiation type	Cu $K\alpha$
μ (mm^{-1})	10.14
Crystal size (mm)	0.26 × 0.04 × 0.03 × 0.05 (radius)
Data collection	
Diffractometer	Rigaku Oxford Diffraction SuperNova
Absorption correction	Multi-scan *SADABS2016*/2 (Bruker,2016/2) was used for absorption correction. wR2(int) was 0.1221 before and 0.0887 after correction. The Ratio of minimum to maximum transmission is 0.6375. The λ/2 correction factor is Not present.
T_{min}, T_{max}	0.481, 0.754
No. of measured, independent and observed [$I > 2\sigma(I)$] reflections	44934, 9025, 8375
R_{int}	0.087
(sin θ/λ)$_{max}$ (Å^{-1})	0.629
Refinement	
$R[F^2 > 2\sigma(F^2)]$, $wR(F^2)$, S	0.055, 0.143, 1.06
No. of reflections	9025
No. of parameters	500
No. of restraints	3
H-atom treatment	H atoms treated by a mixture of independent and constrained refinement
$\Delta\rho_{max}$, $\Delta\rho_{min}$ (e Å^{-3})	0.44, −0.61
Absolute structure	Refined as an inversion twin.
Absolute structure parameter	0.475 (8)

[HL^6][GaCl$_4$]

jl21043_refinalized	
Crystal data	
Chemical formula	$Cl_4Ga{\cdot}C_{18}H_{20.5}N_2O_2$
M_r	508.38
Crystal system, space group	Monoclinic, $P2_1/n$
Temperature (K)	120
a, b, c (Å)	8.6732 (2), 18.8392 (7), 13.8641 (5)
β (°)	104.665 (3)
V (Å^3)	2191.55 (13)
Z	4
Radiation type	Mo $K\alpha$
μ (mm^{-1})	1.76
Crystal size (mm)	0.56 × 0.14 × 0.11
Data collection	
Diffractometer	Xcalibur, Eos
Absorption correction	Multi-scan *CrysAlis PRO* 1.171.41.99a (Rigaku Oxford Diffraction, 2021) Empirical absorption correction using spherical harmonics, implemented in SCALE3 ABSPACK scaling algorithm.
T_{min}, T_{max}	0.502, 1.000
No. of measured, independent and observed [$I > 2\sigma(I)$] reflections	46037, 5160, 4563
R_{int}	0.065
(sin θ/λ)$_{max}$ (Å^{-1})	0.668
Refinement	
$R[F^2 > 2\sigma(F^2)]$, $wR(F^2)$, S	0.051, 0.123, 1.24
No. of reflections	5160
No. of parameters	250
H-atom treatment	H atoms treated by a mixture of independent and constrained refinement
$\Delta\rho_{max}$, $\Delta\rho_{min}$ (e Å^{-3})	1.00, −0.76

$[HL^6][CoCl_4][H_2O]_2[H_3O]$

jl21017_refinalized	
Crystal data	
Chemical formula	$Cl_4Co\cdot C_{18}H_{20.5}N_2O_2\cdot 2(H_2O)\cdot H_3O$
M_r	553.15
Crystal system, space group	Monoclinic, $P2_1/n$
Temperature (K)	120
a, b, c (Å)	9.0978 (2), 11.4600 (3), 23.7020 (7)
β (°)	100.514 (2)
V (Å^3)	2429.70 (11)
Z	4
Radiation type	Mo $K\alpha$
μ (mm^{-1})	1.18
Crystal size (mm)	0.31 × 0.23 × 0.06
Data collection	
Diffractometer	Rigaku Oxford Diffraction XCalibur
Absorption correction	Multi-scan *CrysAlis PRO* 1.171.41.99a (Rigaku Oxford Diffraction, 2021) Empirical absorption correction using spherical harmonics, implemented in SCALE3 ABSPACK scaling algorithm.
T_{min}, T_{max}	0.908, 1.000
No. of measured, independent and observed [$I > 2\sigma(I)$] reflections	33219, 6819, 5626
R_{int}	0.044
(sin θ/λ)$_{max}$ (Å^{-1})	0.722
Refinement	
$R[F^2 > 2\sigma(F^2)]$, $wR(F^2)$, S	0.037, 0.070, 1.03
No. of reflections	6819
No. of parameters	306
No. of restraints	9
H-atom treatment	H atoms treated by a mixture of independent and constrained refinement
$\Delta\rho_{max}$, $\Delta\rho_{min}$ (e Å^{-3})	0.41, −0.36

$[HL^6][ZnCl_4][H_2O]_2[H_3O]$

j2021_1_auto	
Crystal data	
Chemical formula	$Cl_4Zn\cdot 2(H_2O)\cdot C_{18}H_{21}N_2O_2\cdot H_3O$
M_r	559.59
Crystal system, space group	Monoclinic, $P2_1/n$
Temperature (K)	120
a, b, c (Å)	9.1085 (2), 11.4514 (2), 23.7051 (5)
β (°)	100.502 (2)
V (Å^3)	2431.14 (9)
Z	4
Radiation type	Mo $K\alpha$
μ (mm^{-1})	1.48
Crystal size (mm)	0.35 × 0.05 × 0.04
Data collection	
Diffractometer	Rigaku Oxford Diffraction XCalibur
Absorption correction	Multi-scan *CrysAlis PRO* 1.171.40.53 (Rigaku Oxford Diffraction, 2019) Analytical numeric absorption correction using a multifaceted crystal model based on expressions derived by R.C. Clark & J.S. Reid. (Clark, R. C. & Reid, J. S. (1995). Acta Cryst. A51, 887-897) Empirical absorption correction using spherical harmonics, implemented in SCALE3 ABSPACK scaling algorithm.
T_{min}, T_{max}	0.811, 0.962
No. of measured, independent and observed [$I > 2\sigma(I)$] reflections	44451, 4437, 3625
R_{int}	0.073
$(\sin \theta/\lambda)_{max}$ (Å^{-1})	0.602
Refinement	
$R[F^2 > 2\sigma(F^2)]$, $wR(F^2)$, S	0.031, 0.066, 1.04
No. of reflections	4437
No. of parameters	308
No. of restraints	9
H-atom treatment	H atoms treated by a mixture of independent and constrained refinement
$\Delta\rho_{max}$, $\Delta\rho_{min}$ (e Å^{-3})	0.33, −0.27

$[HL^6]_2[PtCl_6][H_2O]$

mo_jl21009x1_0m	
Crystal data	
Chemical formula	$Cl_6Pt·2(C_{18}H_{21}N_2O_2)·2(H_2O)$
M_r	1038.56
Crystal system, space group	Triclinic, $P\bar{1}$
Temperature (K)	100
a, *b*, *c* (Å)	8.7579 (10), 11.0954 (14), 12.0668 (15)
α, β, γ (°)	113.978 (5), 103.941 (5), 96.913 (5)
V ($Å^3$)	1007.8 (2)
Z	1
Radiation type	Mo *K*α
μ (mm^{-1})	3.93
Crystal size (mm)	0.40 × 0.19 × 0.09
Data collection	
Diffractometer	Bruker D8 Venture
Absorption correction	Multi-scan *SADABS2016*/2 (Bruker,2016/2) was used for absorption correction. wR2(int) was 0.1037 before and 0.0540 after correction. The Ratio of minimum to maximum transmission is 0.6929. The λ/2 correction factor is Not present.
T_{min}, T_{max}	0.518, 0.748
No. of measured, independent and observed [$I > 2\sigma(I)$] reflections	91497, 12086, 11750
R_{int}	0.045
$(\sin \theta/\lambda)_{max}$ ($Å^{-1}$)	0.910
Refinement	
$R[F^2 > 2\sigma(F^2)]$, $wR(F^2)$, *S*	0.025, 0.051, 1.06
No. of reflections	12086
No. of parameters	259
No. of restraints	4
H-atom treatment	H atoms treated by a mixture of independent and constrained refinement
$\Delta\rho_{max}$, $\Delta\rho_{min}$ (e $Å^{-3}$)	1.07, −2.74

$[HL^6]_2[SnCl_6][H_2O]$

jl20018x1_refinalized	
Crystal data	
Chemical formula	$Cl_6Sn\cdot 2(C_{18}H_{21}N_2O_2)\cdot 1.265(H_2O)$
M_r	948.83
Crystal system, space group	Triclinic, $P\bar{1}$
Temperature (K)	120
a, *b*, *c* (Å)	8.7720 (4), 11.1752 (5), 12.0751 (6)
α, β, γ (°)	113.632 (4), 103.282 (4), 97.177 (4)
V (Å^3)	1023.69 (9)
Z	1
Radiation type	Mo $K\alpha$
μ (mm^{-1})	1.06
Crystal size (mm)	0.19 × 0.12 × 0.04
Data collection	
Diffractometer	Rigaku Oxford Diffraction SuperNova
Absorption correction	Multi-scan *CrysAlis PRO* 1.171.40.84a (Rigaku Oxford Diffraction, 2020) Empirical absorption correction using spherical harmonics, implemented in SCALE3 ABSPACK scaling algorithm.
T_{min}, T_{max}	0.533, 1.000
No. of measured, independent and observed [$I > 2\sigma(I)$] reflections	18433, 5179, 4332
R_{int}	0.063
$(\sin \theta/\lambda)_{max}$ (Å^{-1})	0.699
Refinement	
$R[F^2 > 2\sigma(F^2)]$, $wR(F^2)$, S	0.041, 0.070, 1.05
No. of reflections	5179
No. of parameters	258
No. of restraints	4
H-atom treatment	H atoms treated by a mixture of independent and constrained refinement
$\Delta\rho_{max}$, $\Delta\rho_{min}$ (e Å^{-3})	0.71, −0.59

[HL^9][AuCl$_4$]

jl21026	
Crystal data	
Chemical formula	$AuCl_4\cdot C_{18}H_{19}Cl_2N_2O_2\cdot 2(CHCl_3)$
M_r	943.75
Crystal system, space group	Triclinic, *P*1
Temperature (K)	120
a, *b*, *c* (Å)	7.9204 (7), 13.3982 (13), 16.9237 (15)
α, β, γ (°)	100.679 (8), 102.829 (8), 106.113 (8)
V (Å^3)	1622.8 (3)
Z	2
Radiation type	Mo *K*α
μ (mm^{-1})	5.54
Crystal size (mm)	0.15 × 0.13 × 0.04 × 0.05 (radius)
Data collection	
Diffractometer	Rigaku Oxford Diffraction SuperNova
Absorption correction	Multi-scan *CrysAlis PRO* 1.171.41.99a (Rigaku Oxford Diffraction, 2021) Spherical absorption correction using equivalent radius and absorption coefficient. Empirical absorption correction using spherical harmonics, implemented in SCALE3 ABSPACK scaling algorithm.
T_{min}, T_{max}	0.664, 0.671
No. of measured, independent and observed [$I > 2\sigma(I)$] reflections	19179, 19179, 14783
R_{int}	n/a
(sin θ/λ)$_{max}$ (Å^{-1})	0.605
Refinement	
$R[F^2 > 2\sigma(F^2)]$, $wR(F^2)$, S	0.056, 0.120, 0.96
No. of reflections	19179
No. of parameters	678
No. of restraints	994
H-atom treatment	H atoms treated by a mixture of independent and constrained refinement
$\Delta\rho_{max}$, $\Delta\rho_{min}$ (e Å^{-3})	2.45, −1.31
Absolute structure	Classical Flack method preferred over Parsons because s.u. lower.
Absolute structure parameter	0.387 (6)

[HL^9][FeCl$_4$]

jl21028_refinalized	
Crystal data	
Chemical formula	$4(Cl_4Fe)\cdot 2(CHCl_3)\cdot 4(C_{18}H_{19}Cl_2N_2O_2)$
M_r	2494.34
Crystal system, space group	Monoclinic, *Pc*
Temperature (K)	120
a, b, c (Å)	7.9491 (3), 38.6279 (8), 17.3716 (3)
β (°)	92.920 (2)
V (Å^3)	5327.1 (2)
Z	2
Radiation type	Mo $K\alpha$
μ (mm^{-1})	1.34
Crystal size (mm)	0.24 × 0.17 × 0.09
Data collection	
Diffractometer	SuperNova, Dual, Cu at home/near, Atlas
Absorption correction	Gaussian *CrysAlis PRO* 1.171.41.99a (Rigaku Oxford Diffraction, 2021) Numerical absorption correction based on gaussian integration over a multifaceted crystal model Empirical absorption correction using spherical harmonics, implemented in SCALE3 ABSPACK scaling algorithm.
T_{min}, T_{max}	0.622, 1.000
No. of measured, independent and observed [$I > 2\sigma(I)$] reflections	58750, 19661, 17265
R_{int}	0.049
(sin θ/λ)$_{max}$ (Å^{-1})	0.625
Refinement	
$R[F^2 > 2\sigma(F^2)]$, $wR(F^2)$, S	0.068, 0.166, 1.07
No. of reflections	19661
No. of parameters	1205
No. of restraints	111
H-atom treatment	H-atom parameters constrained
	$w = 1/[\sigma^2(F_o^2) + (0.0683P)^2 + 15.7611P]$ where $P = (F_o^2 + 2F_c^2)/3$
$\Delta\rho_{max}$, $\Delta\rho_{min}$ (e Å^{-3})	2.28, −0.71
Absolute structure	Flack x determined using 5879 quotients [(I+)-(I-)]/[(I+)+(I-)] (Parsons, Flack and Wagner, Acta Cryst. B69 (2013) 249-259).
Absolute structure parameter	0.012 (12)

[HL^{10}][AuCl$_4$]

jl21044	
Crystal data	
Chemical formula	$1.333(AuCl_4)\cdot 0.667(CHCl_3)\cdot 1.333(C_{20}H_{25}N_2O_4)$
M_r	1007.83
Crystal system, space group	Triclinic, $P\overline{1}$
Temperature (K)	120
a, *b*, *c* (Å)	8.7082 (4), 16.4279 (9), 19.4687 (9)
α, β, γ (°)	83.918 (4), 83.792 (4), 84.635 (4)
V (Å^3)	2743.7 (2)
Z	4
Radiation type	Cu *K*α
μ (mm^{-1})	15.26
Crystal size (mm)	0.15 × 0.06 × 0.04
Data collection	
Diffractometer	SuperNova, Dual, Cu at home/near, Atlas
Absorption correction	For a sphere *CrysAlis PRO* 1.171.40.53 (Rigaku Oxford Diffraction, 2019) Spherical absorption correction using equivalent radius and absorption coefficient. Empirical absorption correction using spherical harmonics, implemented in SCALE3 ABSPACK scaling algorithm.
T_{min}, T_{max}	0.548, 0.583
No. of measured, independent and observed [$I > 2\sigma(I)$] reflections	38642, 10698, 7623
R_{int}	0.143
$(\sin \theta/\lambda)_{max}$ (Å^{-1})	0.629
Refinement	
$R[F^2 > 2\sigma(F^2)]$, $wR(F^2)$, S	0.098, 0.274, 1.02
No. of reflections	10698
No. of parameters	603
No. of restraints	3
H-atom treatment	H-atom parameters constrained
	$w = 1/[\sigma^2(F_o^2) + (0.1788P)^2 + 16.4901P]$ where $P = (F_o^2 + 2F_c^2)/3$
$\Delta\rho_{max}$, $\Delta\rho_{min}$ (e Å^{-3})	5.53, −3.76

$[HL^{10}][FeCl_4]$

jl21029_refinalized	
Crystal data	
Chemical formula	$1.333(Cl_4Fe)\cdot 1.333(CHCl_3)\cdot C_{26.667}H_{33.333}N_{2.667}O_{5.333}$
M_r	899.25
Crystal system, space group	Monoclinic, $P2_1/c$
Temperature (K)	120
a, b, c (Å)	12.5469 (5), 9.3433 (3), 25.4346 (11)
β (°)	101.837 (4)
V (Å^3)	2918.3 (2)
Z	3
Radiation type	Mo $K\alpha$
μ (mm^{-1})	1.19
Crystal size (mm)	0.62 × 0.07 × 0.04
Data collection	
Diffractometer	SuperNova, Dual, Cu at home/near, Atlas
Absorption correction	Gaussian *CrysAlis PRO* 1.171.41.99a (Rigaku Oxford Diffraction, 2021) Numerical absorption correction based on gaussian integration over a multifaceted crystal model Empirical absorption correction using spherical harmonics, implemented in SCALE3 ABSPACK scaling algorithm.
T_{min}, T_{max}	0.464, 1.000
No. of measured, independent and observed [$I > 2\sigma(I)$] reflections	70099, 7231, 6175
R_{int}	0.069
(sin θ/λ)$_{max}$ (Å^{-1})	0.667
Refinement	
$R[F^2 > 2\sigma(F^2)]$, $wR(F^2)$, S	0.059, 0.104, 1.21
No. of reflections	7231
No. of parameters	324
H-atom treatment	H atoms treated by a mixture of independent and constrained refinement
$\Delta\rho_{max}$, $\Delta\rho_{min}$ (e Å^{-3})	0.57, −0.77

NMR Spectra relevant to chapter 7

3,5,5-Trimethylhexanamide, L[1]

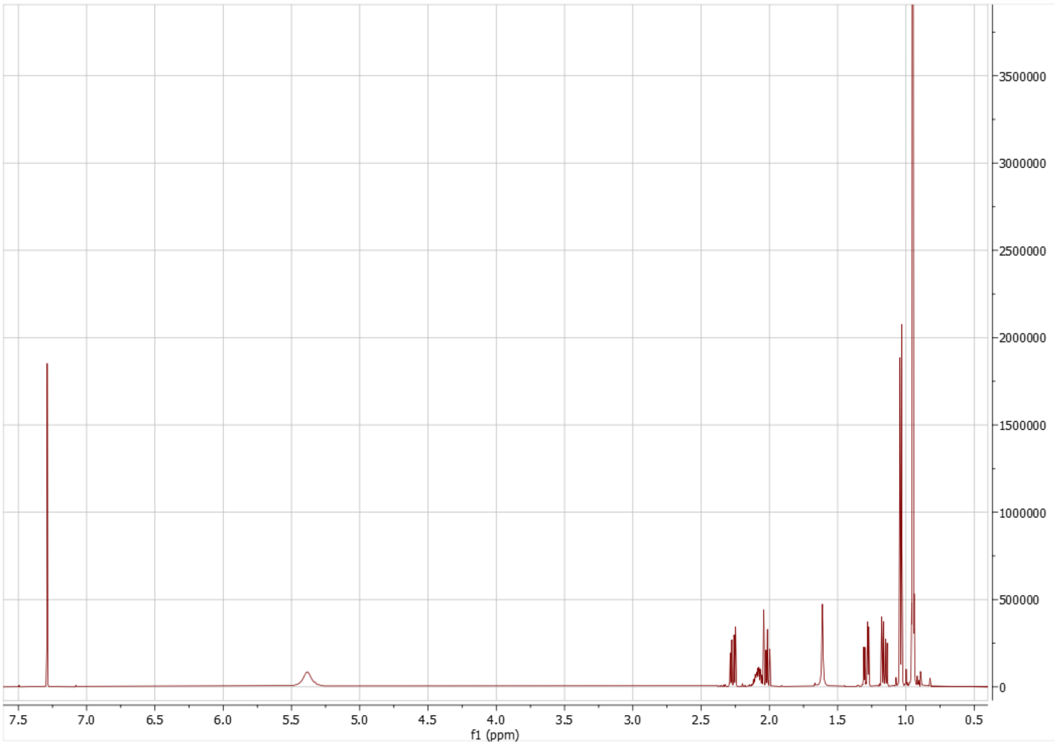

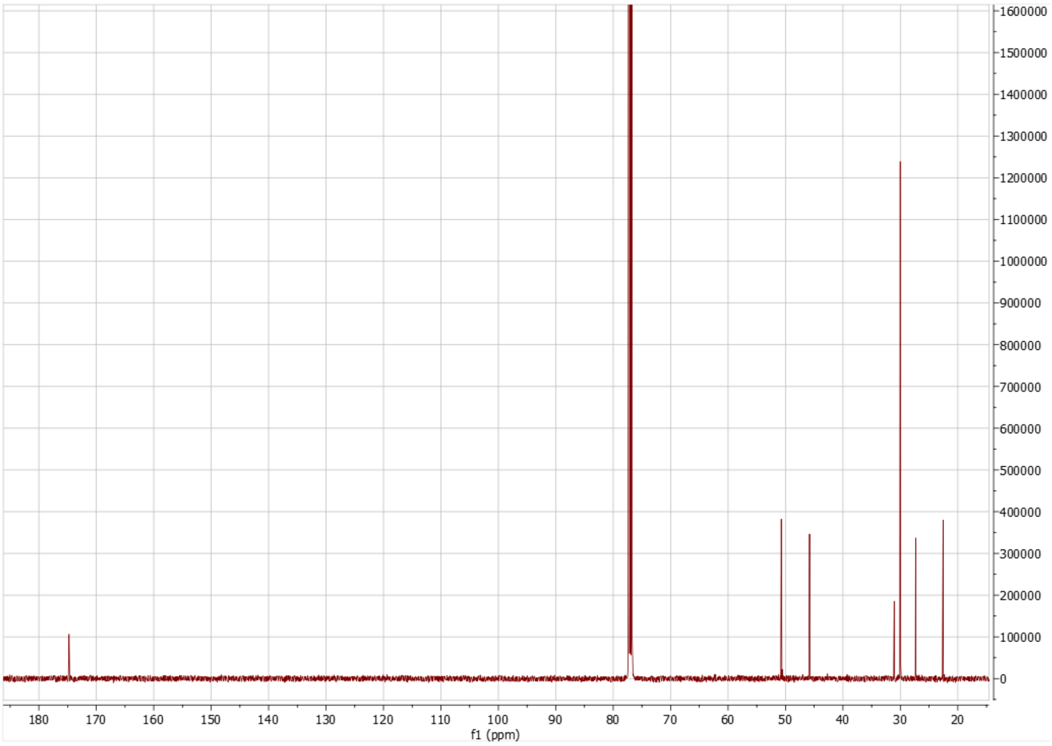

N,3,5,5-Tetramethylhexanamide, L[2]

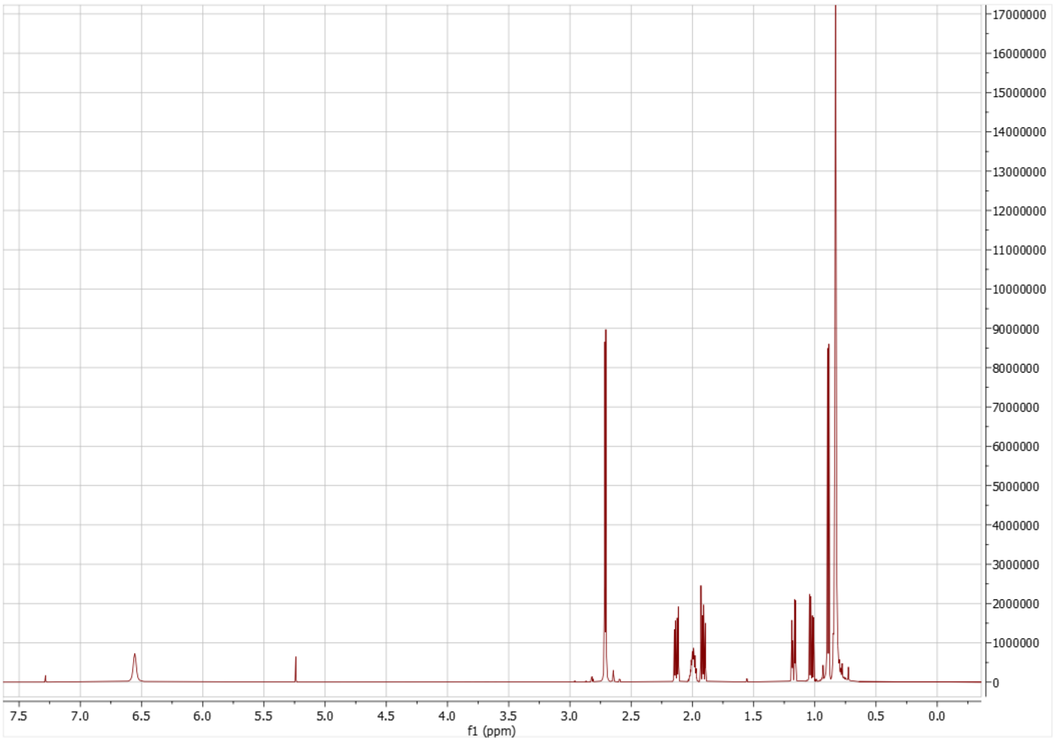

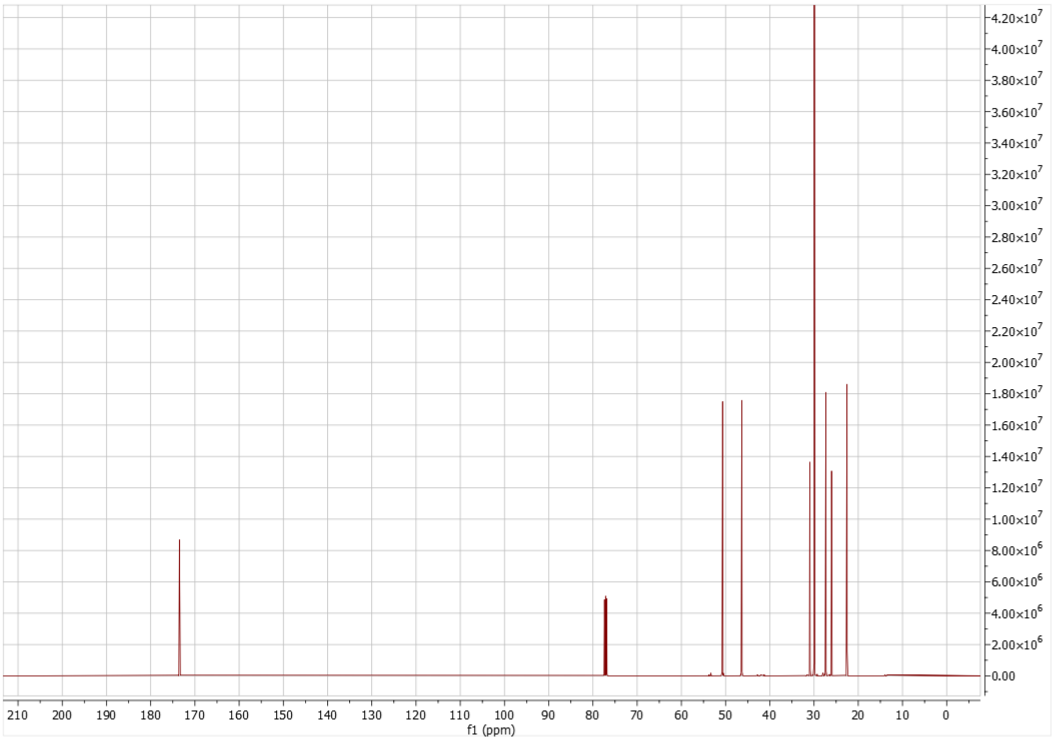

N,N,3,5,5-Pentamethylhexanamide, L^3

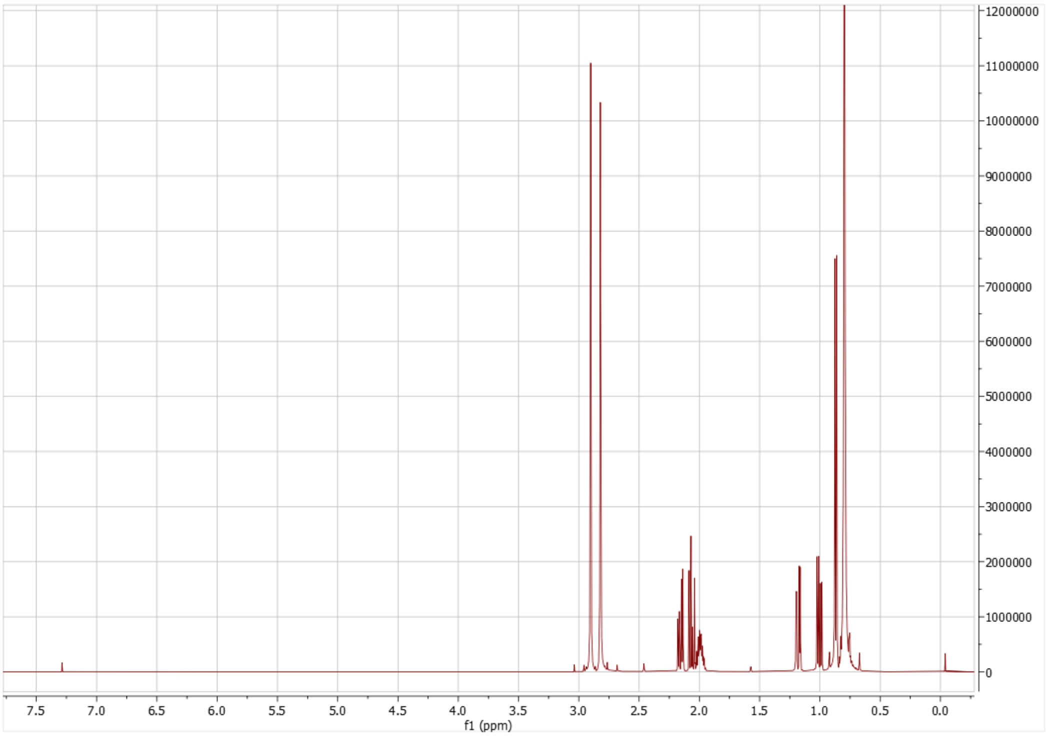

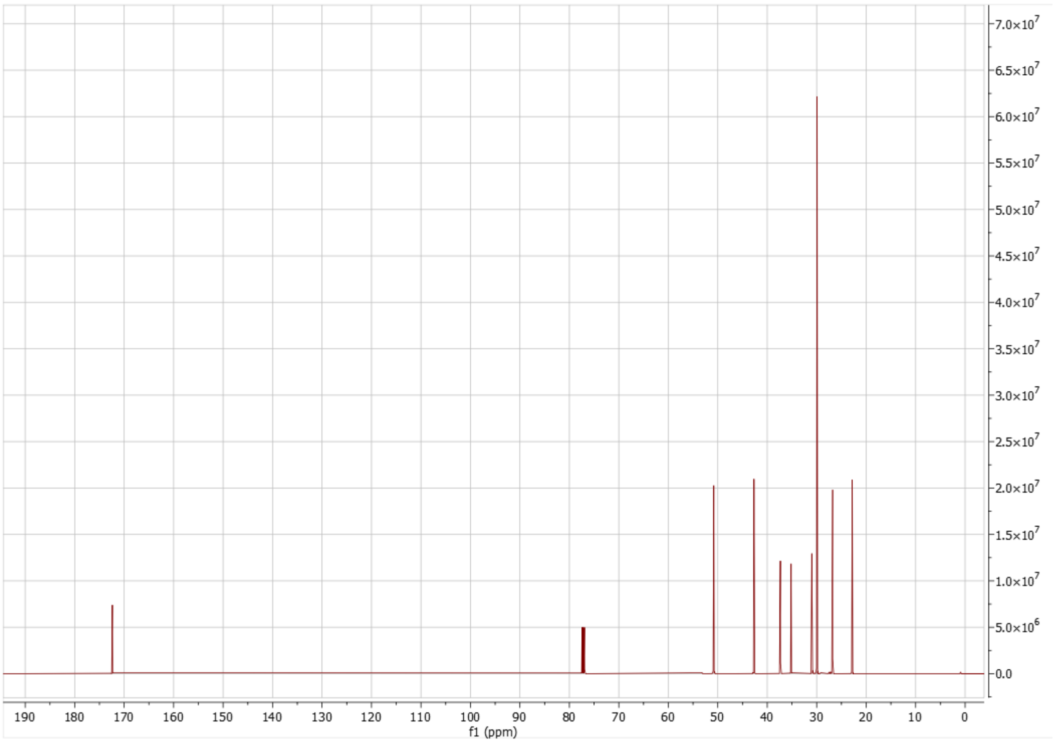

N,N’-(ethane-1,2-diyl)bis(N,3,5,5-tetramethylhexanamide), L^4

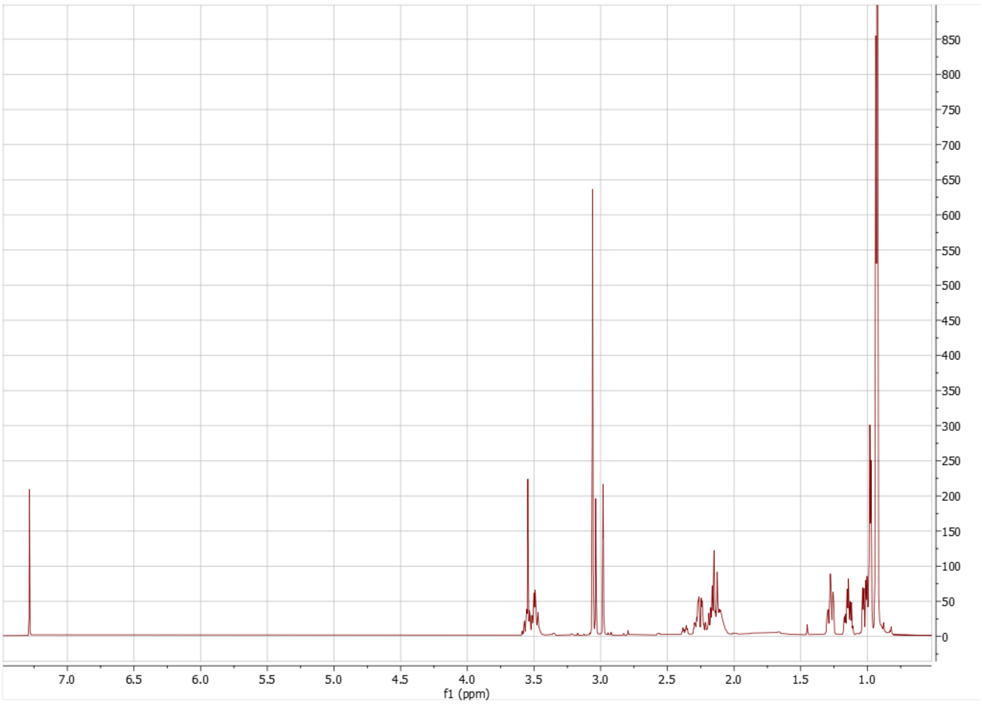

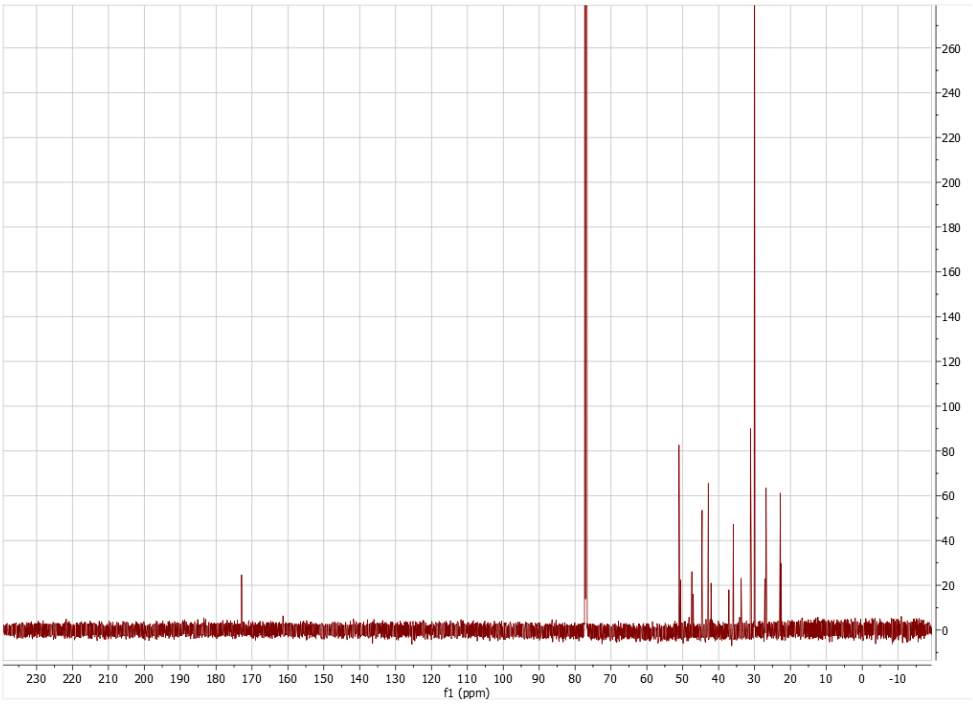

N,N'-(1,2-Ethanediyl)bis(2,2-dimethyl-N-methylpropanamide), L^5

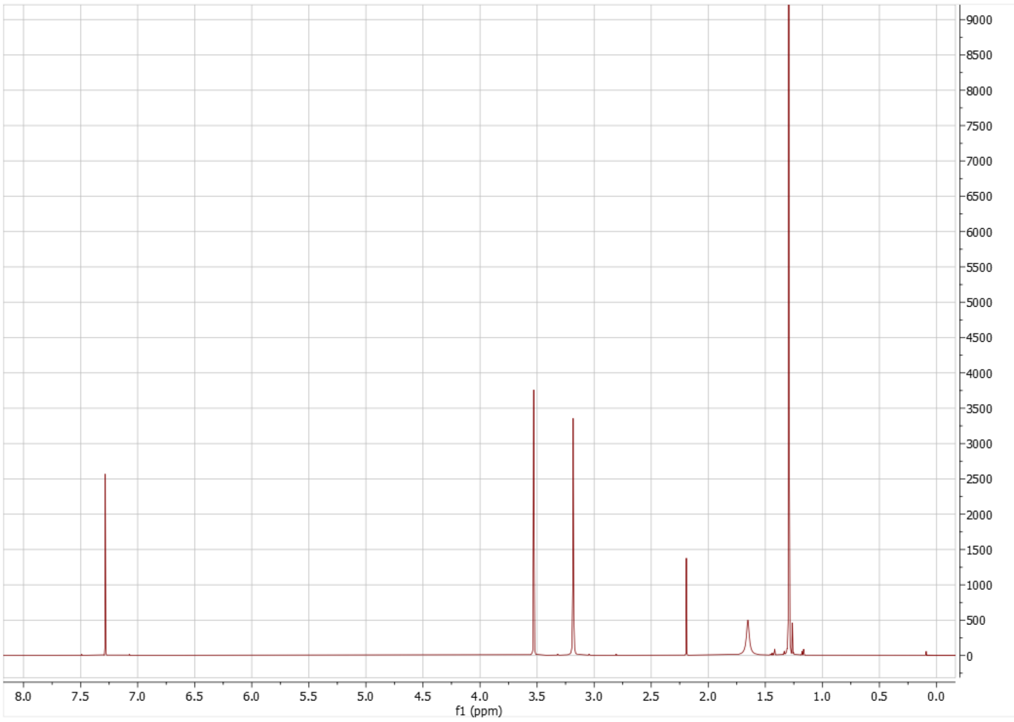

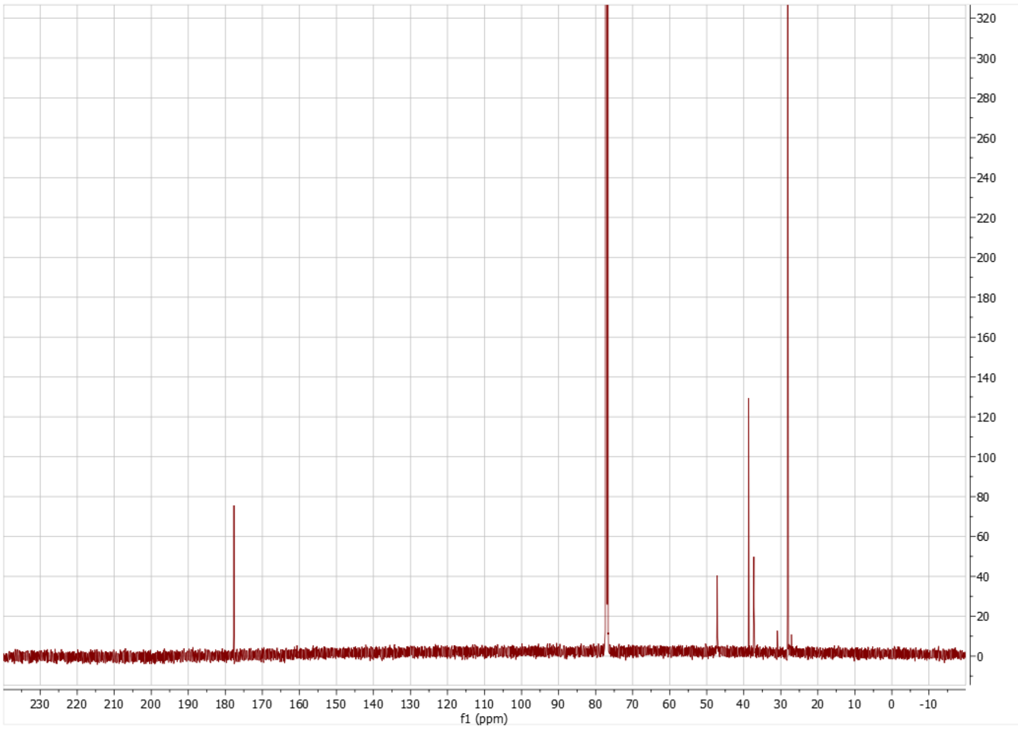

N,N′-(Ethane-1,2-diyl)bis(N-methylbenzamide), L^6

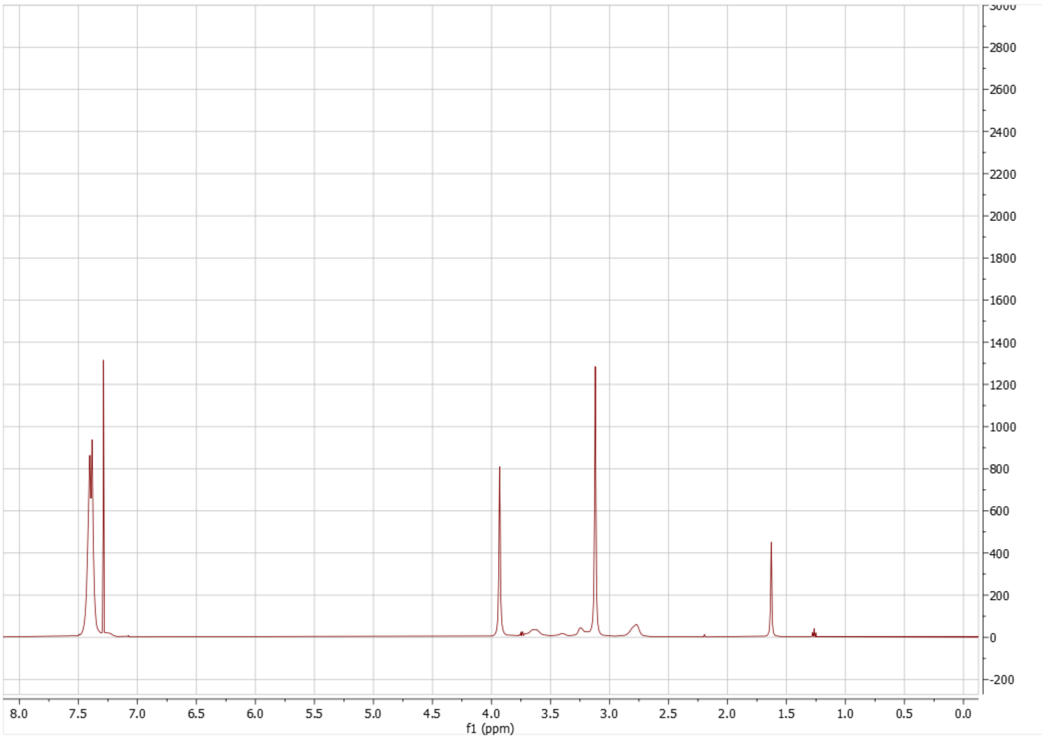

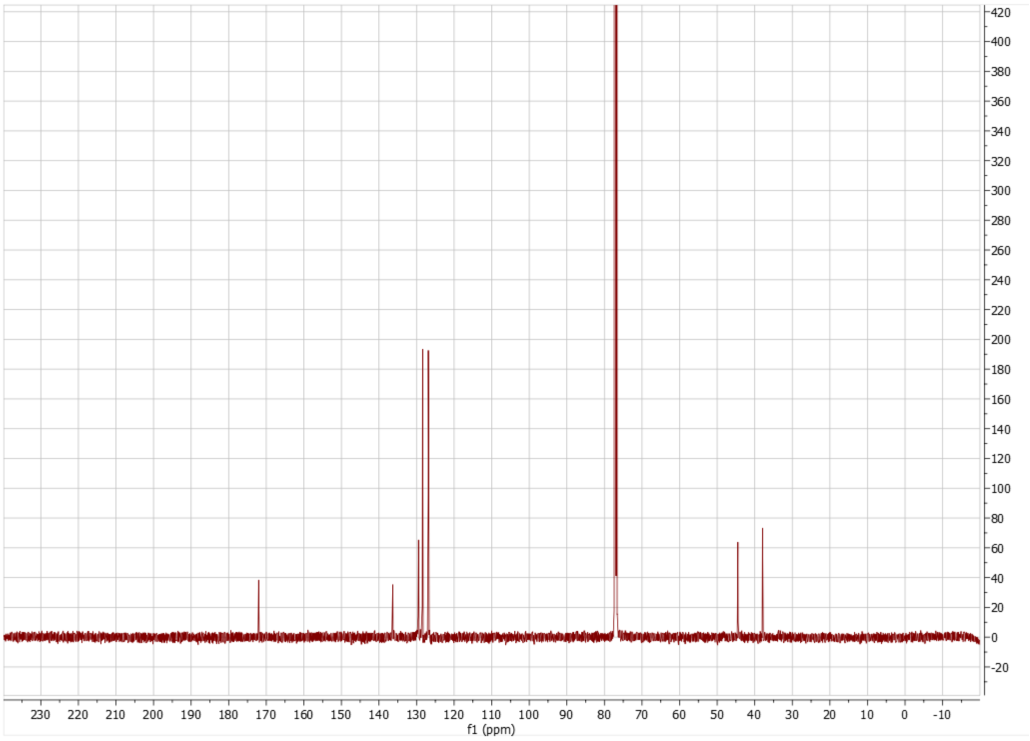

N,N′-(Ethane-1,2-diyl)bis(pentafluoro-N-methylbenzamide), L[8]

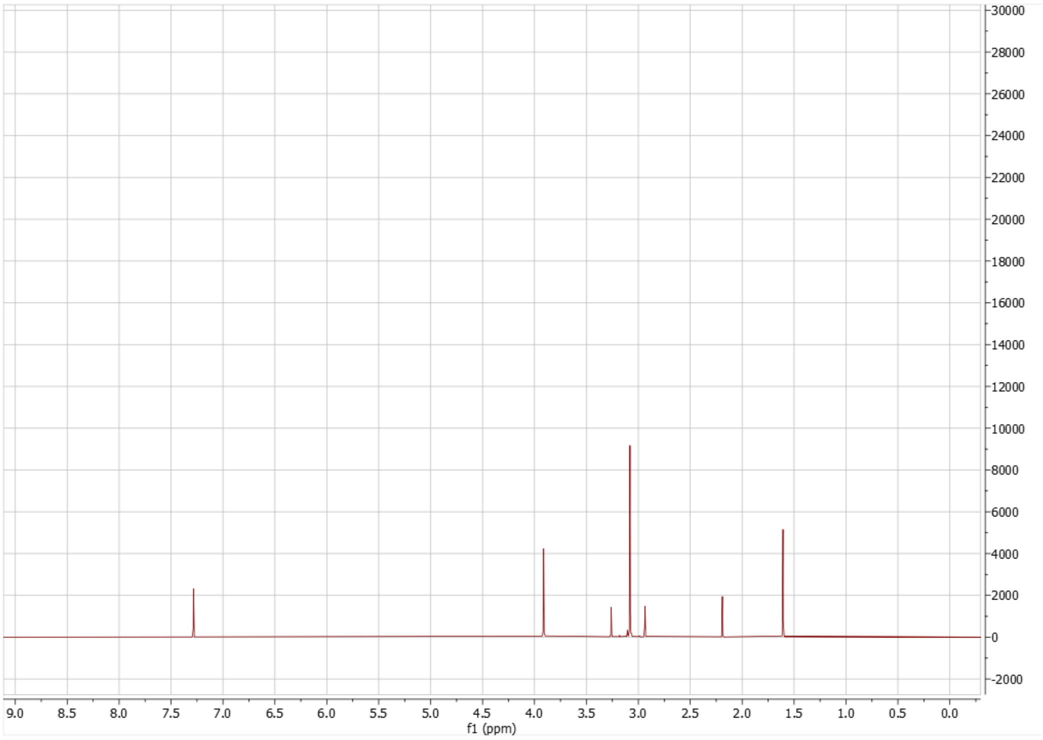

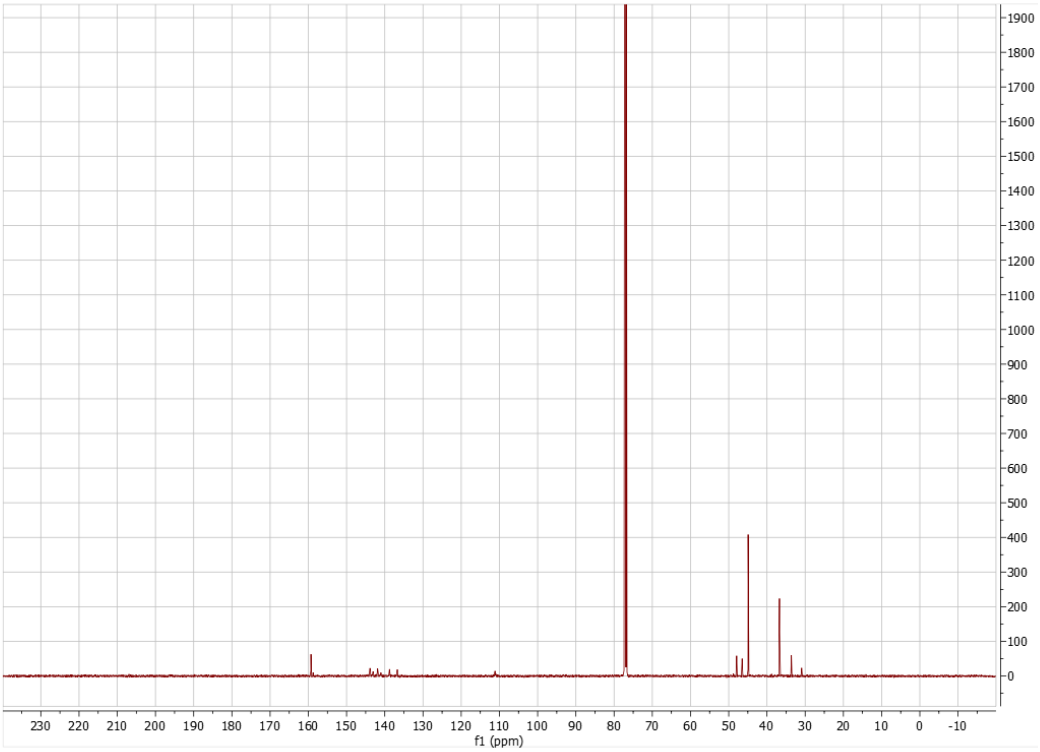

N,N′-(Ethane-1,2-diyl)bis(4-chloro-N-methylbenzamide), L^9

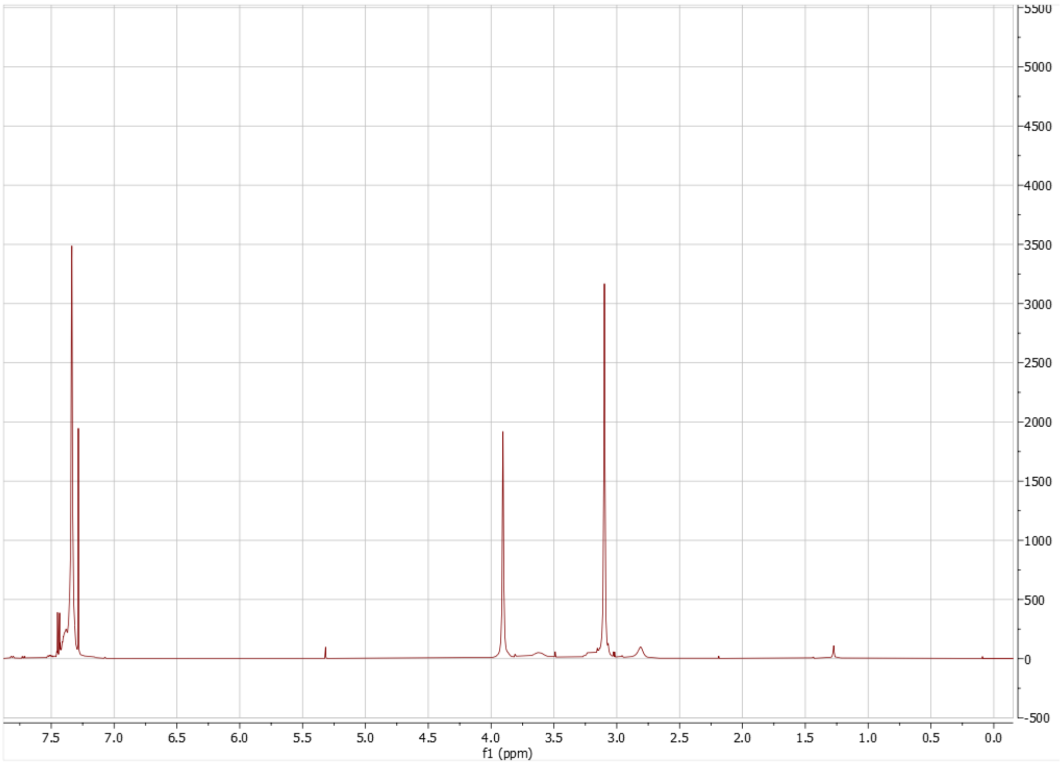

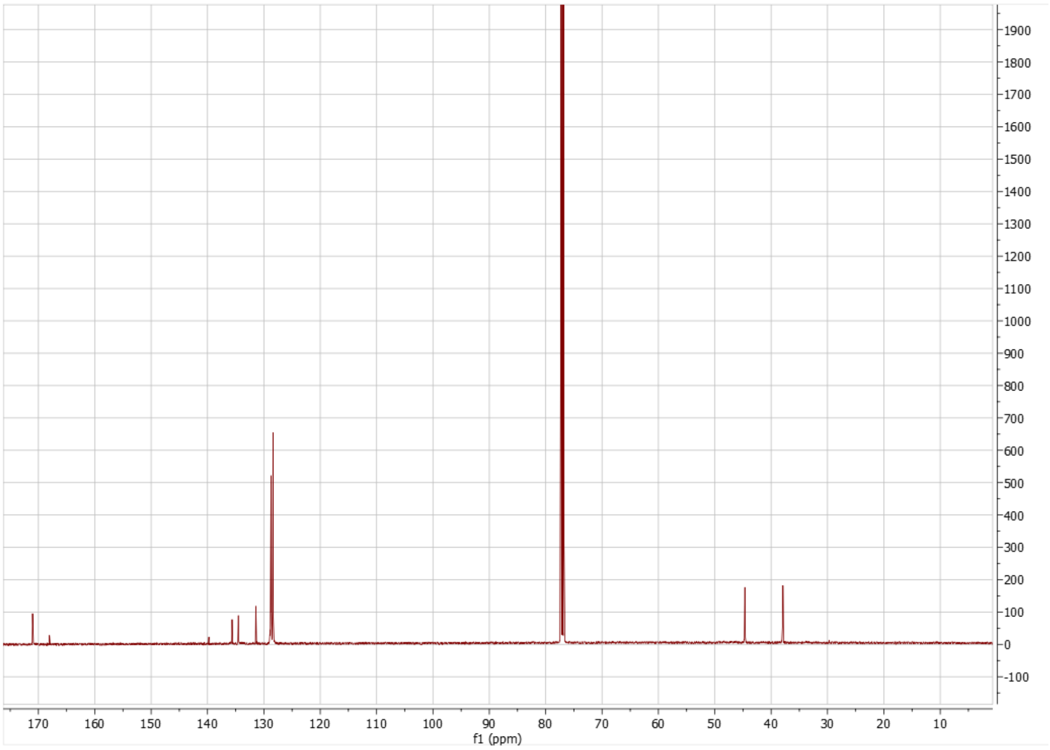

N,N'-(Ethane-1,2-diyl)bis(4-methoxy-N-methylbenzamide), L^{10}

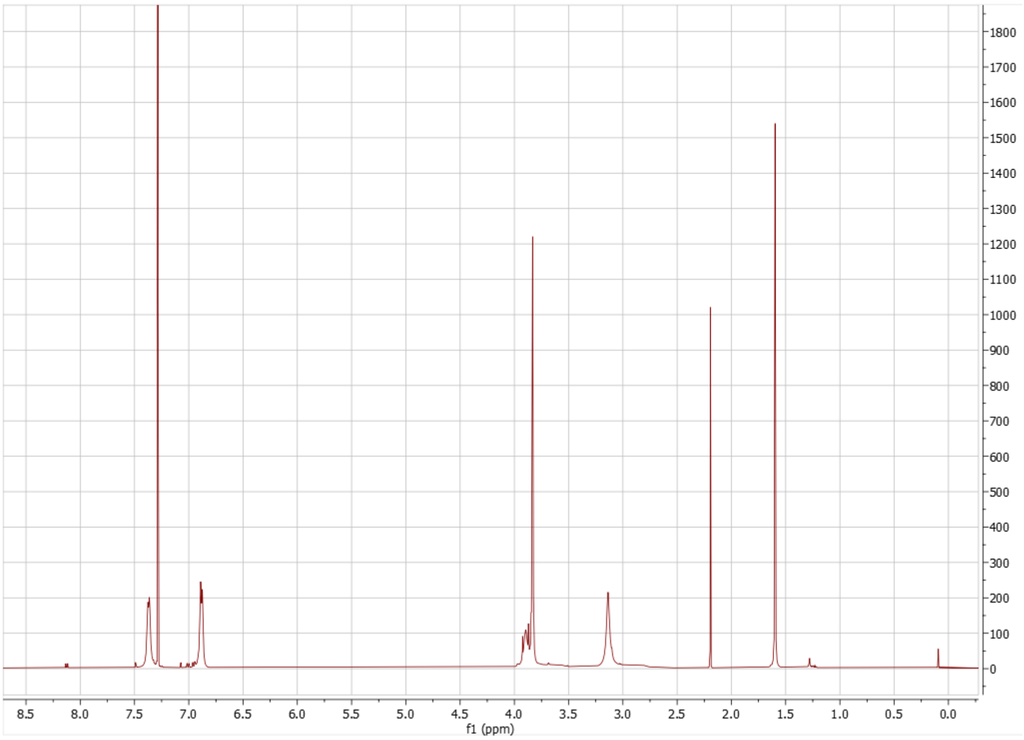

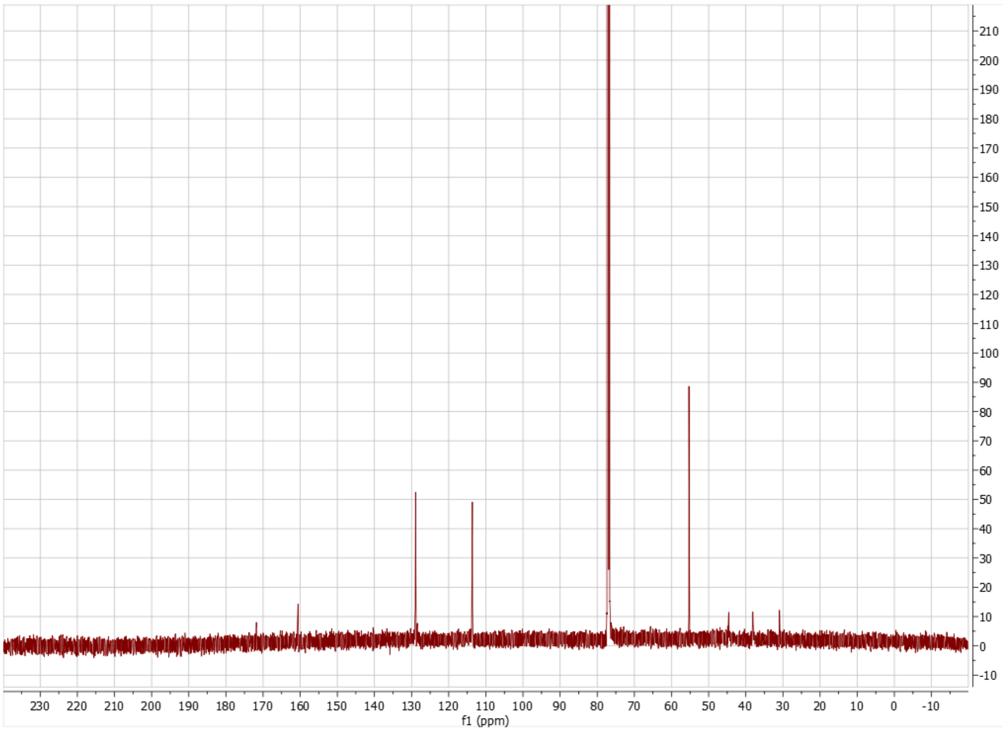

N,N'-(ethane-1,2-diyl)dibenzamide, L[11]

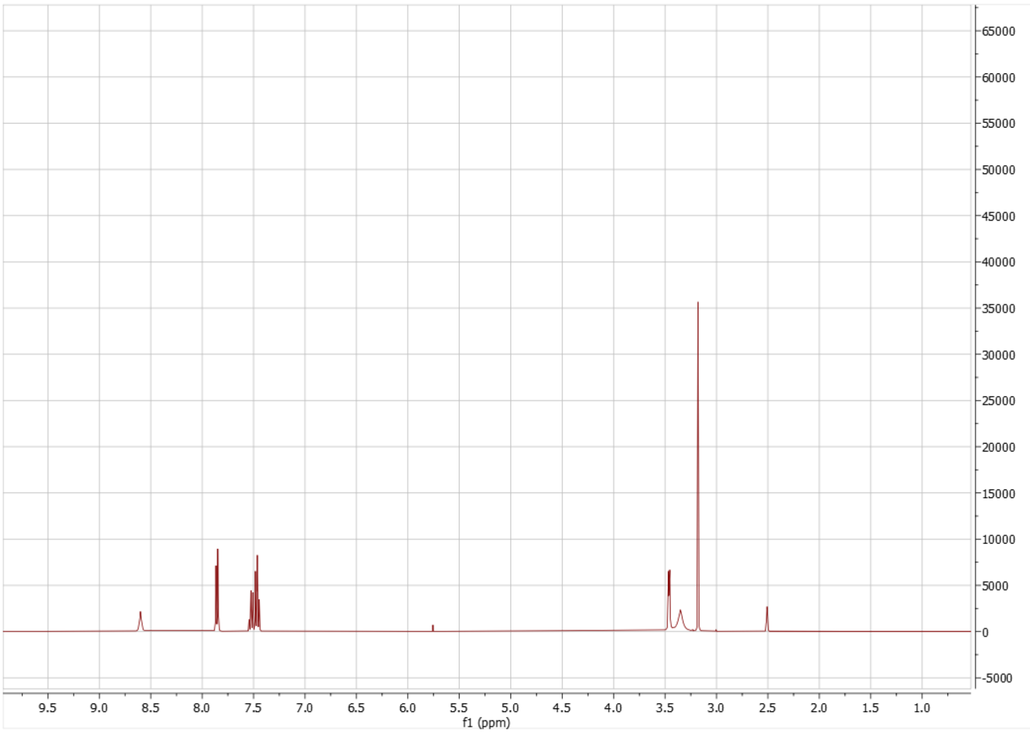

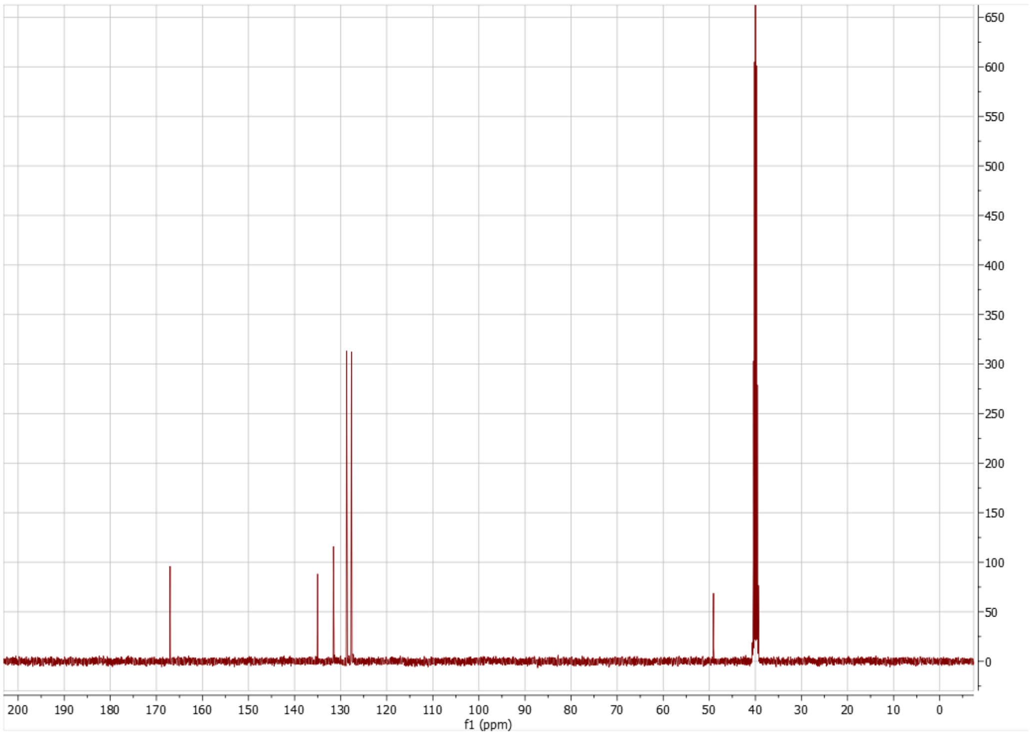

N,N'-(propane-1,3-diyl)dibenzamide, L^{12}

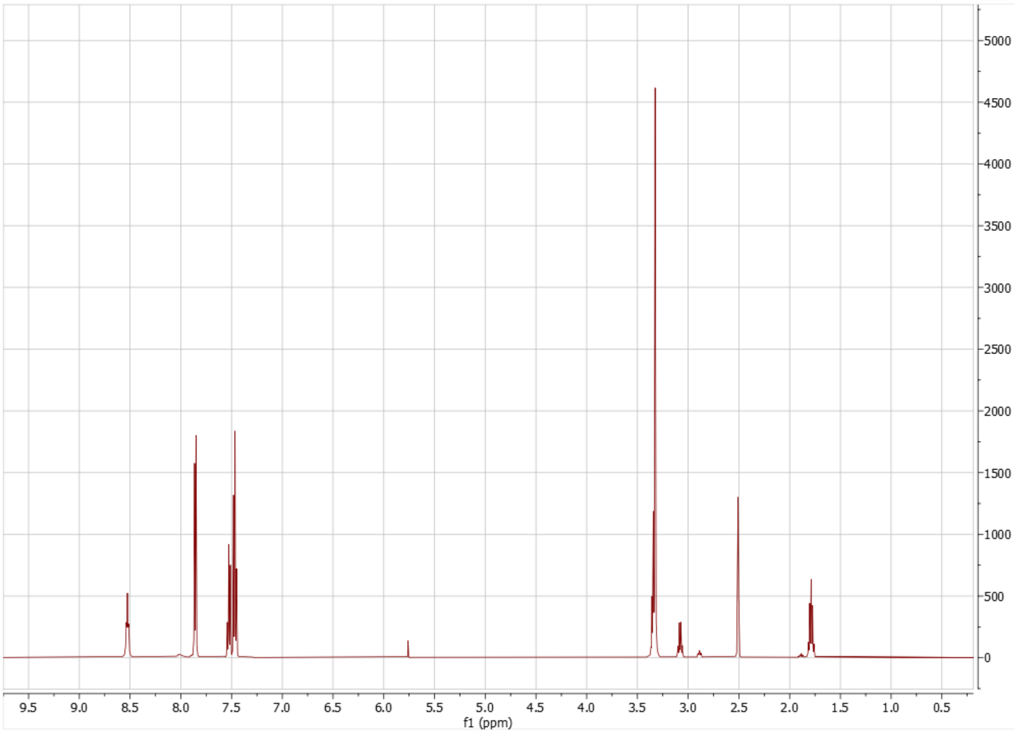

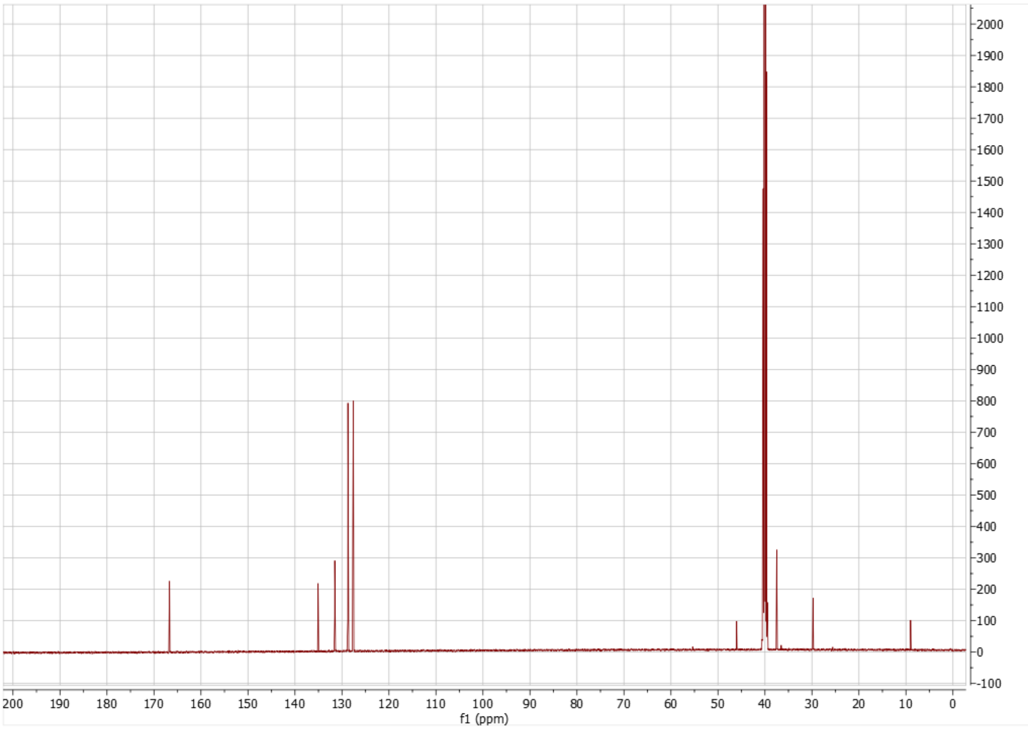

N,N'-(butane-1,4-diyl)dibenzamide, L^{13}

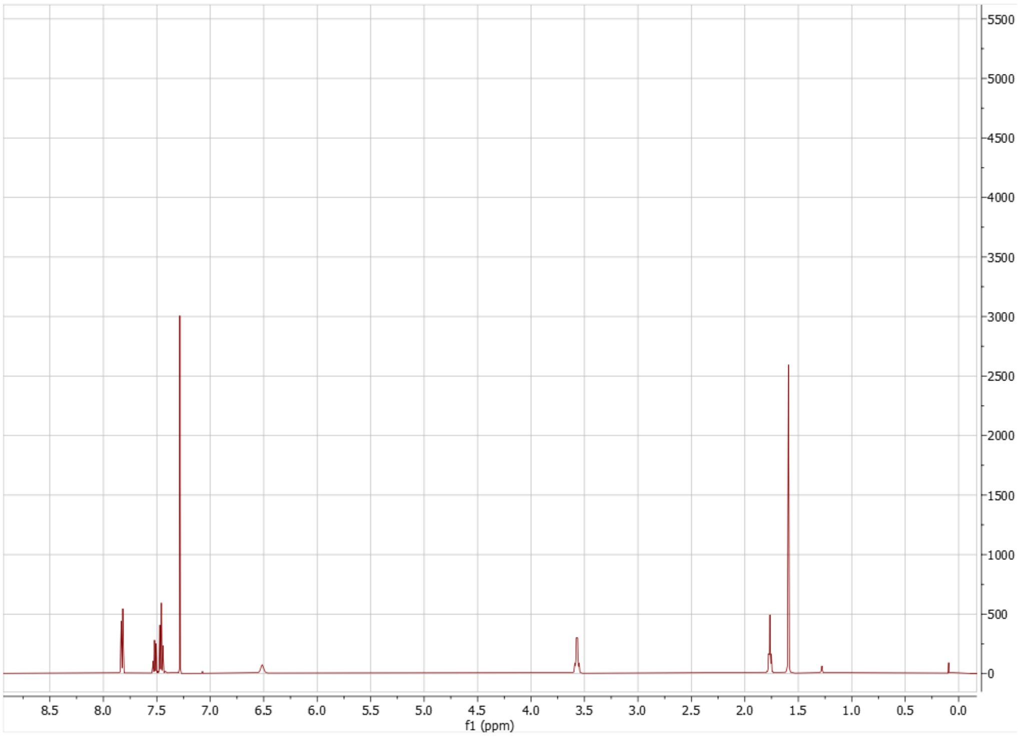

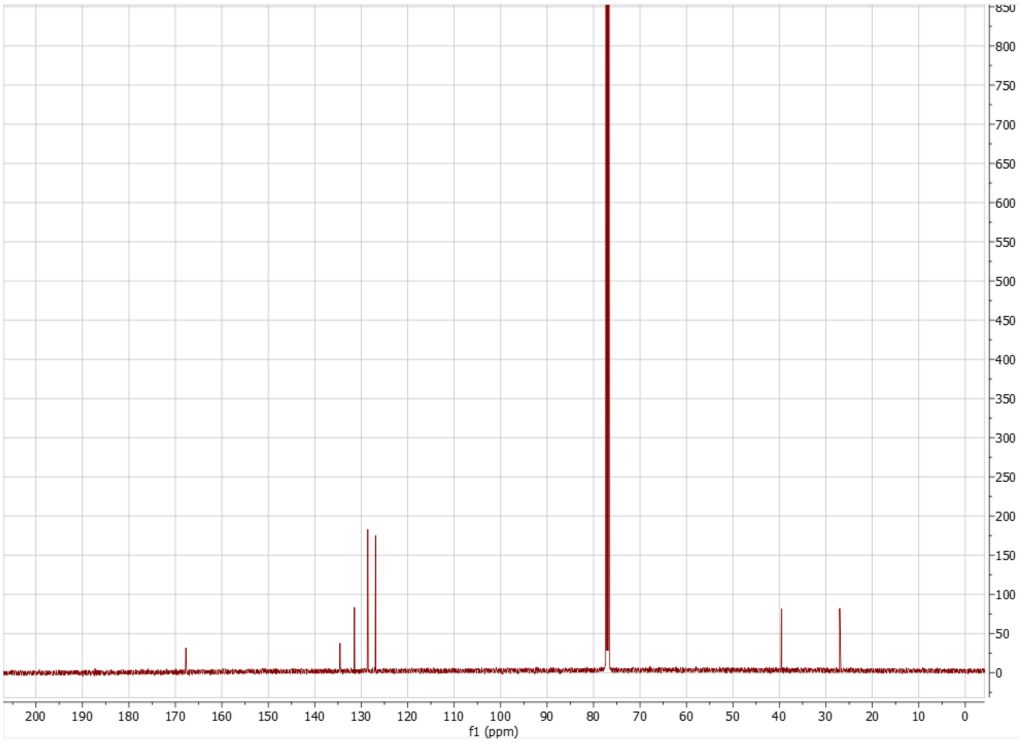

N,N'-(hexane-1,6-diyl)dibenzamide), L^{14}

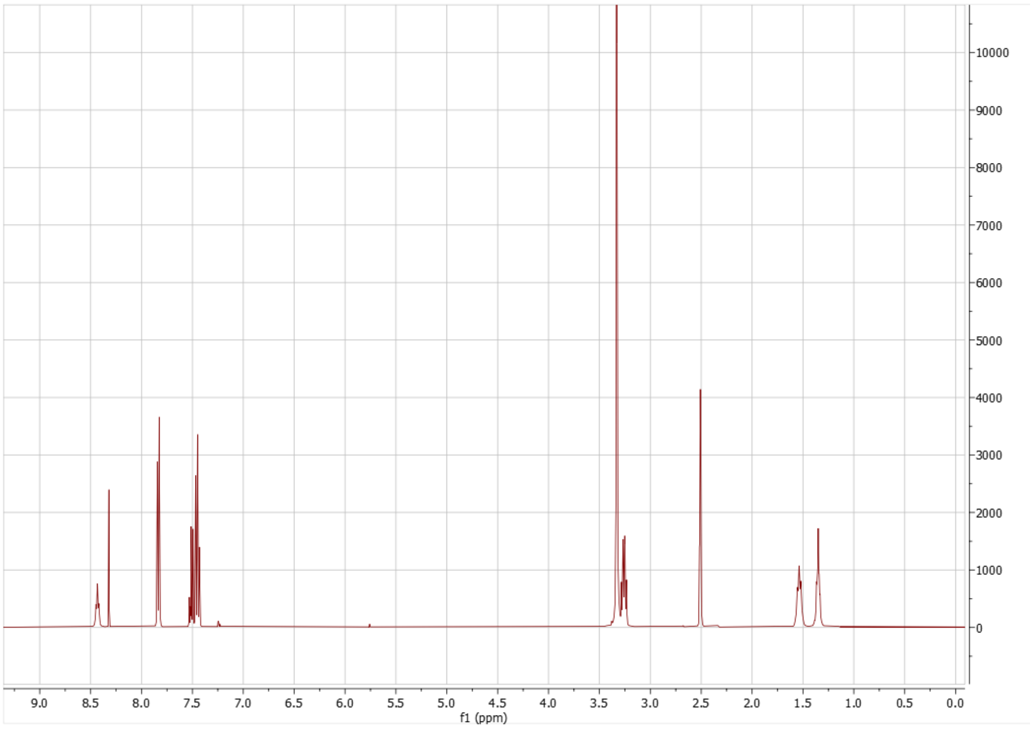

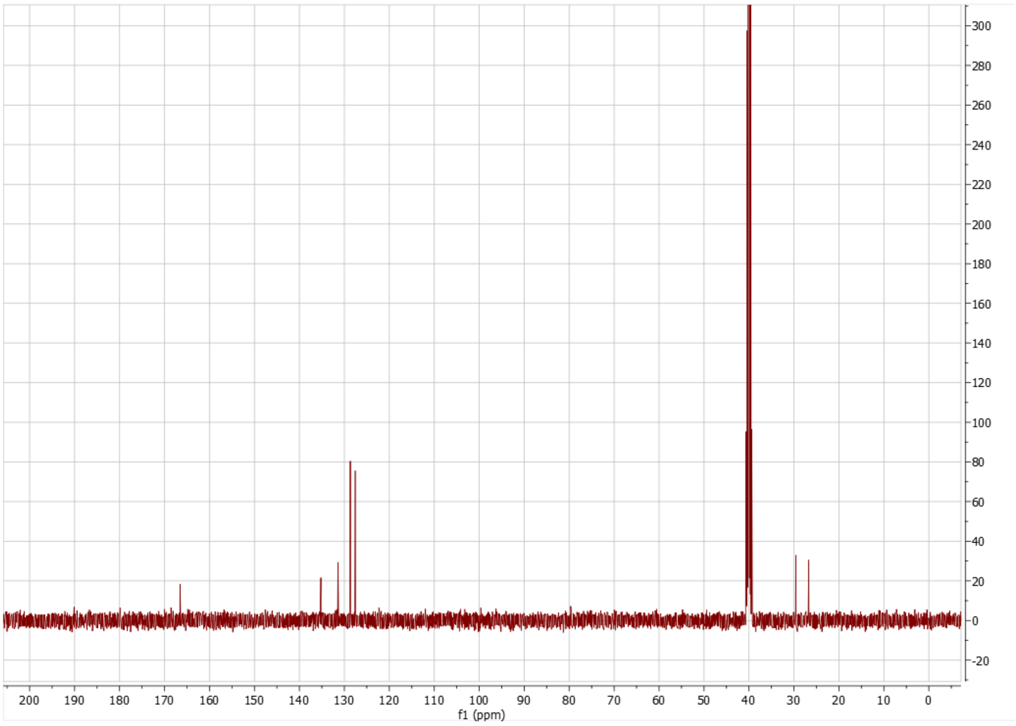

N,N’-(1,3-phenylene)dibenzamide, L[15]

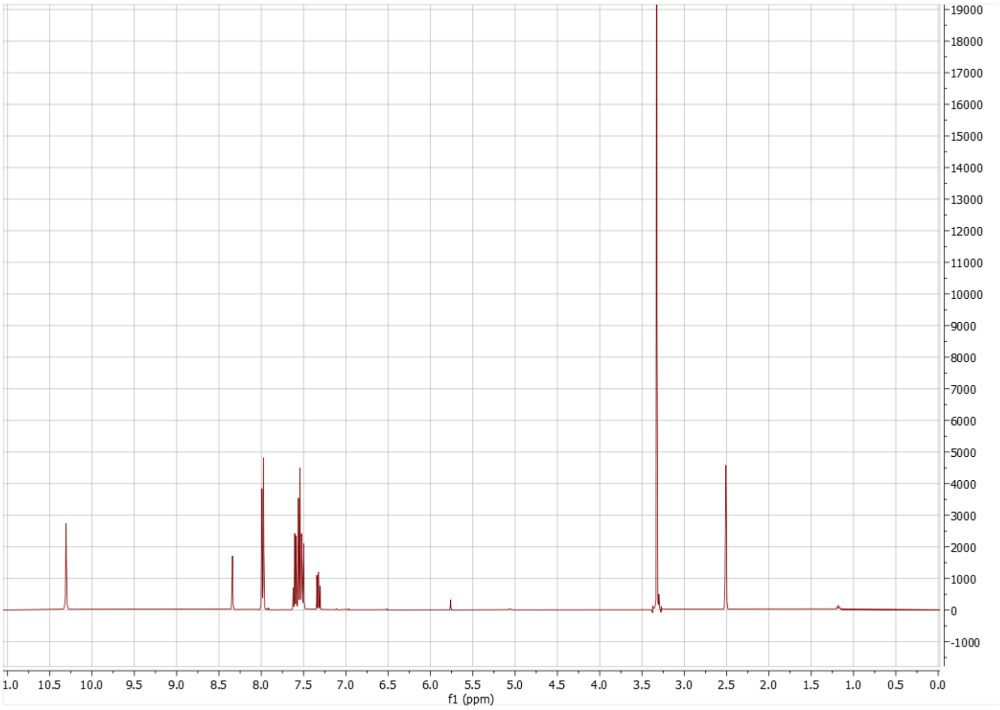

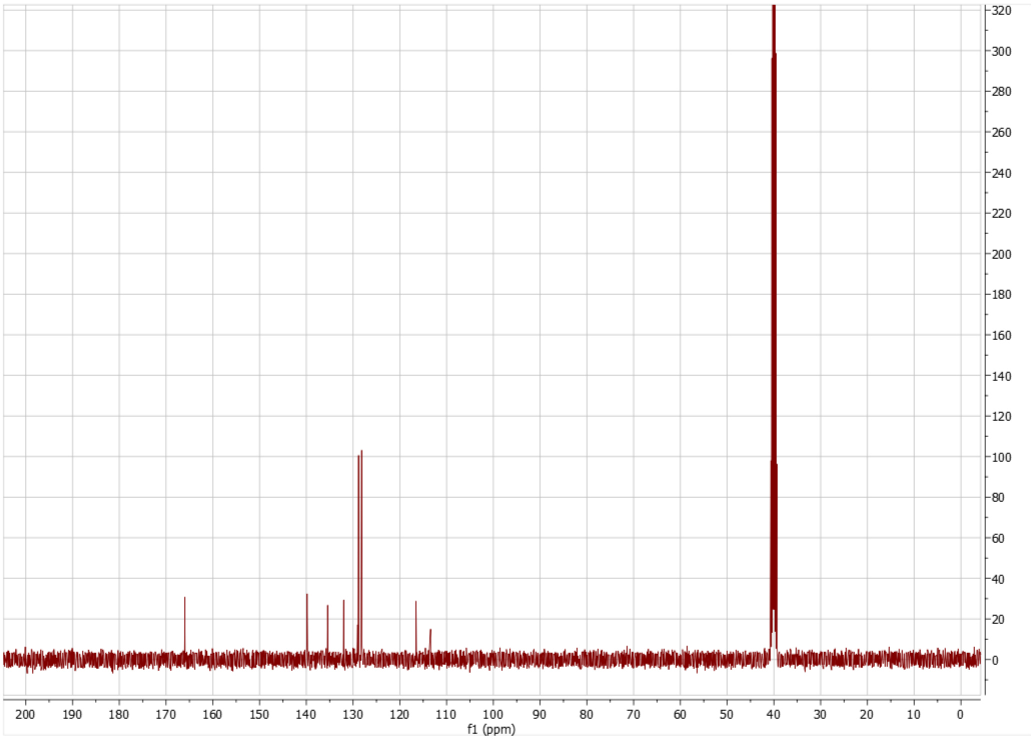

N,N’-(1,4-phenylene)dibenzamide, L[16]

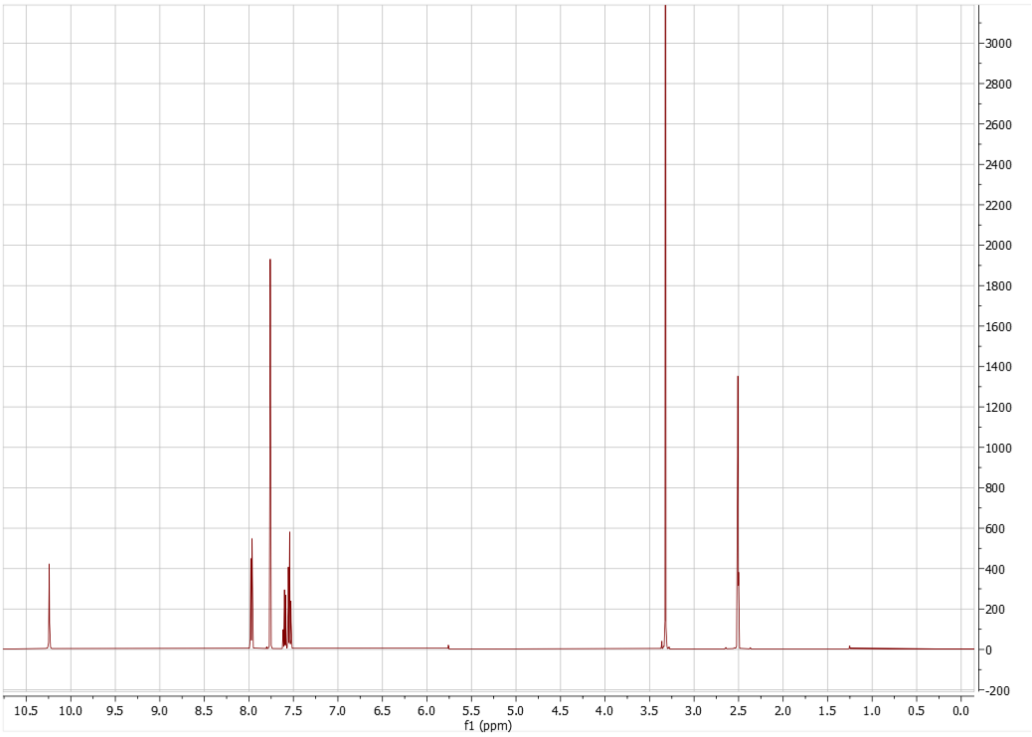

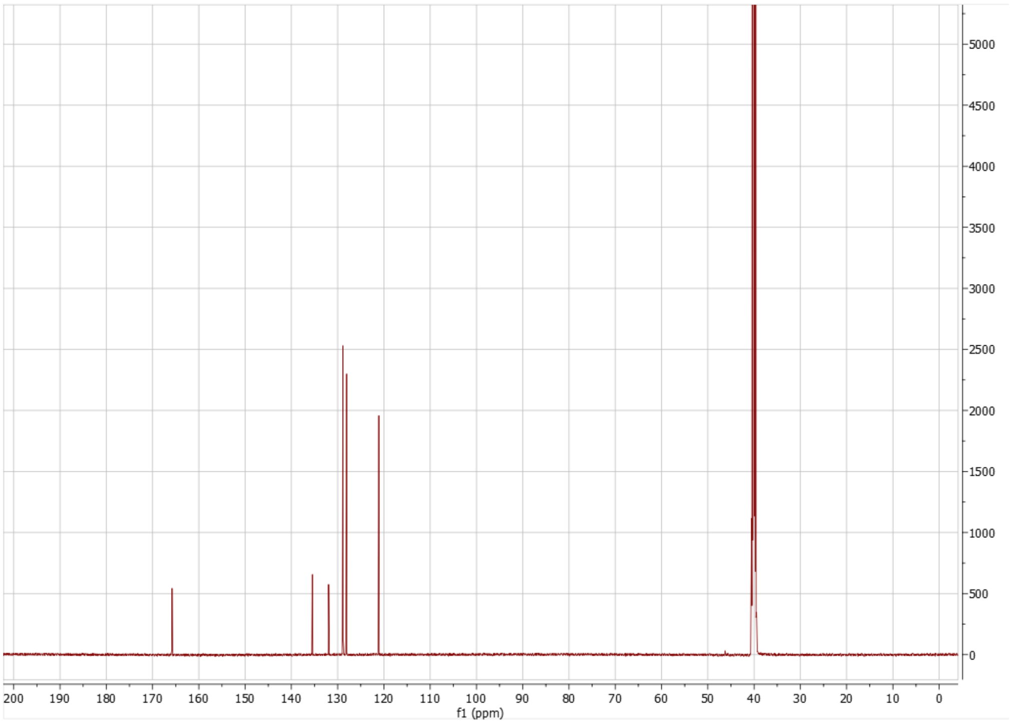

N,N’-(1,2-phenylene)dibenzamide, L^{17}

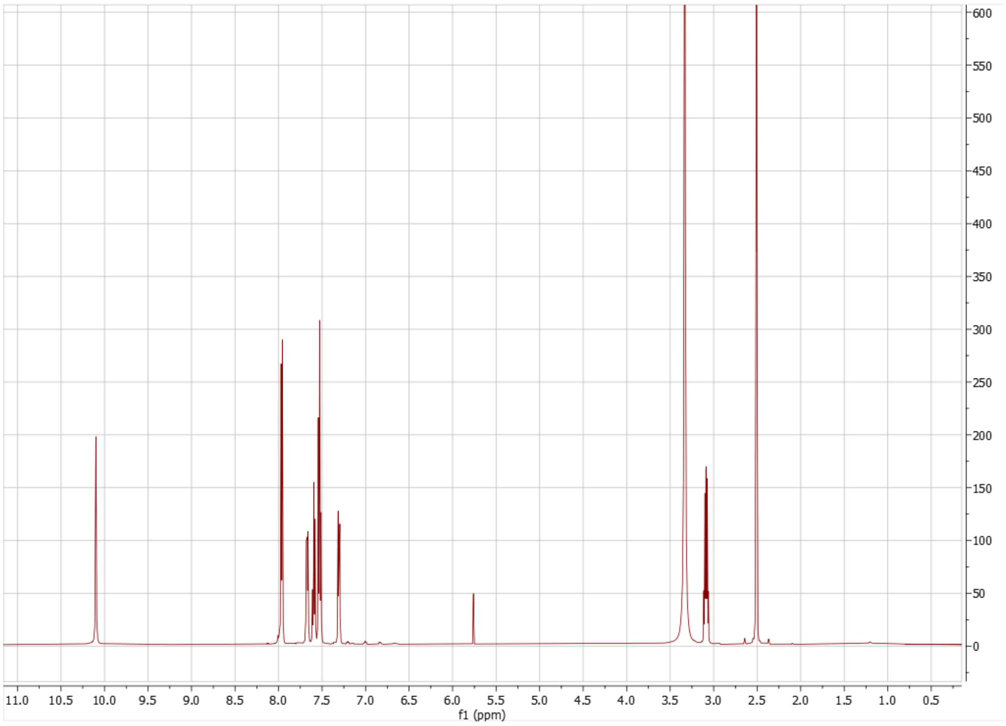

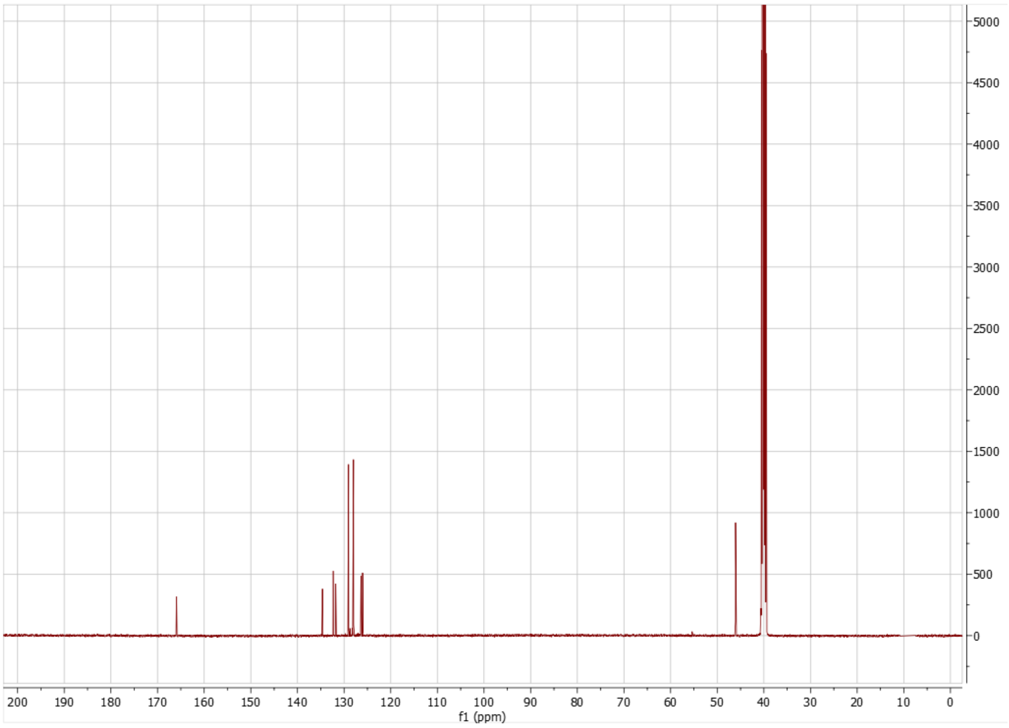

N,N’-(1,3-phenylene)bis(N-methylbenzamide), L^{18}

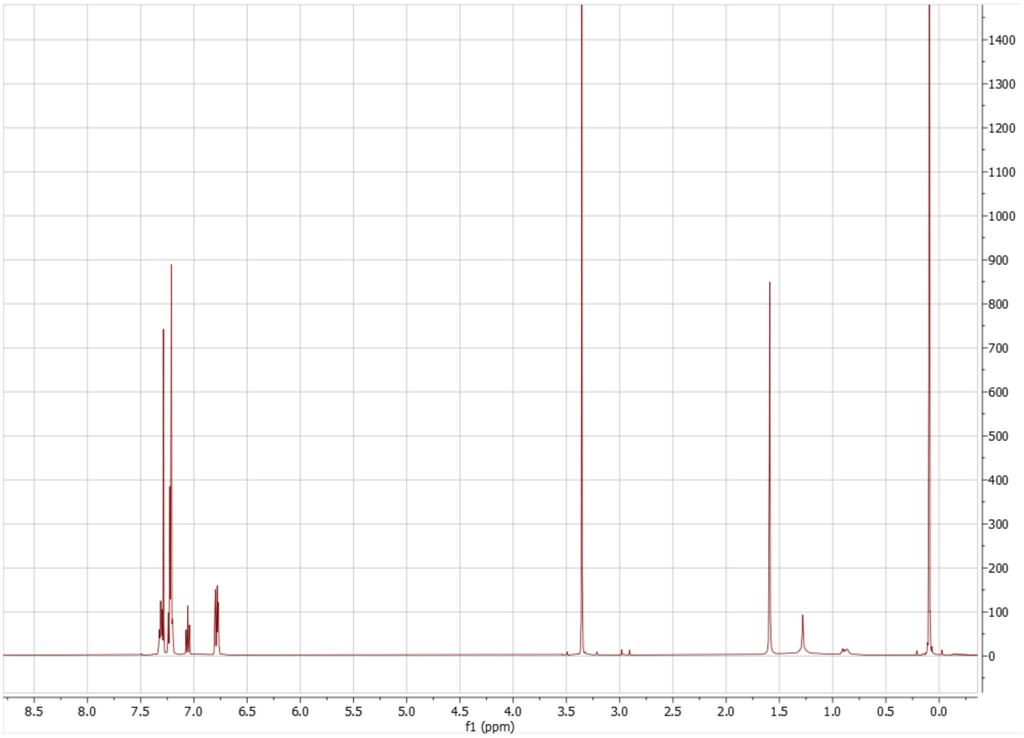

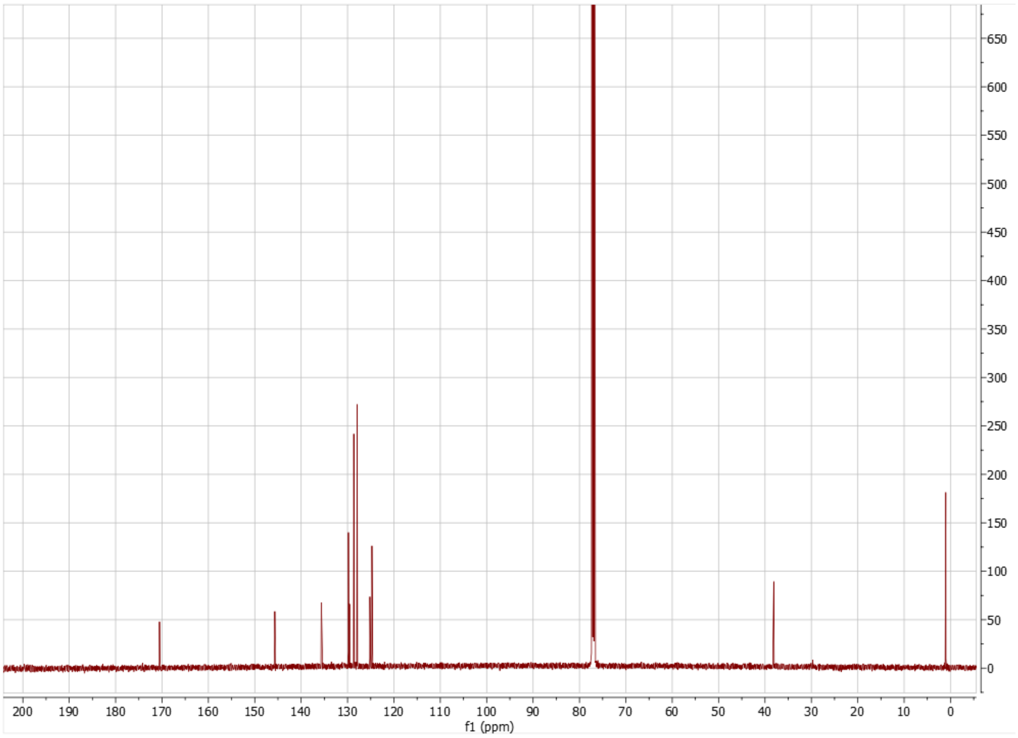

N,N’-(1,4-phenylene)bis(N-methylbenzamide), L[19]

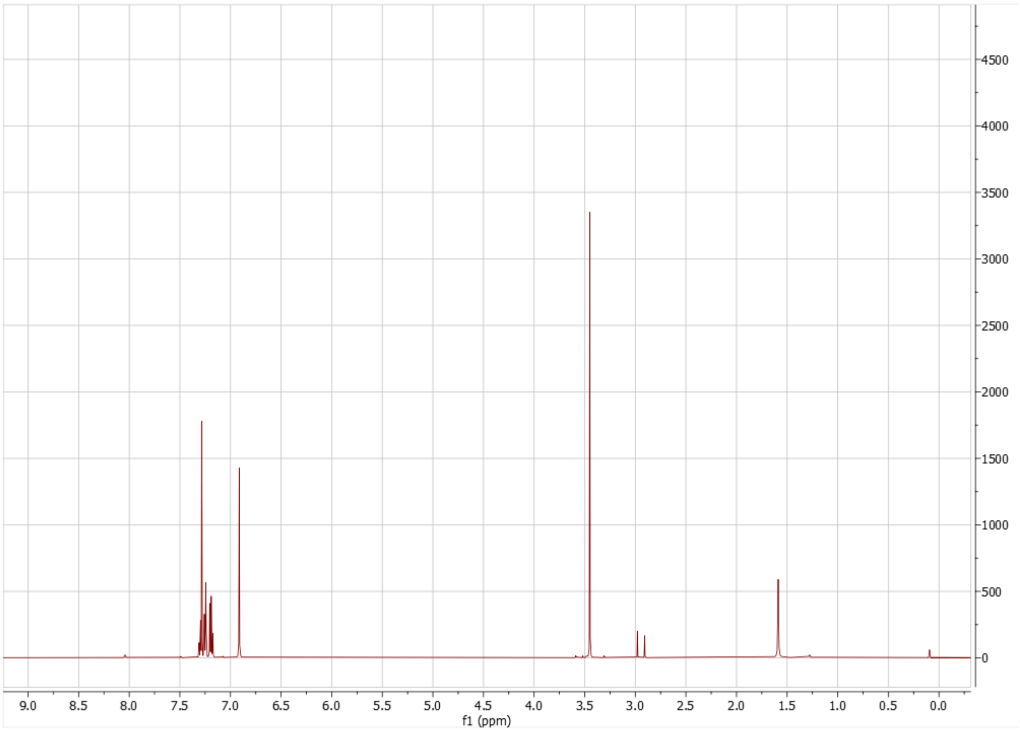

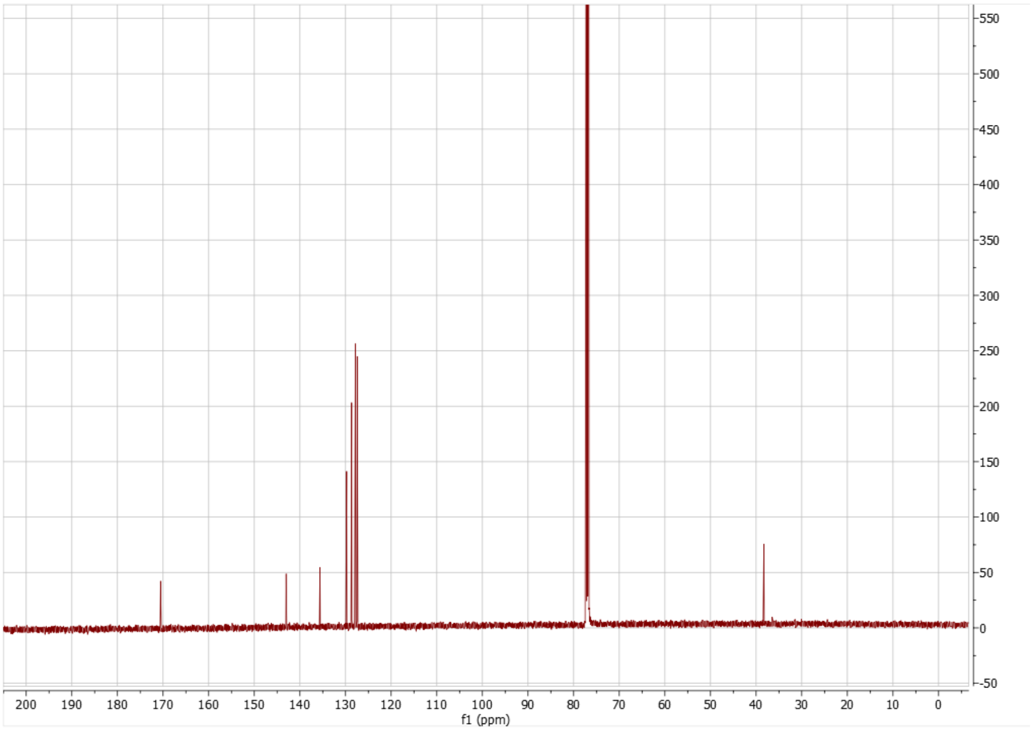

N,N'-dimethyl-N,N'-diphenylsuccinamide, L[21]

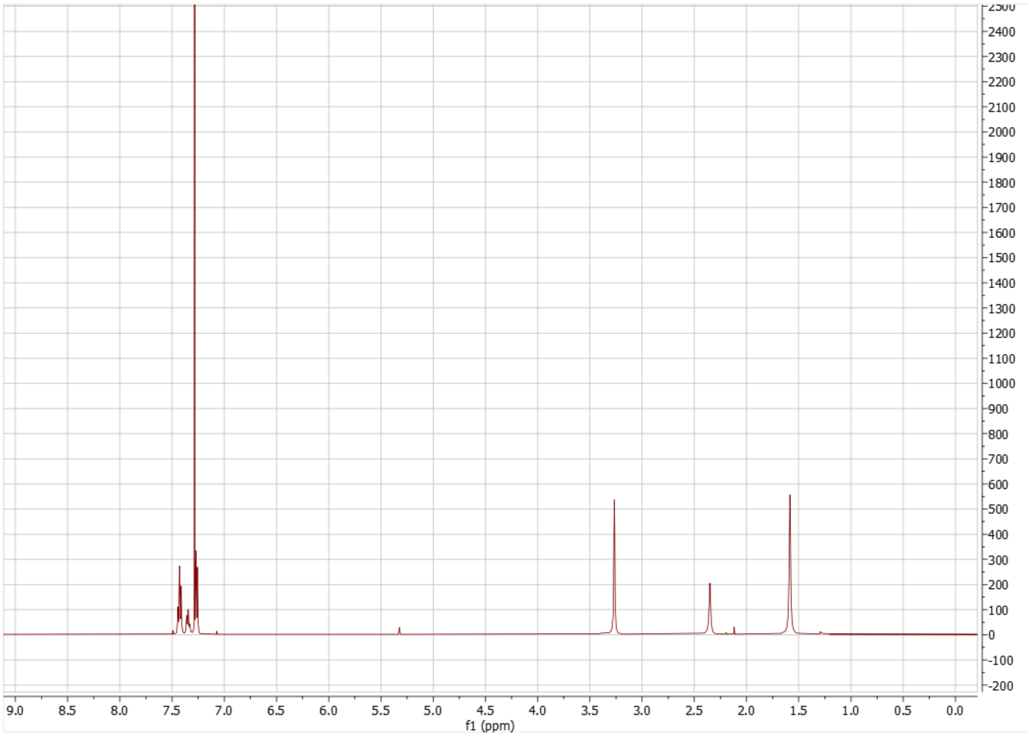

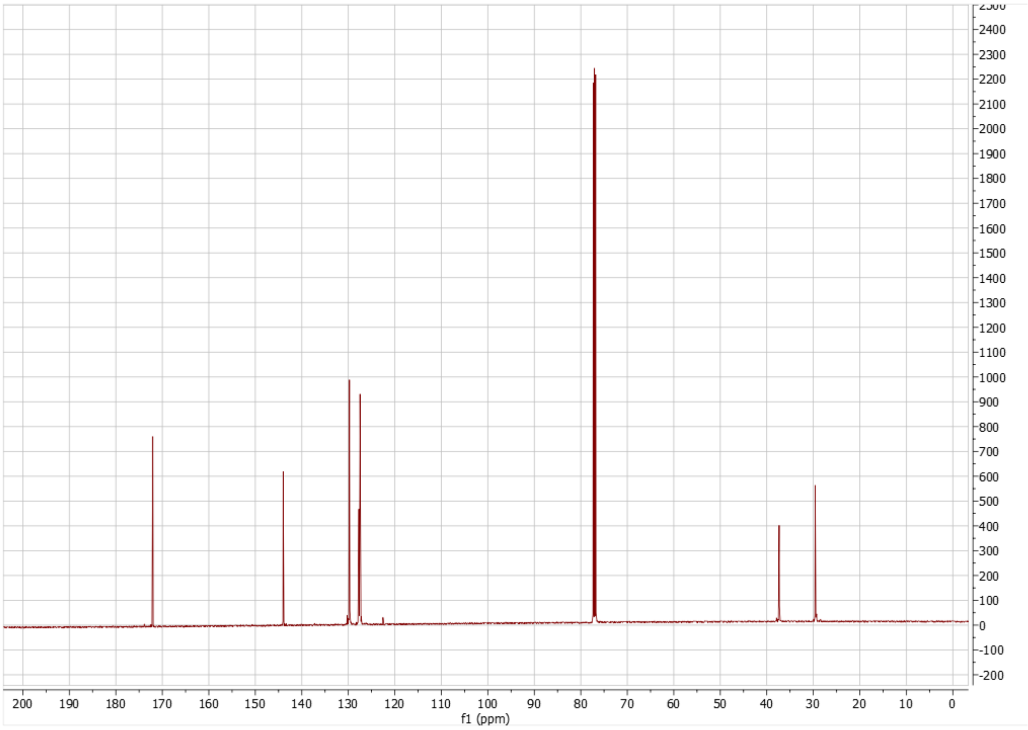

N,N′-(Ethane-1,2-diyl)bis(N-methylcyclohexanamide), L^{22}

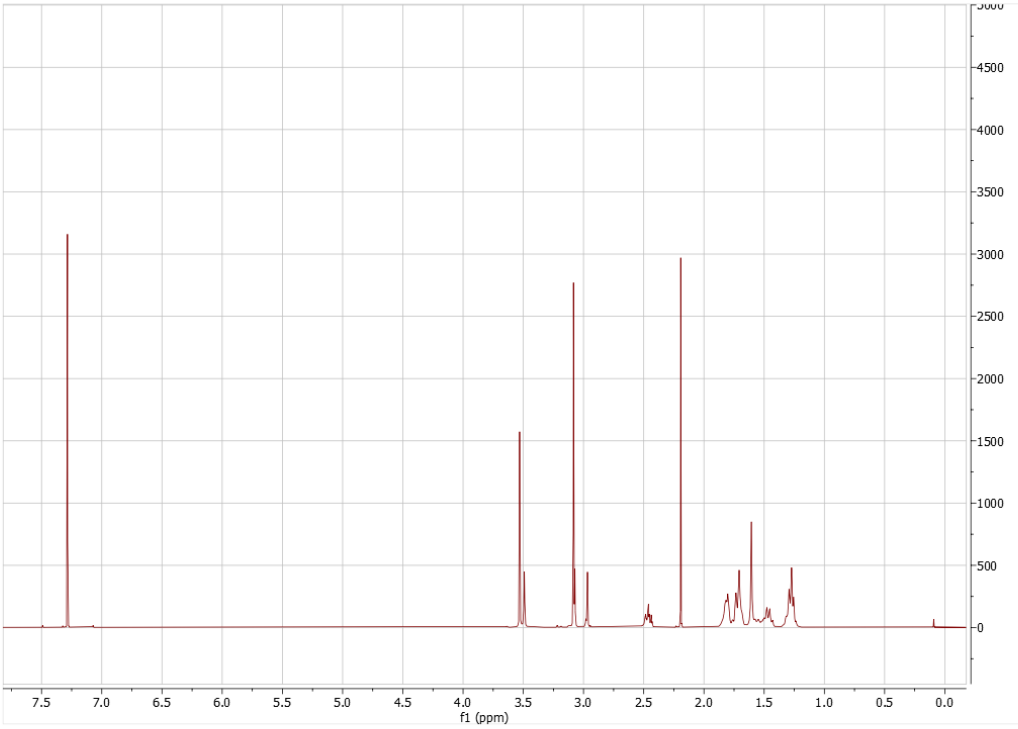

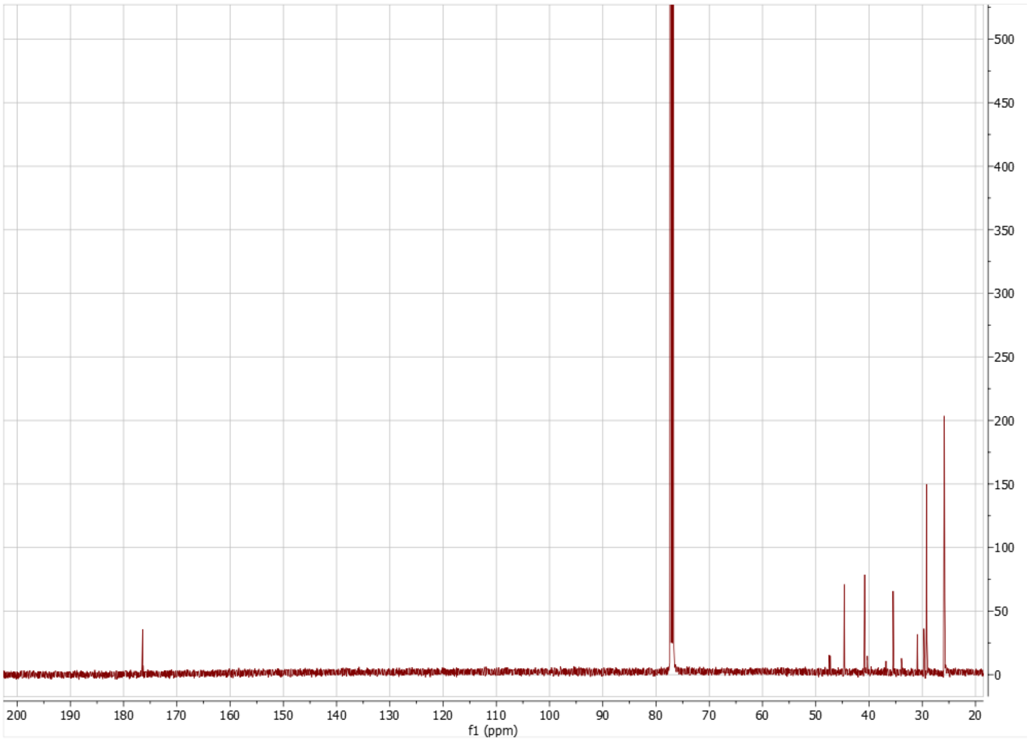

Methyltrioctylammonium iodide, [MTOA][I]